

# **Study of Rydberg blockade in thermal atomic vapor**

By

Arup Bhowmick

PHYS11201204007

National Institute of Science Education and Research  
Bhubaneswar

*A thesis submitted to the  
Board of Studies in Physical Sciences*

*In partial fulfillment of requirements  
For the Degree of*

**DOCTOR OF PHILOSOPHY**  
*of*

**HOMI BHABHA NATIONAL INSTITUTE**

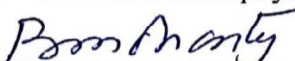


February, 2019

# Homi Bhabha National Institute<sup>1</sup>

## Recommendations of the Viva Voce Committee


As members of the Viva Voce Committee, we certify that we have read the dissertation prepared by Arup Bhowmick entitled "Study of Rydberg blockade in thermal atomic vapor" and recommend that it may be accepted as fulfilling the thesis requirement for the award of Degree of Doctor of Philosophy.

Chairman – Prof. Bedangadas Mohanty  Date: 14/2/2019


Guide / Convener – Dr. Ashok K. Mohapatra  Date: 14/02/2019

Co-guide -  Date: 14/2/19

Examiner – Prof. C. S. Unnikrishnan Date:

Member 1- Dr. Ritwick Das  Date: 14/02/2019

Member 2- Dr. V. Ravi Chandra  Date: 14-2-2019

Member 3- Dr. Rajan Jha  Date: 14/02/2019

Final approval and acceptance of this thesis is contingent upon the candidate's submission of the final copies of the thesis to HBNI.

I/We hereby certify that I/we have read this thesis prepared under my/our direction and recommend that it may be accepted as fulfilling the thesis requirement.

Date: 14/02/2019

Place: Jatani

  
Dr. Ashok K. Mohapatra


<sup>1</sup> This page is to be included only for final submission after successful completion of viva voce.



## **STATEMENT BY AUTHOR**

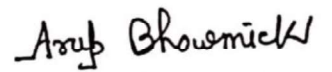
This dissertation has been submitted in partial fulfillment of requirements for an advanced degree at Homi Bhabha National Institute (HBNI) and is deposited in the Library to be made available to borrowers under rules of the HBNI.

Brief quotations from this dissertation are allowable without special permission, provided that accurate acknowledgment of source is made. Requests for permission for extended quotation from or reproduction of this manuscript in whole or in part may be granted by the Competent Authority of HBNI when in his or her judgment the proposed use of the material is in the interests of scholarship. In all other instances, however, permission must be obtained from the author.

  
(Arup Bhowmick)

## DECLARATION

I, hereby declare that the investigation presented in the thesis has been carried out by me. The work is original and has not been submitted earlier as a whole or in part for a degree/diploma at this or any other Institution/University.

  
(Arup Bhowmick)

## List of Publication arising from the thesis

### Journal:

1. "Optical nonlinearity of Rydberg electromagnetically induced transparency in thermal vapor using the optical-heterodyne-detection technique", **Arup Bhowmick**, Sushree S. Sahoo, and Ashok K. Mphapatra, Phys. Rev. A, **2016**, 94, 023839 1-7.
2. "High-sensitivity measurement of Rydberg population via two-photon excitation in atomic vapor using optical heterodyne detection technique", **Arup Bhowmick**, Dushmanta Kara, and Ashok K. Mphapatra, arXiv:1709.07750, **2017**. [Accepted in Pramana]
3. "Study of Rydberg blockade in thermal vapor", **Arup Bhowmick**, Dushmanta Kara, and Ashok K. Mphapatra, arXiv:1802.06599, **2018**. [Communicated]

### Conferences:

1. International school and conference of Atomic Physics and Quantum Optics, 2012, Goa, arranged by IISER, Pune, India.
2. School and workshop on physics of cold atom, 2013, HRI, Allahabad, India. The title of the poster presentation is "Study of optical non-linearity of Rydberg-EIT system using optical heterodyne detection technique" by **Arup Bhowmick**, and Ashok K. Mohapatra.
3. School and discussion meeting on frontiers in Light-Matter interaction, 2014, IACS, Kolkata, arranged by ICTS, Bangalore, India. The title of the poster presentation is "Rydberg blockade mediated optical non-linearity in thermal vapor using optical heterodyne detection technique" by **Arup Bhowmick**, and Ashok K. Mohapatra.
4. The International School and Conference on Quantum Information (IPQI), 2014, IOP, Bhubaneswar, India. The title of of the poster presentation is "Study of Rydberg blockade in thermal vapor" by **Arup Bhowmick**, and Ashok K. Mohapatra.
5. APS March meeting, 2016, Baltimore, USA. The title of the oral presentation is "Study

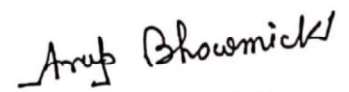
of Rydberg blockade mediated optical non-linearity in thermal vapor” by **Arup Bhowmick**, and Ashok K. Mohapatra.

**Other journal publications:**

1. "Polarization rotation of light propagating through a medium with efficient four-wave mixing and cross-phase modulation", Sushree S. Sahoo, **Arup Bhowmick** and Ashok K. Mohapatra, J. Phys. B: At. Mol. Opt. Phys., **2017**, 50, 055501 1-9.

2. "Rydberg interaction induced enhanced excitation in thermal atomic vapor", Dushmanta Kara, **Arup Bhowmick**, and Ashok K. Mohapatra, Scientific Reports, **2018**, 8, 5256 1-9.

3. Study of the effect of Multi-atom decoherence in super-atom model of the Rydberg blockade. [Under preparation]

  
(Arup Bhowmick)

*To my Mother, & Father*

---



## ACKNOWLEDGEMENTS

First I like to show my sincere gratitude to my Ph.D. supervisor Dr. Ashok K. Mohapatra. It has been an honor and privilege to be his first Ph.D. student. He taught me, both consciously and unconsciously, how nice experimental physics can be done and how deep the level of understanding can be driven. I appreciate his contribution of time and ideas which makes my Ph.D. experience adventures, productive and stimulating. His enthusiasm and optimistic point of view towards the work was contagious and motivational for me, even during tough times in the Ph.D. pursuit.

I am thankful to my lab members Dushmanta Kara, Sushree S. Sahoo, Snigdha S. Pati, Tanim Firdoshi, Akshaya Sahoo and Sujit Garain for maintaining nice research environment and their friendly attitude towards me. Specifically, Dushmanta and Tanim are also part of the project I was involved with. We had a number of nice and prompt discussions during the course of my Ph.D.

I would like to thank the former M. Sc. students and project students Sabyasachi Barik, Surya N. Sahoo, Gaurav Nirala, Gentle Dash, Ananya Sahoo, Titash, Sreya Bagchi, Piyalee Pattanaik, Soumen Mandal. We used to have nice discussions. All of them are always very friendly to me and we spent a great time together.

I would like to thank my wife for giving me wonderful life and support me one of the most difficult days of my life.

I like to thank my batch-mates Sougata, Avenendra, Srijani, Rita, Pratick, Koushik, Mukesh, Samir, Kishora, Vantari, Sony, Shrikant for their psychological support throughout the time. I also like to thank my four best friends Subhajit Das, Sandeep Chaubey, Debadrita Dutta and Eeshita Manna for always being my side.

I want to thank my siblings Anindia, Tiyaasha, Rima, Riku, Sushmita, Rashmita and Souvik to make my life beautiful.

Last but not the least, I like to thank my mother for everything and patiently experiencing my ups and downs of my Ph.D. life.

# Contents

Table of Contents . . . . .	xii
List of Figures . . . . .	xxvi
List of Tables . . . . .	xxviii
<b>1 Introduction</b>	<b>1</b>
1.1 Rydberg blockade and enhanced optical non-linearity . . . . .	2
1.2 Review of the study of Rydberg blockade in cold atoms . . . . .	3
1.3 Motivation to study of Rydberg atoms in thermal vapor . . . . .	4
1.4 Review of the Rydberg excitations in thermal atomic ensemble . . . . .	4
1.5 Contribution of the thesis . . . . .	5
1.6 Layout of the thesis . . . . .	6
<b>2 Rydberg atoms and Rydberg interactions</b>	<b>13</b>
2.1 Quantum defect . . . . .	14
2.2 Scaling laws of Rydberg atoms . . . . .	15
2.3 Interacting Rydberg atoms . . . . .	17
2.3.1 van der Waals interaction . . . . .	17
2.3.2 Dipole-dipole interaction . . . . .	18
2.3.3 Rydberg blockade interaction . . . . .	19
2.3.4 Rydberg anti-blockade interaction . . . . .	21
2.4 Conclusion . . . . .	23
<b>3 Atomic properties and atom-light interaction</b>	<b>28</b>
3.1 Atomic properties . . . . .	28
3.1.1 Fine structure splitting . . . . .	29
3.1.2 Hyperfine structure splitting . . . . .	30
3.1.3 Zeeman effect on hyperfine states . . . . .	31
3.2 Atom light interaction . . . . .	32

3.2.1	2-level system . . . . .	32
3.2.2	For the case, $\Delta \gg  \Omega $ . . . . .	33
3.2.3	For the case, $\Delta = 0$ . . . . .	34
3.2.4	Optical Bloch equation for 2-level system . . . . .	34
3.2.5	Optical Bloch equation for 3-level system . . . . .	35
3.2.6	Large probe detuning in two-photon resonance process . . . . .	39
3.2.7	Adiabatic elimination of intermediate state . . . . .	39
3.2.8	Optical Bloch equations for effective 2-level system . . . . .	40
3.3	Hyperfine pumping spectroscopy (HPS) . . . . .	42
3.4	Laser stabilisation using HPS . . . . .	45
<b>4</b>	<b>Study of Rydberg EIT using OHDT</b>	<b>50</b>
4.1	Rydberg-EIT . . . . .	50
4.2	Optical heterodyne detection technique . . . . .	53
4.2.1	Measurement of absorption and dispersion of a probe field . . . . .	56
4.2.2	Demonstration of Rydberg EIT using OHDT . . . . .	57
4.3	Model of EIT using OHDT . . . . .	60
4.3.1	Construction of master equation . . . . .	62
4.3.2	0th order OBE . . . . .	62
4.3.3	1st order OBE . . . . .	63
4.3.4	Calculation of susceptibility . . . . .	65
4.3.5	Reduced OBE . . . . .	67
4.4	The EIT peak of the weak probe dressed by the strong probe beam . . . . .	69
4.5	Study of Optical nonlinearity of Rydberg-EIT medium . . . . .	70
4.5.1	Nonlinearity measurement from transmission . . . . .	70
4.5.2	SPM at weak probe limit . . . . .	71
4.5.3	Measurement of nonlinearity . . . . .	73
4.6	Conclusion and outlook . . . . .	74
<b>5</b>	<b>Study of two-photon Rydberg excitation using OHDT</b>	<b>79</b>
5.1	OHDT to observe two-photon Rydberg excitation . . . . .	79
5.1.1	Atomic level scheme . . . . .	80
5.1.2	AOM setup to generate OHDT probes . . . . .	81
5.1.3	Experimental realisation of two-photon Rydberg excitation . . . . .	82

5.2	Model for two-photon Rydberg excitation . . . . .	85
5.2.1	Calculation of susceptibility . . . . .	87
5.2.2	Lineshape of dispersion . . . . .	87
5.3	Intensity dependent dispersion . . . . .	89
5.4	Calibration of phase sensitivity of the electronic wave-form mixer . . . . .	91
5.5	Sensitivity and the precision of the measurement . . . . .	93
5.6	Precision of the Rydberg population measurement . . . . .	95
5.7	Comparison between OHDT and direct absorption measurement (DAM) . . . .	96
5.8	Conclusion . . . . .	98
<b>6</b>	<b>Study of Rydberg blockade in thermal vapor</b>	<b>103</b>
6.1	Initial experiment to realise Rydberg blockade . . . . .	104
6.1.1	Classical model of Rydberg blockade . . . . .	105
6.1.2	Intensity dependent dispersion . . . . .	106
6.1.3	Population dependent dephasing . . . . .	107
6.2	Superatom model of Rydberg blockade . . . . .	108
6.2.1	Many-body superatom equation (MSE) of Rydberg blockade . . . . .	111
6.2.2	Dephasing method . . . . .	113
6.2.3	Superatom dephasing . . . . .	113
6.3	Analysis of density dependent phase-shift measurement using MSE . . . . .	115
6.3.1	Gain of the OHDT experiment . . . . .	115
6.3.2	Density dependent phase shift and the evaluation of Rydberg blockade radius $r_b(n)$ . . . . .	118
6.3.3	$r_b^3$ scaling with respect to the principal quantum number $n^*$ . . . . .	123
6.4	Conclusion and application . . . . .	124
<b>7</b>	<b>Experiment towards Ultra-cold atoms</b>	<b>131</b>
7.1	Design of cold-atom setup . . . . .	132
7.2	Optical setup . . . . .	132
7.2.1	Generation and stabilisation of repump laser . . . . .	134
7.2.2	Stabilisation of TA-SHG-Pro . . . . .	135
7.3	Vacuum setup . . . . .	136
7.3.1	Design of vacuum chamber and flange multiplexer . . . . .	137
7.3.2	Integrated mechanical design for vacuum setup . . . . .	139

7.3.3	Opto-Mechanical cage system design . . . . .	140
<b>8</b>	<b>Summary and future plan</b>	<b>146</b>
<b>Appendix A</b>	<b>Design of a fast photo-detector</b>	<b>152</b>
<b>Appendix B</b>	<b>Electronic design of AOM driver</b>	<b>154</b>
<b>Appendix C</b>	<b>Fitting of a function numerically and goodness of fitting</b>	<b>156</b>
C.1	$\chi^2$ -fitting . . . . .	156
C.2	Goodness of the fitting . . . . .	157



## Synopsis

Study of Rydberg atoms has decades of history. When the highly excited Hydrogen atom was first studied in atomic spectroscopy for the Balmer series, it became the foundation of Bohr's atom modelling [1, 2]. These early studies prompted then the research going towards the high resolution absorption spectroscopy [3, 4]. The exotic properties of Rydberg atoms such as scaling laws [5] and high sensitivity of external electric field [6, 7] of Rydberg atoms make the physics very rich. The dynamical properties of Rydberg atoms explored the relationship between the stationary description of quantum wave function and the classical orbital dynamics of electron wave packets around the atomic ion [8–10]. Later on the long lifetime and the huge dipole moment of Rydberg atoms inside a high-Q cavity allowed the quantum nondemolition photon state measurement [11, 12]. With the advent of laser cooling and laser trapping, a new era of Rydberg interaction studies has been introduced. The strong interaction between two Rydberg atoms gives rise to many body collective behaviour [13, 14]. This collective behaviour of ultra-cold Rydberg atoms enhances Kerr type nonlinearity at the single photon level [15–17]. This area of study introduces the historical foundation of strong photon-photon interaction and naturally address a fundamental question, that is using this phenomenon is it possible to entangle photons which could lead to building of quantum computer using photons [18]. The nature of Rydberg nonlinearity is fundamentally different because of the Rydberg blockade phenomenon [19]. In an ensemble of dense gas, the many-body Rydberg state is shifted outside the line-width by a single Rydberg excitation within a particular length scale. The phenomenon is called Rydberg blockade and the length scale is called Rydberg blockade radius. Rydberg blockade can increase Kerr nonlinearity to a great extent [16, 20].

The objective of this thesis is to inspect the existence of Rydberg blockade due to strong van der Waals interaction in thermal atomic vapor. The strength of the interaction,  $C_6$  increases with principal quantum number of Rydberg excited atom as  $n^{*11}$ , where  $n^* = n - \delta(n)$  with  $\delta(n)$  is the quantum defect. The Rydberg blockade radius is defined as the length scale where the interaction shift is equal to the line-width of the excitation. For van der Waals interaction, Rydberg blockade radius for cold atom system is defined as  $r_b^{(CA)} = \sqrt[6]{\frac{C_6}{\hbar\Omega}}$  and that of thermal atoms is  $r_b^{(TA)} = \sqrt[6]{\frac{C_6}{\hbar\Gamma_d}}$ , where  $\Omega$  is the Rabi frequency and  $\Gamma_d$  is the doppler width. The ratio between these two radii is given by,  $\frac{r_b^{(CA)}}{r_b^{(TA)}} = \sqrt[6]{\frac{\Gamma_d}{\Omega}} \approx 2.5$  for  $\Omega = 5$  MHz and  $\Gamma_d = 1$  GHz. This calculation shows that the Rydberg blockade radius in thermal atoms is in the range of 2-3 factor lesser than that of cold atoms. This simple inspection motivates the investigation

of Rydberg blockade in thermal atomic ensemble. In cold atomic system the Rydberg blockade interaction has been studied by detecting Rydberg excited atom using micro-channel plate (MCP) [21]. In the thermal vapor cell, it is difficult to pursue experiment with MCP because of the presence of surface charges. We developed the optical heterodyne detection technique (OHDT) to observe the Rydberg excitation in thermal vapor and first use the technique to study Rydberg EIT (electromagnetically induced transparency).

In this technique, two light fields are generated from an external cavity diode laser (ECDL) and a frequency offset of 50 MHz was introduced using acousto-optic modulators (AOM). Both of the beams were superimposed using a polarising beam splitter (PBS). The interference beat signals of the light fields were detected using two fast photo detectors by introducing polarisers at both output ports of PBS. The beat signal directly measured at one output port of the PBS is called reference beat. The other beat signal was detected after passing the probe fields through a magnetically shielded rubidium vapor cell of 5 cm length and is called as signal beat. A coupling laser beam derived from a frequency doubled diode laser operating at 478-482 nm counter-propagates the probe beams through the vapor cell. Since the frequency offset between the probe fields is larger than the line-width of the Rydberg EIT resonance in thermal vapor [24], they undergo different phase shift and absorption while scanning the coupling laser through EIT resonance. Since the signal and reference beats are from the same interferometer, the noise due to vibration or acoustic disturbances is strongly suppressed. The intensity of the superimposed probe fields at the signal detector is,  $I_s \propto |E_1|^2 e^{-k_p l \text{Im}[\chi(\omega)]} + |E_2|^2 e^{-k_p l \text{Im}[\chi(\omega+\delta)]} + 2|E_1||E_2| e^{-k_p l \text{Im}[\chi(\omega)+\chi(\omega+\delta)]} \cos(\delta t + \phi_s + \phi_{off})$ .  $E_1$  and  $E_2$  are the electric-field amplitudes of the strong and weak probes respectively. The length of the rubidium vapor cell is given by  $l$ .  $\phi_s = \frac{k_p l}{2} \text{Re}[\chi_{3L}(\omega) - \chi_{3L}(\omega + \delta)]$  and  $\phi_{off}$  is the phase difference of the probe beams in the absence of the coupling field. We define the susceptibility due to two photon resonance of two probes as,  $\chi_{3L}(\omega_p) = \chi(\omega_p) - \chi_{2L}(\omega_p)$  and  $\chi_{3L}(\omega_p + \delta) = \chi(\omega_p + \delta) - \chi_{2L}(\omega_p + \delta)$ , where  $\chi_{2L}$  is the susceptibility of probe in absence of coupling laser. The signal detected in the detector in presence of a high-pass filter,  $D_s = A_s e^{-\frac{k_p l}{2} \text{Im}[\chi_{3L}(\omega) - \chi_{3L}(\omega + \delta)]} \cos(\delta t + \phi_s + \phi_{off})$ , where  $A_s \propto 2|E_1||E_2|$ . The beat signal detected at the reference detector,  $D_r = A_r \cos(\delta t + \phi_r)$ , where  $A_r$  and  $\phi_r$  are the amplitude and the phase of the reference beat. The two beat signals are multiplied by an electronic waveform mixer and pass through a low pass filter which gives,  $S_L = 2A_r A_s e^{-\frac{k_p l}{2} \text{Im}[\chi_{3L}(\omega) + \chi_{3L}(\omega + \delta)]} \cos(\phi_s + \phi_{off})$ . Assuming  $\phi_s$  to be small and setting  $\phi_{off} = 0$ , the signal  $S_L$  becomes sensitive to the amplitude

of probe beams and hence gives the information about transmission. By setting  $\phi_{off} = \pi/2$ ,  $S_L$  becomes strongly sensitive to  $\phi_s$  and hence the refractive index of the probe due to Rydberg-EIT can be measured. The signal becomes,  $S_L \approx 2A_s A_r e^{-\frac{k_p l}{2} \text{Im}[\chi_{3L}(\omega) + \chi_{3L}(\omega + \delta)]} \phi_s$ . The observed dispersive signal depends linearly on  $\phi_s$  and proportional to  $\text{Re}[\chi_{3L}(\omega) - \chi_{3L}(\omega + \delta)]$ . In the experiment, the phase  $\phi_{off}$  has been changed optically to work with the absorption and dispersion regime. The absorption and dispersion signal observed in the experiment can not be explained by standard EIT model consists of a single probe laser and a coupling laser. In order to explain the experimental data, a model of two probe fields and one coupling field in a three level system has been presented. In the model a frequency offset of  $\delta$  was introduced between the probes. The Hamiltonian of the system is given by,  $H = \frac{\hbar}{2}[2(\Delta_p - k_p v)|e\rangle\langle e| + 2(\Delta_2 - \Delta k v)|r\rangle\langle r| + \{(\Omega_{p1} + \Omega_{p2}e^{-i\delta t})|e\rangle\langle g| + \Omega_c|r\rangle\langle e| + c.c.\}]$ , where  $\Omega_{p1}$ ,  $\Omega_{p2}$  and  $\Omega_c$  are the Rabi frequencies of the strong probe, weak probe and the coupling beams respectively.  $k_p$  ( $k_c$ ) is the wave-vector of probe (coupling) and  $\Delta k = k_p - k_c$ . The two photon detuning is given by  $\Delta_2 = \Delta_p + \Delta_c$ , where  $\Delta_p$  ( $\Delta_c$ ) is the probe (coupling) laser detuning and  $v$  is the velocity of the atoms. The optical Bloch equation for the system,  $\dot{\rho} = -\frac{i}{\hbar}[H, \rho] + L_D(\rho)$ , where  $L_D(\rho)$  is the Lindblad operator which takes care of the decoherences of the system. The steady state density matrix equations were solved perturbatively. A similar approach has been applied to calculate four wave mixing (FWM) in 2-level atoms as discussed in [25]. The density matrix of the system can be expanded as,  $\rho = \rho^{(0)} + \rho^{(1)}e^{-i\delta t} + \rho^{(-1)}e^{i\delta t}$ , neglecting higher order terms. The density matrix equations for  $\rho_{ij}^{(0)} \forall i, j$  does not contain any higher order of density matrix elements, hence can be solved independently. The first order density matrix contains few zeroth order matrix elements. The solution of the zeroth order matrix elements substituted in first order equations and solved for  $\rho_{eg}^{(1)}$ . The susceptibilities of the strong and the weak probes are respectively given by,  $\chi(\omega_p) = \frac{2N|\mu_{eg}|^2}{\epsilon_0 \hbar \Omega_{p1}} \frac{1}{\sqrt{\pi} v_p} \int_{-\infty}^{+\infty} \rho_{eg}^{(0)} e^{-v^2/v_p^2} dv$  and  $\chi(\omega_p + \delta) = \frac{2N|\mu_{eg}|^2}{\epsilon_0 \hbar \Omega_{p2}} \frac{1}{\sqrt{\pi} v_p} \int_{-\infty}^{+\infty} \rho_{eg}^{(1)} e^{-v^2/v_p^2} dv$ . Here  $v_p$  is the most probable speed of atoms,  $N$  is the density and  $\mu_{eg}$  is the dipole moment of the transition  $|g\rangle \rightarrow |e\rangle$ . The calculated susceptibilities using the model matches with experimental observation quite well as presented in reference [22]. We also presented an analysis of the experimental observation which gives the estimation of the third order ( $\chi^{(3)}$ ) and fifth order ( $\chi^{(5)}$ ) nonlinear susceptibility [23]. This technique can also be used to measure the cross phase modulation of a light passing through the highly dispersive medium.

OHDT can also be used to study Rydberg blockade. Here we have used the technique to study blockade in thermal ensemble of atoms [22]. In the experiment, the probe beam was

stabilised at 1.3 GHz blue detuned to the D2 line of  $^{85}\text{Rb}$ . With this detuning, absorption of the probe beams is negligible due to interaction with the D2 line at  $130^\circ\text{C}$ . The coupling laser frequency was scanned to observe the dispersion of the signal probe beam by measuring its phase shift due to the two-photon excitations to the Rydberg state. The polarisation of the coupling beam is chosen to be  $\sigma^+$  and the probe beams to be  $\sigma^+$  and  $\sigma^-$ . The probe beam with  $\sigma^+$  polarisation can not couple the two-photon transition,  $5S_{1/2} \rightarrow nS_{1/2}$  and doesn't go through any phase shift due to two-photon process. We use it as the reference beam. However, the other beam with  $\sigma^-$  polarization can couple the same two-photon transition and hence, goes through a phase shift due to two-photon excitation to the Rydberg state. We have modulated the intensity of the coupling laser beam and lock-in detection was done in order to improve the signal to noise ratio of the dispersion signal. Here the 2-photon resonance peaks corresponding to the transitions,  $^{87}\text{Rb}$ :  $5S_{1/2}F=2 \rightarrow 5P_{3/2} \rightarrow nS_{1/2}$  and  $^{85}\text{Rb}$ :  $5S_{1/2}F=2 \rightarrow 5P_{3/2} \rightarrow nS_{1/2}$  are observed and used to normalise the frequency axis. The dispersion peak corresponding to the  $^{85}\text{Rb}$ :  $5S_{1/2}F=3 \rightarrow 5P_{3/2} \rightarrow nS_{1/2}$  transition was analysed for further study of Rydberg excitation. In the experiment, an absorptive like dispersion profile is observed in the regime  $\Omega_p \gg \Omega_c$ . In order to explain such unusual profile a model has been formulated. We have calculated  $\text{Re}(\rho_{eg})$  from 3-level system with the approximation  $\Delta_p \gg \Gamma_{eg}$ ,  $\Omega_p$  and  $\rho_{ee} \approx 0$  and found that,  $\text{Re}(\rho_{eg}) = \frac{\Omega_p}{2\Delta_p} \rho_{rr} - \frac{\Omega_c}{\Delta_p} \text{Re}(\rho_{gr})$ . The 3-level system was also approximated as an effective 2-level system by adiabatically eliminating the intermediate state [26] to calculate  $\rho_{gr}$  to find  $\text{Re}(\rho_{gr}) = \frac{2\Delta_p}{\Omega_p} \frac{\Delta_{eff}}{\Omega_{eff}} \rho_{rr}$ . Here  $\Delta_{eff}$  and  $\Omega_{eff}$  are the effective detuning and effective Rabi frequency of the approximated 2-level system respectively. The total susceptibility of the system can be expressed as  $\chi = \chi_{2L} + \chi_{3L}$ .  $\chi_{2L}$  is the susceptibility of the 2-level system (in absence of coupling laser) appeared due to the interaction of the probe laser with the transition  $5S_{1/2} \rightarrow 5P_{3/2}$ .  $\chi_{3L}$  is the susceptibility experienced by the probe laser in the presence of coupling laser. Using this model, the dispersion can be expressed as  $\text{Re}(\chi_{3L}) = \frac{N|\mu|^2}{\epsilon_0\hbar} [\frac{\Omega_p}{2\Delta_p} - \frac{\Omega_c}{\Omega_p} \frac{\Delta_{eff}}{\Omega_{eff}}] \rho_{rr}$ . Since dispersion is proportional to the Rydberg population, the suppression of population due to Rydberg blockade interaction can lead to suppression of dispersion.

In a further study, the sensitivity of the OHDT was determined. This technique is sensitive enough to measure a minimum phase shift of  $3.3 \mu\text{rad}$  with given experimental parameter. We have used a suitable model of two-photon excitation on a 3-level system to show that the minimum phase shift measured in our experiment corresponds to the probe absorption of the order

of  $10^{-7}$ . We observed that the direct probe absorption is not reliable in our experiment at this level. The effects due to polarisation impurity in the polarisation optical elements may have obscured this small absorption. Whereas the OHDT is insensitive to polarisation impurity in the probe and coupling laser beam and hence, provides reliable measurement of the Rydberg population.

In order to study Rydberg blockade, the experimental observation of suppression of dispersion and hence the Rydberg population with the increment of 2-photon Rabi frequency has to be modelled. We have formulated a model based on statistical analysis. Let us consider  $N_b$  atoms inside the blockade sphere. The probability of  $n$  atoms out of  $N_b$  atoms simultaneously getting excited to the Rydberg state is  $P_n = \frac{N_b!}{n!(N_b-n)!} \rho_{rr}^n (1 - \rho_{rr})^{(N_b-n)}$ , where  $\rho_{rr}$  is the Rydberg population. Because of the blockade interaction, only one excitation out of  $n$  is allowed, then the effective Rydberg population will be modified as  $\rho_{rr}^{(b)} = P_0 + \sum_1^{N_b} \frac{P_n}{n}$ . The dispersion of the probe due to Rydberg blockade interaction can be calculated by replacing  $\rho_{rr}$  by  $\rho_{rr}^{(b)}$  in the expression of  $Re(\chi_{3L})$ . This model qualitatively explains the suppression of dispersion. This model also gives a quantitative prediction of Rydberg blockade radius for  $n = 60$  which is found to be  $2.2 \mu\text{m}$ . However the model is based on classical statistical counting problem. The quantum collective effect is not considered anywhere in the model. In this study, we also confirmed that the amount of suppression observed in the dispersion can not be due to the population dependent dephasing or interaction induced dephasing. This model study only confirms that the Rydberg blockade effect can be observed in thermal atomic vapor. A many-body quantum model with thermal averaging is required to get an insight to study of Rydberg blockade in thermal vapor.

We first studied the model with 2-interacting atoms. From the model it has been observed that the atoms with same velocity can only participate in blockade interaction. If they are having different velocities, then the thermal effect obscures the blockade interaction. Using the symmetry in the density matrix elements of blockade interaction for  $N$ -interacting atoms, in strong blockade regime, the system can be reduced to effective 3-level system. We have also performed a calculation for 3-interacting-atom and hence generalised to  $N$ -interacting-atom model. The detailed calculation has been done by D. Kara et al. in [28]. However, super-atom model [29] is used where many-body Rabi oscillation [15] occurs with Rabi frequency  $\sqrt{N_b} \Omega_{eff}$ . Then we can have an empirical formula for Rydberg population as,  $\rho_{rr}(N_b) =$



$\frac{1}{N_b} \frac{(\sqrt{N_b} \Omega_{eff})^2}{4\Delta_{eff}^2 + 2N_b \Omega_{eff}^2 + \Gamma_{rg}^2}$ . This formula matches with the population calculated from exact 2-atom, 3-atom and 10-atom model [28]. All the atoms inside the blockade volume participating in cooperative blockade process collectively are called as a single superatom. The average number of atoms inside the blockade sphere can be found as  $\bar{N}_b = n_0 V_b$ , where  $n_0$  is the density of the atomic vapor and  $V_b$  is the blockade volume. The number of atoms present in each blockade sphere follows the Poisson distribution which is characterized by  $\bar{N}_b$ . The distribution can be written as,  $P(\bar{N}_b, N_b) = \frac{\bar{N}_b^{N_b} e^{-\bar{N}_b}}{N_b!}$ . Then the total susceptibility of the probe can be represented as

$$\chi = \sum_{N_b=1}^{\infty} P(\bar{N}_b, N_b) \chi_{sup}(N_b) \quad (1)$$

Here  $\chi_{sup}(N_b)$  is the susceptibility experienced by the probe due to a superatom containing  $N_b$  number of atoms inside the blockade sphere. The  $\chi_{sup}(N_b)$  is calculated by using MSE.

As we have seen from Eq. (6.15), the number of atoms present in each superatom follows the Poisson distribution. Therefore, the  $\rho_{avg}$  can also be calculated as

$$\rho_{avg} = \sum_{N=1}^{\infty} P(\bar{N}_b, N) \rho_{rr}(N) \quad (2)$$

Where  $P(\bar{N}_b, N)$  is a Poisson distribution function. It is observed that due to the wave-vector mismatch, all the atoms present in the blockade sphere cannot contribute to the Rydberg blockade process. The atoms within the velocity range from  $\tilde{v} - \frac{\Omega_{eff}}{2\Delta k}$  to  $\tilde{v} + \frac{\Omega_{eff}}{2\Delta k}$  contribute to the Rydberg blockade process, where  $\tilde{v}$  is velocity of atoms which resonantly interact with the probe and the coupling laser.  $\tilde{v}$  can be found from the equation  $\Delta_{eff}(\tilde{v}) = 0$ , which gives,  $\tilde{v} = \frac{1}{\Delta k} [\Delta_p + \Delta_c + \frac{\Omega_p^2 - \Omega_c^2}{4(\Delta_p - \Delta_c)}]$ . The number of atoms per blockade can be calculated as,  $N_b = \frac{4\pi}{3} r_b^3 n_0 f(\tilde{v}) \left( \frac{\Omega_{eff}}{\Delta k} \right)$ . The fitting function for the density dependent phase-shift is given by,

$$V_s = G n_0 \int_{-\infty}^{\infty} \xi(v) f(v) \rho_{ang} dv \quad (3)$$

For the fitting, we need to construct the Gradient vector and Hessian matrix as discussed in Appendix C. Here,  $r_b^3$  is a fitting parameter. Therefore, it is required to find a differentiation of the fitting equation with respect to  $r_b^3$ . The average number of atoms  $\bar{N}_b$  contributing to the Rydberg blockade process strongly depend on  $r_b^3$ . The transit time decay due to transverse velocity of atoms  $\Gamma_{vt}$  is a function of Rydberg blockade radius  $r_b$ . Hence, the Rydberg population

$\rho_{rr}$  also depends on  $r_b$  but it is a slowly varying function of  $r_b$  and hence the  $r_b$  dependence of  $\rho_{rr}$  can be neglected [67]. Then, the differentiation of  $\rho_{avg}$  with respect to  $r_b^3$  is given by,

$$\frac{\partial}{\partial r_b^3}[\rho_{avg}] = \frac{4\pi}{3}n_0f(\tilde{v})\frac{\Omega_{eff}}{\Delta k}\sum_{N=1}^{\infty}\left(\frac{N}{\bar{N}_b}-1\right)P(\bar{N}_b, N)\rho_{rr}(N) \quad (4)$$

Eq. (6.18) is used to construct the Hessian matrix for  $\chi^2$ -fitting of the experimental data.

The empirical formula given by the super-atom picture expected to explain the Rydberg blockade phenomenon in thermal atoms. In the experiment we observed a dramatic suppression of Rydberg population in thermal atoms which is similar to the experimental result of Rydberg blockade in cold atom system [30–33]. The suppression of Rydberg population has been observed in terms of suppression of dispersion since it is proportional to Rydberg population. In our experiment, the dispersion spectrum contains both the contributions from Rydberg blockade as well as anti-blockade interaction. In the picture of two atoms excitation process, in presence of repulsive Rydberg interaction the two atom excited state will shift to the blue detuned side of the resonant peak of the non-interacting atoms. On the blue detuned side of the 2-photon resonance peak the Rydberg population will be enhanced due to interaction which is known as anti-blockade. Anti-blockade in thermal vapor has been studied in details and reported in [34]. The contribution of the anti-blockade is negligibly small in the red detuned side of the resonance peak and the blockade will dominate. Hence, pursued the density dependent dispersion measurement at the red detuned side of the resonance peak. The same study was repeated for different principal quantum number states,  $n = 35, 40, 45, 50$  and  $53$ . It has been observed that the suppression of dispersion is stronger with increase in principal quantum number states. In order to fit the experimental density dependent dispersion data the expression,  $Re(\chi_{3L})(G, r_b^3) = G \int_{-\infty}^{+\infty} [\frac{\Omega_p}{2\Delta_p(v)} - \frac{\Omega_c}{\Omega_p} \frac{\Delta_{eff}(v)}{\Omega_{eff}}] \rho_{rr}^{eff} e^{v^2/v_p^2} dv$  was used, where  $\rho_{rr}^{eff}$  is calculated from the empirical super-atom model.  $G$  accounts for the overall gain in the experiment. The experimental data of density dependent dispersion has error in both density and dispersion measurements. Normal distributions of density as well as of dispersion were generated by taking respective errors as full width half maxima (FWHM). Using the scaling law for Rabi frequency  $\Omega \propto n^{3/2}$ , same two-photon effective Rabi coupling was maintained in the experiment with all principal quantum number states. Moreover, all the experimental parameters were also kept same, hence  $G$  should be same for all the experimental data.  $\chi^2$ -fitting of the dispersion data was done for low densities of  $n = 35$  where Rydberg blockade interaction is expected to be negligible. The fitting has been done in order to generate the statistics for the parameter  $G$

which is found to be  $\langle G \rangle = 0.39$  V/mrad with the error  $\sigma_G = 0.047$  V/mrad. Then  $\chi^2$ -fitting of dispersion as function of density was done for all the principal quantum numbers by taking  $r_b^3$  as a fitting parameter. Further, the statistics of  $r_b^3$  was generated for all the quantum number states. Using these statistics, we have generated the normal distributions of  $r_b^3$  was generated for different  $n^*$ , where  $n^* = n - \delta$  with  $\delta$  being the quantum defect.  $\chi^2$ -fitting for all the data of  $r_b^3$  as function of  $n^*$  was done to find the scaling as,  $r_b^3 \sim n^{*5.47 \pm 0.3}$ . The scaling exponent found from the fitting is consistent with the usual scaling of  $C_6$  within 6% error.

Similar experiments to be pursued with ultra-cold atomic ensemble, I was involved in designing the ultra-high vacuum (UHV) and optical setup for magneto optical trap (MOT). The ultra-high vacuum design includes UHV chamber with other vacuum accessories and also the mechanical set up to support the vacuum system. The optical setup includes the planning of AOM alignments to generate the beams for laser cooling and magneto optical trap, sub-Doppler cooling, optical pumping, probe beams for heterodyne detection in ultra-cold sample and also blue laser for Rydberg excitation. Also, the electronic circuits for the AOM devices were designed.

# Bibliography

- [1] H. E. White, Introduction to Atomic Spectra (McGraw- Hill, New York, 1934).
- [2] J. R. Rydberg, Phil. Mag. 5th Ser, 43, 390 (1883).
- [3] A. Walsh, *Spectrochim. Acta* 7, 108, (1955).
- [4] F. Twyman, ”*The Spectrochemical Analysis of Metals and Alloys*”. C. Griffin and Co. Ltd. London, Chapter 1 (1941).
- [5] T. F. Gallagher, Rydberg atoms (Cambridge univ. press, 1994).
- [6] M. L. Zimmerman, M. G. Littman, M. M. Kash and D. Kleppner, Phys. Rev. A 20, 2251 (1979).
- [7] T. Pohl, H. R. Sadeghpour and P. Schmelcher, Phys. Rep. 484, 181 (2009).
- [8] J. A. Yeazell and C. R. Stroud, Jr., Phys. Rev. Lett. 60, 1494 (1988).
- [9] R. R. Jones, Phys. Rev. Lett. 77, 2420 (1996).
- [10] J. Ahn, D. N. Hutchinson, C. Rangan and P. H. Bucksbaum, Phys. Rev. Lett. 86, 1179 (2001).
- [11] J. M. Raimond, M. Brune and S. Haroche, Rev. Mod. Phys, 73, 565 (2001).
- [12] S. Gleyzes, S. Kuhr, C. Guerlin, J. Bernu, S. Deléglise, U. B. Hoff, M. Brune, J.-M. Raimond and S. Haroche, Nature 446, 297 (2007).
- [13] W. R. Anderson, J. R. Veale and T. F. Gallagher, Phys. Rev. Lett. 80, 249 (1998).
- [14] I. Mourachko, D. Comparat, F. de Tomasi, A. Fioretti, P. Nosbaum, V. M. Akulin and P. Pillet, Phys. Rev. Lett. 80, 253 (1998).
- [15] Y. O. Dudin and A. Kuzmich, Science 336, 8879 (2012).

- [16] T Peyronel, O Firstenberg, Q Liang, S Hofferberth, A Gorshkov, T Pohl, M Lukin and V Vuletic, *Nature* 488, 57 (2012).
- [17] D. Maxwell, D. J. Szwer, D. Paredes-Barato, H. Busche, J. D. Pritchard, A. Gauguet, K. J. Weatherill, M. P. A. Jones and C. S. Adams, *Phys. Rev. Lett.* 110, 103001 (2013).
- [18] Shapiro J H 2006 *Phys. Rev. A* 73 062305
- [19] Lukin M D, Fleischhauer M, Cote R, Duan L M, Jaksch D, Cirac J I and Zoller P 2001 *Phys. Rev. Lett.* 87 037901.
- [20] O. Firstenberg et al., *Nature* 502, 71 (2013).
- [21] Günter, G. et al. Interaction Enhanced Imaging of Individual Rydberg Atoms in Dense Gases. *Phys. Rev. Lett.* 108, 013002 (2012).
- [22] A. Bhowmick, D. Kara and A. K. Mohapatra, arXiv: 1605.06603v1 (2016).
- [23] Arup Bhowmick, Sushree S. Sahoo, and Ashok K. Mohapatra *Phys. Rev. A* 94, 023839.
- [24] A. K. Mohapatra, T. R. Jackson, and C. S. Adams, *Phys. Rev. Lett.* **98**, 113003 (2007).
- [25] R. W. Boyd, *Nonlinear optics*, 3rd ed., (Academic, New York, 2008).
- [26] R. Han, H. K. Ng, and B. G. Englert, *J. of Mod. Opt.* 60, 255 (2013)
- [27] F. Letscher, O. Thomas, T. Niederprüm, H. Ott, and M. Fleischhauer *Phys. Rev. A* 95, 023410 (2017)
- [28] Annual report of Dushmanta Kara (2017).
- [29] T. M. Weber, M. Hönig, T. Niederprüm, T. Manthey, O. Thomas, V. Guarrera, M. Fleischhauer, G. Baronttni and H. Ott, *Nature phys.*, 11, 157 (2015).
- [30] T. Vogt, M. Viteau, J. Zhao, A. Chotia, D. Comparat and P. Pillet, *Phys. Rev. Lett.* 97, 083003 (2006).
- [31] T. A. Johnson, E. Urban, T. Henage, L. Isenhower, D. D. Yovuz, T. G. Walker and M. Saffman, *Phys. Rev. Lett.* 100, 113003 (2008).
- [32] A. Gaötan, Y. Miroshnychenko, T. Wilk, A. Chotia, M. Viteau, D. Comparat, P. Pillet, A. Browaeys and P. Grangier, *Nature Phys.* 5,115 (2009).



- [33] E. Urban, T. A. Johnson, T. Henage, L. Isenhower, D. D. Yavuz, T. G. Walker and M. Saffman, *Nature Phys.* 5, 110 (2009).
- [34] D. Kara, A. Bhowmick and A. K. Mohapatra, "Study of interaction induced enhanced excitation in thermal vapour". (Manuscript under communication).

### **Journal:**

1. "Optical nonlinearity of Rydberg electromagnetically induced transparency in thermal vapor using the optical-heterodyne-detection technique", Arup Bhowmick, Sushree S. Sahoo, and Ashok K. Mphapatra, Phys. Rev. A, 2016, 94, 023839 1-7.
2. "High-sensitivity measurement of Rydberg population via two-photon excitation in atomic vapor using optical heterodyne detection technique", Arup Bhowmick, Dushmanta Kara, and Ashok K. Mphapatra, arXiv: 1709.07750, 2017. [Accepted in Pramana]
3. "Study of Rydberg blockade in thermal vapor", Arup Bhowmick, Dushmanta Kara, and Ashok K. Mphapatra, arXiv:1802.06599, 2018. [Communicated]

### **Other journal publications:**

1. "Polarization rotation of light propagating through a medium with efficient four-wave mixing and cross-phase modulation", Sushree S. Sahoo, Arup Bhowmick and Ashok K. Mohapatra, J. Phys. B: At. Mol. Opt. Phys., 2017, 50, 055501 1-9.
2. "Rydberg interaction induced enhanced excitation in thermal atomic vapor", Dushmanta Kara, Arup Bhowmick, and Ashok K. Mohapatra, Scientific Reports, 2018, 8, 5256 1-9.
3. Study of the effect of Multi-atom decoherence in super-atom model of the Rydberg blockade. [Under preparation]

### **Conferences:**

1. International school and conference of Atomic Physics and Quantum Optics, 2012, Goa, arranged by IISER, Pune, India.
2. School and workshop on physics of cold atom, 2013, HRI, Allahabad, India. The title of the poster presentation is "Study of optical non-linearity of Rydberg-EIT system using optical heterodyne detection technique" by Arup Bhowmick, and Ashok K. Mohapatra.

3. School and discussion meeting on frontiers in Light-Matter interaction, 2014, IACS, Kolkata, arranged by ICTS, Bangalore, India. The title of the poster presentation is "Rydberg blockade mediated optical non-linearity in thermal vapor using optical heterodyne detection technique" by Arup Bhowmick, and Ashok K. Mohapatra.

4. The International School and Conference on Quantum Information (IPQI), 2014, IOP, Bhubaneswar, India. The title of the poster presentation is "Study of Rydberg blockade in thermal vapor" by Arup Bhowmick, and Ashok K. Mohapatra.

5. APS March meeting, 2016, Baltimore, USA. The title of the oral presentation is "Study of Rydberg blockade mediated optical non-linearity in thermal vapor" by Arup Bhowmick, and Ashok K. Mohapatra.

**List of National and International laboratory visited and work presented:**

1. National Physical Laboratory: Time and frequency standard department (2014), Delhi, India: Group: Dr. Ashis Agarwal and Dr. Subhadeep De. Title of the oral presentation: Study of optical nonlinearity due to strongly interacting Rydberg atoms in thermal vapor.
2. University of Maryland, College Park, 2016, USA: Group: Prof. William Philips and Prof. Steven Rolston. Title of the oral presentation: Study of Rydberg blockade mediated optical nonlinearity in thermal vapor.
3. Massachusetts Institute of Technology (MIT), 2016, Boston, USA: Group: Prof. Vladan Vuletic. Title of the oral presentation: Study of Rydberg blockade interaction in thermal vapor.

# List of Figures

2.1	Schematic atomic level diagram of rubidium atoms . . . . .	14
2.2	van der Waal interaction between two dipoles . . . . .	18
2.3	Schematic representation of the Rydberg blockade interaction . . . . .	19
2.4	Superatom formation due to Rydberg excitation . . . . .	20
2.5	Schematic representation of Rydberg anti-blockade interaction . . . . .	22
3.1	$D_1$ and $D_2$ transitions for $^{85}\text{Rb}$ . . . . .	29
3.2	$D_1$ and $D_2$ transitions for $^{87}\text{Rb}$ . . . . .	30
3.3	Two level system in presence of an external field . . . . .	32
3.4	Light shift of atomic levels . . . . .	33
3.5	Dressing of atomic levels . . . . .	34
3.6	3-level system . . . . .	36
3.7	EIT transmission and refractive index . . . . .	38
3.8	two-photon resonance signal for large probe detuning . . . . .	39
3.9	Comparison of 3-level numerical solution and the effective 2-level solution for large probe detuning . . . . .	41
3.10	Experimental setup for hyperfine pumping spectroscopy. . . . .	42
3.11	Doppler broadened absorption lines of D2 rubidium transition. . . . .	43
3.12	Hyperfine pumping spectroscopy signal. . . . .	44
3.13	Spectroscopy signal for individual transition manifold. . . . .	45
3.14	Block diagram representing the laser frequency stabilization using HPS. . . . .	46
4.1	Rydberg EIT. . . . .	51
4.2	Optical set up to generate heterodyne probe beams. . . . .	54
4.3	Measurement of transmission and dispersion using OHDT . . . . .	55
4.4	Optical phase shifter (OPS). . . . .	57
4.5	Realisation of Rydberg EIT using OHDT . . . . .	58

4.6	Experimental observation of probe transmission and dispersion for Rydberg-EIT.	59
4.7	Energy level diagram for Rydberg-EIT model . . . . .	60
4.8	Imaginary and real part of $\chi_{3L}(\omega_p)$ and $\chi_{3L}(\omega_p + \delta)$ as a function of coupling laser detuning (calculated from the model). . . . .	65
4.9	Comparison of transmission and dispersion calculated from the model with experimental data. . . . .	67
4.10	Study of dressed state transmission using the model presented. . . . .	69
4.11	Transmission peak height measurement due to EIT. . . . .	70
4.12	Estimation of intensity dependent nonlinearity. . . . .	73
5.1	Atomic level scheme for two-photon Rydberg excitation. . . . .	80
5.2	SAS lines representing the stabilisation frequencies of probe and reference laser.	81
5.3	AOM setup for the generation of reference and probe beams for OHDT two-photon Rydberg excitation experiment. . . . .	82
5.4	Schematic of the experimental set up for two-photon Rydberg excitation using OHDT. . . . .	83
5.5	Typical dispersion spectrum of a probe beam due to two-photon resonance to the Rydberg state. . . . .	84
5.6	two-photon spectrum of the probe by scanning coupling laser detuning. . . . .	88
5.7	Experimental and model matching of normalised dispersion peak height. . . . .	90
5.8	Setup for calibration of phase measurement of electronic waveform mixer. . . . .	91
5.9	Calibration of phase sensitivity of wave-form mixer. . . . .	92
5.10	Schematic block diagram of electronic operation of beat signals. . . . .	93
5.11	Measurement of phase shift of the probe due to two-photon resonance. . . . .	95
5.12	Experimental setup for direct absorption measurement (DAM) of probe. . . . .	96
5.13	Comparative study of DAM and OHDT. . . . .	97
6.1	A simplified schematic of the experimental setup (a). The atomic-level diagram to explain the observed dispersion signal (b). In the experiment we collected dispersion signal by varying the density of the vapor, The green point depicted on the signal is the dispersion is studied experimentally. . . . .	104
6.2	Measured dispersion peak height as a function of peak probe Rabi frequency of probe beam coupling to the Rydberg state $n = 60$ . . . . .	106

6.3	The dispersion signal for two-photon resonance signal. The Rydberg blockade and Rydberg anti-blockade interaction regimes are depicted. . . . .	109
6.4	Experimental data of density dependent phase-shift. . . . .	110
6.5	Schematic energy level diagram of N-interacting atoms. . . . .	112
6.6	The phase difference due to atoms in different longitudinal velocity. . . . .	114
6.7	Evaluation of overall gain of the experiment. . . . .	117
6.8	Goodness of the gain fitting. . . . .	118
6.9	The variation of non-linear absolute phase shift of the probe measured in the experiment with vapor density due to the two-photon transition to the Rydberg states with principal quantum number as a parameter. . . . .	121
6.10	Goodness of the density dependent phase shift fitting. . . . .	122
6.11	$r_b^3$ as a function of $n^*$ . . . . .	123
6.12	Goodness of the principal quantum number dependent $r_b^3$ fitting. . . . .	124
7.1	Frequencies of light required to trap atoms and for generation of probe lights for the experiment. . . . .	133
7.2	Optical setup to trap atoms and to do experiment. . . . .	134
7.3	Generation and stabilisation of repump laser. . . . .	135
7.4	Setup for stabilisation of blue laser on Rydberg-EIT signal. . . . .	136
7.5	Realisation of experiment on Rydberg excited cold atoms. . . . .	137
7.6	Design of vacuum chamber and flange multiplexer. . . . .	138
7.7	Pump and gauge assembly with vacuum chamber. . . . .	139
7.8	Design of cage adapter. . . . .	140
7.9	Opto-mechanical cage assembly . . . . .	141
8.1	Ordered phase created by the Rydberg blockade interaction. . . . .	148
8.2	Rydberg-EIT in the thin atomic vapor cell. . . . .	149
A.1	Electronic design of fast photodetector circuit . . . . .	152
B.1	Electronic design of an AOM driver. . . . .	154
B.2	VCO characteristic curve. . . . .	155
C.1	A representation of $\chi^2$ difference of a set of data points from a function with an arbitrary parameter space and the same function with optimised parameter space.	157

# List of Tables

2.1	Quantum defect of the alkali atoms for $l = 0 - 3$ . . . . .	15
2.2	Scaling of physical properties of the Rydberg atoms with principal quantum number . . . . .	16
4.1	Fitting with $1 + a\Omega_p^2$ . . . . .	74
6.1	Gaussian fitting of the gain distribution. . . . .	117
6.2	Blockade radius from the statistical analysis of density dependent phase shift data	122

# Chapter 1

## Introduction

The building of useful and controllable quantum system is always an outstanding challenge in the field of research of the atomic, molecular and optical (AMO) physics. It encourages the progressively increasing technological interests towards the experimental realization of a perfect quantum system, quantum computer, and quantum simulator. It requires complete isolation of the system from the surrounding world and precise control over the interaction between quantum particles of the system. In the linear optical medium, photons do not interact with each other whereas the non-linear optical medium facilitate strong photon-photon interaction. Strong interaction for single photons are essential for building the quantum devices like single photon switch, optical transistor, photonic phase gate and deterministic source for single photon. It triggers the search of the nonlinear optical system in order to introduce the interaction between photons and control the interaction via non-linear medium.

Rydberg quantum optics is one of the field which is expected to address all these fundamental questions. By coupling the Rydberg excited state via electromagnetically induced transparency (EIT) a large self phase modulation (SPM) [1–18] and cross phase modulation (XPM) [19–24, 29] is observed. These phase modulation processes posses large intensity dependent nonlinearity for the Rydberg interacting systems. The state-dependent interaction mediated by the Rydberg blockade enhances optical non-linearity which essentially can be used to introduce correlation between photons while studying atom-light interaction for the system. In the advent of the technique to slow down and trap an ensemble of atoms in the magneto-optical trap (MOT) [30–32], a number of possible studies on photons using atoms have emerged.



## 1.1 Rydberg blockade and enhanced optical non-linearity

Rydberg states are the highly excited state with very large principal quantum number. The Rydberg excited electron is loosely bound to the core nucleus and hence the interactions between the atoms in Rydberg states are orders of magnitude larger than the atoms in the ground states. The typical interaction is van Der Waals type in the absence of any electric field and can be repulsive or attractive in nature depending on the orbital angular momentum of the Rydberg state. Strong Rydberg-Rydberg interaction makes the system very unique while an ensemble of atoms are excited using monochromatic light field. In a dilute vapour where the average inter-atomic separation is of the order of micron, the ground-ground state or ground-Rydberg state interactions can be safely neglected whereas the Rydberg-Rydberg interaction is appreciable. If one Rydberg atom is excited by a resonant monochromatic laser field, it shifts the energy level of the Rydberg state of the neighbouring atoms making them out of resonance from the same laser field and hence can not be excited. This phenomenon is called Rydberg blockade which allows a single excitation of an ensemble of atoms inside a macroscopic volume called as blockade sphere. The radius of the blockade sphere can be a few micron which is related to the van der Waals interaction strength and the probability of Rydberg excitation which is related to the Rabi coupling of the laser field. All the atoms inside the blockade sphere collectively participate in the single Rydberg excitation. As a result, the coherently driven system becomes an interesting quantum many body system. Also the Rabi coupling is enhanced by  $\sqrt{N}$  where  $N$  is the number of atoms in a single blockade sphere. Comparing the system with a cavity, where the Rabi coupling of a single photon with a single atom is also enhanced by  $\sqrt{N}$  where the  $N$  is the number multiple reflections it goes through the cavity.

The development of a high finesse cavity boosts the study of optical nonlinearity due to atom-photon interaction using cavity. The interaction of a field with a single atom trapped inside a cavity [33, 34] is studied which helps to make all-optical switch [29]. It is also used to study photon blockade [35] and photon turnstile dynamics [36]. The interaction of a single photon with a single trapped atom inside a cavity is studied which has significant application towards the design of the scalable architecture for quantum computation. Study of the interaction of few photons with an ensemble of cold Rydberg atoms trapped inside a cavity [37–39] has very important application in designing of photonic phase gate.

## 1.2 Review of the study of Rydberg blockade in cold atoms

The suppression is experimentally observed in a frozen ensemble of atoms having van der Waals interaction [40–42]. Since all the atoms in the blockade sphere are identical, the system falls in many-body entangled state [43, 44]. The net susceptibility experienced by a photon while passing through the medium is not the simple addition of the susceptibility due to all the individual atoms. In the presence of the blockade interaction, the number of atoms inside the blockade sphere contributes to the susceptibility collectively. The coherent collective effect due to Rydberg excitation is also experimentally observed in the frozen ensemble of atoms [45, 46] and between two individually trapped atoms [47, 48]. The many-body effect due to dipole blockade interaction among Rydberg atoms is also experimentally investigated [49, 50]. A precision measurement of van der Waals interaction strength is done by using two trapped atoms interacting strongly via Rydberg blockade interaction [51]. In presence of the Rydberg blockade interaction, the frozen ensemble atoms show crystalline structure [52].

The Rydberg atoms claimed to be an efficient system to build quantum phase gate which can be used for quantum computation. The optical nonlinearity observed in the system is not only large but also different in nature due to the state-dependent interaction property of the Rydberg blockade [53]. The idea of building the controlled NOT gate using photons require large nonlinearity mediated by Rydberg-Rydberg interaction. In this regard, a very basic question that asked was that even if the Rydberg interaction induces large optical nonlinearity is it sufficient to build a quantum computer [54]. In order to address the question, the researchers continue the experiments towards the Rydberg blockade in a frozen ensemble of atoms and found large optical nonlinearity at the single photon level [6, 55]. Optical  $\pi$  phase-shift is measured for single photon which is mediated by Rydberg blockade [56]. It is also observed that the multi-atom coherence due to the superatom formation in cold-atoms enhances single photon nonlinearity significantly [25–27, 44, 46]. Rydberg blockade in electromagnetically induced transparency (EIT) medium posses strong single photon nonlinearity for the atoms in MOT [6, 7], the atoms in cavity [57] and two atoms trapped separately by optical tweezers [58]. It has wide application in quantum simulation [59, 60] with photons and all-optical quantum information processing (QIP) [14, 53, 54, 61–63].

### 1.3 Motivation to study of Rydberg atoms in thermal vapor

For van der Waals interaction between the atoms, the Rydberg blockade radius is defined as,  $R_b = [\frac{C_6}{\hbar\nu}]^{1/6}$ , where  $\nu = \max\{\Gamma_d, \Omega\}$ . Here,  $\Gamma_d$  is the Doppler width of the transition and  $\Omega$  is the Rabi frequency of the Rydberg excitation. The Rydberg blockade for the cold atomic system is given by,  $R_b^{(ca)} = [\frac{C_6}{\hbar\Omega}]^{1/6}$ , since the Doppler width is very small compared to the Rabi frequency of the transition. The Rabi coupling of the Rydberg transition can be taken as,  $\Omega = 5$  MHz. In case of the thermal atoms, the Doppler width of the transition dominates over the Rabi frequency of the Rydberg excitation. So, the blockade radius for the thermal atoms can be defined by,  $R_b^{(th)} = [\frac{C_6}{\hbar\Gamma_d}]^{1/6}$  [64]. The typical Doppler width of the transition is given by  $\Gamma_d = 1$  GHz. The ratio between the cold atom and the thermal atom blockade radius is given by,  $\frac{R_b^{(ca)}}{R_b^{(th)}} = [\frac{\Gamma_d}{\Omega}]^{1/6} \approx 2.5$ . This implies that the blockade radius in thermal atoms should be 2-3 factor smaller than that of the cold atom. The Rydberg blockade radius for cold atomic system for the Rydberg excited state with principal quantum number  $n = 60$  is  $6 \mu\text{m}$  for  $s$ -state and  $8 \mu\text{m}$  for  $d$ -state [4, 28, 46]. Then, the Rydberg blockade radius for the thermal atomic ensemble is expected to be  $\sim 2 \mu\text{m}$ , which is a detectable number if the experiment is performed.

### 1.4 Review of the Rydberg excitations in thermal atomic ensemble

The study of cooperative phenomena due to Rydberg-Rydberg interaction in thermal vapor has growing interest because of the technological simplicity in comparison with the cold atoms and hence, it is easily realizable. Detection of coherently driven Rydberg excitation assisted by dipole interaction is detected in thermal atomic vapor [1, 12]. Unlike usual atomic system, the system is found to be extremely sensitive to the electric field which leads to giant electro-optic effect [11]. The multi-wave mixing process due to the Rydberg dressing is also studied [65–67]. A sensitive measurement of Rydberg population due to a coherent driving in electrically contacted rubidium vapor cell is also reported [68]. Optical bistability is observed in thermal atomic vapor in presence of dipole-dipole Rydberg interaction [69].

In order to study the Rydberg blockade interaction in EIT regime, it is required to prepare the ensemble in high density. Here, the single photon resonance causes strong absorption of the probe laser. The optical path of the probe laser can be reduced by using micron size vapor cell where the strong Rydberg blockade interaction is found to be significant while driven by

continuous optical field [64, 65] and pulsed laser [17, 70]. A correlated single photon source is demonstrated using the cooperative Rydberg blockade interaction in thermal vapor [71].

The many-body effect mediated by Rydberg-Rydberg interaction is also studied. Van der Waals interaction driven coherent Rabi oscillation is found in thermal vapor [17]. A partial suppression of Rydberg excitation is observed in atomic beam [72]. In presence of Rydberg interaction, a correlated growth of Rydberg aggregates is also found [73]. The dissipative phase transition driven by the Rydberg blockade interaction is extensively studied [69, 74–76].

## 1.5 Contribution of the thesis

The thesis is dedicated to study the Rydberg blockade due to van der Waals interaction.

(A) An all-optical detection technique based on optical heterodyne is established to study Rydberg-EIT.

- Using the optical heterodyne detection technique (OHDT) the absorption and the dispersion of a probe beam passing through a dispersive medium can efficiently be measured.
- A model of EIT involving 2 probes with a frequency offset and a coupling laser in a three-level system successfully explain the experimental observation.

(B) OHDT is used for two-photon excitation to Rydberg state is done.

- The sensitivity in phase shift measurement is found to be as small as  $3 \mu\text{rad}$  and the Rydberg population to be of the order of  $10^{-7}$ .
- The technique is also found to be insensitive to small polarisation fluctuation which is found to be advantageous over direct absorption measurement.

(C) Study of Rydberg blockade is done using OHDT. The many-body model based on superatom formation due to Rydberg blockade interaction is constructed and used to explain the experimental observation.

- The suppression of Rydberg population due to Rydberg blockade interaction is observed in the experiment while driving a thermal ensemble of atoms by the continuous probe and coupling laser field.

- The analysis of experimental data using a many-body model of Rydberg blockade verifies the scaling law of van der Waals interaction strength ( $C_6$ ) with the principal quantum number.

(D) A design of cold atom setup is also mentioned in the thesis. The prime objective of building the cold-atom setup is to study Rydberg quantum optics.

## 1.6 Layout of the thesis

The thesis contains seven chapters except for introduction and three appendices. The flow of the thesis is briefly described as follows.

In chapter 2, the basic properties of Rydberg atoms such as the scaling laws of physical quantities with the principal quantum number will be discussed. The two types of Rydberg interactions namely the van der Waals and dipole-dipole interactions will also be discussed. The Rydberg interaction leads to cooperative phenomena in atom-light interaction. Contextually, the Rydberg blockade and Rydberg anti-blockade interactions are also discussed in the chapter.

In chapter 3, some of the atomic properties of alkali atoms are described. The discussion is restricted to rubidium atom. Basic atom-light interactions such as the steady-state optical Bloch equation (OBE) of 2-level and 3-level atom in presence of external optical field are also discussed. A very specific discussion on the adiabatic approximation to reduce 3-level system to an effective 2-level system has also been done which will be used in later chapters as a tool to measure dispersion from Rydberg population.

In chapter 4, optical heterodyne detection technique (OHDT) will be discussed to measure the absorption and the dispersion of a probe field while passing through a dispersive medium. The OHDT is established in the Rydberg electromagnetically induced transparency (EIT) medium for a Doppler broadened optically thick atomic system. A model of EIT based on the perturbation theory can explain the experimental observations and hence the nonlinearity of the system is estimated. This limitations and the application of the technique will also be discussed.

In chapter 5, the dispersion spectrum-shape will be explained for a two-photon resonance to the Rydberg excited state using a model of the three-level atom in presence of a probe and

a coupling laser field. The probe laser is detuned 1.3 GHz away from the intermediate atomic state but using a coupling laser it satisfies the two-photon resonance condition. The precision of the measurement of the phase shift due to the dispersion and the measurement of the Rydberg population will also be described in the chapter. A comparative study of OHDT with direct absorption measurement (DAM) of the probe will be done to demonstrate the higher sensitivity of OHDT.

In chapter 6, the Rydberg blockade in thermal atomic vapor will be demonstrated experimentally by two-photon resonance to the Rydberg excited state using OHDT. A model of Rydberg blockade based on classical counting will be presented. The model confirms the existence Rydberg blockade and rules out other possible artifacts. A many-body model based on superatom will be used to explain experimental data for better estimation of physical quantities such as Rydberg blockade radius and the interaction strength. A very precise verification of scaling of the van der Waals interaction strength with the principal quantum number of Rydberg state will be demonstrated by fitting the model with the experimental data.

In chapter 7, the electronic, optical and vacuum design for ultra-cold atom setup will be demonstrated.

In chapter 8, the summary of the thesis will be presented and some prescription will be suggested for the future experiments in order to carry out research in the same field.

In appendix A and B we will describe the electronic design of a fast photodetector and the electronic driver of the acousto-optic modulator (AOM) respectively. These electronic devices are used in OHDT experiment. Appendix C will describe the  $\chi^2$ -fitting process and a way to judge the goodness of the fitting. This will be widely used in chapter 6.

# Bibliography

- [1] I. Friedler, D. Petrosyan, M. Fleischhauer, and G. Kurizki, Phys. Rev. A, **72**, 043803 (2005).
- [2] S. Sevincli, N. Hankel, C. Ates, and T. Pohl, Phys. Rev. Lett., **107**, 153001 (2011).
- [3] A. V. Gorshkov, J. Otterbach, M. Fleischhauer, T. Pohl, and M. D. Lukin, Phys. Rev. Lett., **107**, 133602 (2011).
- [4] J. D. Pritchard, D. Maxwell, A. Gauguier, K. J. Weatherill, M. P. A. Jones, and C. S. Adams, Phys. Rev. Lett., **105**, 193603 (2010).
- [5] V. Parigi, E. Bimbard, J. Stanojevic, A. J. Hilliard, F. Nogrette, R. Tualle-Brouri, A. Ourjoumtsev, and P. Grangier, Phys. Rev. Lett., **109**, 233602 (2012).
- [6] T. Peyronel, O. Firstenberg, Qi-Yu Liang, S. Hofferberth, A. V. Gorshkov, T. Pohl, M. D. Lukin, and V. Vuletić, Nature, **488**, 57 (2012).
- [7] O. Firstenberg, T. Peyronel, Qi-Yu Liang, A. V. Gorshkov, M. D. Lukin, and V. Vuletić, Nature, **502**, 71 (2013).
- [8] S. Baur, D. Tiarks, G. Rempe, and S. Dürr, Phys. Rev. Lett., **112**, 073901 (2014).
- [9] C. Ates, S. Sevincli, and T. Pohl, Phys. Rev. A, **83**, 041802(R) (2011).
- [10] K. J. Weatherill, J. D. Pritchard, R. P. Abel, M. G. Bason, A. K. Mohapatra, and C. S. Adams, J. Phys. B: At. Mol. Opt. Phys., **41**, 201002 (2008).
- [11] A. K. Mohapatra, M. G. Bason, B. Butscher, K. J. Weatherill and C. S. Adams, Nature Phys., **4**, 890 (2008).
- [12] A. K. Mohapatra, T. R. Jackson, and C. S. Adams, Phys. Rev. Lett., **98**, 113003 (2007).

- [13] H. Gorniaczyk, C. Tresp, J. Schmidt, H. Fedder, and S. HOFFEBERTH Phys. Rev. Lett., **113**, 053601 (2014).
- [14] M. Khazali, K. Heshami, and C. Simon, Phys. Rev. A, **91**, 030301(R) (2015).
- [15] Y.-M. Liu, D. Yan, X.-D. Tian, C.-L. Cui, and J.-H. Wu, Phys. Rev. A, **89**, 033839 (2014).
- [16] C. S. Hofmann, G. Günter, H. Schempp, M. Robert-de-Saint-Vincent, M. Gärttner, J. Evers, S. Whitlock, and M. Weidemüller, Phys. Rev. Lett., **110**, 203601 (2013).
- [17] T. Baluktsian, B. Huber, R. Löw, and T. Pfau, Phys. Rev. Lett., **110**, 123001 (2013).
- [18] J. Han, T. Vogt, M. Manjappa, R. Guo, M. Kiffner, and W. Li, Phys. Rev. A, **92**, 063824 (2015).
- [19] H. Schmidt, and A. Imamoglu, Opt. Lett., **21**, 1936 (1996).
- [20] H. Wang, D. Goorskey, and M. Xiao, Phys. Rev. Lett., **87**, 073601 (2001).
- [21] H. Chang, H. Wu, C. Xie, and H. Wang, Phys. Rev. Lett., **93**, 213901 (2004).
- [22] S. Li, X. Yang, X. Cao, C. Zhang, C. Xie, and H. Wang, Phys. Rev. Lett., **101**, 073602 (2008).
- [23] H. Kang, and Y. Zhu, Phys. Rev. Lett., **91**, 093601 (2003).
- [24] H. Lo, P. Su, and Y. Chen, Phys. Rev. A, **81**, 053829 (2010).
- [25] H. Weimer, M. Müller, I. Lesanovsky, P. Zoller, and H. P. Büchler, Nature Phys., **6** 382 (2010).
- [26] Y. O. Dudin, and A. Kuzmich, Science, **336**, 887 (2012).
- [27] C. Tresp. Rydberg polaritons and Rydberg superatoms-novel tools for quantum nonlinear optics, a Ph.D. thesis, Stuttgart university (2017).
- [28] A. Schwarzkopf, R. E. Sapiro, and G. Raithel, Phys. Rev. Lett., **107**, 103001 (2011).
- [29] W. Chen, K. M. Beck, R. Büker, M. Gullans, M. D. Lukin, H. Tanji-Suzuki, and V. Vuletić, Science, **341**, 768 (2013).
- [30] S. Chu, Rev. of Mod. Phys., **70**, 685 (1998).



- [31] C. N. C.-Tannoudji, Rev. of Mod. Phys., **70**, 707 (1998).
- [32] W. D. Phillips, Rev. of Mod. Phys., **70**, 721 (1998).
- [33] J. D. Thompson, T. G. Tiecke, N. P. de Leon, J. Feist, A. V. Akimov, M. Gullans, A. S. Zibrov, V. Vuletić, and M. D. Lukin, Science, **340**, 1202 (2013).
- [34] A. Reiserer, and G. Rempe, Rev. of Mod. Phys., **87**, 1379 (2015).
- [35] K. M. Birnbaum, A. Boca, R. Miller, A. D. Boozer, T. E. Northup, and H. J. Kimble, Nature, **436**, 87 (2005).
- [36] B. Dayan, A. S. Parkins, T. Aoki, E. P. Ostby, K. J. Vahala, and H. J. Kimble, Science, **319**, 1062 (2008).
- [37] J. M. Raimond, M. Brune, and S. Haroche, Rev. of Mod. Phys., **73**, 565 (2001).
- [38] S. Osnaghi, P. Bertet, A. Auffeves, P. Maioli, M. Brune, J. M. Raimond, and S. Haroche, Phys. Rev. Lett., **87**, 037902 (2001).
- [39] J. Sheng, Y. Chao, S. Kumar, H. Fan, J. Sedlacek and J. P. Shaffer, Phys. Rev. A, **96**, 033813 (2017).
- [40] K. Singer, M. Reetz-Lamour, T. Amthor, L. G. Marcassa, and M. Weidemüller, Phys. Rev. Lett., **93**, 163001 (2004).
- [41] D. Tong, S. M. Farooqi, J. Stanojevic, S. Krishnan, Y. P. Zhang, R. Cote, E. E. Eyler, and P. L. Gould, Phys. Rev. Lett., **93**, 063001 (2004).
- [42] U. Raitzsch, V. Bendkowsky, R. Heidemann, B. Butscher, R. Löw, and T. Pfau, Phys. Rev. Lett., **100**, 013002 (2008).
- [43] Y. O. Dudin, L. Li, F. Bariani, and A. Kuzmich, Nature Physics, **8**, 790 (2012).
- [44] T. M. Weber, M. Hönig, T. Niederprüm, T. Manthey, O. Thomas, V. Guarrera, M. Fleischhauer, G. Barontini, and H. Ott, Nature Physics, **11**, 157 (2015).
- [45] T. Cubel Liebisch, A. Reinhard, P. R. Berman, and G. Raithel, Phys. Rev. Lett., **95**, 253002 (2005).
- [46] R. Heidemann, U. Raitzsch, V. Bendkowsky, B. Butscher, R. Löw, Luis Santos, and T. Pfau, Phys. Rev. Lett., **99**, 163601 (2007).

- [47] E. Urban, T. A. Johnson, T. Henage, L. Isenhower, D. D. Yavuz, T. G. Walker, and M. Saffman *Nature Physics*, **5**, 110 (2009).
- [48] A. Gaëtan, Y. Miroshnychenko, T. Wilk, A. Chotia, M. Viteau, D. Comparat, P. Pillet, A. Browaeys, and P. Grangier, *Nature Physics*, **5**, 115 (2009).
- [49] M. Viteau, P. Huillery, M. G. Bason, N. Malossi, D. Ciampini, O. Morsch, E. Arimondo, D. Comparat, and P. Pillet, *Phys. Rev. Lett.*, **109**, 053002 (2012).
- [50] M. Saffman, T. G. Walker, and K. Mølmer, *Rev. Mod. Phys.*, **82**, 2313 (2010).
- [51] L. Béguin, A. Vernier, R. Chicireanu, T. Lahaye, and A. Browaeys, *Phys. Rev. Lett.*, **110**, 263201 (2013).
- [52] T. Phol, E. Demler, and M. D. Lukin, *Phys. Rev. Lett.*, **104**, 043002 (2010).
- [53] M. D. Lukin, M. Fleischhauer, R. Cote, L. M. Duan, D. Jaksch, J. I. Cirac, and P. Zoller, *Phys. Rev. Lett.*, **87**, 037901 (2001).
- [54] J. H. Shapiro, *Phys. Rev. A*, **73**, 062305 (2006).
- [55] D. Maxwell, D. J. Szwer, D. Paredes-Barats, H. Busche, J. D. Pritchard, A. Gauguet, K. J. Weatherill, M. P. A. Jones, and C. S. Adams, *Phys. Rev. Lett.*, **110**, 103001 (2013).
- [56] D. Tiarks, S. Schmidt, G. Rempe, and S. Dürr, *Science Advances*, **2**, 1600036 (2016).
- [57] D. E. Chang, V. Vuletić, and M. D. Lukin, *Nature Photonics*, **8**, 685 (2014).
- [58] H. Busche, P. Huillery, S. W. Ball, T. Ilieva, M. P. A. Jones, and C. S. Adams *et al.*, *Nature Physics*, **13**, 655 (2017).
- [59] A. Aspuru-Guzik, and P. Walther, *Nature Phys.*, **8**, 285 (2012).
- [60] I. M. Georgescu, S. Ashhab, and F. Nori, *Rev. of Mod. Phys.*, **86**, 153 (2014).
- [61] D. Jaksch, J. I. Cirac, P. Zoller, S. L. Rolston, R. Côté, and M. D. Lukin, *Phys. Rev. Lett.*, **85**, 2208 (2000).
- [62] B. He, A. V. Sharypov, J. Sheng, C. Simon, and M. Xiao, *Phys. Rev. Lett.*, **112**, 133606 (2014).
- [63] D. Paredes-Barato, and C. S. Adams, *Phys. Rev. Lett.*, **112**, 040501 (2014).

- [64] H. Kübler, J. P. Shaffer, T. Baluktsian, R. Löw, and T. Pfau, *Nature Phot.*, **4**, 112 (2010).
- [65] A. K. Kölle, G. Epple, H. Kübler, R. Löw, and T. Pfau, *Phys. Rev. A.*, **85**, 063821 (2012).
- [66] Z. Zhang, H. Zheng, X. Yao, Y. Tian, J. Che, X. Wang, D. Zhu, Y. Zhang, and M. Xiao, *Scientific Reports*, **5**, 10462 (2015).
- [67] J. M. Kondo, N. Šibalić, A. Guttridge, C. G. Wade, N. R. D. Melo, C. S. Adams, and K. J. Weatherill, *Optics Lett.*, **40**, 5570 (2015).
- [68] D. Barredo, H. Kübler, R. Daschner, R. Löw and T. Pfau, *Phys. Rev. Lett.*, **110**, 123002 (2013).
- [69] C. Carr, R. Ritter, C. G. Wade, C. S. Adams, and K. J. Weatherill, *Phys. Rev. Lett.*, **111**, 113901 (2013).
- [70] F. Ripka, Y.-H. Chen, R. Löw, and T. Pfau *Phys. Rev. A*, **93**, 053429 (2016).
- [71] M. M. Müller, A. Köle, R. Löw, T. Pfau, and S. Montangero, *Phys. Rev. A*, **87**, 053412 (2013).
- [72] S. Yoshida, J. Burgdörfer, X. Zhang, and F. B. Dunning, *Phys. Rev. A*, **95**, 042705 (2017).
- [73] A. Urvoy, F. Ripka, I. Lekanovsky, D. Booth, J. P. Shaffer, T. Pfau, and R. Löw, *Phys. Rev. Lett.*, **114**, 203002 (2015).
- [74] N. Šibalić, C. G. Wade, C. S. Adams, K. J. Weatherill, and T. Pohl, *Phys. Rev. A*, **94**, 011401(R) (2016).
- [75] N. R. de Melo, C. G. Wade, N. Šibalić, J. M. Kondo, C. S. Adams, and K. J. Weatherill, *Phys. Rev. A*, **93**, 063863 (2016).
- [76] F. Letscher, O. Thomas, T. Niederprüm, M. Fleischhauer, and H. Ott, *Phys. Rev. X*, **7**, 021020 (2017).

## Chapter 2

# Rydberg atoms and Rydberg interactions

The Rydberg atom is any simple atom with one or more electrons being promoted to very large principal quantum number [1]. The Rydberg atoms were discovered in space around 1965 and also later on reported in [2]. It is first reflected in Bohr's original paper on Hydrogen atom where he showed that the atom can be excited to very high principal quantum number state. But during that time Rydberg atoms were not prepared in the laboratories. After the invention of the laser, researchers were able to prepare and detect the Rydberg atoms [3]. This finding gives pedagogical interest to the atomic physicist in the direction of the study of Rydberg atoms. The atoms in the Rydberg state possess exotic physical properties, for example, large dipole moment, high sensitivity to the external electric field etc.

In this chapter, properties of Rydberg atoms are discussed, i.e., scaling behaviour of Rydberg atoms governed by the natural laws. Also, the different types of Rydberg interactions and related cooperative phenomena like Rydberg blockade and Rydberg anti-blockade interaction are discussed. The discussion is restricted to the alkali atoms.

## 2.1 Quantum defect

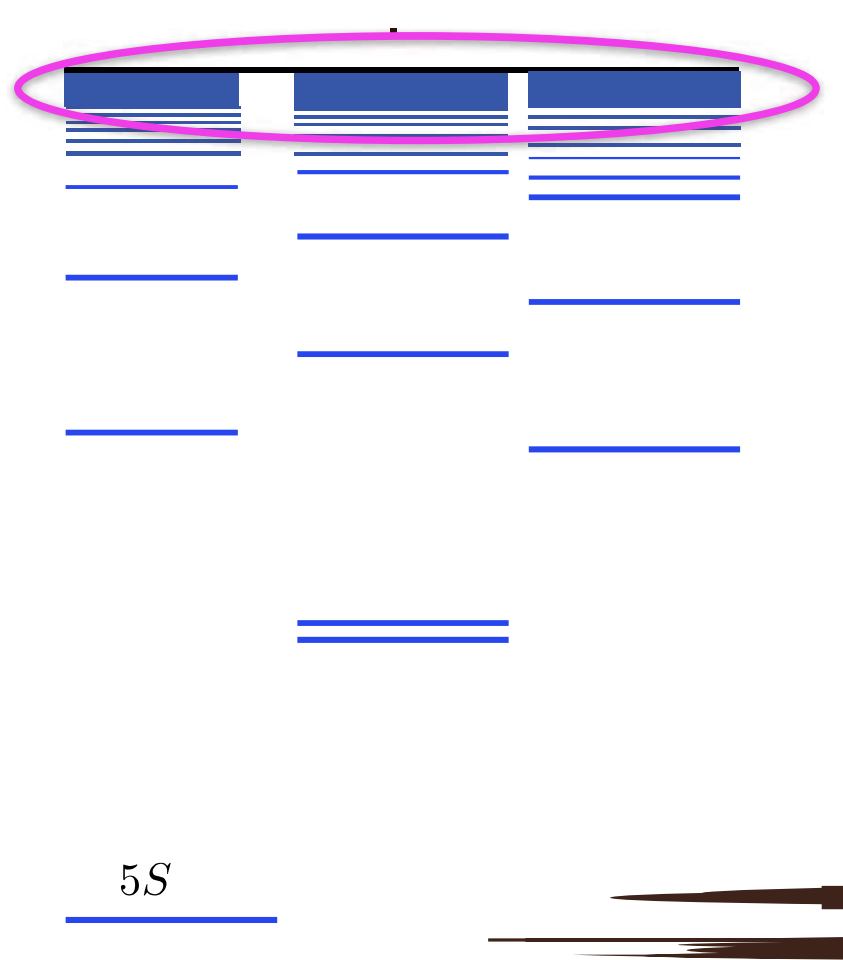


Figure 2.1: Schematic atomic level diagram of rubidium Rydberg atoms. The top most marked states are Rydberg excited states. As quantum number increases they become close to continuum.

The schematic energy level diagram of an alkali atom is depicted in fig. (2.1). Rubidium atom has one valence electron in  $5s_{1/2}$  state which behave like hydrogen like atoms. However the core electrons screen the Coulomb potential and hence the the Hydrogen like energy levels are corrected by introducing quantum defect [4–7] as which is given by,

$$E_n = -\frac{1}{2m(n - \delta_l)^2} \quad (2.1)$$

Where  $m$  is the mass of the atom. We introduce an effective quantum number  $n^* = n - \delta_l$  [4–8].

Table 2.1: Quantum defect of the alkali atoms for  $l = 0 - 3$ .

$l$	Li	Na	K	Rb	Cs
s	0.40	1.35	2.19	3.13	4.06
p	0.04	0.85	1.71	2.66	3.59
d	0.00	0.01	0.25	1.34	2.46
f	0.0	0.0	0.0	0.01	0.02

The quantum defect is found for many atomic species. Particularly for alkali atoms,  $\delta_l$  is found to be very slowly varying with  $n$  for a given value of  $l$ . Thus, the energy-level diagram for such an atom can be split into different series of states, each series corresponding to a different value of  $\delta_l$ . The excited states of such an atom is depicted in fig. (2.1). It also shows that, for a given principal quantum number, the higher angular momentum states are more nearly hydrogenic than the lower angular momentum states. Table (2.1) [4] is a listing of the quantum defects for the first few angular momentum states of the alkali atoms. This table clearly shows the dramatic decrease in  $\delta_l$  with increasing angular momentum. Experimentally, the quantum defect [9] is measured with much higher accuracy up to a relative uncertainty of  $10^{-7}$  [10].

## 2.2 Scaling laws of Rydberg atoms

Due to the excitation to the large quantum state of a Rydberg atom, the electron are loosely bound to the atom. Unlike Hydrogen atom, the required electric field to completely remove the outermost electron from the atoms is 10 V/Cm for  $n = 100$ . Here  $n$  is the principal quantum number of the Rydberg excited state. The scaling laws of the physical properties of the Rydberg atoms with principal quantum number  $n$  is introduced in Tab. 2.2. The ionisation field for the Rydberg electron scales as  $n^{-4}$ . That is why it is easier to pull out the outermost electron easier than the ground state electron. Therefore, ionisation of the Rydberg atoms are easier [11–14]. Also, the size of the atom goes as  $n^2$ , which means if one prepares the atom in  $n = 100$  the size of the atom will be 10,000 times the ground state atom which is mesoscopically large in size.

Table 2.2: Scaling of physical properties of the Rydberg atoms with principal quantum number

Property	n dependance	Typical number / application
Size	$n^2$	Few 100 nm
Binding energy	$n^{-2}$	0.1 eV
Life time	$n^3$	Long lived 100 $\mu$ sec for $n > 40$
Dipole moment	$n^2$	Strong dipolar interaction
Polarisability	$n^7$	Giant Kerr effect
Ionising field	$n^{-4}$	Detection
van der Waals interaction strength ( $C_6$ )	$n^{11}$	Collective interaction and QIP

Because of the large size of the Rydberg atom it has large dipole moment. The enormous dipole moment of the Rydberg atoms triggers strong interaction between atoms and hence leads to a physical phenomenon which is known as dipole blockade [15, 16]. The Rydberg excitation of one atom can be controlled by other atom's excitation via dipole blockade interaction which can serve as basic building block of quantum computation [17, 18] and quantum information processing (QIP) [19–23]. As an application of the ionisation property of the Rydberg atoms (ionising field  $\sim n^{-4}$ ), a detection technique is developed to detect the Rydberg excited atoms. The technique is called micro channel plate (MCP) detection [24–33]. This technique is widely used for the detection of the Rydberg atoms in cold atomic system. The Rydberg atoms also have large polarisability which obeys the scaling law as  $n^7$ , which making them highly sensitive to the external electric field. One can use the Rydberg atoms to measure the electric field whereas normal atoms are very weakly effected by the external electric field. This phenomenon encourages the study of electrometry using the Rydberg atoms. Recently, a giant electro-optic effect which is million fold larger than any other material, is demonstrated using the Rydberg atoms [34].

Rydberg interaction is also demonstrated in the van der Waals interaction regime [35–38]. The excitation of one atoms to the Rydberg state gets suppressed by another Rydberg excited atom via van der Waals interaction potential, which has the form  $V(r) = \frac{C_6}{r^6}$  [38–40]. The van der Waals interaction strength ( $C_6$ ) scales with the principal quantum number of the Rydberg

excitation as  $n^{11}$ . In the case of rubidium, the ground state principal quantum number is given by  $n = 5$ . If one excites the atom to  $n = 50$ , then the interaction strength is increased by  $10^{11}$  times the ground state interaction. This strong interaction induces the many-body effect in the system and also leads to the van der Waals blockade interaction.

## 2.3 Interacting Rydberg atoms

In the absence of the external electric field, vacuum induced dipole interaction between Rydberg atoms leads to van der Waals type interaction. On application of an external electric field, the Rydberg atom gets polarised. These atomic dipoles interact with each other strongly and the interaction is called dipole-dipole interaction. These interactions of the Rydberg atoms leads to cooperative phenomena [41–46] such as the Rydberg blockade and the Rydberg anti-blockade.

### 2.3.1 van der Waals interaction

In order to understand the origin of van der Waal interaction [47] between two Rydberg atoms, let us consider an interaction Hamiltonian which can be described as,

$$H_I = k \frac{(\vec{r}_A \cdot \vec{r}_B)|r|^2 - 3(\vec{r} \cdot \vec{r}_A)(\vec{r} \cdot \vec{r}_B)}{|r|^5} + O(|r|^{-4}) \quad (2.2)$$

Let us choose  $\vec{r}$  to be along  $z$  axis. The orientation of the dipoles are depicted in fig. (2.2). The total Hamiltonian of the system can be written as,  $H_0 + H_I$ , where  $H_0$  is the unperturbed Hamiltonian which consists of the coulomb interaction between nuclei and the valence electrons. Then the first order energy shift due to the interaction can be expressed as  $\Delta_1 E = \frac{k}{|r|^3} \langle \psi | \vec{r}_A \cdot \vec{r}_B - 3z_A z_B | \psi \rangle$ , neglecting higher order terms in multipole expansion. The energy eigenstate of the exact Hamiltonian can be represented as  $|\psi\rangle = |A\rangle \otimes |B\rangle$ . Since there are rotational symmetry in the system and the states  $|A\rangle$  and  $|B\rangle$  are parity eigenstates, the states will follow  $\langle A | r_A | A \rangle = 0$  and  $\langle B | r_B | B \rangle = 0$ . So the first order energy correction vanishes, i.e.,  $\Delta_1 E = 0$ .

The second order energy correction can be given by,

$$\begin{aligned} \Delta_2 E &= - \sum_{i \neq j} \frac{|\langle \psi_i | H_I | \psi_j \rangle|^2}{E_j - E_i} \\ &= - \frac{k^2}{|r|^6} \sum_{i \neq j} \frac{|\langle \psi_i | (\vec{r}_A \cdot \vec{r}_B - 3z_A z_B) | \psi_j \rangle|^2}{E_j - E_i} \\ &= \frac{C_6}{r^6} \end{aligned}$$



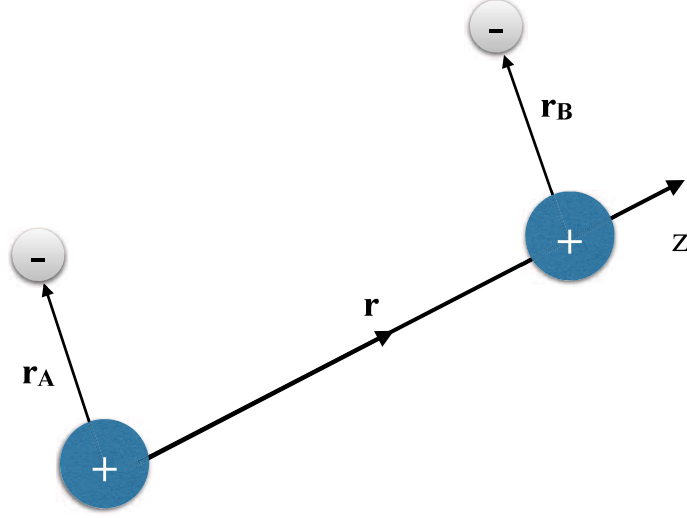


Figure 2.2: Schematic representation of van der Waals interaction between two Rydberg atoms. The nuclei of the Rydberg atoms are separated by the distance  $r$ . The respective nucleus to electron distances are symbolised by  $r_A$  and  $r_B$ .

The strength of the energy shift is given by,  $C_6 = -k^2 \sum_{i \neq j} \frac{|\langle \psi_i | (\vec{r}_A \cdot \vec{r}_B - 3z_A z_B) | \psi_j \rangle|^2}{E_j - E_i}$ . The energy difference  $(E_j - E_i)$  scales as  $n^{-3}$ . Since the size and the dipole moment of the Rydberg atom scales as  $n^2$ , the interaction energy strength scales as,  $C_6 \propto \frac{(n^2 n^2)^2}{n^{-3}} = n^{11}$ .

### 2.3.2 Dipole-dipole interaction

On the application of an external electric field the Rydberg atom polarises which triggers the dipole-dipole interaction between them. The interaction between two dipoles [48] is given by the Eq. (2.2). Here the externally applied electric field  $\vec{F}$  is stronger than all other fields present in the system. Hence, all the atomic dipoles will align along the externally applied electric field. In terms of dipole moment the two-body interaction potential can be rewritten as (using Eq. (2.2)),  $V_{12} = k' \frac{\vec{\mu}_1 \cdot \vec{\mu}_2 - 3(\vec{\mu}_1 \cdot \hat{n})(\vec{\mu}_2 \cdot \hat{n})}{r^3}$ . Let us define an angle  $\theta$  such that  $\cos \theta = \frac{(\hat{n} \cdot \vec{F})}{F}$ , then we have,

$$\begin{aligned} V_{12} &= \frac{k' \mu_1 \mu_2 (1 - \cos^2 \theta)}{r^3} \\ &= \frac{C_3}{r^3} \end{aligned} \quad (2.3)$$

Here the dipole interaction strength is given by,  $C_3 = k' \mu_1 \mu_2 (1 - \cos^2 \theta)$ . For Rydberg atoms the dipole moment,  $\mu \propto n^2$ , then the dipole interaction strength,  $C_3 \propto n^4$ .

### 2.3.3 Rydberg blockade interaction

In order to understand the Rydberg blockade, let us consider a simple picture of two identical atoms interacting via Rydberg excited states. On the application of a resonant monochromatic laser field, one of them can be excited to the Rydberg state but the doubly excited state ( $|rr\rangle$ ) is shifted due to the interaction between the atoms and becomes off resonant to the applied laser field. The interaction between the atoms can be either van der Waals type ( $\frac{C_6}{R^6}$ ) or the dipole-dipole ( $\frac{C_3}{R^3}$ ) interaction, where  $R$  is the relative distance between the atoms.

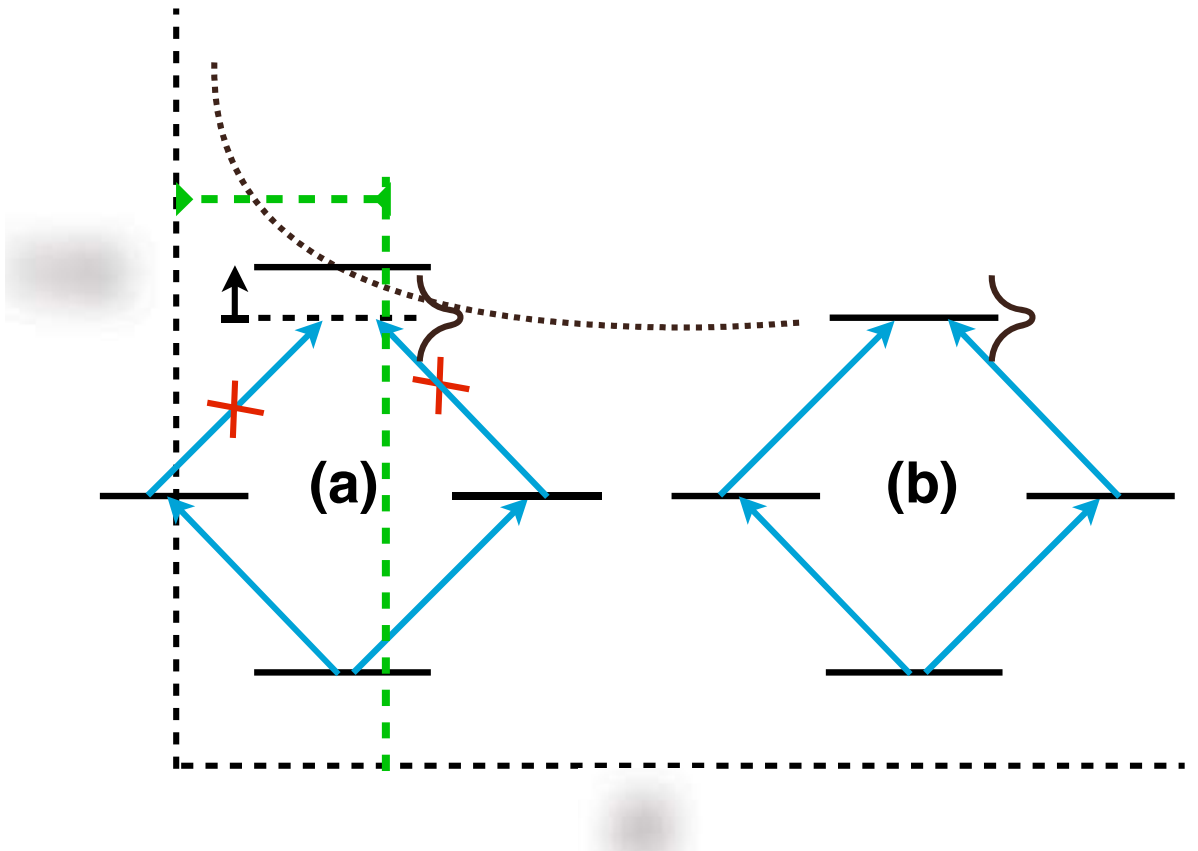


Figure 2.3: Schematic representation of Rydberg blockade interaction. The excitation field is resonantly interacting with the single Rydberg excitation states ( $|rg\rangle$  and  $|gr\rangle$ ). (a) The relative distance between the atoms is below the blockade radius. Here the interaction between the atoms are strong enough to shift the two-atom Rydberg excited state beyond the line-width of the excitation. (b) The relative distance between the atoms is large enough to neglect the Rydberg interaction between them and hence the 2-atom Rydberg excited state will be resonant to the excitation field.

Here  $|rr\rangle$  is a doubly excited state. The state dependent Rydberg interaction start playing role in  $|rr\rangle$  state. In fig. (2.3b), the distance between the atoms is such that they cannot intro-

duce any interaction shift to the doubly excited state  $|rr\rangle$ . In this case, the applied laser field is resonant to the Rydberg transition of the individual atoms and hence the single ( $|rg\rangle$  &  $|gr\rangle$ ) as well as the doubly ( $|rr\rangle$ ) Rydberg excitation can take place.

In fig. (2.3a), the distance between the atoms is such that the interaction shift of doubly excited state ( $|rr\rangle$ ) is outside the line-width of the excitation. However, the single Rydberg excitation ( $|rg\rangle$  &  $|gr\rangle$ ) can take place. For the van der Waals pair interaction, Rydberg blockade radius is defined as,  $R_b = (\frac{C_6}{\hbar\Omega})^{1/6}$ , where  $\Omega$  is the Rabi coupling of the applied laser field with the atoms. The definition of the Rydberg blockade radius is valid if and only if  $\Omega > \Gamma$ , where  $\Gamma$  is the dephasing rate of the system.

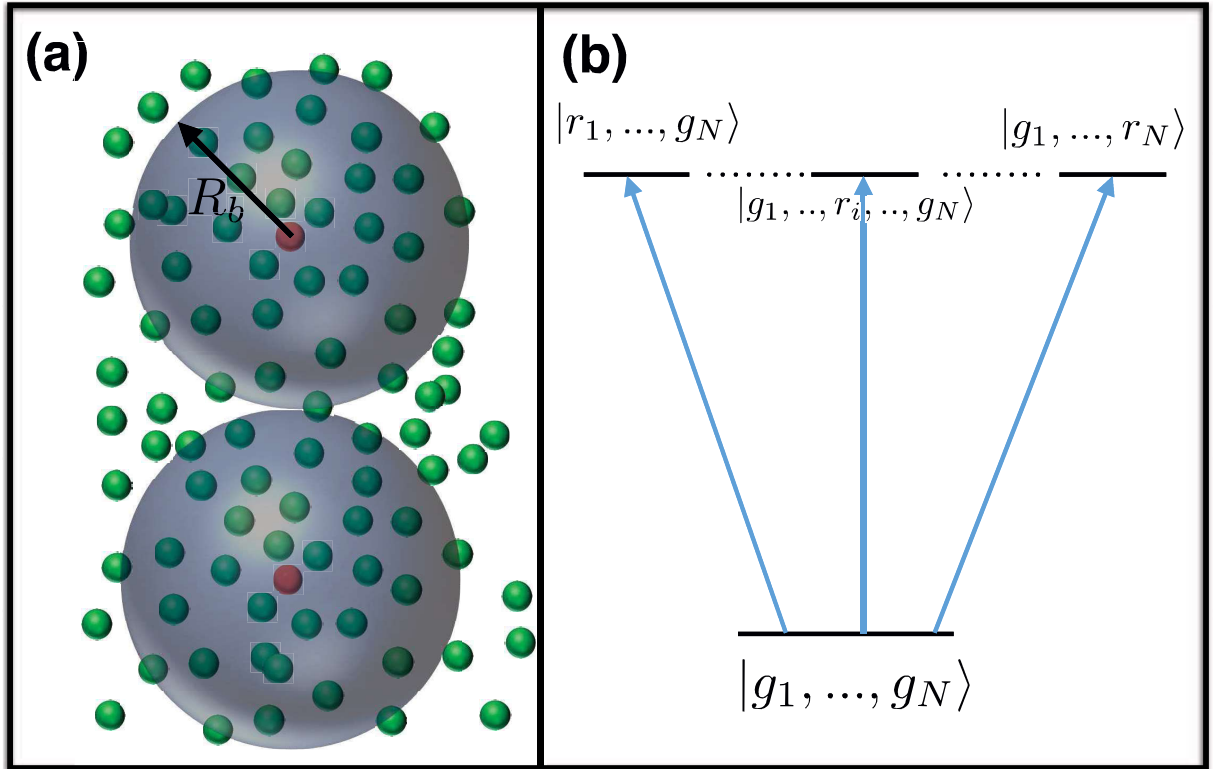


Figure 2.4: (a) A representation of superatom formation due to Rydberg blockade. The big sphere represents the superatom where only the central atom (depicted in red colour) is Rydberg excited. The other atoms inside the superatom are not allowed to get excited in the Rydberg state. Here  $R_b$  represents the blockade radius which also defines the size of the superatom. (b) Atomic level scheme for single Rydberg excitation out of  $N$  atoms present in blockade sphere. Here many-body ground state is represented by  $|g_1, \dots, g_N\rangle$ . The single excited state is defined as  $|g_1, \dots, g_i, \dots, g_N\rangle$ . Here  $i$ th atom is excited to the Rydberg state.

In the strong blockade interaction regime, only one atom is allowed to be excited to the

Rydberg state. Therefore, the state of the system becomes the superposition of single excited state ( $|rg\rangle$  &  $|gr\rangle$ ) which can be represented as,  $|\psi_+\rangle = \frac{1}{\sqrt{2}}(|rg\rangle + |gr\rangle)$ . This is also known as entangled state. The accessible states of the 2-atom Hilbert space can be written as  $|gg\rangle$ ,  $|gr\rangle$ ,  $|rg\rangle$  and  $|rr\rangle$ . The subspace consists of the states  $|gr\rangle$  and  $|rg\rangle$  can be transformed to new basis,  $|\psi_\pm\rangle = \frac{1}{\sqrt{2}}(|rg\rangle \pm |gr\rangle)$ . The dipole matrix element which couples the ground state and the Rydberg excited state is given by  $\mu_{gr} = \langle g|\hat{\mu}|r\rangle$ . For two atom state,  $\langle gg|\hat{\mu}|\psi_+\rangle = \sqrt{2}\mu_{gr}$  and  $\langle gg|\hat{\mu}|\psi_-\rangle = 0$ . Therefore, when both the atoms are driven in the blockade regime the Rabi coupling is enhanced by  $\sqrt{2}$  [49–55]. The enhancement of the Rabi frequency is the signature of the existence of cooperative behaviour in the system.

It can be generalized for  $N$ -atoms interacting via the Rydberg blockade interaction. In this case, the suppression of the multi-atom excitation leads to many-body entangled state which can be represented as,  $|\psi\rangle = \frac{1}{\sqrt{N}} \sum_i |g_1 \dots r_i \dots g_N\rangle$ . A schematic transition for  $N$ -atom Rydberg excitation is depicted in fig. (2.4b). In the entangled state basis, the Rabi coupling modifies as  $\sqrt{N}\Omega$ . Based on the enhancement of Rabi frequency due to multi-atom coherence, a model is constructed namely the superatom model [56, 57]. A representation of superatom is depicted in the fig. (2.4a).

### 2.3.4 Rydberg anti-blockade interaction

In fig. (2.5), the two-atom states are depicted where the nature of the interaction between atoms are repulsive in nature. That is why the energy shift due to the interaction is positive. In fig. (2.5),  $R$  is the relative distance between the atoms and the interaction is proportional to  $\frac{1}{R^6}$ . Therefore, for larger distance the interaction shift is negligible as shown in fig. (2.5.b). For  $R < R_b$ , the energy shift is significantly larger than the line-width of excitation as depicted in fig. (2.5.a). If the frequency of the laser is chosen such that it is outside the line-width of the single atom Rydberg excited state, then no Rydberg excitation is expected from the system. If the laser is blue detuned then the frequency can be set such that the doubly excited state can be resonant to the applied laser. This is called the Rydberg anti-blockade [37, 43, 58–60]. Anti-blockade happens for blue detuned laser for repulsive interaction whereas it happens for red-detuned for attractive interaction. Fig. (2.5.a) shows that for repulsive Rydberg interaction  $|rr\rangle$  shifts above the non-interacting  $|rr\rangle$ -state. According to the energy conservation, the applied laser can be resonant to the interacting  $|rr\rangle$  if and only if it must be blue detuned from the individual atomic resonance. On the other hand, if the Rydberg interaction is considered to be

attractive then the shift of the  $|rr\rangle$  state is below the single atom resonant frequency. With the similar argument using energy conservation, it can be showed that for attractive interaction the applied laser must be red detuned from single atom excitation frequency in order to satisfy two atom excitation. The schematic atomic transition for the process is depicted in the fig. (2.5a). By increasing the interatomic distance the Rydberg interaction can be made absent which is depicted in fig. (2.5b). In this situation, no Rydberg excitation will be found in the system.

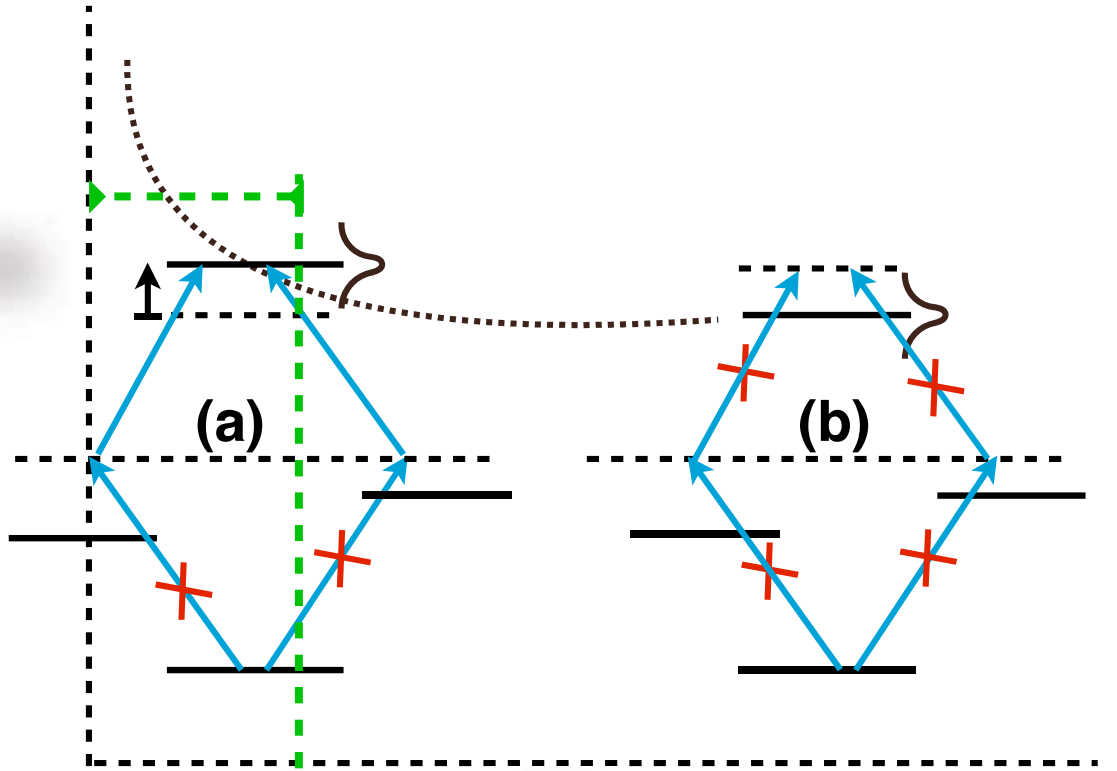


Figure 2.5: Schematic representation of the Rydberg anti-blockade interaction. The frequency of the excitation field is such that it is outside the line-width of the single Rydberg excitation states ( $|rg\rangle$  and  $|gr\rangle$ ). (a) The relative distance between the atoms is below the blockade radius. The applied laser is blue detuned to the single Rydberg excitation. Since the atoms are inside the blockade radius, the Rydberg interaction assists the two-atom excited state to satisfy resonance condition. (b) The relative distance between the atoms is large enough to neglect the Rydberg interaction between them. Here neither single Rydberg excitation nor multiple Rydberg excitation will occur.

## 2.4 Conclusion

The scaling laws followed by the physical properties of the Rydberg atoms makes it a distinguished interesting system. Due to the large intrinsic dipole moment of the Rydberg atom, it has very strong state-dependent interaction nature. This strongly interacting system gives rise to many-body effect in the system. In cold atom system, Rydberg blockade mediated many-body effects are already established. This phenomenon has significant application in the field of Rydberg quantum optics in low light level. In this thesis, the Rydberg blockade interaction in the thermal atomic ensemble will be investigated.

# Bibliography

- [1] Thomas F. Gallagher. Rydberg Atoms. Cambridge University Press. ISBN 0-521-02166-9 (1994).
- [2] Yu. N. Gnedin, A. A. Mihajlov, Lj. M. Ignjatovic, N. M. Sakan, V. A. Sreckovic, M. Yu. Zakharov, N. N. Bezuglov, and A. N. Klycharev, *New Astronomy Reviews.*, **53** 259 (2009).
- [3] L. Moi, C. Fabre, P. Goy, M. Gross, S. Haroche, P. Encrenaz, G. Beaudin, and B. Lazareff, *Optics Comm.*, **33**, 47 (1980).
- [4] C. E. Burkhardt and J. J. Leventhal. Topics in atomic physics. Springer Science+Business Media, Inc., 233 Spring Street, New York, NY 10013, USA (2006).
- [5] G. W. F. Drake, and R. A. Swainson, *Phys. Rev. A*, **44**, 5448 (1991).
- [6] B. Sanguinetti, H. O. Majeed, M. L. Jones, and B. T. H. Varcoe, *J. Phys. B: At. Mol. Opt. Phys.*, **42**, 165004 (2009).
- [7] V. A. Sautenkov, S. A. Saakyan, E. V. Vilshanskaya, D. A. Murashkin, B. B. Zelener, and B. V. Zelener, *Laser Phys.*, **26**, 115701 (2016).
- [8] J. D. Pritchard. Cooperative Optical Non-linearity in a blockaded Rydberg Ensemble, a Ph.D. thesis. Durham University (2011).
- [9] V. A. Kosteleck and M. M. Nieto, *Physical Review A*, **32**, 3243 (1985).
- [10] M. Mack, F. Karlewski, H. Hattermann, S. Höckh, F. Jessen, D. Cano, and J. Fortágh, *Phys. Rev. A*, **83**, 052515 (2011).
- [11] H. J. Korsch, and R. Möhlenkamp, *Z. Phys. A- Atom and Nuclei*, **314**, 267 (1983).
- [12] B. C. Yang and F. Robicheaux, *Physical Review A*, **91**, 043407 (2015).

- [13] A. J. McCulloch, R. W. Speirs, J. Grimm, B. M. Sparkes, D. Comparat, and R. E. Scholten, *Physical Review A*, **95**, 063845 (2017).
- [14] S. E. Anderson, and G. Raithel, *Nature Comm.*, **4**, 2967 (2013).
- [15] D. Comparat and P. Pillet, *Journal of the Optical Society of America B*, **27**, A208 (2010).
- [16] M. Zwiernik and P. Kok, *Phys. Rev. A*, **79**, 022304 (2009).
- [17] M. D. Lukin, M. Fleischhauer, R. Cote, L. M. Duan, D. Jaksch, J. I. Cirac, and P. Zoller, *Phys. Rev. Lett.*, **87**, 037901 (2001).
- [18] J. Gillet, G. S. Agarwal, and T. Bastin, *Phys. Rev. A*, **81**, 013837 (2010).
- [19] M. Saffman, T. G. Walker, and K. Mølmer, *Rev. Mod. Phys.*, **82**, 2313 (2010).
- [20] D. Jaksch, J. I. Cirac, P. Zoller, S. L. Rolston, R. Côté, and M. D. Lukin, *Phys. Rev. Lett.*, **85**, 2208 (2000).
- [21] J. Schmiedmayer, R. Folman, and T. Calarco, *Journal of Modern Optics*, **49**, 1375 (2010).
- [22] P. S. Jessen, I. H. Deutsch, and R. Stock, *Quantum Information Processing*, **3**, 91 (2004).
- [23] X. L. Zhang, L. Isenhower, A. T. Gill, T. G. Walker, and M. Saffman, *Phys. Rev. A*, **82**, 030306(R) (2010).
- [24] A. C. L. Jones, A. M. Piñeiro, E. E. Roeder, H. J. Rutbeck-Goldman, H. W. K. Tom, and A. P. Mills Jr., *Review of Scientific Instruments*, **87**, 113307 (2016).
- [25] Limei Wang, Hao Zhang, Linjie Zhang, Changyong Li, Yonggang Yang, Jianming Zhao, Georg Raithel and Suotang Jia, *New J. Phys.*, **17**, 063011 (2015).
- [26] T. Cubel Liebisch, A. Reinhard, P. R. Berman, and G. Raithel, *Phys. Rev. Lett.*, **98**, 109903 (2007).
- [27] M. P. Robinson, B. Laburthe Tolra, Michael W. Noel, T. F. Gallagher, and P. Pillet, *Phys. Rev. Lett.*, **85**, 4466 (2000).
- [28] S. D. Hogan and F. Merkt, *Phys. Rev. Lett.*, **100**, 043001 (2008).
- [29] K. Singer, M. Reetz-Lamour, T. Amthor, L. G. Marcassa, and M. Weidemüller, *Phys. Rev. Lett.*, **93**, 163001 (2004).



- [30] E. Vliegen, S. D. Hogan, H. Schmutz, and F. Merkt, Phys. Rev. A, **76**, 023405 (2007).
- [31] A. Schwarzkopf, R. E. Sapiro, and G. Raithel, Phys. Rev. Lett., **107**, 103001 (2011).
- [32] T. Vogt, M. Viteau, A. Chotia, J. Zhao, D. Comparat, and P. Pillet, Phys. Rev. Lett., **99**, 073002 (2007).
- [33] C. S. Hofmann, G. Gnter, H. Schempp, M. Robert-de-Saint-Vincent, M. Gärttner, J. Evers, S. Whitlock, and M. Weidemüller, Phys. Rev. Lett., **110**, 203601 (2013).
- [34] A. K. Mohapatra, M. G. Bason, B. Butscher, K. J. Weatherill and C. S. Adams, Nature Phys., **4**, 890 (2008).
- [35] L. Béguin, A. Vernier, R. Chicireanu, T. Lahaye, and A. Browaeys, Phys. Rev. Lett., **110**, 263201 (2013).
- [36] T. Baluktsian, B. Huber, R. Lw, and T. Pfau, Phys. Rev. Lett., **110**, 123001 (2013).
- [37] D. Kara, A. Bhowmick, and A. K. Mohapatra, Scientific Reportsvolume, **8**, 5256 (2018).
- [38] A. Bhowmick, D. Kara, and A. K. Mohapatra arXiv: 1802.06599v1 (2018).
- [39] T. G. Walker, and M. Saffman, Phys. Rev. A, **77**, 032723 (2008).
- [40] R. Heidemann, U. Raitzsch, V. Bendkowsky, B. Butscher, R. Löw, Luis Santos, and T. Pfau, Phys. Rev. Lett., **99**, 163601 (2007).
- [41] I. Mourachko, D. Comparat, F. de Tomasi, A. Fioretti, P. Nosbaum, V. M. Akulin, and P. Pillet, Phys. Rev. Lett., **80**, 253 (1998).
- [42] T. J. Carroll, S. Sunder, and M. W. Noel, Phys. Rev. A, **73**, 032725 (2006).
- [43] C. Ates, T. Pohl, T. Pattard, and J. M. Rost, Phys. Rev. A, **76**, 013413 (2007).
- [44] J. Honer, H. Weimer, T. Pfau, and H. P. Büchler, Phys. Rev. Lett., **105**, 160404 (2010).
- [45] A. Reinhard, K. C. Younge, and G. Raithel, Phys. Rev. A, **78**, 060702(R) (2008).
- [46] I. Mourachko, W. Li, and T. F. Gallagher, Phys. Rev. A, **70**, 031401(R) (2004).
- [47] A. C. Ipsen and K. Splittorff, arXiv:1401.8141v2 (2014).

- [48] E. Altieri, D.P. Fahey, M. W. Noel, R. J. Smith and T. J. Carroll, Phys. Rev. A, **84**, 053431 (2011).
- [49] B. Sun, and F. Robicheaux, New J. Phys., **10**, 045032 (2008).
- [50] T. M. Weber, M. Höning, T. Niederprüm, T. Manthey, O. Thomas, V. Guarrera, M. Fleischhauer, G. Barontini, and H. Ott, Nature Physics, **11**, 157 (2015).
- [51] J. Stanojevic, and R. Côté, Phys. Rev. A, **80**, 033418 (2009).
- [52] R M W van Bijnen, S Smit, K A H van Leeuwen, E J D Vredenburg and S J J M F Kokkelmans, J. Phys. B: At. Mol. Opt. Phys., **44**, 184008 (2011).
- [53] A. Gaëtan, Y. Miroshnychenko, T. Wilk, A. Chotia, M. Viteau, D. Comparat, P. Pillet, A. Browaeys, and P. Grangier, Nature Physics, **5**, 115 (2009).
- [54] E. Urban, T. A. Johnson, T. Henage, L. Isenhower, D. D. Yavuz, T. G. Walker, and M. Saffman Nature Physics, **5**, 110 (2009).
- [55] J. Zeiher, P. Schauß, S. Hild, T. Macr, I. Bloch, and C. Gross, Phys. Rev. X, **5**, 031015 (2015).
- [56] H. Weimer, M. Müller, I. Lesanovsky, P. Zoller, and H. P. Büchler, Nature Phys., **6** 382 (2010).
- [57] C. Tresp. Rydberg polaritons and Rydberg superatoms-novel tools for quantum nonlinear optics, a Ph.D. thesis, Stuttgart University (2017).
- [58] T. Amthor, C. Giese, C. S. Hofmann, and M. Weidemüller, Phys. Rev. Lett., **104**, 013001 (2010).
- [59] M. Mattioli, Al. W. Glätzle, and W. Lechner, New J. Phys., **17**, 113039 (2015).
- [60] H. Zheng, Y. Zhao, C. Yuan, Z. Zhang, J. Che, Y.i Zhang, Y. Zhang, and Y. Zhang, Optics Express, **21**, 11728 (2013).

# Chapter 3

## Atomic properties and atom-light interaction

Interaction of light with atoms is the basis for many aspects of quantum optics and atomic physics. A simple model of a two-level system interacting with the light field can explain many fundamental as well as applied quantum mechanical phenomena such as quantum sensing [1], Rabi oscillations [2, 3] and atom trapping by light field [4–7] which based on the principle of mechanical force experienced by an atom due to the light field. Study of atom-light interaction also has significant importance in the field of nonlinear optics to study cross phase [8, 9] and self-phase modulation [10, 11]. Light fields cannot interact with each other in free space but can interact via an atomic dispersive medium. A probe photon propagating through the atomic medium, in presence of a control field, can experience phase-shift due to the dispersive medium. The control laser field polarises the atomic medium and there is a back action of the atomic medium on probe polarisation. This is possible if and only if the response of the medium is beyond the linear dependence of the electric field of the applied laser.

In this chapter, we will discuss basic atomic properties and laser-atom interactions using two and three level system. It is to be noted that the discussion is restricted to rubidium atom. Also the saturation spectroscopy is used for the frequency stabilisation.

### 3.1 Atomic properties

The transition wavelength from the ground state to the first excited state for rubidium is in infrared regime which is advantageous because it can be driven by an optical field. The lasers for the transition is commercially available which allows the neutral rubidium trapped in a magneto optical trap (MOT). The rubidium atoms are good candidate to study Rydberg physics

which is the prime objective of the thesis.

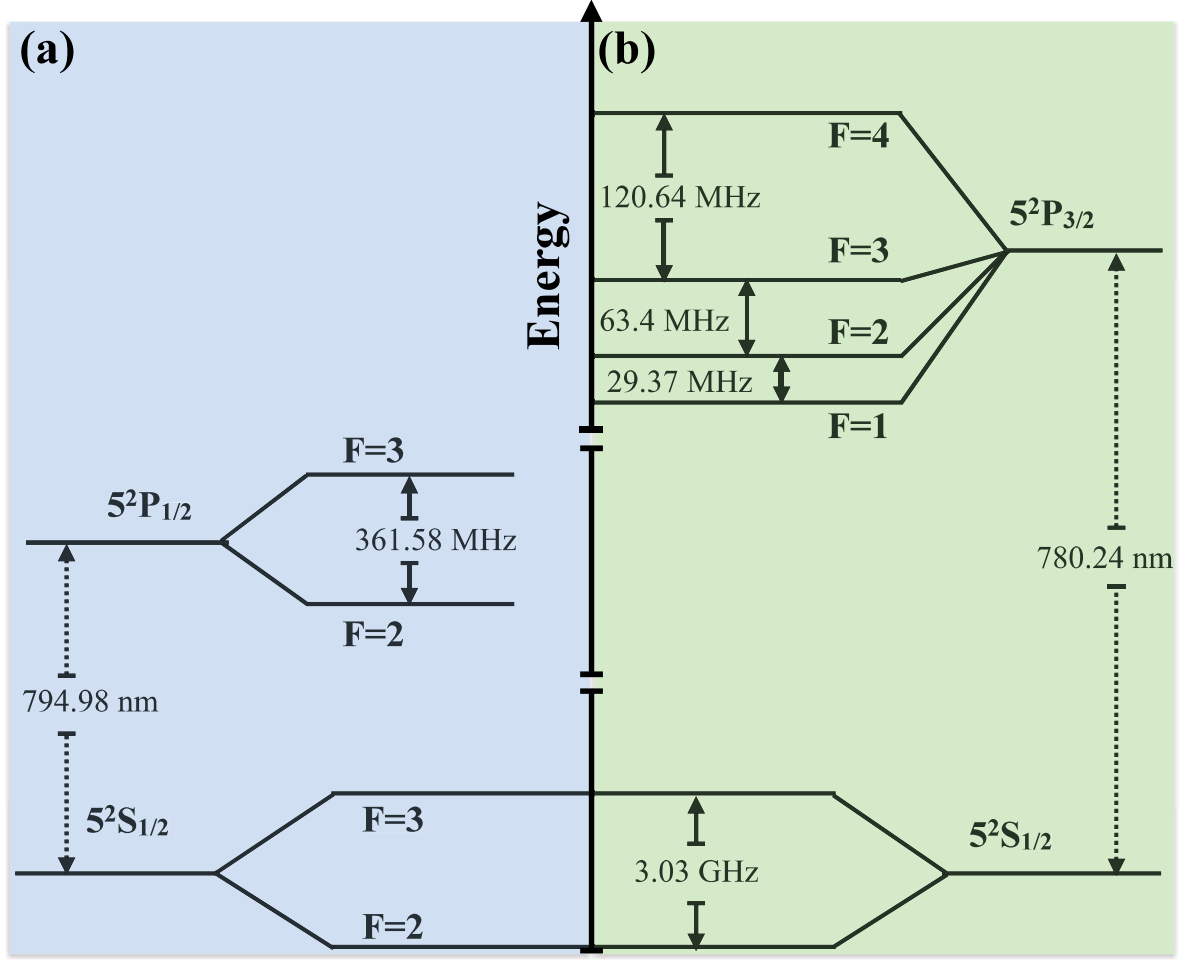


Figure 3.1: (a)  $D_1$  transition for  $^{85}\text{Rb}$ . (b)  $D_2$  transition for  $^{85}\text{Rb}$ . The transition wave-lengths for  $D_1$  and  $D_2$  transitions are  $\sim 795$  nm and  $\sim 780$  nm respectively [12]. The atomic transitions are governed by the dipole selection rule  $\Delta F = 0, \pm 1$ .

### 3.1.1 Fine structure splitting

Fine structure splitting occurs due to the spin-orbit coupling i.e., the degeneracy of the orbital angular momentum is lifted due to the coupling with the spin angular momentum. The total angular momentum  $j$  is defined as  $j = l + s$ . For the ground state of rubidium,  $l = 0$  as it is  $S$ -state. From the addition of angular momentum, the possible states of  $j$  can be predicted as  $|l - s| \leq j \leq |l + s|$ . The  $j$ -value of the state is given by  $j = 0 + 1/2 = 1/2$  since the spin angular momentum quantum number  $s$  is  $1/2$ . The ground  $5S_{1/2}$  state is singlet under fine structure coupling. For  $P$ -state,  $l = 1$ , then the  $j$ -values are  $j = 1 - 1/2 = 1/2$  and  $j = 1 + 1/2 = 3/2$ . Here the transition between the levels is governed by the fine structure

dipole selection rule,  $\Delta l = \pm 1$ . The ground state transitions for rubidium,  $5^2S_{1/2} \rightarrow 5^2P_{1/2}$  and  $5^2S_{1/2} \rightarrow 5^2P_{3/2}$  are known as  $D_1$  and  $D_2$  transition lines respectively.

### 3.1.2 Hyperfine structure splitting

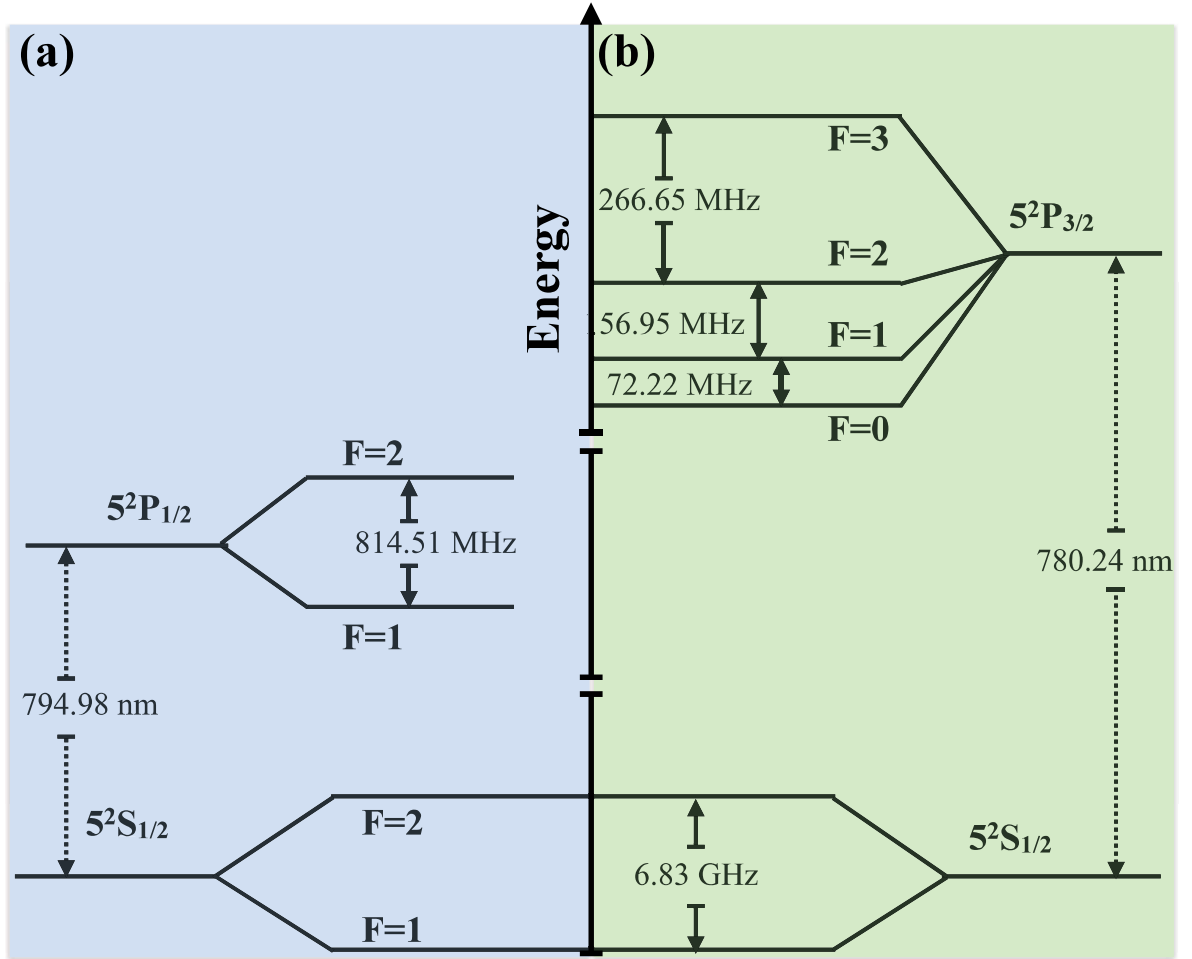


Figure 3.2: (a)  $D_1$  transition for  $^{87}\text{Rb}$ . (b)  $D_2$  transition for  $^{87}\text{Rb}$ . The transition wave-lengths for  $D_1$  and  $D_2$  transitions are  $\sim 795$  nm and  $\sim 780$  nm respectively [13]. The atomic transitions are governed by the dipole selection rule  $\Delta F = 0, \pm 1$ .

Hyperfine splitting occurs due to the coupling of the magnetic moment of the nuclear spin angular momentum  $I$  with the magnetic moment of the total angular momentum of electron  $j$ . The total angular momentum  $F$  of the atom is defined as,  $F = I + j$ . For  $^{85}\text{Rb}$  and  $^{87}\text{Rb}$  isotope the nuclear spins are respectively given by  $I = 5/2$  and  $I = 3/2$ . From the addition of angular momentum the possible states of  $F$  can be predicted as  $|j - I| \leq F \leq |j + I|$ .

The degeneracy of the ground state  $5^2S_{1/2}$  of  $^{85}\text{Rb}$  is lifted by the states  $|F = 5/2 + 1/2 = 3\rangle$  and  $|F = 5/2 - 1/2 = 2\rangle$ . Here, the hyperfine states are represented using the basis representation  $|F = I + j\rangle$ . The hyperfine levels of  $5^2P_{1/2}$  are  $|F = 5/2 + 1/2 = 3\rangle$  and  $|F = 5/2 - 1/2 = 2\rangle$ . The  $5^2P_{3/2}$  manifold contains  $|F = 5/2 + 3/2 = 4\rangle$ ,  $|F = 5/2 + 1/2 = 3\rangle$ ,  $|F = 5/2 - 1/2 = 2\rangle$  and  $|F = 5/2 - 3/2 = 1\rangle$ . For  $^{85}\text{Rb}$ , the hyperfine states with respective energy splittings are depicted in the fig. (3.1).

The degeneracy of the ground state  $5^2S_{1/2}$  of  $^{87}\text{Rb}$  is lifted by the states  $|F = 3/2 + 1/2 = 2\rangle$  and  $|F = 3/2 - 1/2 = 1\rangle$ . Here, the hyperfine states are represented using the basis representation  $|F = I + j\rangle$ . The hyperfine levels of  $5^2P_{1/2}$  are  $|F = 3/2 + 1/2 = 2\rangle$  and  $|F = 3/2 - 1/2 = 1\rangle$ . The  $5^2P_{3/2}$  manifold contains  $|F = 3/2 + 3/2 = 3\rangle$ ,  $|F = 3/2 + 1/2 = 2\rangle$ ,  $|F = 3/2 - 1/2 = 1\rangle$  and  $|F = 3/2 - 3/2 = 0\rangle$ . For  $^{87}\text{Rb}$ , the hyperfine states are depicted in the fig. (3.2). The atomic transitions are governed by the dipole selection rule  $\Delta F = 0, \pm 1$ .

### 3.1.3 Zeeman effect on hyperfine states

The number of Zeeman sub-levels for a hyperfine state with total angular momentum quantum number  $F$  is given by  $2F + 1$ . The quantum number for the Zeeman sub-levels is given by  $m_F$  which has the range  $m_F = -F, \dots, -1, 0, +1, \dots, +F$ . The Zeeman states are characterised by  $|F, m_F\rangle$ . In the absence of the magnetic field, the Zeeman sub-levels are degenerate. On application of an external magnetic field ( $\vec{B}$ ), the degeneracy is lifted. The Hamiltonian of the system is given by,  $H = H_0 + H_I$ , where  $H_0$  is the unperturbed Hamiltonian of the atom and the interacting Hamiltonian is given by,  $H_I = -\vec{\mu} \cdot \vec{B}$ , the magnetic dipole moment is given by  $\vec{\mu} = g_F \mu_B \vec{F}$ , where  $\mu_B$  is the Bohr magneton and  $g_F = g_J \frac{F(F+1) + J(J+1) - I(I+1)}{2F(F+1)}$ . The Lande g factor is given by,

$$g_J = 1 + \frac{J(J+1) + S(S+1) - L(L+1)}{2J(J+1)} \quad (3.1)$$

Then the first order energy correction due the external magnetic field perturbation is,

$$\Delta E_{m_F} = -g_F \mu_B m_F B \quad (3.2)$$

This is called energy shift due to linear Zeeman effect. This approximation does not hold true when the energy shift due to the perturbation becomes comparable to the hyperfine splitting. This is the effect of quadratic Zeeman effect.

## 3.2 Atom light interaction

Basic atom-light interaction for two and three level system are discussed in this section.

### 3.2.1 2-level system

Let us consider a two level atom, with resonant frequency  $\omega_0$  driven under the influence of an external light field of frequency  $\omega_L$  as shown in figure (3.3) [14, 15]. The atomic Hamiltonian of the system is given by,  $H_A = \hbar\omega_0|e\rangle\langle e|$ . The applied electric field is given by,  $\vec{\varepsilon} = \vec{\varepsilon}_0 e^{-i\omega_L t} + c.c.$ , with  $\vec{\varepsilon}$  being the electric field amplitude of the applied laser.

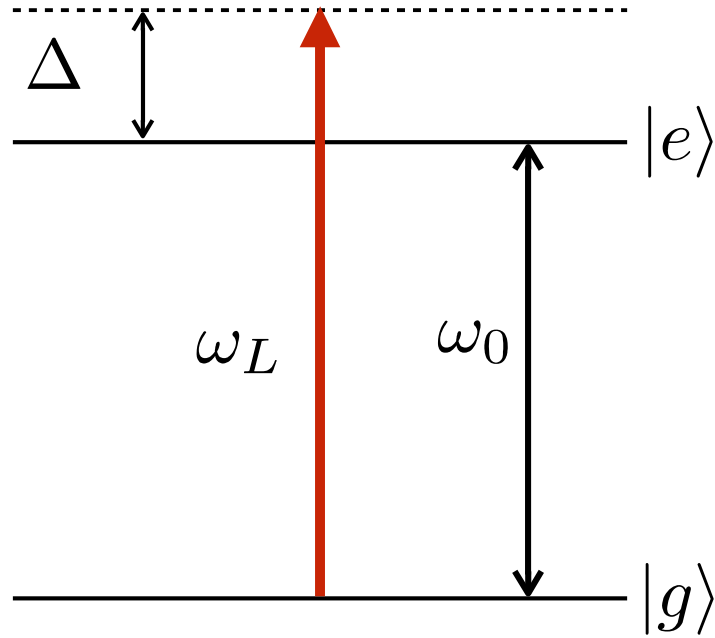


Figure 3.3: Two level system in presence of an external field.

The interaction Hamiltonian can be written as,  $H_I = -\vec{\varepsilon} \cdot \vec{\hat{\mu}} = -\varepsilon(\mu_{ge}|g\rangle\langle e| + \mu_{eg}|e\rangle\langle g|)$ . Under suitable unitary transformation the Hamiltonian,  $H_A + H_I$  can be made time independent. Using rotating wave approximation (RWA), the time independent Hamiltonian can be expressed as,  $H = -\frac{\hbar}{2}[2\Delta|e\rangle\langle e| + \Omega^*|g\rangle\langle e| + \Omega|e\rangle\langle g|]$ . Here  $\Omega$  is the Rabi frequency which is defined as,  $\Omega = \frac{2\varepsilon_0\mu_{eg}}{\hbar}$ , where  $\mu_{eg}$  is the dipole matrix element which is defined as  $\langle e|\hat{\mu}|g\rangle$ . The energy eigenvalues are given by,  $E_{\pm} = -\frac{\hbar}{2}(\Delta \pm \sqrt{\Delta^2 + |\Omega|^2})$ . Corresponding energy eigenstates are,

$$\begin{aligned} |+\rangle &= \sin\frac{\theta}{2}e^{-i\phi}|g\rangle + \cos\frac{\theta}{2}|e\rangle \\ |-\rangle &= \cos\frac{\theta}{2}e^{-i\phi}|g\rangle - \sin\frac{\theta}{2}|e\rangle \end{aligned}$$

Here we have substituted  $\Delta = \Omega' \cos \theta$  and  $|\Omega| = \Omega' \sin \theta$ . The effective Rabi frequency is defined as,  $\Omega' = \sqrt{\Delta^2 + |\Omega|^2}$ . Here,  $\tan \theta = \frac{|\Omega|}{\Delta}$  and  $\phi$  is phase due to the laser field. The phase  $\phi$  can be set to zero without losing any generality.

$$|+\rangle = \sin \frac{\theta}{2} |g\rangle + \cos \frac{\theta}{2} |e\rangle \quad (3.3)$$

$$|-\rangle = \cos \frac{\theta}{2} |g\rangle - \sin \frac{\theta}{2} |e\rangle \quad (3.4)$$

Here  $|+\rangle$  and  $|-\rangle$  are known as dressed states.

### 3.2.2 For the case, $\Delta \gg |\Omega|$

For  $\Delta \gg |\Omega|$  the energy eigenvalues can be approximated as  $E_+ = -\hbar(\Delta + \frac{|\Omega|^2}{4\Delta})$  and  $E_- = \hbar\frac{|\Omega|^2}{4\Delta}$ . The bare ground state and excited state energies are  $E_g = 0$  and  $E_e = -\hbar\Delta$  respectively. The ground state contain atomic ground state energy and a single photon energy. The excited state energy contains only the atomic excited state, since the single photon is absent. Therefore, the energy content of the ground state is higher than that of excited state. The energy shift of the individual levels in presence of the laser field are depicted in fig.(3.4) and mathematically are given by,

$$\Delta E_g = E_- - E_g = \frac{\hbar|\Omega|^2}{4\Delta} \quad (3.5)$$

$$\Delta E_e = E_+ - E_e = -\frac{\hbar|\Omega|^2}{4\Delta} \quad (3.6)$$

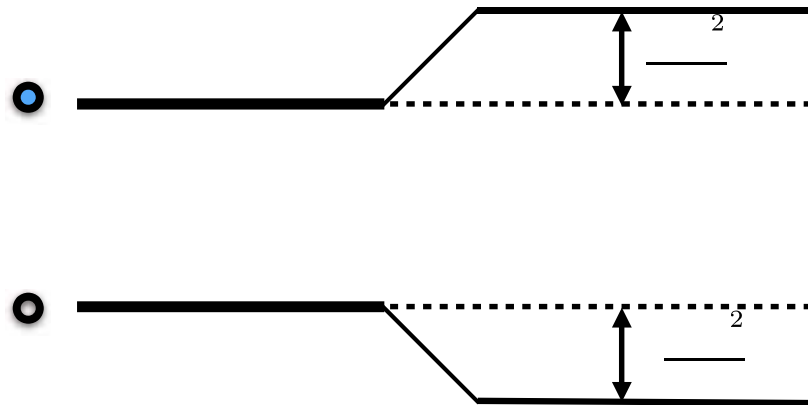


Figure 3.4: Light shift of atomic levels. The ground state contains atomic ground state with a single photon state and the excited state is the atomic excited state in the absence of the single photon state. The left side of the figure represents the bare states and the right side of the figure represents the light shifted states ( $|\pm\rangle$ ).



Since the energy shift is proportional to the intensity of the light and is called as light shift. The energy eigenstates for  $|\Omega| \ll \Delta$  are simplified as,

$$|+\rangle \approx |e\rangle + \frac{|\Omega|}{2\Delta}|g\rangle \quad (3.7)$$

$$|-\rangle \approx |g\rangle - \frac{|\Omega|}{2\Delta}|e\rangle \quad (3.8)$$

### 3.2.3 For the case, $\Delta = 0$

The energy eigenvalues can be given by,  $E_+ = -\frac{\hbar|\Omega|}{2}$  and  $E_- = \frac{\hbar|\Omega|}{2}$ . Then the energy shifts due to dressing are given by,

$$\Delta E_g = E_- - E_g = \frac{\hbar|\Omega|}{2} \quad (3.9)$$

$$\Delta E_e = E_+ - E_e = -\frac{\hbar|\Omega|}{2} \quad (3.10)$$

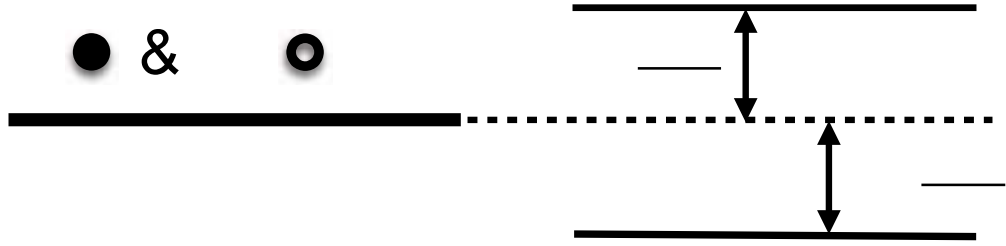


Figure 3.5: Dressing of atomic levels when applied field is close to the atomic resonance.

The dressed energy levels are depicted in fig.(3.5).

The energy eigen states are given by,

$$|+\rangle = \frac{1}{\sqrt{2}}(|g\rangle + |e\rangle) \quad (3.11)$$

$$|-\rangle = \frac{1}{\sqrt{2}}(|g\rangle - |e\rangle) \quad (3.12)$$

### 3.2.4 Optical Bloch equation for 2-level system

The master equation for the system can be written as,  $i\hbar\dot{\rho} = [\hat{H}, \rho] + i\hbar\hat{L}_D(\rho)$ . Where  $\hat{H}$  is the Hamiltonian derived in the previous section and  $\hat{L}_D(\rho)$  is the Linblad operator which takes

care of all the decay and decoherence time scales of the system.

$$\hat{L}_D(\rho) = \begin{pmatrix} \Gamma_{eg}\rho_{ee} & -\frac{\Gamma_{eg}}{2}\rho_{ge} \\ -\frac{\Gamma_{eg}}{2}\rho_{eg} & \Gamma_{eg}\rho_{ee} \end{pmatrix}.$$

In this system we have only one decay channel  $\Gamma_{eg}$  (decay:  $|e\rangle \rightarrow |g\rangle$ ). Optical Bloch equations for the system are given by,

$$\dot{\rho}_{ee} = \frac{i}{2}(\Omega\rho_{ge} - \Omega^*\rho_{eg}) - \Gamma_{eg}\rho_{ee} \quad (3.13)$$

$$\dot{\rho}_{eg} = \frac{i}{2}[\Omega(1 - 2\rho_{ee}) + 2\Delta\rho_{eg}] - \frac{\Gamma_{eg}}{2}\rho_{eg} \quad (3.14)$$

The steady state solution of the coherence term of the density matrix is given by,

$$\rho_{eg} = -\frac{(\Delta - i\frac{\Gamma_{eg}}{2})\Omega}{2\Delta^2 + \Omega^2 + \frac{\Gamma_{eg}^2}{2}} \quad (3.15)$$

$$\rho_{ee} = \frac{\Omega^2}{4\Delta^2 + 2\Omega^2 + \Gamma_{eg}^2} \quad (3.16)$$

The susceptibility of the system is given by,  $\chi = \frac{2n_0|\mu_{eg}|^2}{\epsilon_0\hbar\Omega}\rho_{eg}$  [14]. Here  $n_0$  is the density of non-interacting identical atoms. The real part of the susceptibility gives the dispersion and the absorption of laser field due to the medium can be found from the imaginary part of the susceptibility as,  $I = I_0 e^{-kl\text{Im}(\chi)}$ .  $I_0$  and  $I$  are the intensities of the incident and transmitted beam intensities respectively. Here  $k = \frac{2\pi}{\lambda}$ ,  $\lambda$  is the wave-length of the laser beam and  $l$  is the length of the sample.

### 3.2.5 Optical Bloch equation for 3-level system

Consider a 3-level atom in presence of two laser fields as shown in fig (3.6). The transition  $|g\rangle \rightarrow |e\rangle$  and  $|e\rangle \rightarrow |r\rangle$  are dipole allowed whereas the direct transition  $|g\rangle \rightarrow |r\rangle$  is not a dipole allowed transition. The atomic Hamiltonian of the system,  $H_A = \hbar\omega_{eg}|e\rangle\langle e| + \hbar(\omega_{eg} + \omega_{er})|r\rangle\langle r|$ . The dipole interaction Hamiltonian  $H_I = -E_p(\mu_{ge}|g\rangle\langle e| + \mu_{eg}|e\rangle\langle g|) - E_c(\mu_{er}|e\rangle\langle r| + \mu_{re}|r\rangle\langle e|)$ . The probe and coupling electric fields respectively are given by,

$$\vec{\mathcal{E}}_p = \vec{\mathcal{E}}_{p0}e^{-i\omega_p t} + c.c.$$

$$\vec{\mathcal{E}}_c = \vec{\mathcal{E}}_{c0}e^{-i\omega_c t} + c.c.$$

Here,  $\vec{\mathcal{E}}_{p0}$  and  $\vec{\mathcal{E}}_{c0}$  are the electric field amplitudes of probe and coupling laser field respectively.  $\omega_p$  and  $\omega_c$  are the frequencies of the probe and the coupling laser field respectively. The total Hamiltonian is  $H = H_A + H_I$ . The atomic level scheme is depicted in the fig. (3.6). The probe

and the coupling detuning of the laser fields from the atomic transitions are respectively given by,  $\Delta_p = \omega_p - \omega_{eg}$  and  $\Delta_c = \omega_c - \omega_{er}$ .

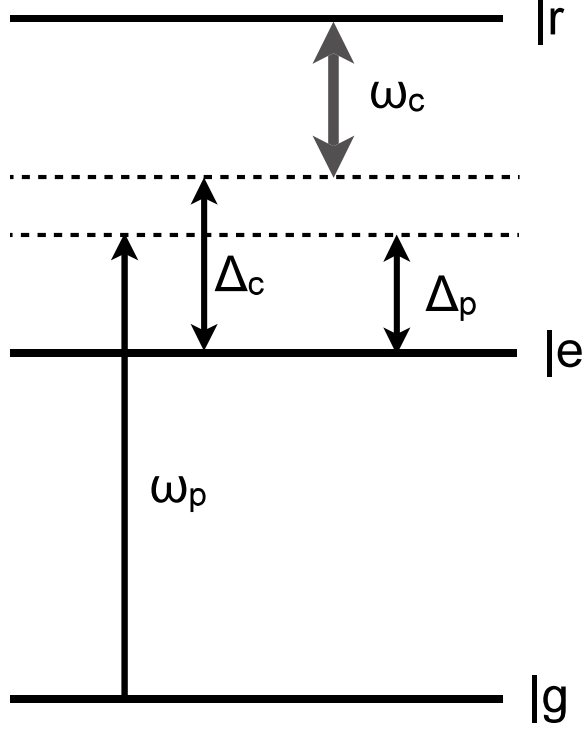


Figure 3.6: Energy level diagram of 3-level atom in presence of two laser fields.

Using the rotating wave approximation (RWA), the time independent Hamiltonian in a suitable rotating frame takes the form,  $\mathbf{H} = -\hbar[\Delta_p|e\rangle\langle e| + \delta|r\rangle\langle r|] - \frac{\hbar}{2}[\Omega_p|e\rangle\langle g| + \Omega_c|r\rangle\langle e| + h.c.]$ . Here the Rabi frequencies are given by,  $\Omega_p = \frac{2\mu_{eg}\epsilon_{p0}}{\hbar}$  and  $\Omega_c = \frac{2\mu_{re}\epsilon_{c0}}{\hbar}$ . The two-photon detuning is defined as,  $\delta = \Delta_p + \Delta_c$ . In this system, the transition  $|g\rangle \rightarrow |r\rangle$  is carried out by two dipole allowed single photon transitions. The detunings of respective transitions ( $\Delta_p$  and  $\Delta_c$ ) have to be chosen such that the two-photon detuning  $\delta = 0$  which is the condition of two-photon resonance. The master equation for the system can be written as,  $\dot{\rho} = \frac{i}{\hbar}[\rho, \mathbf{H}] + L_D(\rho)$ . The Linblad operator  $L_D(\rho)$  accounts for the decoherences in the system and takes the form as,

$$L_D(\rho) = \begin{pmatrix} (\Gamma_{eg}\rho_{ee} + \Gamma_{rg}\rho_{rr}) & -\frac{\Gamma_{eg}}{2}\rho_{ge} & -\frac{1}{2}(\Gamma_{re} + \Gamma_{rg})\rho_{gr} \\ -\frac{\Gamma_{eg}}{2}\rho_{eg} & (\Gamma_{re}\rho_{rr} - \Gamma_{eg}\rho_{ee}) & -\frac{1}{2}(\Gamma_{eg} + \Gamma_{re} + \Gamma_{rg})\rho_{er} \\ -\frac{1}{2}(\Gamma_{re} + \Gamma_{rg})\rho_{rg} & -\frac{1}{2}(\Gamma_{eg} + \Gamma_{re} + \Gamma_{rg})\rho_{re} & -(\Gamma_{re} + \Gamma_{rg})\rho_{rr} \end{pmatrix}.$$

$\Gamma_{eg}$  is the population decay from the state  $|e\rangle$  to the state  $|g\rangle$ . For rubidium, the typical decay rate ( $5P_{3/2} \rightarrow 5S_{1/2}$ ) is 6 MHz.  $\Gamma_{re}$  is the decay rate from the state  $|r\rangle$  to the state  $|e\rangle$ .  $\Gamma_{rg}$  has one contribution from relative laser noise between probe and coupling laser fields and another contribution appeared due to transit time. In the steady state, the OBE of the system are found

to be,

$$\frac{i}{2}(\Omega_p \rho_{eg} - \Omega_p^* \rho_{ge}) + \Gamma_{eg} \rho_{ee} + \Gamma_{rg} \rho_{rr} = 0 \quad (3.17)$$

$$\frac{i}{2}[\Omega_p(2\rho_{ee} + \rho_{rr}) - \Omega_p - (\Omega_c^* \rho_{gr} + 2\Delta_p \rho_{ge})] - \frac{\Gamma_{eg}}{2} \rho_{ge} = 0 \quad (3.18)$$

$$\frac{i}{2}[\Omega_p \rho_{er} - \Omega_c \rho_{ge} - 2\delta \rho_{gr}] - \frac{1}{2}(\Gamma_{re} + \Gamma_{rg}) \rho_{gr} = 0 \quad (3.19)$$

$$\frac{i}{2}(\Omega_c^* \rho_{er} - \Omega_c \rho_{re}) - (\Gamma_{re} + \Gamma_{rg}) \rho_{rr} = 0 \quad (3.20)$$

$$\frac{i}{2}[\Omega_p^* \rho_{gr} + \Omega_c(\rho_{rr} - \rho_{ee}) - 2\Delta_c \rho_{er}] - \frac{1}{2}(\Gamma_{eg} + \Gamma_{re} + \Gamma_{rg}) \rho_{er} = 0 \quad (3.21)$$

This system of equations can numerically be solved for the density matrix element  $\rho_{eg}$  which gives the information about the transmission and dispersion properties of the probe field due to the medium.

For low probe limit, the populations  $\rho_{ee} = 0 = \rho_{rr}$  and since the excited and Rydberg level are barely populated, the coherence associated with them will vanish i.e,  $\rho_{er} = 0$ . Assuming the Rabi frequencies to be real, the equations (3.18) and (3.19) will have the form,

$$\Omega_p + \Omega_c \rho_{gr} + (2\Delta_p + \frac{\Gamma_{eg}}{2}) \rho_{ge} = 0 \quad (3.22)$$

$$\Omega_c \rho_{ge} + [2\delta - \frac{(\Gamma_{re} + \Gamma_{rg})}{2}] \rho_{gr} = 0 \quad (3.23)$$

The solution of the above pair of equations are given by,

$$\rho_{eg} = \frac{\Omega_p(2\delta + i\Gamma_2)}{\Omega_c^2 - 4\Delta_2\Delta_p + \Gamma_2\Gamma_{eg} + 2i(\Delta_2\Gamma_{eg} + \Delta_p\Gamma_2)} \quad (3.24)$$

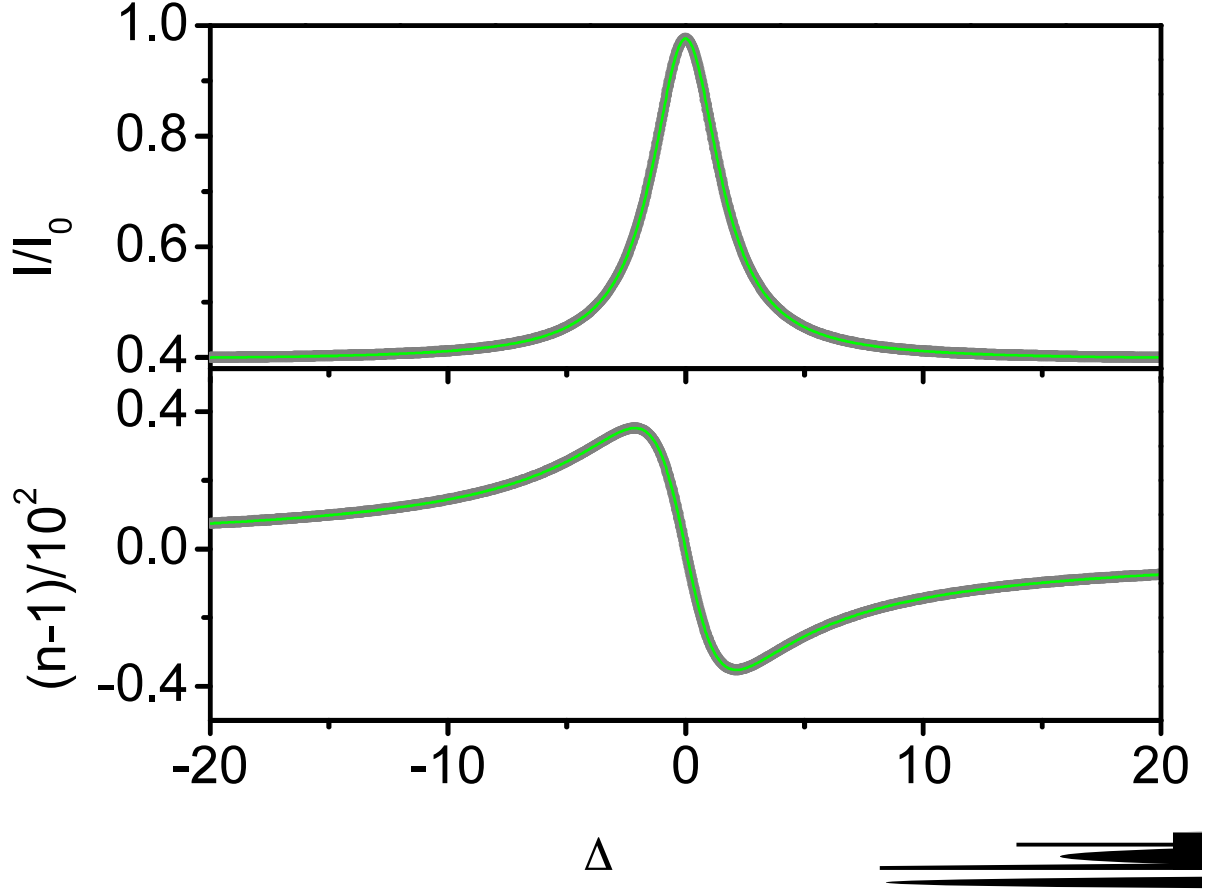


Figure 3.7: EIT transmission (a) and refractive index (b) for cold atom system. Typical density and the optical path length of the cold atom are taken as  $10^{10}$  c.c. and 1 mm respectively. The curves are generated for probe and coupling Rabi frequencies 100 kHz and 5 MHz respectively. The dephasing rates for the calculation are taken as  $\Gamma_{re} = 10$  kHz,  $\Gamma_{rg} = 100$  kHz and  $\Gamma_{eg} = 6$  MHz. The probe detuning  $\Delta_p$  is taken to be zero and coupling laser is scanned over the two photon resonance. The points ( $\bullet$ ) are generated from the numerical solution of 3-level OBE in EIT regime and the solid lines ( $\text{---}$ ) are generated from the exact solution of OBE using EIT approximation.

The susceptibility of the probe field is given by,  $\chi = \frac{2n_0|\mu_{eg}|^2}{\epsilon_0\hbar\Omega_p}\rho_{eg}$ . The refractive index of the probe due to the medium is given by,  $n = 1 + \frac{Re(\chi)}{2}$ . The transmitted intensity of the probe field from the medium is given by,  $I = I_0 e^{-k_p l Im(\chi)}$ , where  $I_0$  is the incident intensity of the probe laser beam,  $l$  is the length of the sample,  $k_p$  is the probe wave vector and  $l$  is the optical length of the atomic sample. This gives the transmission information of the probe field in presence of the coupling laser. From Fig.(3.7), it can be observed that at the vicinity of the two-photon resonance, the probe light is getting transmitted instead of getting absorbed. This is called electromagnetically induced transparency (EIT) [16–19].

### 3.2.6 Large probe detuning in two-photon resonance process

Let us consider that the probe laser is stabilised well outside the line-width of the single-photon resonance. Then the two-photon resonance can be satisfied by varying the coupling laser frequency. An interesting phenomenon is observed in the absorption and the dispersion spectral shape in this regime. If the probe Rabi frequency increases, then the dispersion spectrum takes the shape of absorption and also absorption spectrum takes the shape of dispersion, as shown in fig.(3.8). It is also observed that the spectrum with higher Rabi frequency experience a frequency shift. This is because the contribution from the light-shift (as discussed in section 3.2.2) gets significant with the increment of the probe Rabi frequency.

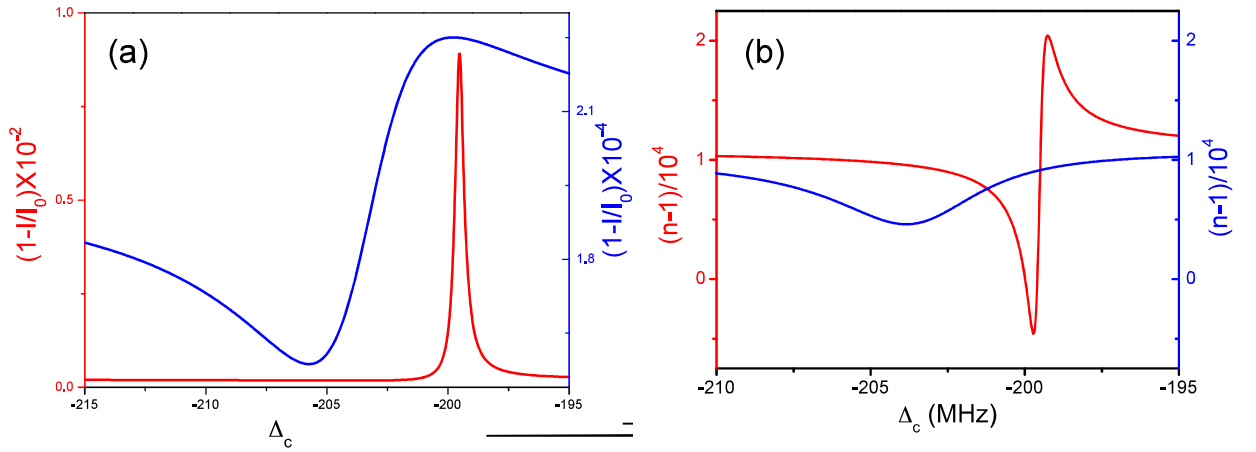


Figure 3.8: The curve in (a) and (b) are the transmission and refractive index signal respectively. The probe detuning is taken as  $\Delta_p = 200$  MHz. The dephasing rates for the calculation are taken as  $\Gamma_{re} = 10$  kHz,  $\Gamma_{rg} = 100$  kHz and  $\Gamma_{eg} = 6$  MHz. The coupling Rabi frequency is taken as  $\Omega_c = 20$  MHz. The blue curves are the signals corresponding to the probe Rabi frequency  $\Omega_p = 6$  MHz and the red curves are the signals corresponding to the probe Rabi frequency  $\Omega_p = 60$  MHz. Typical density and the size of the cold atom are taken respectively as  $10^{10}$  c.c. and 1 mm.

### 3.2.7 Adiabatic elimination of intermediate state

For,  $\Delta_p \gg \Omega_p$  and  $\Gamma_{eg}$ , the three level system can be approximated to an effective two-level system. For further simplicity let us define the average detuning as,  $\Delta = \frac{1}{2}(\Delta_p - \Delta_c)$  and two-photon detuning as,  $\delta = \Delta_p + \Delta_c$ . If we use the translation to the Hamiltonian  $H \Rightarrow -H - \frac{\hbar}{2}I\delta$ , the Hamiltonian will be,

$$\bar{H} = \frac{\hbar}{2} \begin{pmatrix} -\delta & \Omega_p^* & 0 \\ \Omega_p & 2\Delta & \Omega_c^* \\ 0 & \Omega_c & \delta \end{pmatrix}.$$

Consider any arbitrary time dependent state in the same Hilbert space which can be expressed as,  $|\psi\rangle = C_g(t)|g\rangle + C_e(t)|e\rangle + C_r(t)|r\rangle$ . Then the time-dependent Schrödinger equation can be written as,  $i\hbar\frac{\partial}{\partial t}|\psi(t)\rangle = \bar{H}|\psi(t)\rangle$ . Using the fact of linear independence of orthonormal set of basis, the relations of complex coefficients can be expressed as,

$$2i\frac{\partial}{\partial t}C_g(t) = -\delta C_g(t) + \Omega_p^* C_e(t) \quad (3.25)$$

$$2i\frac{\partial}{\partial t}C_e(t) = \Omega_p C_g(t) + 2\Delta C_e(t) + \Omega_c^* C_r(t) \quad (3.26)$$

$$2i\frac{\partial}{\partial t}C_r(t) = \Omega_c C_e(t) + \delta C_r(t) \quad (3.27)$$

If  $\Delta_p \gg \Omega_p$  and  $\Gamma_{eg}$ , then the population corresponding to the intermediate state ( $|e\rangle$ ) will not change with time. Hence, the slowly varying approximation or adiabatic approximation of the population ( $\frac{\partial}{\partial t}C_e(t) = 0$ ) can be used [20]. Therefore from equation (3.26),  $C_e(t) = -\frac{\Omega_p}{2\Delta}C_g(t) - \frac{\Omega_c^*}{2\Delta}C_r(t)$ . On substitution in equation (3.25) and (3.27), an effective two level Hamiltonian can be constructed which is given by,

$$H_{eff} = -\frac{\hbar}{2} \begin{pmatrix} \delta + \frac{|\Omega_p|^2}{2\Delta} & \frac{\Omega_p^* \Omega_c}{2\Delta} \\ \frac{\Omega_p \Omega_c}{2\Delta} & -\delta + \frac{|\Omega_c|^2}{2\Delta} \end{pmatrix}.$$

Hamiltonian of a two-level atom in presence of a laser field is given by,  $H = -\frac{\hbar}{2}[\Omega^*|g\rangle\langle r| + \Omega|r\rangle\langle g| + 2\Delta|r\rangle\langle r|]$ . Comparing the effective Hamiltonian matrix with the Hamiltonian of a 2-level atom, we can define an effective Rabi frequency as,  $\Omega_{eff} = \frac{\Omega_p \Omega_c}{2\Delta}$  and detuning as,  $\Delta_{eff} = (-\delta + \frac{|\Omega_c|^2}{2\Delta}) - (\delta + \frac{|\Omega_p|^2}{2\Delta}) = -2\delta + \frac{(\Omega_c|^2 - \Omega_p|^2)}{2\Delta}$ .

### 3.2.8 Optical Bloch equations for effective 2-level system

The master equation of the effective 2-level system can be written as,  $\dot{\rho} = \frac{i}{\hbar}[\rho, H_{eff}] + L_{D,eff}(\rho)$ . The quantity  $L_{D,eff}(\rho)$  is called the Linblad operator, which can be expressed as,  $L_{D,eff}(\rho) = \Gamma_{rg}[|g\rangle\langle g|\rho_{rr} - \frac{1}{2}(|r\rangle\langle r|\rho + \rho|r\rangle\langle r|)]$ . Here,  $\Gamma_{rg}$  is the decay rate due to transit time and the relative laser noise. The optical Bloch equations (OBE) for the effective 2-level system [20] can be written as,

$$\dot{\rho}_{gg} = -i(\Omega_{eff}\rho_{gr} - \Omega_{eff}^*\rho_{rg}) + \Gamma_{rg}\rho_{rr} \quad (3.28)$$

$$\dot{\rho}_{rg} = -i(\Delta_{eff}\rho_{rg} + \Omega_{eff}(2\rho_{rr} - 1)) - \frac{\Gamma_{rg}}{2}\rho_{rg} \quad (3.29)$$

In steady state the equation (3.28) and (3.29) give the set of equations,

$$Im(\rho_{rg}) = \frac{\Gamma_{rg}}{2\Omega_{eff}} \rho_{rr} \quad (3.30)$$

$$Re(\rho_{rg}) = \frac{2\Delta_{eff}}{\Omega_{eff}} \rho_{rr} \quad (3.31)$$

$$\rho_{rr} = \frac{4\Omega_{eff}^2}{2\Delta_{eff}^2 + 8\Omega_{eff}^2 + \Gamma_{rg}^2} \quad (3.32)$$

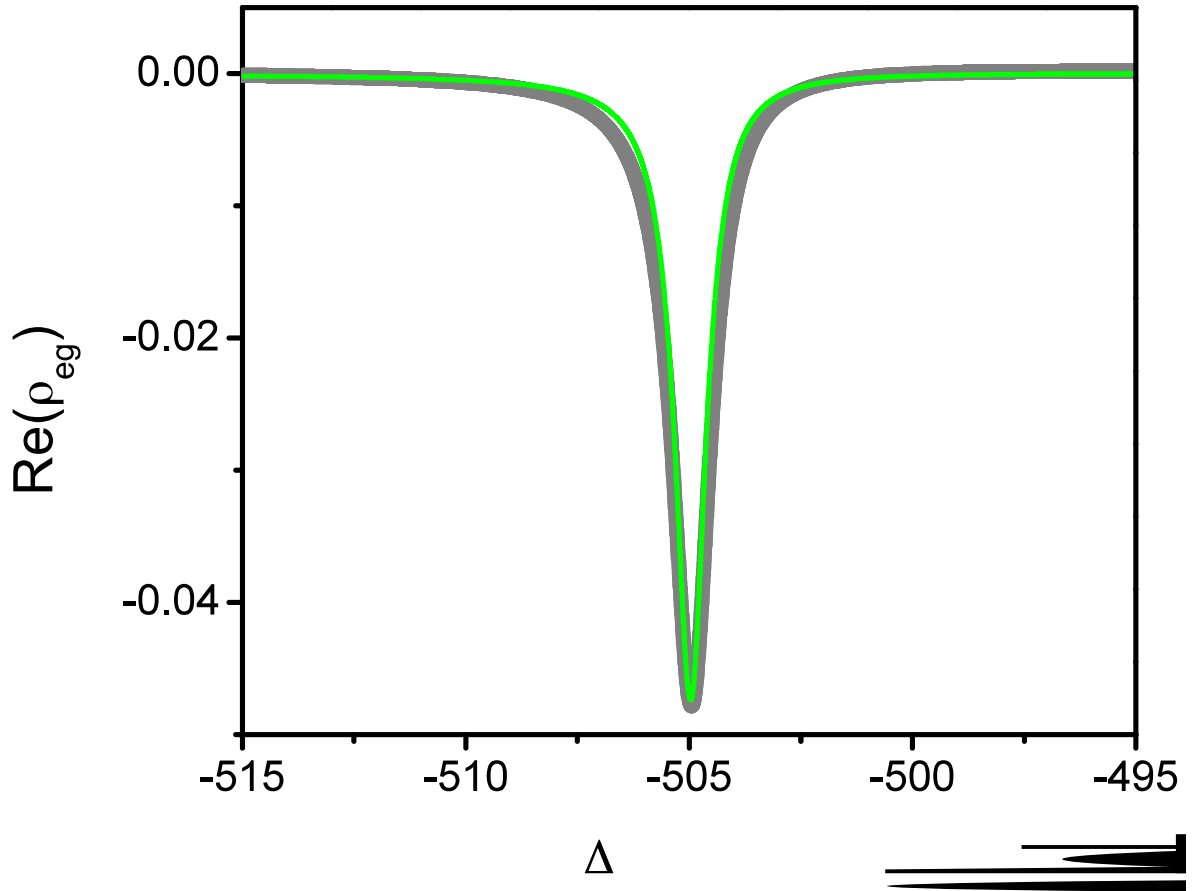


Figure 3.9: The grey data points (●) are generated from the numerical solution of OBE for large probe detuning and the green curve (—) is the solution of the effective 2-level OBE. The probe detuning is taken as  $\Delta_p = 500$  MHz. The dephasing rates for the calculation are taken as  $\Gamma_{re} = 10$  kHz,  $\Gamma_{rg} = 100$  kHz and  $\Gamma_{eg} = 6$  MHz. The coupling and the probe Rabi frequencies are taken as  $\Omega_c = 6$  MHz and  $\Omega_p = 80$  MHz respectively.

By comparing the solutions (3.30) and (3.31) with equations of exact 3-level system at steady state (specifically 3.17 and 3.18) we can get,

$$Re(\rho_{eg}) = -\frac{\Omega_p}{2\Delta_p} + \frac{\Omega_p}{2\Delta_p} \rho_{rr} - \frac{\Omega_c}{2\Delta_p} Re(\rho_{gr}) + \frac{\Gamma_{eg}\Gamma_{rg}}{2\Delta_p\Omega_p} \rho_{rr} \quad (3.33)$$



The first term of the equation (3.33) is the contribution from two level system ( $|g\rangle \rightarrow |e\rangle$ ). Similar to the other terms, the third term is also proportional to the population  $\rho_{rr}$  (from equation 3.31). Therefore, the dispersion of the probe field is proportional to the population of the most excited state,  $|r\rangle$ . In other words, if a three-level system can be reduced to 2-level system as discussed then the population,  $\rho_{rr}$  can directly be calculated from dispersion whereas the dispersion of the probe field is a experimentally measurable quantity.

### 3.3 Hyperfine pumping spectroscopy (HPS)

The atomic spectroscopies serve as a reference for laser frequency used in the experiment. The velocity of the atoms is governed by the Maxwell-Boltzmann velocity distribution corresponding to the temperature of the ensemble of atoms. The random velocity of atoms broadened the atomic transition line-width which is known as Doppler broadening. The hyperfine pumping spectroscopy is based on the velocity selective saturation of a Doppler-broadened atomic transition [21]. The experimental setup for HPS is depicted in fig. (3.10).

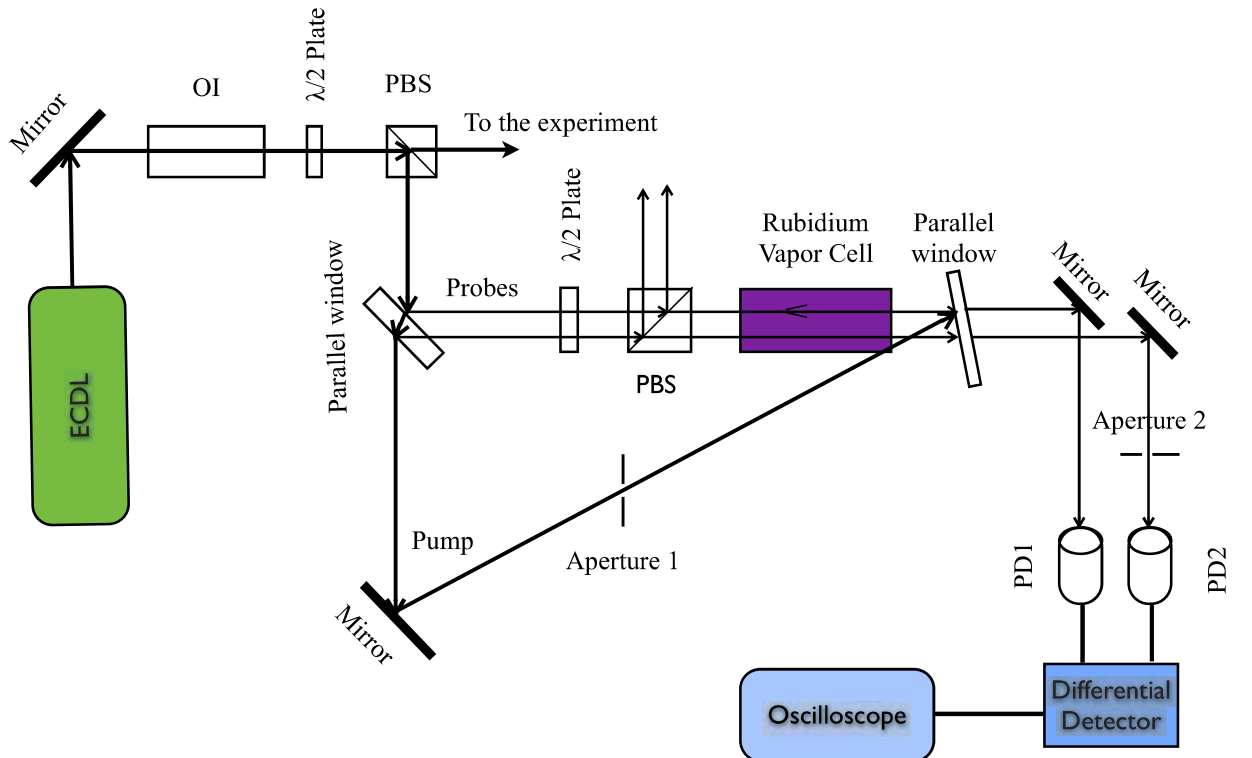


Figure 3.10: Experimental setup for hyperfine pumping spectroscopy.

An external cavity diode laser operating at the wavelength of 780 nm is used to observe ru-

bidium D2 transition lines (fig.3.1(b) & 3.2(b)). The optical isolator (OI) is used to restrict the optical feedback from other optical elements used in the experiment. The  $\frac{\lambda}{2}$ -plate and the polarising beam splitter (PBS) is used to control the power which has to be used in SAS. A parallel window is used to derive a pair of probe beams by the 4% reflection of the incident laser beam from the front and the rare face of the window. The transmitted light from the parallel window is used as the pump beam for saturation absorption. These two probes pass through a rubidium vapor cell and detected by the detectors PD1 and PD2 respectively. One of the probes experiences the counter-propagating pump beam while passing through the medium. A differential detection is performed using the electronic signal of PD1 and PD2 and the output is observed using an oscilloscope. The details of the photodiode operation and design is described in Appendix. A.

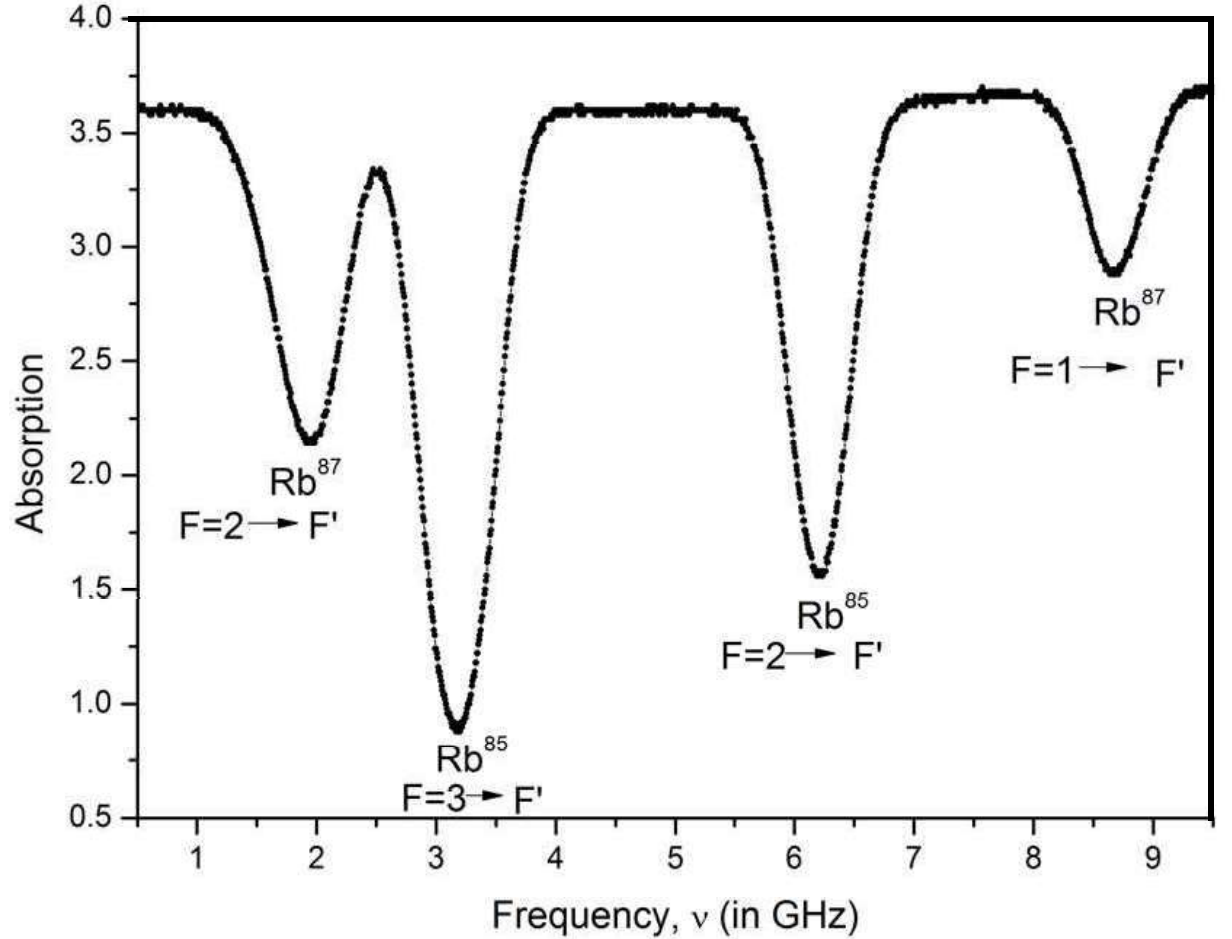


Figure 3.11: Doppler broadened absorption lines of D2 rubidium transition.

If the aperture 1 and 2 are closed then it is just a doppler spectroscopy. The spectroscopic signal is depicted in the fig. (3.11). The respective doppler broadened transition manifold is

mentioned in the figure. But the individual transition lines for a particular manifold cannot be observed in Doppler spectroscopy.

If aperture 1 is open but 2 is closed, the individual lines of each manifold is observed due to the selective saturation by the pump laser beam as shown in fig. (3.12). In order to have doppler free hyperfine pumping spectroscopy signal the aperture 1 and 2 both has to be kept open. The probe detected in PD1 is a signal depicted in fig. (3.11) which gets subtracted from the signal detected in PD2 fig. (3.12) gives doppler free spectroscopy signal. The doppler free HPS signal for individual transition manifolds  $^{87}\text{Rb}$ :  $F = 2 \rightarrow F'$ ,  $^{85}\text{Rb}$ :  $F = 3 \rightarrow F'$ ,  $^{85}\text{Rb}$ :  $F = 2 \rightarrow F'$  and  $^{87}\text{Rb}$ :  $F = 1 \rightarrow F'$  are respectively depicted in fig. 3.13(A, B, C & D).

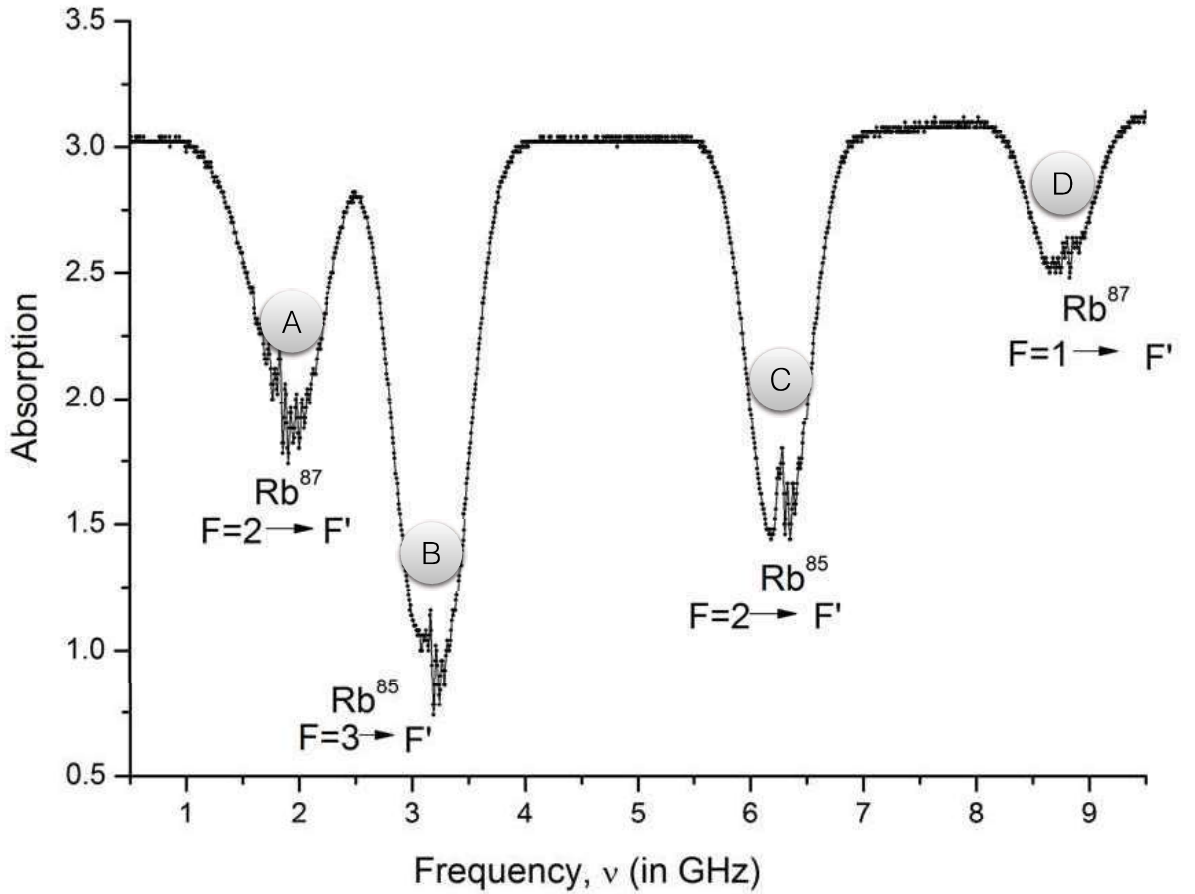


Figure 3.12: Hyperfine pumping spectroscopy signal.

As we can see from fig. (3.1.b & 3.2.b) that each manifold should have three dipole allowed transitions, but each panel of fig. (3.13) has six transition lines. Three of them are atomic transitions and rest of them are the cross-over transition lines. If the laser frequency is exactly

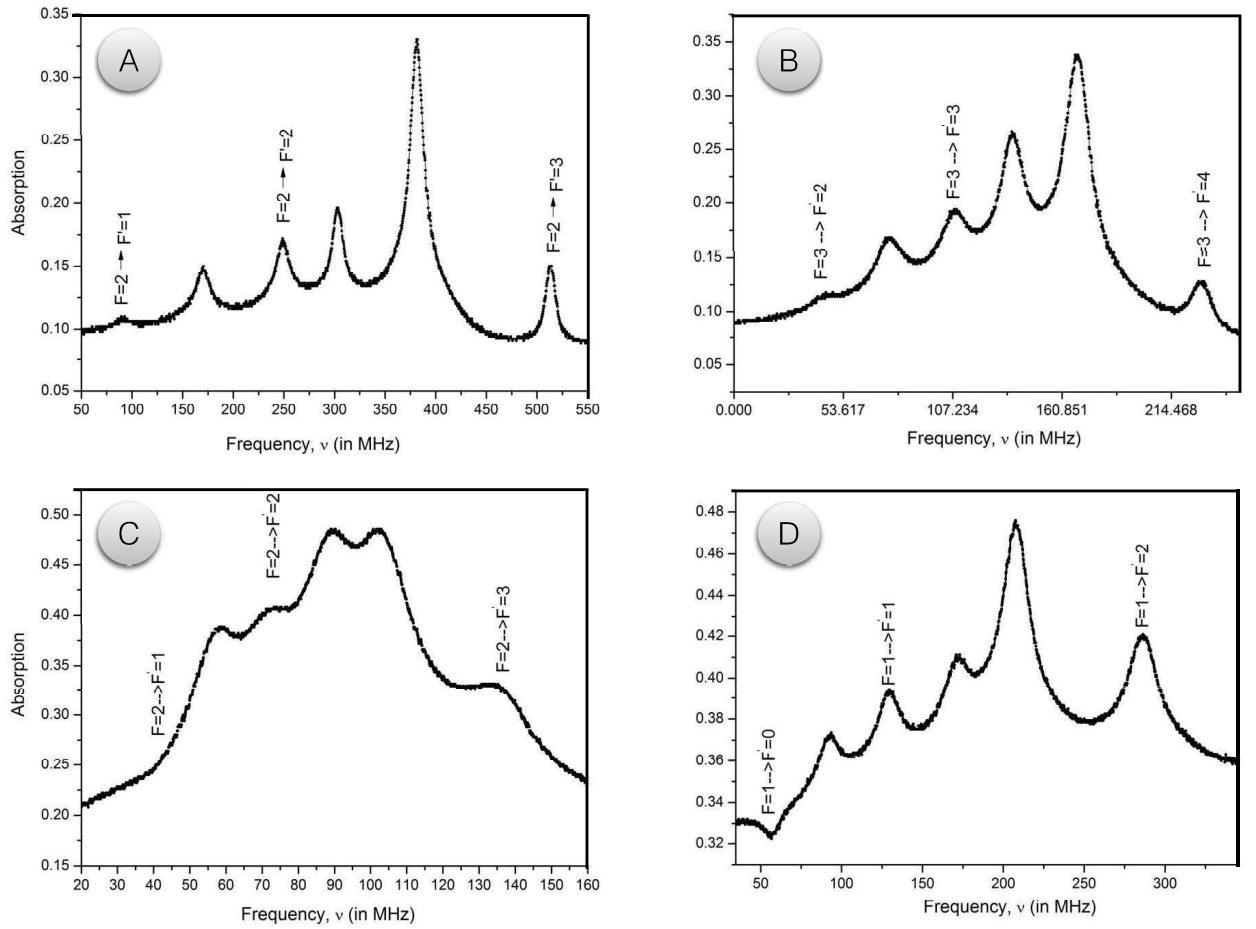


Figure 3.13: Spectroscopy signal for individual transition manifold.

at the middle of two dipole allowed hyperfine transition lines then a particular non-zero velocity class of atoms can be resonant to both the transitions and hence the crossover transition line is observed. Since the crossover transition line has the contribution from both the adjacent hyperfine lines, the signal strength is expected to be stronger than both. But it also depends on the frequency difference between the adjacent levels. The crossover signal strength can decrease with the frequency difference of those hyperfine levels because the number of atoms for higher velocity class decreases since they follow Maxwell Boltzmann velocity distribution.

### 3.4 Laser stabilisation using HPS

Hyperfine pumping spectroscopy can be used for laser frequency stabilization. The stabilization of laser on an atomic spectral line reduces the laser frequency noise typically below 100 kHz. A schematic block diagram representation is given in fig. (3.14) for HPS signal of rubidium.

An external cavity diode laser (ECDL) of Toptica DL-100-Pro is used to generate a laser beam for the experiment. The rotation of the grating stage of the laser is controlled by a piezoelectric material. The piezoelectric is driven by a ramp voltage generated from an external scan control module (SC-110). The HPS optical signal is detected by an FPD (fast photo-diode) and the electronic signal of FPD is taken to an external PID-controller module called Digilock module (Digilock-110). The control output of Digilock-110 is connected to SC-110. The example of HPS spectrum given in fig. (3.14) corresponds to the transition  $^{87}\text{Rb}: F = 2 \rightarrow F'$  (same as shown in fig. (3.13a)). In fig. (3.14), the laser is stabilized at the side of a cross-over fringe. According to the locking point frequency, a control signal is generated by the Digilock-

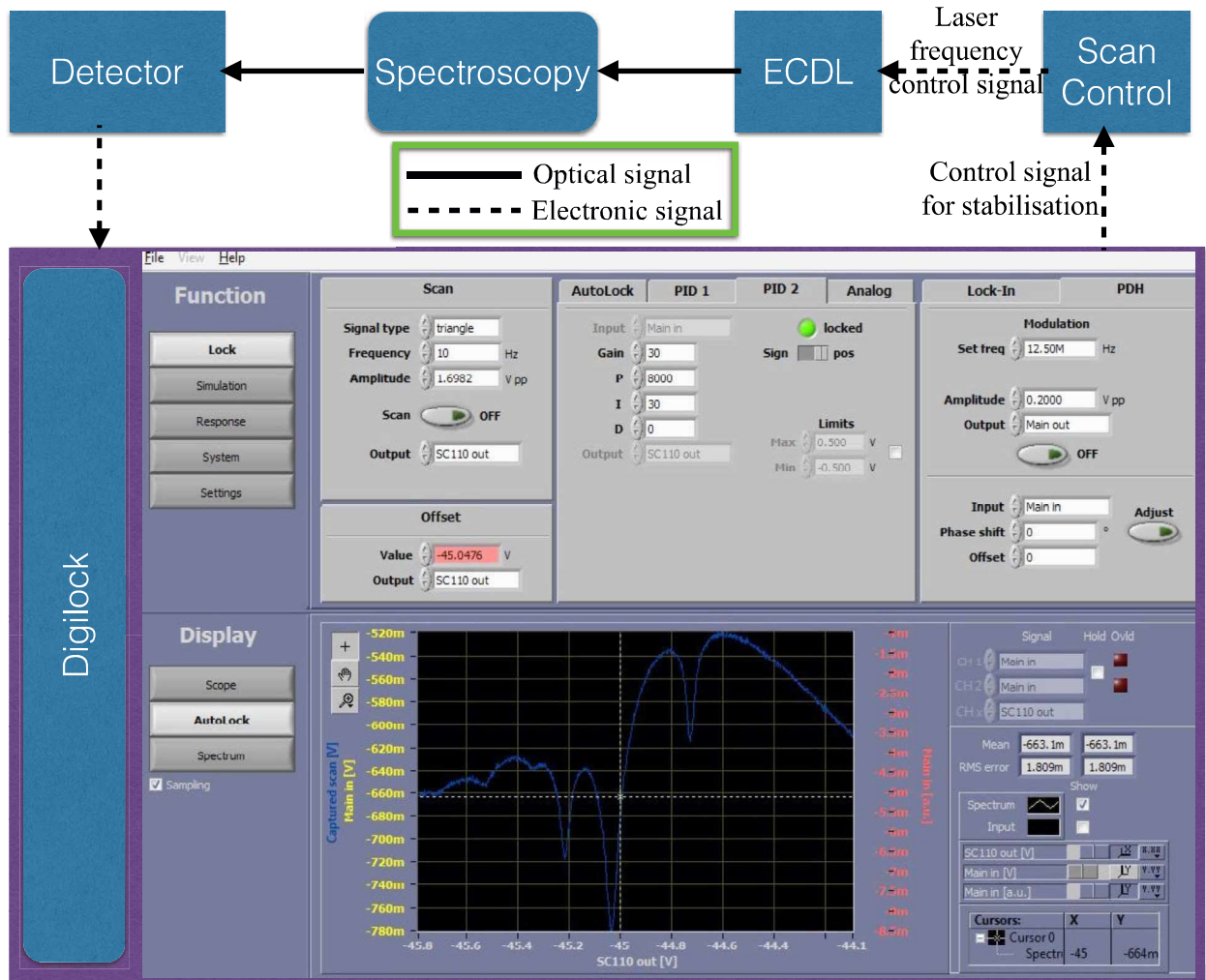


Figure 3.14: Block diagram represents the laser frequency stabilization using HPS.

110. The control voltage decides a dc voltage of the SC-110 which corresponds to a particular frequency of the laser. The frequency (the setpoint frequency) of the laser may change due to

any mechanical or acoustic or electronic disturbances. In that case, Digilock-110 decides the control voltage accordingly in order to bring back the setpoint frequency. The drawback of the working with Digilock-110 is that it can not lock the laser at the top of the fringe. The laser frequency can also be stabilized on an atomic transition line.

# Bibliography

- [1] C. L. Degen, F. Reinhard and P. Cappellaro, Rev. of Mod. Phys., **89**, 035002 (2017).
- [2] S. Ashhab, J. R. Johansson and F. Nori, New J. of Phys., **8**, 103 (2006).
- [3] I. Gerhardt, G. Wrigge, G. Zumofen, J. Hwang, A. Renn, and V. Sandoghdar, Phys. Rev. A, **79**, 011402(R) (2009).
- [4] E. L. Raab, M. Prentiss, Alex Cable, Steven Chu, and D. E. Pritchard, Phys. Rev. Lett., **59**, 2631 (1987).
- [5] S. Chu Rev. of Mod. Phys., **70**, 685 (1998).
- [6] C. N. C.-Tannoudji Rev. of Mod. Phys., **70**, 707 (1998).
- [7] W. D. Phillips Rev. of Mod. Phys., **70**, 721 (1998).
- [8] G. Dmochowski, A. Feizpour, M. Hallaji, C. Zhuang, A. Hayat, and A. M. Steinberg Phys. Rev. Lett., **116**, 173002 (2016).
- [9] H.Sun, Y. Niu, S.Jin and S. Gong J. Phys. B: At. Mol. Opt. Phys., **40**, 3037 (2007).
- [10] A. A. Drozdov, S. A. Kozlov, A. A. Sukhorukov, and Y. S. Kivshar Phys. Rev. A, **86**, 053822 (2012).
- [11] D. Turchinovich, J. M. Hvam, and M. C. Hoffmann Phys. Rev. B, **85**, 201304(R) (2012).
- [12] *Rubidium 85 D line data*, D. A. Steck, Oregon Center for Optics and Department of Physics, University of Oregon, (2013). <http://steck.us/alkalidata>
- [13] *Rubidium 87 D line data*, D. A. Steck, Oregon Center for Optics and Department of Physics, University of Oregon, (2013). <http://steck.us/alkalidata>
- [14] R. W. Boyd. Nonlinear Optics. London: Academic Press, 2015.

- [15] L. Allen and J. H. Eberly. Optical Resonance and Two-Level Atoms. New York: Dover Publications, 2015.
- [16] S. E. Harris, Phys. Rev. Lett., **70**, 552 (1993).
- [17] S. E. Harris, Phys. Rev. Lett., **72**, 52 (1994).
- [18] S. E. Harris, Phys. Rev. Lett., **77**, 5357 (1996).
- [19] S. E. Harris, Phys. Rev. Lett., **85**, 4032 (2000).
- [20] Rui Han, Hui Khoon Ng, Berthold-Georg Englert, J. of Mod. Opt., **60**, 255 (2013).
- [21] D. A. Smith, and I. G. Hughes, Am. J. Phys., **72**, 631 (2004).



# Chapter 4

## Study of Rydberg EIT using OHDT

Electromagnetically induced transparency (EIT) involves three atomic states coupled by a probe laser field and a coupling laser field. In the presence of a coupling laser resonantly drive an atomic medium, for the frequency of the weak probe laser the medium becomes transparent at the single-photon resonance in the process of EIT. In this system, Coupling to a Rydberg state with EIT gives self phase modulation (SPM) [1–18]. The phase of the probe field can also be varied by changing the intensity of the coupling laser. This phenomenon is called cross-phase modulation (XPM). This process is proposed [19] and demonstrated using the EIT medium [20–25]. Therefore, EIT becomes an interesting system to study the optical nonlinearity in atomic vapor.

In this chapter, we will demonstrate a technique based on optical heterodyne to study transmission and dispersion of a probe beam in Rydberg-EIT medium. We will also discuss some technical issues which has to be taken care while using this technique. A suitable model of EIT will be presented in order to explain the experimental data. The optical nonlinearity due to SPM in Rydberg-EIT medium in the non-interacting regime also is presented. While propagating through a Rydberg-EIT medium, a probe laser field goes through a large nonlinear phase shift due to SPM which is induced by the Rydberg blockade interaction.

### 4.1 Rydberg-EIT

Electromagnetically induced transparency with Rydberg atoms gives the provision to probe strong interaction among probe photons. Suppression of EIT transmission due to cooperative Rydberg interaction can lead to strong many body effects [26]. Dark state polaritons is observed in Rydberg-EIT [27] and also dark state resonance is observed with a line-width less than 100

kHz [28]. Rydberg-EIT is studied in thermal vapor cell [18, 29, 30]. The Rydberg-EIT can be

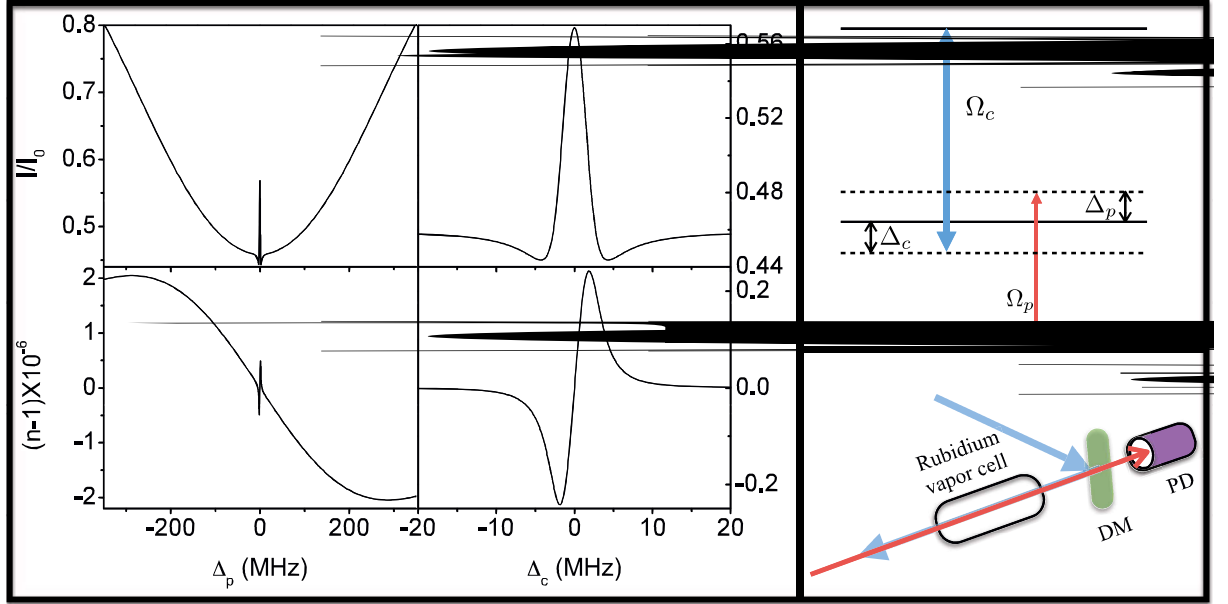


Figure 4.1: The transmission and dispersion due to Rydberg-EIT for probe laser scanning is given in (a) and (b) respectively. (c) and (d) are the same for coupling laser scanning. The atomic level scheme is depicted in (e). The experimental realisation of Rydberg-EIT is depicted in (f). The Rydberg-EIT signal is observed for  $\Omega_c = 2.4$  MHz and  $\Omega_p = 600$  kHz. The optical path length inside the medium is taken to be 5 cm. The dephasing rates are taken as  $\Gamma_{eg} = 6$  MHz,  $\Gamma_{re} = 100$  kHz and  $\Gamma_{rg} = 200$  kHz. At the room temperature the signals are averaged over the Maxwell Boltzmann velocity distribution and the Rydberg-EIT linewidth is found to be 6 MHz.

modelled by a probe and a coupling laser field in a three level system as shown in fig. (4.1). The Hamiltonian of the 3-level atom in presence of a probe and coupling laser field with the respective Rabi frequencies  $\Omega_p$  and  $\Omega_c$ , can be given by  $H = -\hbar[|e\rangle\langle e|(\Delta_p - k_p v) + |r\rangle\langle r|(\Delta_p + \Delta_c - \Delta k v)] - \hbar(|g\rangle\langle e|\Omega_p + |e\rangle\langle r|\Omega_c + h.c.)$ . Here,  $\Delta k = k_p - k_c$ , where the probe and coupling laser wavevectors are defined as  $k_p$  and  $k_c$  respectively. The probe and coupling laser detunings are respectively given by,  $\Delta_p$  and  $\Delta_c$ . The probe and coupling Rabi frequencies are defined as,  $\Omega_p = \frac{\mu_{ge}\varepsilon_p}{\hbar}$  and  $\Omega_c = \frac{\mu_{er}\varepsilon_c}{\hbar}$  respectively. The probe and the coupling electric fields are respectively defined as,  $E_p = \varepsilon_p e^{-i\omega_p t} + c.c.$  and  $E_c = \varepsilon_c e^{-i\omega_c t} + c.c.$ .  $\mu_{ge}$  and  $\mu_{er}$  are the dipole moment for the transition  $|g\rangle \rightarrow |e\rangle$  and  $|e\rangle \rightarrow |r\rangle$  respectively. The optical Bloch equation for the system can be written as,  $\dot{\rho} = -\frac{i}{\hbar}[H, \rho] + L_D(\rho)$ , where  $\rho$  is the density matrix of the system. The Lindblad operator  $L_D(\rho)$  is defined as,  $L_D(\rho) = \sum_{if} \Gamma_{if} (C_{if} \rho C_{if}^\dagger - \frac{1}{2} \{C_{if}^\dagger C_{if}, \rho\})$ , where  $C_{if} = |f\rangle\langle i|$ .  $|i\rangle$  and  $|f\rangle$  signify the initial and the final state of decay respectively. It is

calculated for the system as,

$$L_D(\rho) = \begin{pmatrix} (\Gamma_{eg}\rho_{ee} + \Gamma_{rg}\rho_{rr}) & -\frac{\Gamma_{eg}}{2}\rho_{ge} & -\frac{1}{2}(\Gamma_{re} + \Gamma_{rg})\rho_{gr} \\ -\frac{\Gamma_{eg}}{2}\rho_{eg} & (\Gamma_{re}\rho_{rr} - \Gamma_{eg}\rho_{ee}) & -\frac{1}{2}(\Gamma_{eg} + \Gamma_{re} + \Gamma_{rg})\rho_{er} \\ -\frac{1}{2}(\Gamma_{re} + \Gamma_{rg})\rho_{rg} & -\frac{1}{2}(\Gamma_{eg} + \Gamma_{re} + \Gamma_{rg})\rho_{re} & -(\Gamma_{re} + \Gamma_{rg})\rho_{rr} \end{pmatrix}.$$

Here, the decay rate  $\Gamma_{eg}$  is typically taken to be  $2\pi \times 6$  MHz. The Rydberg state to the intermediate state decay is taken as,  $\Gamma_{re} = 2\pi \times 10$  kHz. The Rydberg state to the ground state decay is mostly dominated by the thermal transit of the atoms through the laser beam. When an excited atom leaves the laser field, it can be regarded as a decay of atoms from excited state. This phenomenon is equivalent to the decay of an excited atom to ground state due to thermal transit and hence, the decay process is called transit time decay. This is the consequence of the transverse component of velocity of atoms with respect to the laser propagation direction. The transit time is defined by,  $\tau_{\text{transit}} = \frac{D_{\text{beam}}}{v_p}$ , where  $D_{\text{beam}}$  is the diameter of the beam and  $v_p$  is the most probable velocity of the atoms determined from the Maxwell Boltzmann velocity distribution corresponding to a particular temperature of the system. If the temperature of the vapor is  $80^\circ\text{C}$ , then the most probable velocity of atoms,  $v_p \approx 260 \text{ ms}^{-1}$ . For the beam diameter  $D_{\text{beam}} = 2 \text{ mm}$ , the transit time dephasing rate is given by  $130 \text{ kHz}$ . The dipole between the states  $|r\rangle$  and  $|g\rangle$  dephases due to the relative laser frequency noise between the probe and the coupling laser.

The optical Bloch equations (OBE) at steady state is given by,

$$\frac{\Omega_p}{2}\rho_{eg} - \frac{\Omega_p^*}{2}\rho_{ge} - i\Gamma_{eg}\rho_{ee} - i\Gamma_{rg}\rho_{rr} = 0 \quad (4.1)$$

$$\frac{\Omega_c^*}{2}\rho_{er} - \frac{\Omega_c}{2}\rho_{re} + i\Gamma_{2}\rho_{rr} = 0 \quad (4.2)$$

$$\left(\Delta_p - k_p v - i\frac{\Gamma_{eg}}{2}\right)\rho_{ge} - \frac{\Omega_p}{2}(2\rho_{ee} + \rho_{rr} - 1) + \frac{\Omega_c^*}{2}\rho_{gr} = 0 \quad (4.3)$$

$$\left(\Delta_2 - \Delta k v - i\frac{\Gamma_2}{2}\right)\rho_{gr} - \frac{\Omega_p}{2}\rho_{er} + \frac{\Omega_c}{2}\rho_{ge} = 0 \quad (4.4)$$

$$\left(\Delta_c + k_c v - i\frac{\Gamma_3}{2}\right)\rho_{er} - \frac{\Omega_c}{2}(\rho_{rr} - \rho_{ee}) - \frac{\Omega_p^*}{2}\rho_{gr} = 0 \quad (4.5)$$

This set of equations are solved for  $\rho_{eg}$  and velocity-averaged over Maxwell Boltzmann velocity distribution to evaluate the susceptibility. The susceptibility  $\chi$  is related to  $\rho_{eg}$  as,  $\chi = \frac{2n_0|\mu_{eg}|^2}{\epsilon_0\hbar\Omega_p}\rho_{eg}$ , where  $n_0$  is the density of the atomic vapor.

In thermal atomic ensemble, the atoms are in motion. The velocity of the atoms follow the Maxwell Boltzmann (MB) velocity distribution which is given by the expression,  $f(v) = \frac{1}{\sqrt{\pi}v_p} e^{-\frac{v^2}{v_p^2}}$ . Here  $v_p$  is the most probable velocity of the ensemble of atoms corresponding to a particular temperature  $T$  which is given by,  $v_p = \sqrt{\frac{2k_B T}{m}}$ . Let us consider that a laser field is applied to the system of atoms in the z-direction. The applied laser frequency seen from the atomic reference frame is given by the relation,  $\Delta_{\text{Doppler}} = -\vec{k} \cdot \vec{v}$ , where the laser field wave-vector is given by,  $|\vec{k}| = \frac{2\pi}{\lambda}$ . Here  $\lambda$  is the wavelength of the applied laser field. Therefore, the susceptibility has to be averaged over the Maxwell-Boltzmann distribution. The EIT transmission ( $e^{-k_p l \text{Im}(\chi)}$ ) and dispersion ( $\frac{1}{2} \text{Re}(\chi)$ ) which are also averaged over MB velocity distribution are shown in fig. (4.1a & c) and fig. (4.1b & d) respectively, where  $l$  is the length of the vapor cell.

## 4.2 Optical heterodyne detection technique

In this section, we will discuss an all-optical detection technique namely optical heterodyne detection technique (OHDT). Using the technique absorption and dispersion of a probe laser field can be measured [31]. Also, the phase shift of the probe light due to SPM and XPM can also be measured [23, 24, 32, 33] using OHDT.

In this technique, a laser beam is generated from an external cavity diode laser (ECDL) and split into two parts using a  $\frac{\lambda}{2}$ -plate and a polarising beam splitter (PBS). An optical isolator (OI) is placed in front of the ECDL in order to prevent any optical feedback from the optical elements used in the experiment. One part of the laser beam is taken to double pass through AOM1 setup and another is taken to AOM2 setup as shown in fig. (4.2). The AOM1 operating at 80 MHz is driven by a commercial AOM driver (here frequency shift is fixed). Therefore, the double pass AOM shifts the light frequency by 160 MHz. The output of the AOM1 setup partially is taken to saturation absorption spectroscopy (SAS) to stabilize the laser to a  $^{87}\text{Rb}$  transition line as discussed in Sec. 3.4. The rest of the AOM1 output is taken to OHDT experiment and marked as frequency  $\omega$  in fig. (4.2). The AOM2 is also operating at 80 MHz but is driven by a handmade AOM driver (Appendix B). Here, the frequency shift of the laser can be controlled by changing the dc control voltage of a voltage controlled oscillator of AOM-driver. The output of the AOM2 setup is taken to OHDT experiment which is symbolized as  $\omega + \delta$ . The frequency of AOM2 is set such that the frequency offset between the heterodyne beams should be 50 MHz ( $\delta$ ). The  $\delta$  is an order of magnitude greater than the Rydberg-EIT linewidth

in thermal vapor, which is typically 6 MHz as shown in fig. (4.1c & d).

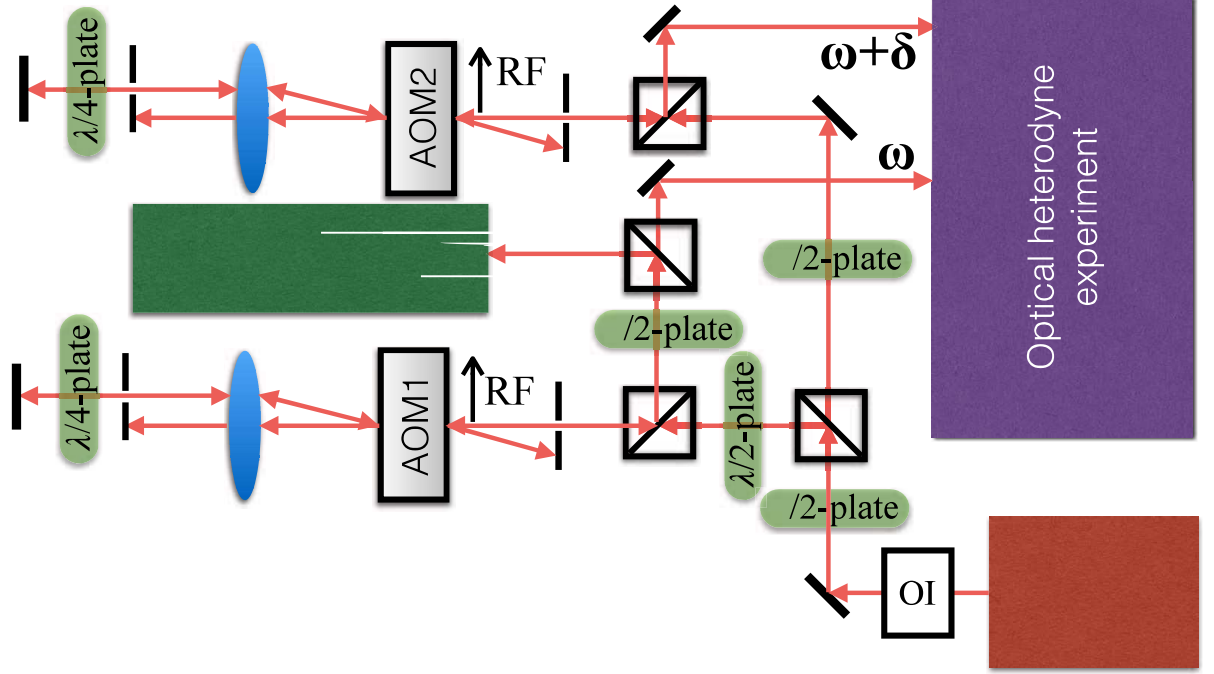


Figure 4.2: Optical set up to generate heterodyne probe beams.

The generated beams are superimposed on a PBS as shown in fig.(4.3a). The beams are termed as heterodyne probes. A part of the superimposed beams propagating through the dispersive medium undergoes different phase-shift in presence of a counter-propagating coupling laser. The phase shift experienced by the probes are different because they cannot be on resonance simultaneously while scanning the probe laser frequency. The differential phase shift appears in the beat signal which is measured by a fast detector (FPD) as shown in fig. (4.3a). At the other side of the PBS, the superimposed beam is directly detected by another FPD, which is used as a reference. An electronic arrangement is done to measure the differential phase shift. The measurement procedure is based on the differential detection technique, hence any acoustic disturbances cannot affect the experimental observations. Similarly, an all-optical interferometric technique is extensively used for the measurement of absorption and dispersion of coherent two-photon transition in an atomic ensemble, anomalous dispersion due to Zeeman coherence in 2-level atom [34] and for the study of SPM and XPM [23, 24, 32].

The electric fields of the incident laser lights to the medium can be expressed as,  $E_1^i(\omega) =$

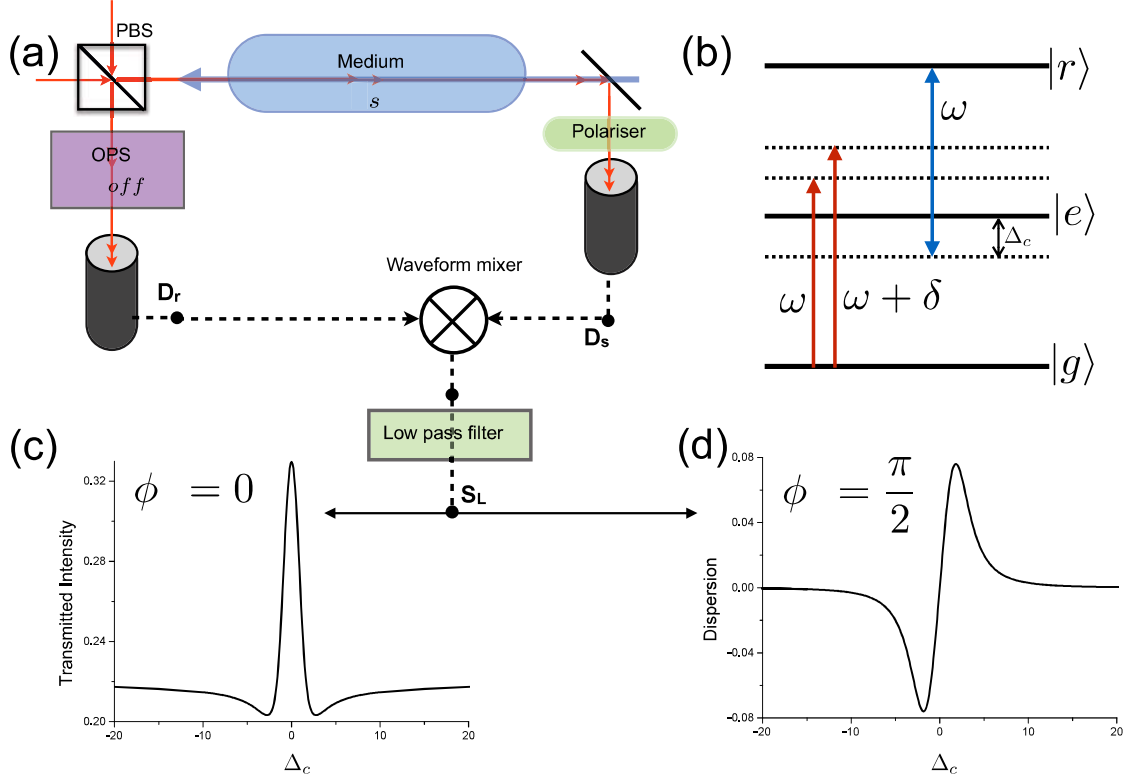


Figure 4.3: (a) OHDT setup to measure absorption and dispersion. A PBS is used to superimpose two incoming beams. One of the output of the PBS is directly taken to a detector after passing OPS. The other output passes through a dispersive medium and a polariser to a detector. Atomic level diagram is depicted in (b). (c) and (d) are the transmission and dispersion signal respectively measured by OHDT. The probe and the coupling Rabi frequencies used in the experiment are 500 kHz and 2.5 MHz respectively.

$E_1 e^{-i\omega t} + c.c.$  and  $E_2^i(\omega + \delta) = E_2 e^{-i[(\omega + \delta)t + \phi_{\text{off}}]} + c.c.$  respectively, where  $\phi_{\text{off}}$  is the relative phase difference between two probes which is a constant quantity if laser frequency kept constant during the experiment. The electric fields of transmitted lasers from the medium are given by,  $E_1^t(\omega) = \tilde{E}_1 e^{-i(\omega t - \phi_s)} + c.c.$  and  $E_2^t(\omega + \delta) = \tilde{E}_2 e^{-i[(\omega + \delta)t + \phi_{\text{off}}]} + c.c.$  respectively. Since the electric field corresponding to the laser frequency  $\omega$  is resonant to the atom, it experiences a phase shift of  $\phi_s$ . While passing through the medium the probes also suffer absorption. The transmitted electric fields are respectively expressed as,  $\tilde{E}_1 = E_1 e^{-\frac{kl}{2} \text{Im}[\chi(\omega)]}$

and  $\tilde{E}_2 = E_2 e^{-\frac{kl}{2} \text{Im}[\chi(\omega+\delta)]}$ . Therefore, the intensity detected by the detector is given by,

$$\begin{aligned} I &= |\tilde{E}_1 e^{-i(\omega t - \phi_s)} + \tilde{E}_2 e^{-i[(\omega+\delta)t + \phi_{\text{off}}]}|^2 \\ &= |E_1|^2 e^{-kl \text{Im}[\chi(\omega)]} + |E_2|^2 e^{-kl \text{Im}[\chi(\omega+\delta)]} \\ &\quad + 2|E_1||E_2| e^{-\frac{kl}{2} \text{Im}[\chi(\omega) + \chi(\omega+\delta)]} \cos(\delta t + \phi_s + \phi_{\text{off}}) \end{aligned} \quad (4.6)$$

Here  $\phi_s = \frac{kl}{2} \text{Re}[\chi_{3L}(\omega) - \chi_{3L}(\omega + \delta)]$ . The total susceptibility of the each probe can be expressed as,  $\chi = \chi_{2L} + \chi_{3L}$  where  $\chi_{2L}$  is the probe susceptibility of the 2-level transition,  $|g\rangle \rightarrow |e\rangle$  and  $\chi_{3L}$  is the probe susceptibility corresponding to the 3-level transition,  $|g\rangle \rightarrow |e\rangle \rightarrow |r\rangle$  as shown in the atomic level diagram depicted in fig. (4.3b).

### 4.2.1 Measurement of absorption and dispersion of a probe field

In this section, we will discuss regarding the measurement of the absorption and dispersion of a probe light using OHDT. Since, there is an ac filter connected to the detector  $D_s$ , the measured signal will have only time varying function. Therefore, all the dc part of Eq. 4.6 will not appear in the detection. So, the detector signal will have the form,

$$D_s = A_s e^{-\frac{kl}{2} \text{Im}[\chi_{3L}(\omega) + \chi_{3L}(\omega+\delta)]} \cos(\delta t + \phi_s + \phi_{\text{off}})$$

The beat signal detected after the medium is called the signal beat (measured by the detector  $D_s$ ) and the beat signal detected without any medium is called the reference beat (measured by the detector  $D_r$ ). The amplitude of the signal beat,  $A_s \propto 2|E_1||E_2|$ . Similarly the beat signal at the reference detector has the form,  $D_r = A_r \cos(\delta t + \phi_r)$ , where  $A_r$  and  $\phi_r$  are the amplitude and phase of the beat signal of the reference detector. These two beat signals are multiplied externally by using an RF wave-form mixer (Mini-Circuits ZAD-6+) and passed through a low pass filter (LPF) (Mini-Circuits BLP-1.9+). The dc part of the multiplied signal is allowed by the LPF which has the form,  $S_L = 2A_r A_s e^{-\frac{kl}{2} \text{Im}[\chi_{3L}(\omega) + \chi_{3L}(\omega+\delta)]} \cos(\phi_s + \phi_0)$ , where  $\phi_0 = \phi_r + \phi_{\text{off}}$ .

$\phi_0$  can be controlled optically by an optical phase shifter (OPS) as depicted in the setup of fig.(4.3a).  $\phi_0$  can be controlled electronically which requires expertise in RF electronics. Simplest way to change the phase is cable length but it can not be varied continuously. In case of OPS, the phase from 0 to  $\pi$  without compromising the change in amplitude. The optical phase shifter (OPS) can be realized as a combination of a  $\frac{\lambda}{4}$ -plate and a polarizer as is depicted in fig. (4.4), which is used to control the phase  $\phi_0$ . If a pair of orthogonal linearly polarised light passing through the  $\frac{\lambda}{4}$ -plate, thus become circularly polarised light  $\sigma^+$  and  $\sigma^-$ . It can be expressed

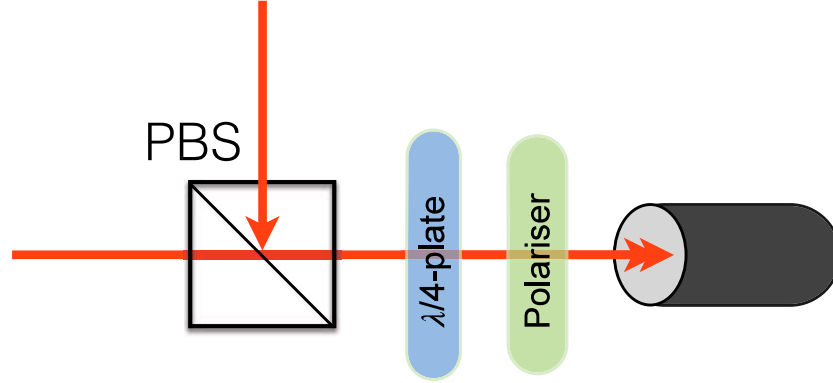


Figure 4.4: Optical phase shifter (OPS).

as,  $|\sigma^\pm\rangle = \frac{1}{\sqrt{2}}(|H\rangle + e^{\pm i\frac{\pi}{2}}|V\rangle)$ . If only  $|H\rangle$ -polarised light is transmitted by the polarizer, then the phase difference between the beams falling on the detector is zero, whereas in case of the  $|V\rangle$ -polarised light the phase difference between them becomes  $\pi$ . Hence, by rotating the optic axis of the polarizer, the phase  $\phi_0$  of the beat signal can be continuously varied between 0 to  $\pi$ .

If  $\phi_0$  is set to zero by OPS then the signal  $S_L$  becomes sensitive to the amplitude of probe fields. Therefore,  $S_L$  gives the probe transmission signal. The form of the transmission signal after subtracting the signal offset is given by,

$$S_L \approx 2A_r A_s [e^{-\frac{kl}{2} \text{Im}[\chi_{3L}(\omega) + \chi_{3L}(\omega + \delta)]} - 1]$$

The transmission signal is depicted in fig.(4.3c).

For  $\phi_0 = \frac{\pi}{2}$ ,  $S_L$  is sensitive to the phase  $\phi_s$ , which is proportional to the refractive index of the probe field in presence of the dispersive medium. Then, the measured signal will have the form,  $S_L \approx 2A_r A_s e^{-\frac{kl}{2} \text{Im}[\chi_{3L}(\omega) + \chi_{3L}(\omega + \delta)]} \phi_s$ . Here,  $\phi_s \propto \text{Re}[\chi_{3L}(\omega) - \chi_{3L}(\omega + \delta)]$ . The dispersion signal is depicted in fig. (4.3d).

## 4.2.2 Demonstration of Rydberg EIT using OHDT

In this section, we will describe the realization of Rydberg-EIT using OHDT for the vapor of rubidium 87 isotope. The frequency of probe and coupling beam is chosen such that the two-photon resonance will be satisfied in order to observe Rydberg-EIT for  $^{87}\text{Rb}$ . The atomic level scheme is depicted in the fig. (4.5b).



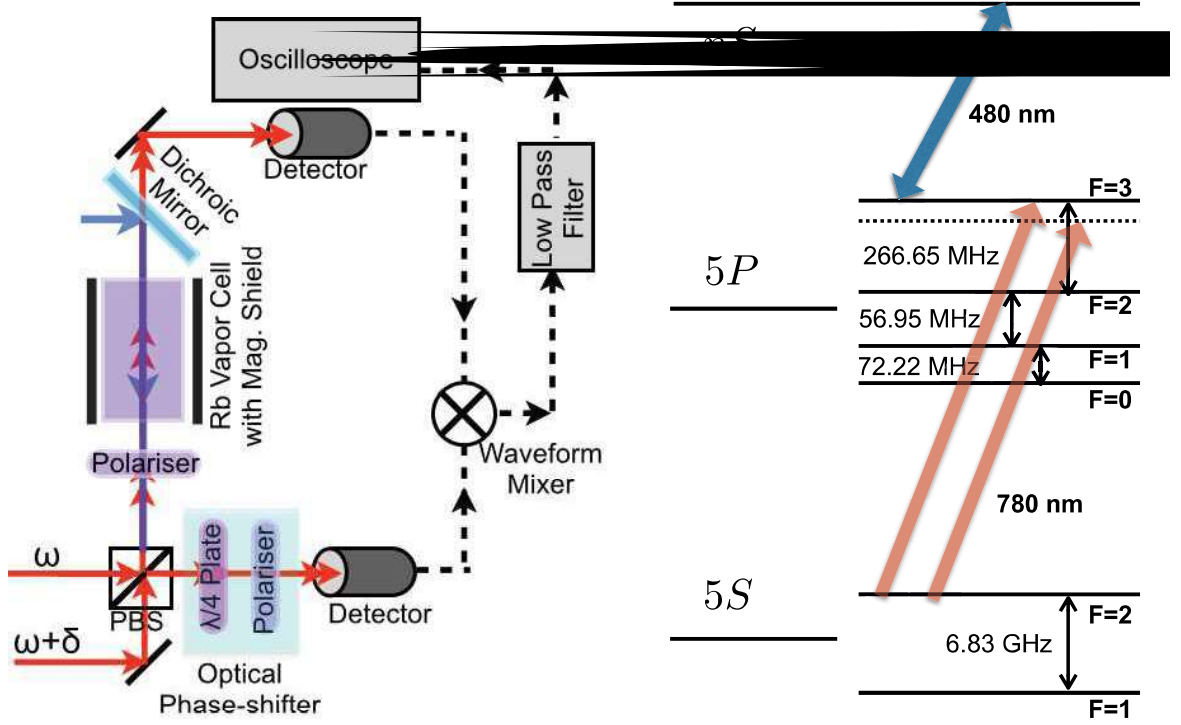


Figure 4.5: (a) Schematic of the experimental setup. (b) Atomic-level scheme of Rydberg EIT for  $^{85}\text{Rb}$  isotope.

The experimental setup based on OHDT is depicted in fig. (4.5a). Two probe beams of 780 nm with a frequency offset 50 MHz are generated from an external cavity diode laser (ECDL). The frequency offset is generated by using two acousto-optic modulators. The typical EIT line-width of Rydberg-EIT signal in thermal atomic vapor is found to 5 to 6 MHz [18]. The frequency offset is chosen such that the Rydberg-EIT signal corresponding to the individual probes should not overlap. Both the probes are superimposed using a polarising cube beam splitter (PBS). The interference beat of the probes is detected using two fast photo-detectors by introducing polarisers at both the output ports of the PBS. The probe beams coming out of one of the output ports of the PBS propagate through a magnetically shielded rubidium vapor cell. The length of the rubidium vapor cell is 5 cm. The coupling beam is derived from a frequency-doubled diode laser operating at 478 – 482 nm and it is counter-propagated to the probe beams through the vapor cell. The beat detected at the other output port of the PBS was used as a reference. The  $1/e^2$  radius of the probe and the coupling are respectively given by 0.7 mm and 1.2 mm. The frequency offset between the probes is chosen such that it is an order of magnitude larger than the line-width of Rydberg-EIT. That is why the probes experience a different phase shift while scanning the coupling laser through the EIT resonance. The measurement of

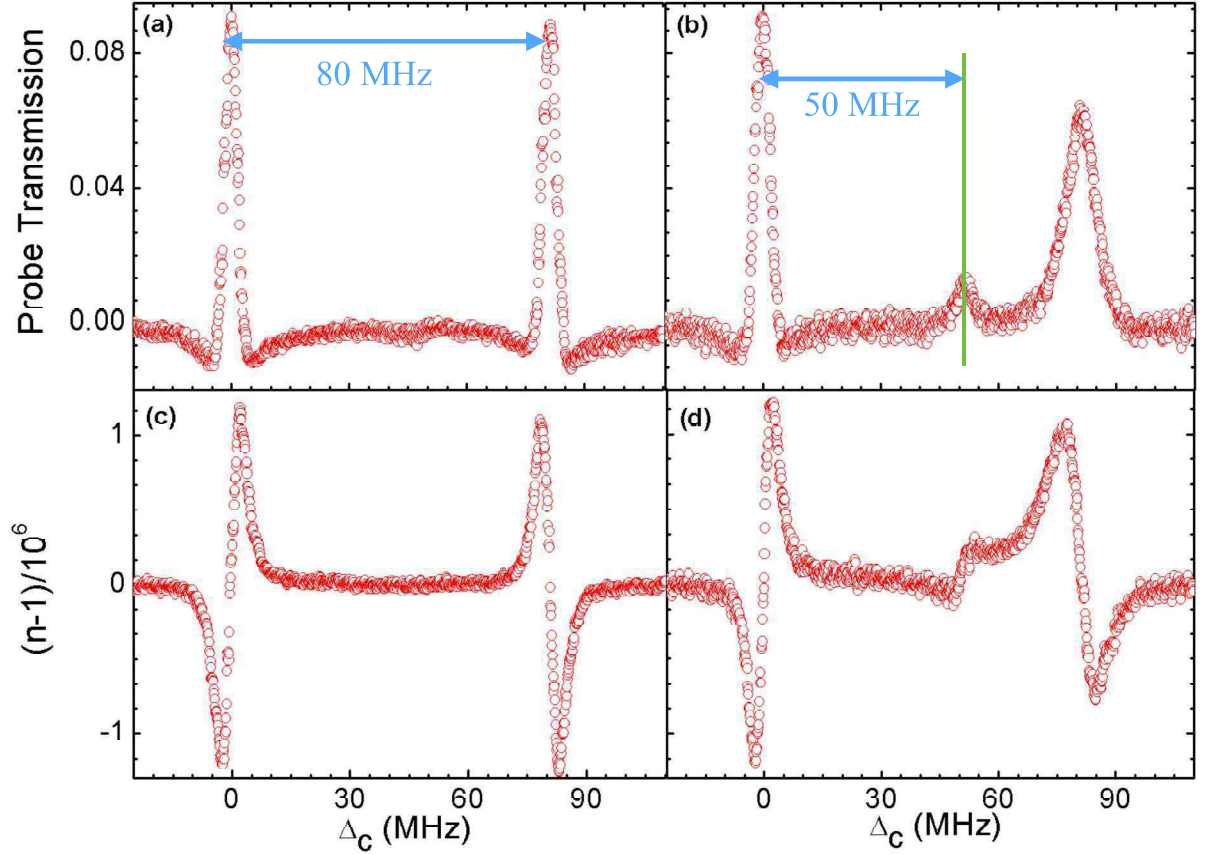


Figure 4.6: (a) The transmission and (c) the dispersion of the probes due to Rydberg-EIT with Rabi frequency 600 kHz each. (b) The transmission and (d) the dispersion signals due to Rydberg-EIT of both the probes with Rabi frequencies, 600 kHz, and 6.5 MHz, respectively. The coupling Rabi frequency is set to 2.5 MHz in all the cases. The spectrum is observed with respect to the variation of the coupling laser frequency while probe laser frequencies are kept constant. The offset of all the spectrum are zero because the OHDT is sensitive to two-photon transition only. Normally, the offset intensity for transmission is 50% of the total transmission.

the differential phase shift is done by comparing the phase of the signal beat with the phase of the reference beat.

The transmission and dispersion spectrum measured using OHDT are depicted in the fig.(4.6). The measurement is carried out by using the process as discussed in the section 4.2.1. From the fig. (4.6), it can be observed that the frequency difference of the spectrum corresponding to both the probes in all the cases (fig.4.6a, b, c & d) is more than 50 MHz. The associated frequency difference of the finite velocity classes of atoms resonating with the EIT resonances for both the probes is scaled by the factor  $\frac{k_c}{k_p}$  with the frequency offset between the probes. Here,  $k_p$  and  $k_c$  are the wave vector of the probe and the coupling laser respectively. Additionally, it

can also be observed that a small signal appears almost at the probe frequency offset which is 50 MHz when one of the probes has higher Rabi frequency.

The probe Rabi frequencies are estimated using the relation,  $\frac{I}{I_{sat}} = \frac{2|\Omega_p|^2}{\Gamma^2}$ , where  $I$  is the intensity of the probe laser. For  $^{85}\text{Rb}$ ,  $I_{sat} = 1.64 \text{ mW/cm}^2$  and  $\Gamma = 2\pi \times 6 \text{ MHz}$ . Coupling Rabi frequency is estimated by fitting the Rydberg EIT signal with a weak probe beam without focusing and then scaling it with the intensity of the beam.

### 4.3 Model of EIT using OHDT

A model of EIT using one probe beam and a single coupling beam in a three level atomic system as discussed in Sec. 4.1, can explain the individual EIT spectrum corresponding to both the probes. But, it can not explain the appearance of the intermediate small signal.

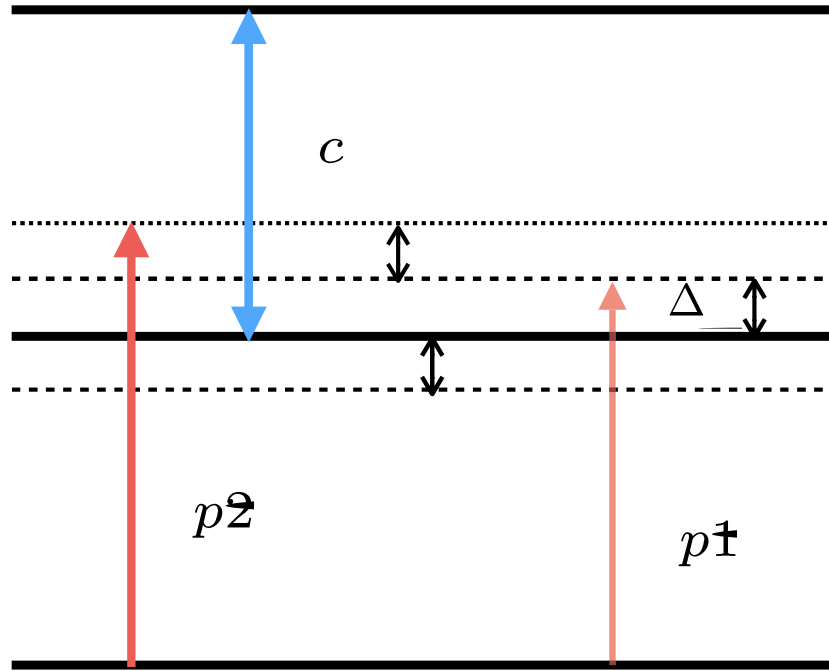


Figure 4.7: Energy level diagram for Rydberg EIT in  $^{87}\text{Rb}$ . Two probe beam couple the transition  $5S_{1/2}, F = 2(|g\rangle) \rightarrow 5P_{3/2}(|e\rangle)$ . The coupling laser couples the transition  $5P_{3/2}(|e\rangle) \rightarrow nS_{1/2}(|r\rangle)$ . The probe detuning is  $\Delta_{p1}$  and frequency offset between the probe beams is  $\delta$ .

In order to explain the complete spectrum of observed transmission (fig.(4.6a & b)) and dis-

persion (fig.(4.6c & d)) including the small signal, we consider an EIT model consisting two probes and a coupling laser fields.

The atomic Hamiltonian of a three level system is given by,

$$H_A = \hbar\omega_{ge}|e\rangle\langle e| + \hbar(\omega_{ge} + \omega_{er})|r\rangle\langle r|$$

One coupling and two probe electric fields are given by,

$$\begin{aligned} E_c &= \varepsilon_c e^{-i\omega_c t} + c.c. \\ E_{p1} &= \varepsilon_0 e^{-i\omega_{p1} t} + c.c. \\ E_{p2} &= \varepsilon_1 e^{-i\omega_{p2} t} + c.c. \end{aligned}$$

Here,  $E_{p1}$  and  $E_{p2}$  are the electric fields corresponding to the probes.  $\varepsilon_0$  and  $\varepsilon_1$  are the respective electric field amplitudes.  $E_c$  is the coupling electric field and  $\varepsilon_c$  is the electric field amplitude of the coupling field. Total probe electric field can be defined as,

$$E = E_{p1} + E_{p2} = \varepsilon e^{-i\omega_{p1} t} + c.c.$$

Where  $\varepsilon = \varepsilon_0 + \varepsilon_1 e^{-i\delta t}$  and  $\omega_{p2} - \omega_{p1} = \delta$  is the frequency offset between the probes. The model transition scheme is depicted in the fig.(4.7). The laser-atom interaction Hamiltonian can be written as,

$$H_I = -(\mu_{ge}|g\rangle\langle e| + \mu_{ge}^*|e\rangle\langle g|)E - (\mu_{er}|e\rangle\langle r| + \mu_{er}^*|r\rangle\langle e|)E_c$$

With proper unitary transformation and rotating wave approximation (RWA), the total Hamiltonian will be,

$$\mathbf{H} = \frac{\hbar}{2} \begin{pmatrix} 0 & \Omega^* & 0 \\ \Omega & 2\Delta_{p1} & \Omega_c^* \\ 0 & \Omega_c & 2\Delta_2 \end{pmatrix}.$$

Where,  $\Omega$  is the total probe Rabi frequency which is given by,

$$\begin{aligned} \Omega &= \frac{2\mu_{eg}}{\hbar} \varepsilon \\ &= \frac{2\mu_{eg}}{\hbar} (\varepsilon_0 + \varepsilon_1 e^{-i\delta t}) \\ &= \Omega_{p1} + \Omega_{p2} e^{-i\delta t} \end{aligned}$$

The coupling Rabi frequency is defined as,  $\Omega_c = \frac{2\mu_{re}\varepsilon_c}{\hbar}$ .  $\Omega_{p1}$  and  $\Omega_{p2}$  are the Rabi frequencies of stronger and weaker probe respectively.  $\Delta_2 = \Delta_{p1} + \Delta_c$ , where  $\Delta_{p1}$  and  $\Delta_c$  are the probe and coupling laser detuning.

### 4.3.1 Construction of master equation

The density matrix equation of motion can be constructed as,  $\dot{\rho} = \frac{i}{\hbar}[H, \rho] + L_D(\rho)$ . The quantity  $L_D(\rho)$  is called the Lindblad operator which is defined as,

$$L_D(\rho) = \sum_{if} \Gamma_{if} (C_{if} \rho C_{if}^\dagger - \frac{1}{2} \{C_{if}^\dagger C_{if}, \rho\})$$

Where  $C_{if} = |f\rangle\langle i|$  and  $\Gamma_{if}$  are the decoherence and decay time scales for the system  $\forall i$  and  $j$ .

The Lindblad operator for the system can be evaluated as,

$$\mathbf{L}_D(\rho) = \begin{pmatrix} (\Gamma_{eg}\rho_{ee} + \Gamma_{rg}\rho_{rr}) & -\frac{\Gamma_{eg}}{2}\rho_{ge} & -\frac{\Gamma_2}{2}\rho_{gr} \\ -\frac{\Gamma_{eg}}{2}\rho_{eg} & (\Gamma_{re}\rho_{rr} - \Gamma_{eg}\rho_{ee}) & -\frac{\Gamma_3}{2}\rho_{er} \\ -\frac{\Gamma_2}{2}\rho_{rg} & -\frac{\Gamma_3}{2}\rho_{re} & -\Gamma_2\rho_{rr} \end{pmatrix}.$$

Here,  $\Gamma_2 = \Gamma_{re} + \Gamma_{rg}$  and  $\Gamma_3 = \Gamma_{rg} + \Gamma_{re} + \Gamma_{rg}$ . The population decay rate of the channels,  $|r\rangle \rightarrow |e\rangle$  is denoted by  $\Gamma_{re}$  and  $|e\rangle \rightarrow |g\rangle$  is denoted by  $\Gamma_{eg}$ . In our model, the decay time scales are used are  $\Gamma_{rg} = 10$  kHz,  $\Gamma_{eg} = 6$  MHz. The corresponding dipole dephasing rate  $\frac{\Gamma_{rg}}{2} + \Gamma_{rel} = 100$  kHz is taken in our model, where  $\Gamma_{rel}$  is the relative frequency noise of the probe and the coupling laser. The system of atoms are in thermal motion where the velocity of the atoms is governed by the Maxwell Boltzmann velocity distribution corresponding to the temperature of the system. In order to interact with the atoms having same velocity the probe and coupling detuning has to be modified as,  $\Delta_{p1} \rightarrow \Delta_{p1} - k_p v$  and  $\Delta_c \rightarrow \Delta_c + k_c v$ , where  $v$  is the velocity of atoms.

### 4.3.2 0th order OBE

We have used the perturbative method to solve the density matrix equation in steady state. Similar approach is used to calculate the 4-wave mixing in 2-level atoms as discussed in reference [35]. The density matrix elements of the system can be expanded as,

$$\rho_{ji} = \rho_{ji}^{(0)} + \rho_{ji}^{(1)} e^{-i\delta t} + \rho_{ji}^{(-1)} e^{i\delta t}$$

For all  $i$  and  $j$ . In order to characterise the density matrix elements, we have taken the complex conjugate of the above equation and by subtracting the above equation from it we get,  $(\rho_{ij}^{(0)*} - \rho_{ji}^{(0)}) + (\rho_{ij}^{(1)*} - \rho_{ji}^{(1)}) e^{-i\delta t} + (\rho_{ij}^{(-1)*} - \rho_{ji}^{(-1)}) e^{i\delta t} = 0$ . For unperturbed density matrix element,  $\rho_{ji}^* = \rho_{ji}$ , because the density matrix is hermitian.  $\{1, e^{\pm i\delta t}\}$  forms complete set of orthonormal basis if higher order terms are neglected. Using the property of linear independence of the basis state, we can draw the following relations,  $\rho_{ij}^{(0)*} = \rho_{ji}^{(0)}$  and  $\rho_{ij}^{(\pm 1)*} = \rho_{ji}^{(\mp 1)}$ . For first

order density matrix, we have to compute all the matrix elements.

Similarly the diagonal matrix elements can be expanded as,  $\rho_{ii} = \rho_{ii}^{(0)} + \rho_{ii}^{(1)} e^{-i\delta t} + \rho_{ii}^{(-1)} e^{i\delta t}$ . The diagonal elements of the unperturbed density matrix signify the population of the individual states. Hence, all  $\rho_{ii}$  are real quantity. Using the condition  $Im(\rho_{ii}) = 0$  in the above equation we get,  $Im(\rho_{ii}^{(0)}) + [Im(\rho_{ii}^{(-1)}) + Im(\rho_{ii}^{(1)})] \cos \delta t + [Re(\rho_{ii}^{(-1)}) - Re(\rho_{ii}^{(1)})] \sin \delta t = 0$ .  $\{1, \cos \delta t, \sin \delta t\}$  also forms orthonormal basis set. Using the condition of linear independence it can be concluded that only zeroth order diagonal density matrix elements are real quantities whereas the first order diagonal density matrix elements are not strictly real quantity.

The perturbative expansion of density matrix can be substituted in the master equation. Equating the coefficients of  $e^{-i\delta t}$  with  $\delta = 0$  gives the zeroth order equations at steady state as,

$$\frac{\Omega_{p1}}{2} \rho_{eg}^{(0)} - \frac{\Omega_{p1}^*}{2} \rho_{ge}^{(0)} - i\Gamma_{eg} \rho_{ee}^{(0)} - i\Gamma_{rg} \rho_{rr}^{(0)} = 0 \quad (4.7)$$

$$\frac{\Omega_c^*}{2} \rho_{er}^{(0)} - \frac{\Omega_c}{2} \rho_{re}^{(0)} + i\Gamma_2 \rho_{rr}^{(0)} = 0 \quad (4.8)$$

$$\left( \Delta_p - k_p v - i\frac{\Gamma_{eg}}{2} \right) \rho_{ge}^{(0)} - \frac{\Omega_{p1}}{2} (2\rho_{ee}^{(0)} + \rho_{rr}^{(0)} - 1) + \frac{\Omega_c^*}{2} \rho_{gr}^{(0)} = 0 \quad (4.9)$$

$$\left( \Delta_2 - \Delta k v - i\frac{\Gamma_2}{2} \right) \rho_{gr}^{(0)} - \frac{\Omega_{p1}}{2} \rho_{er}^{(0)} + \frac{\Omega_c}{2} \rho_{ge}^{(0)} = 0 \quad (4.10)$$

$$\left( \Delta_c + k_c v - i\frac{\Gamma_3}{2} \right) \rho_{er}^{(0)} - \frac{\Omega_c}{2} (\rho_{rr}^{(0)} - \rho_{ee}^{(0)}) - \frac{\Omega_{p1}^*}{2} \rho_{gr}^{(0)} = 0 \quad (4.11)$$

Where  $\Delta k = k_p - k_c$ . This set of equations can be solved exactly for strong probe beam.

### 4.3.3 1st order OBE

As we have seen that the first order density matrix is not hermitian, therefore, all the matrix elements has to be computed. Equating the coefficients of  $e^{-i\delta t}$  gives the first order equations, which can be solved if the 2nd order terms are neglected. Hence, this model is valid if one of

the probe beam is weak. The first order equations at the steady state are given by,

$$\begin{aligned} & \left( \Delta_p + \delta - k_p v + i \frac{\Gamma_{eg}}{2} \right) \rho_{eg}^{(1)} + \frac{\Omega_c}{2} \rho_{rg}^{(1)} - \frac{\Omega_{p1}}{2} (2\rho_{ee}^{(1)} + \rho_{rr}^{(1)}) \\ & - \frac{\Omega_{p2}}{2} (2\rho_{ee}^{(0)} + \rho_{rr}^{(0)} - 1) = 0 \end{aligned} \quad (4.12)$$

$$\left( \Delta_2 + \delta - \Delta k v + i \frac{\Gamma_2}{2} \right) \rho_{rg}^{(1)} + \frac{\Omega_c}{2} \rho_{eg}^{(1)} - \frac{\Omega_{p1}}{2} \rho_{re}^{(1)} - \frac{\Omega_{p2}}{2} \rho_{re}^{(0)} = 0 \quad (4.13)$$

$$\left( \Delta_c + \delta + k_c v + i \frac{\Gamma_3}{2} \right) \rho_{re}^{(1)} - \frac{\Omega_{p1}}{2} \rho_{rg}^{(1)} - \frac{\Omega_c}{2} (\rho_{rr}^{(1)} - \rho_{ee}^{(1)}) = 0 \quad (4.14)$$

$$\left( \Delta_p - \delta - k_p v - i \frac{\Gamma_{eg}}{2} \right) \rho_{ge}^{(1)} + \frac{\Omega_c}{2} \rho_{gr}^{(1)} - \frac{\Omega_{p1}}{2} (2\rho_{ee}^{(1)} + \rho_{rr}^{(1)}) = 0 \quad (4.15)$$

$$\left( \Delta_2 - \delta - \Delta k v - i \frac{\Gamma_2}{2} \right) \rho_{gr}^{(1)} + \frac{\Omega_c}{2} \rho_{ge}^{(1)} - \frac{\Omega_{p1}}{2} \rho_{er}^{(1)} = 0 \quad (4.16)$$

$$\left( \Delta_c - \delta + k_c v - i \frac{\Gamma_3}{2} \right) \rho_{er}^{(1)} + \frac{\Omega_c}{2} (\rho_{ee}^{(1)} - \rho_{rr}^{(1)}) - \frac{\Omega_{p2}}{2} \rho_{gr}^{(0)} - \frac{\Omega_{p1}}{2} \rho_{gr}^{(1)} = 0 \quad (4.17)$$

$$\frac{\Omega_c}{2} (\rho_{re}^{(1)} - \rho_{er}^{(1)}) - \delta \rho_{rr}^{(1)} - i \Gamma_2 \rho_{rr}^{(1)} = 0 \quad (4.18)$$

$$\begin{aligned} & \frac{\Omega_{p1}}{2} (\rho_{eg}^{(1)} - \rho_{ge}^{(1)}) + \frac{\Omega_c}{2} (\rho_{er}^{(1)} - \rho_{re}^{(1)}) + \frac{\Omega_{p2}}{2} \rho_{ge}^{(0)} - \delta \rho_{ee}^{(1)} \\ & - i \Gamma_{eg} \rho_{ee}^{(1)} + i \Gamma_{re} \rho_{rr}^{(1)} = 0 \end{aligned} \quad (4.19)$$

The solution of the zeroth order equations are substituted in the first order equations and are solved numerically. Then, the solutions are averaged over the Maxwell Boltzmann distribution of the atoms corresponding to the given temperature.

#### 4.3.4 Calculation of susceptibility

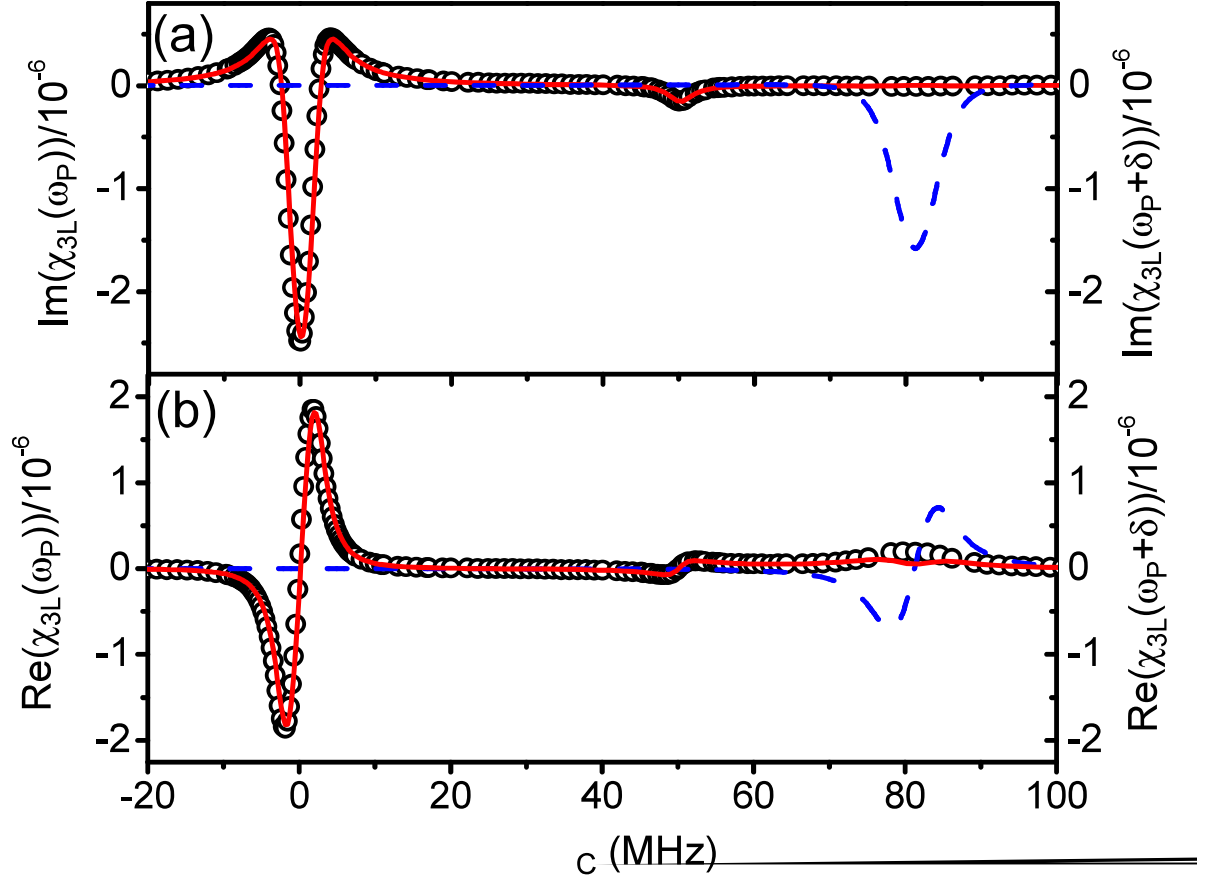


Figure 4.8: Imaginary (a) and real (b) part of  $\chi_{3L}(\omega_p)$  and  $\chi_{3L}(\omega_p + \delta)$  as a function of coupling laser detuning. The parameter used in the model are  $\Delta_p = -50$  MHz,  $\delta = 50$  MHz,  $\Omega_{p1} = 5$  MHz,  $\Omega_{p2} = 0.5$  MHz and  $\Omega_c = 2.5$  MHz. The susceptibilities are Doppler averaged over Maxwell Boltzmann velocity distribution corresponding to the temperature of the atomic vapor which is given by,  $T = 300$  K. The blue dashed (---) and red solid lines (—) are susceptibilities of the strong and the weak probe beam, respectively. The open circles (o) are the approximated susceptibility of the weak probe.

Zeroth order equations are solved numerically in steady state for the zeroth order matrix elements  $\rho_{i,j}^{(0)} \forall i, j$  and they are substituted in the first order equations. The first order equations are then solved numerically in steady state to determine  $\rho_{eg}^{(1)}$ . The susceptibility of the strong probe is averaged over the thermal motion of the atoms which can be calculated as,

$$\chi(\omega_p) = \frac{2n_0 |\mu_{eg}|^2}{\epsilon_0 \hbar \Omega_{p1}} \frac{1}{\sqrt{2\pi} v_p} \int_{-\infty}^{\infty} \rho_{eg}^{(0)} e^{-v^2/2v_p^2} dv$$



Where  $n_0$  is the density of atoms and  $\mu_{eg}$  is the dipole moment of the transition  $|g\rangle \rightarrow |e\rangle$ . Similarly, the susceptibility of the weak probe can be determined as,

$$\chi(\omega_p + \delta) = \frac{2n_0 |\mu_{eg}|^2}{\epsilon_0 \hbar \Omega_{p2}} \frac{1}{\sqrt{2\pi} v_p} \int_{-\infty}^{\infty} \rho_{eg}^{(1)} e^{-v^2/2v_p^2} dv$$

Heterodyne detection technique is sensitive only to the two-photon transition and hence the susceptibility of the probe in the absence of the coupling beam can't be detected. The susceptibilities of the probes due to two-photon transition are respectively defined as,  $\chi_{3L}(\omega_p) = \chi(\omega_p) - \chi_{2L}(\omega_p)$  and  $\chi_{3L}(\omega_p + \delta) = \chi(\omega_p + \delta) - \chi_{2L}(\omega_p + \delta)$ , where  $\chi_{2L}$  is the susceptibility of the probes in the absence of the coupling beam. This will help us to compare with the experimental measurement.  $\chi_{3L}$  calculated from the model is depicted in figure (4.8). The frequency difference between the signal peaks associated with Rydberg-EIT corresponding to different probes is not exactly equal to the frequency offset between them since the offset is scaled as  $\frac{k_c}{k_p} \delta$ . The EIT equations easily explains the fact. EIT resonance peak for the strong probe is observed if  $\Delta_2 - \Delta k v = 0$  and  $\Delta_p - k_p v = 0$ . So EIT resonance of the strong probe appears at  $\Delta_c = -\frac{k_c}{k_p} \Delta_p$ . Similarly, EIT peak for the weak probe is observed if  $\Delta_2 + \delta - \Delta k v = 0$  and  $\Delta_p + \delta - k_p v = 0$ . Hence, EIT peak of the weak probe appears at  $\Delta_{c1} = -\frac{k_c}{k_p} (\Delta_p + \delta)$ . So, the spectral difference between the EIT peaks,  $(\Delta_{c1} - \Delta_c)$  is found to be  $\frac{k_c}{k_p} \delta$ . As a similar effect of wave vector mismatch, spectral difference of Rydberg EIT peaks associated with the hyperfine transition in rubidium thermal vapor is scaled by  $(1 - \frac{k_p}{k_c})$  and is reported in the reference [18].

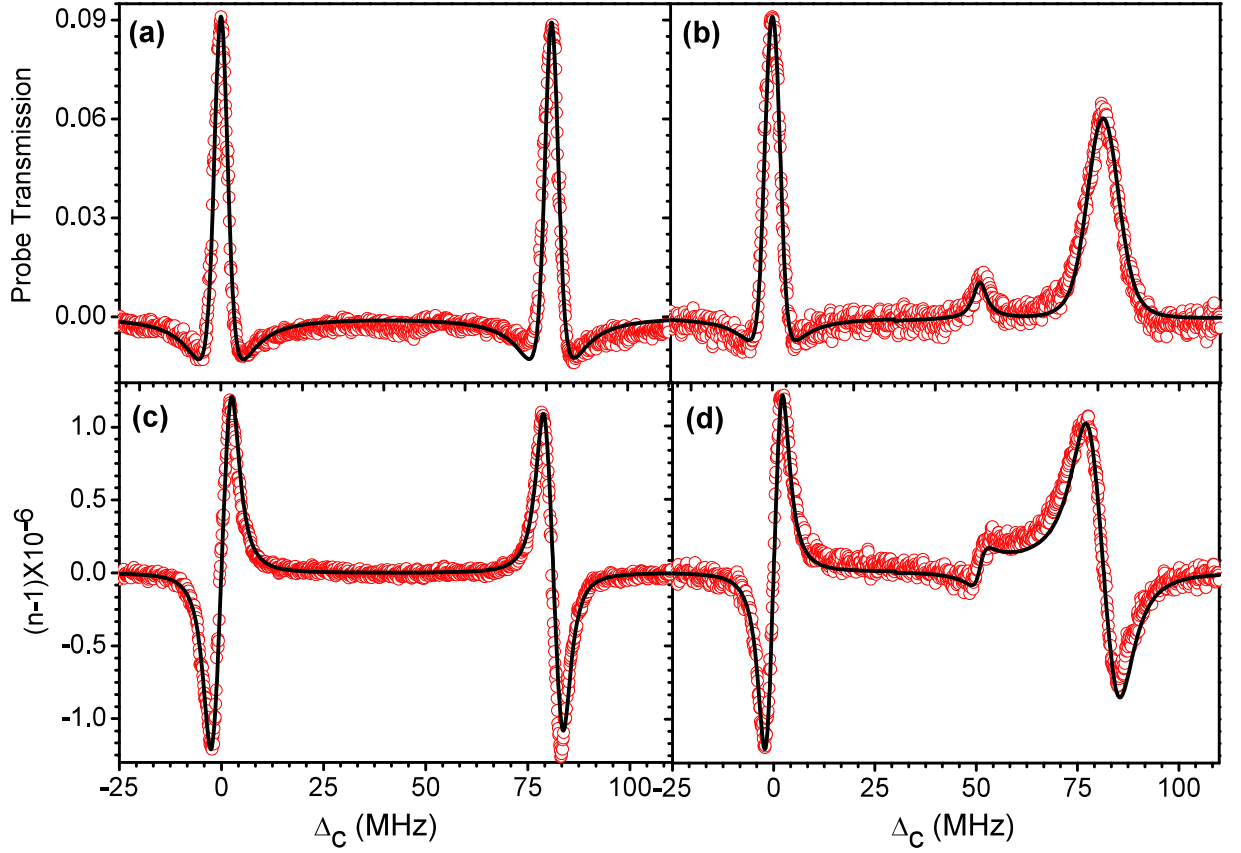


Figure 4.9: The red open circles ( $\circ$ ) are experimental data points and the black solid lines ( $—$ ) is the curve generated by the model. The parameters are same as in fig. (4.6).

It can be seen that the transmission and dispersion of the probe beam calculated from the model agrees significantly with the experimental data as shown in fig. (4.9). The model data is generated for the same parameter as in the experiment. The model also matches with the small signal observed in dispersion as well as for transmission.

#### 4.3.5 Reduced OBE

As shown in figure (4.8), a small peak is observed for the weak probe susceptibility when coupling laser is detuned by 50 MHz from the weak probe EIT peak. In order to get an insight of the origin of this peak, we use the following approximations to simplify the first order equations. Since the probe beam is weak, it cannot raise the population in the excited states. Hence,

$\rho_{ee}^{(1)} \approx \rho_{rr}^{(1)} \approx 0$ . Using this approximations, the first order equations are reduced to

$$\left( \Delta_p + \delta - k_p v + i \frac{\Gamma_{eg}}{2} \right) \rho_{eg}^{(1)} + \frac{\Omega_c}{2} \rho_{rg}^{(1)} + \frac{\Omega_{p2}}{2} (2\rho_{ee}^{(0)} + \rho_{rr}^{(0)} - 1) = 0 \quad (4.20)$$

$$\left( \Delta_2 + \delta - \Delta k v + i \frac{\Gamma_2}{2} \right) \rho_{rg}^{(1)} + \frac{\Omega_c}{2} \rho_{eg}^{(1)} - \frac{\Omega_{p1}}{2} \rho_{re}^{(1)} - \frac{\Omega_{p2}}{2} \rho_{re}^{(0)} = 0 \quad (4.21)$$

$$\left( \Delta_c + \delta + k_c v + i \frac{\Gamma_3}{2} \right) \rho_{re}^{(1)} - \frac{\Omega_{p1}}{2} \rho_{rg}^{(1)} = 0 \quad (4.22)$$

In the absence of the strong probe beam,  $\Omega_{p1} = 0$  and all the zeroth order matrix elements are equal to zero and Eq. (4.22) leads to  $\rho_{re}^{(1)} = 0$ . Under this condition, it can be shown that Eq. (4.20) and (4.21) exactly give the EIT equations in the weak probe limit. The strong probe is 50 MHz detuned from the atomic resonance since the low probe is stabilised at the atomic resonance and the frequency offset between the strong probe and the low probe is  $\delta = 50$  MHz. Due to the presence of the strong probe the extra term in zeroth order equations is responsible for the appearance of the small peak. To understand it further, let the weak probe interact with the zero velocity class of atoms. So, the main EIT peak of the weak probe appears at  $\Delta_c = 0$  MHz. The strong probe dresses the same zero velocity class of atoms which are excited to the  $|r\rangle$  state via two-photon resonance, for  $\Delta_c = 50$  MHz. Hence,  $\rho_{rr}^{(0)}$  in Eq. (4.20) and (4.21) are non-zero for zero velocity class of atoms which interact with the weak probe beam and contribute to  $\chi_{3L}(\omega_p + \delta)$ . Since, the strong probe beam resonantly interacts with a different velocity class of atoms, the two-photon resonance for that velocity class is shifted due to wave vector mismatch and the corresponding EIT peak appears at 81.25 MHz. To show that the above approximation is valid, we calculated  $\chi_{3L}(\omega_p + \delta)$  using Eq. (4.20) and (4.21), which is shown in figure (4.8) and the approximation holds very well. Due to the wave vector mismatch in this case, the small peak is resolved from the EIT peak of the strong probe and a standard model for EIT with a single probe field and a coupling field can be used to compare with the experimental data. If the wave vectors are same, e.g. in the case of  $\Lambda$  EIT in alkali atoms, the small peak can't be resolved from the EIT peak of the strong probe and hence, the model with two probes fields and a coupling field presented here should be used to compare with the experiment. Alternatively, the small peak can be reduced by changing the offset frequency.

## 4.4 The EIT peak of the weak probe dressed by the strong probe beam

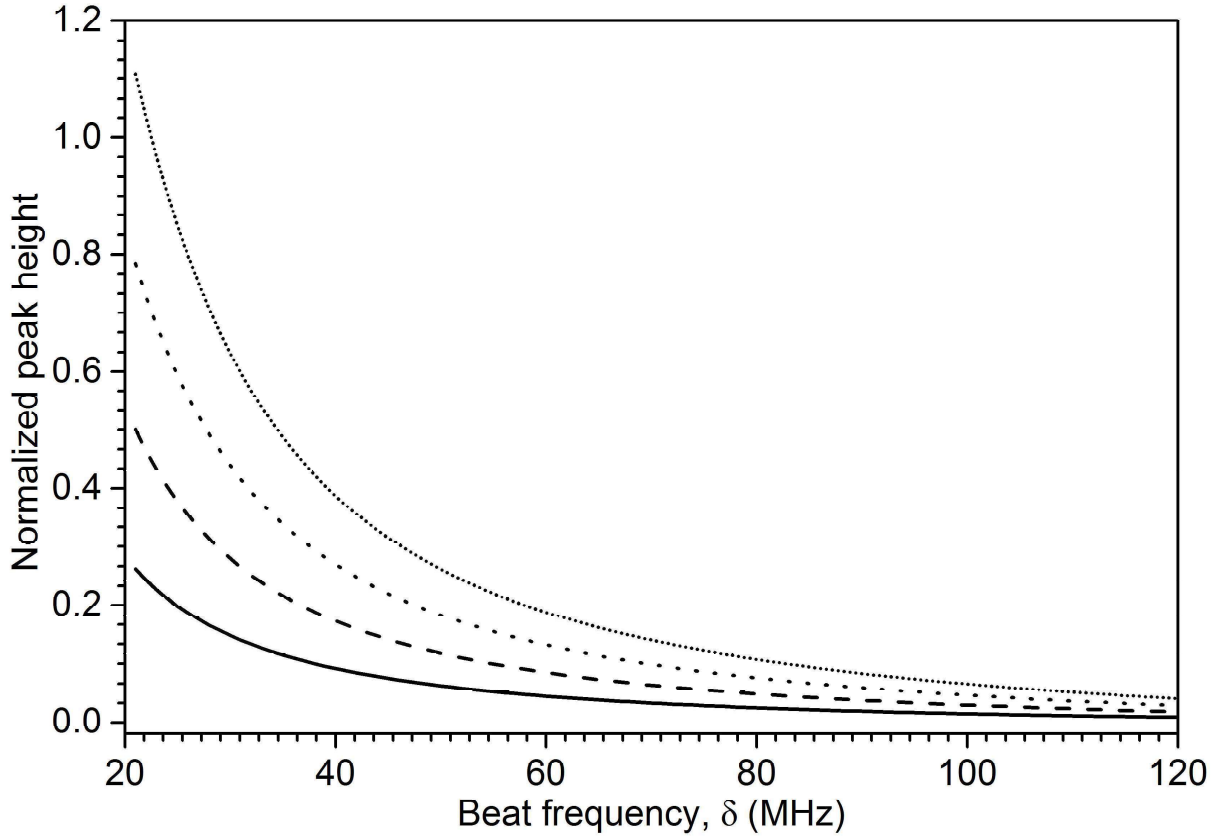


Figure 4.10: Theoretical plot for variation of small peak height with beat frequency. The data is taken for coupling Rabi frequency  $\Omega_c = 2.5$  MHz and four different probe Rabi frequency  $\Omega_p$ . Solid line corresponds to  $\Omega_p = 4$  MHz, dashed line corresponds to  $\Omega_p = 6$  MHz, big dotted line corresponds to  $\Omega_p = 8$  MHz and small dotted line corresponds to  $\Omega_p = 10$  MHz.

In order to explore the good working regime of the technique, the transmission peak height is studied with respect to the frequency offset for different probe Rabi frequencies using the model presented, as shown in figure (4.10). It is observed that the peak height of the EIT transmission due to dressed atoms reduces exponentially for beat frequency much larger than the probe Rabi frequency. In this regime, the effect due to the dressed atoms will have a negligible contribution and hence, the simple EIT model consisting of a single probe beam and a coupling field can be used to model the system accurately and also the quantification of the nonlinear absorption coefficient and nonlinear refractive index will be accurate.

## 4.5 Study of Optical nonlinearity of Rydberg-EIT medium

The intensity dependent non-linearity can be measured for the Rydberg-EIT system. From fig. (4.9), it can be observed that the transmission (fig. 4.9a to b), as well as dispersion (fig. 4.9c to d) of the probe field, are suppressed as corresponding probe Rabi frequency increases. In this section, we will discuss the nonlinear measurement using EIT transmission signal.

### 4.5.1 Nonlinearity measurement from transmission

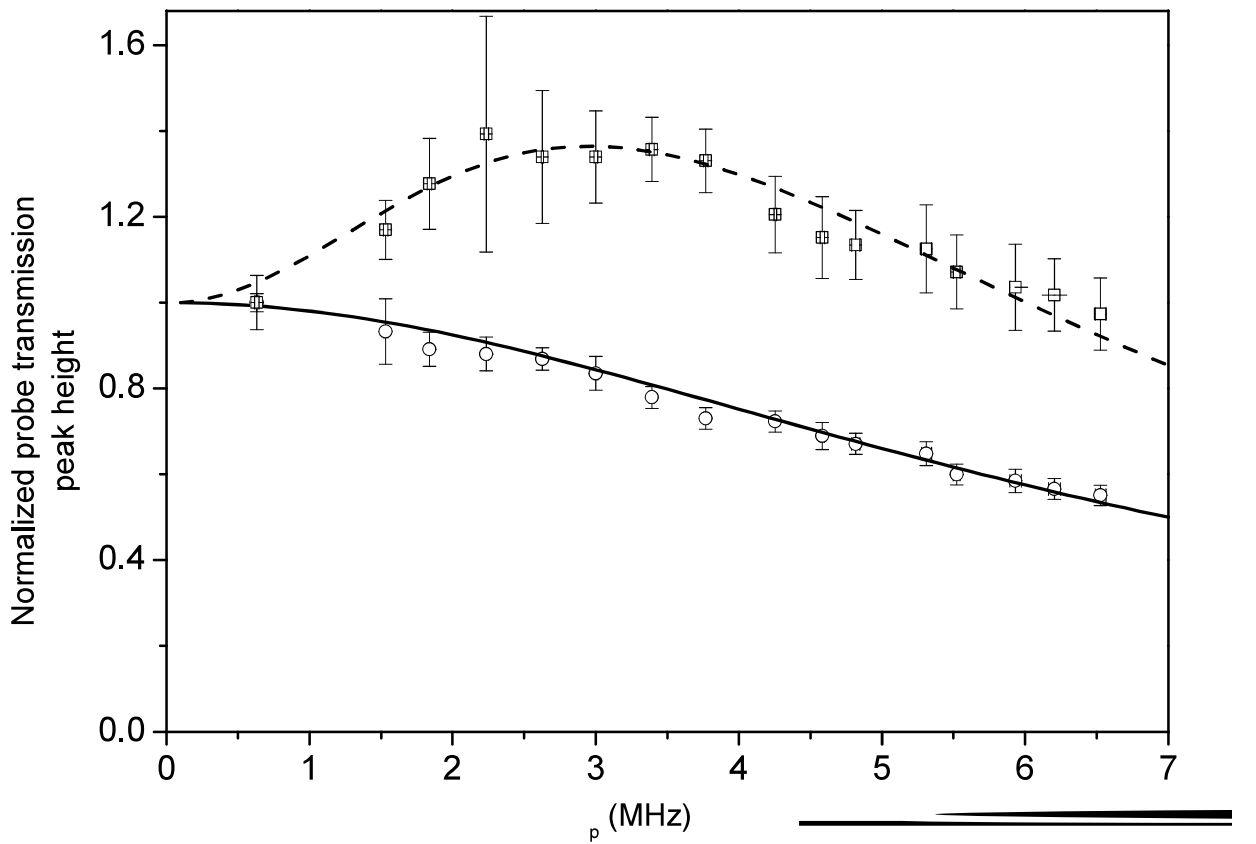


Figure 4.11: The transmission peak height is studied with the variation of probe Rabi frequency while the coupling Rabi frequency is fixed at 2.5 MHz ( $\circ$ ) and 800 kHz ( $\square$ ). The curves depicted in the figure as the solid line (—) and the dashed lines (- - -) are generated using the model for the same experimental parameters.

It is observed from fig. (4.9a) to fig. (4.9b) that the low probe transmission signal is unaffected while changing the Rabi frequency of the other probe. We kept low probe transmission signal as the reference of nonlinear transmission peak height measurement. The transmission peak

height data as a function of probe Rabi frequency is normalized with respect to the EIT peak height corresponding to the low probe (which is kept fixed throughout the peak height measurement). In order to resolve the small signal due to the dressed atom from the signal due to the strong probe, the frequency offset between the probes is set accordingly. The study of normalized peak height with the variation of the probe Rabi frequency is depicted in fig. (4.11). The model generated curves for the same parameters as in the experiment, matches significantly with the experimental data which is clearly observed in fig. (4.11). In this regard, it has to be noted that for the system where probe and coupling wave vectors are the same, the small signal will not get resolved from EIT peak. In that case, the choice of frequency offset has to be large enough (as discussed Sec. 4.4) in order to carry out nonlinear measurement accurately.

For better estimation of the nonlinear susceptibility, we have analysed the transmission peak height data in weak probe regime.

#### 4.5.2 SPM at weak probe limit

To determine the contributions of the higher order susceptibilities to the EIT peak, we do the following analysis.

The EIT peak height of weak probe is given by,

$$\begin{aligned} P_w &= S_L(\Delta_c = 0) \\ &= 2A_s A_r \left[ e^{-\frac{kl}{2} \text{Im}[\chi_{3L}(\omega+\delta)]} - 1 \right] \end{aligned}$$

Similarly, the EIT peak height of the strong probe beam is given by,

$$\begin{aligned} P_s &= S_L(\Delta_c = \frac{k_c}{k_p} \delta) \\ &= 2A_s A_r \left[ e^{-\frac{kl}{2} \text{Im}[\chi_{3L}(\omega)]} - 1 \right] \end{aligned}$$

Assuming  $\chi_{3L}(\omega)$  and  $\chi_{3L}(\omega + \delta)$  to be small, the ratio is  $\frac{P_s}{P_w} \approx \frac{\text{Im}[\chi_{3L}(\omega)]}{\text{Im}[\chi_{3L}(\omega+\delta)]}$ .

The Taylor expansion of the susceptibility is given by,

$$\begin{aligned} \chi_{3L} &= [\chi_{3L}]_{\Omega_p=0} + \frac{1}{2!} \left[ \frac{\partial^2 \chi_{3L}}{\partial \Omega_p^2} \right]_{\Omega_p=0} \Omega_p^2 \\ &\quad + \frac{1}{4!} \left[ \frac{\partial^4 \chi_{3L}}{\partial \Omega_p^4} \right]_{\Omega_p=0} \Omega_p^4 + \dots \end{aligned}$$

Since  $\chi_{3L}$  is an even function of  $\Omega_p$ , all the odd order terms in the expansion are zero.  $\chi_{3L}$  can

be expressed as,

$$\begin{aligned}\chi_{3L} &= \chi_{3L}^{(1)} + \chi_{3L}^{(3)} E_p^2 + \chi_{3L}^{(5)} E_p^4 + \dots \\ &= \chi_{3L}^{(1)} + \chi_{3L}^{(3)} \left[ \frac{\hbar}{2\mu} \right]^2 \Omega_p^2 + \chi_{3L}^{(5)} \left[ \frac{\hbar}{2\mu} \right]^4 \Omega_p^4 + \dots\end{aligned}$$

Where  $E_p$  is the probe electric field. Comparing both the equations, we get  $\chi_{3L}^{(1)} = \chi_{3L}(\Omega_p = 0)$ ,  $\chi_{3L}^{(3)} = \frac{1}{2!} \left[ \frac{2\mu}{\hbar} \right]^2 \left[ \frac{\partial^2 \chi_{3L}}{\partial \Omega_p^2} \right]_{\Omega_p=0}$ ,  $\chi_{3L}^{(5)} = \frac{1}{4!} \left[ \frac{2\mu}{\hbar} \right]^4 \left[ \frac{\partial^4 \chi_{3L}}{\partial \Omega_p^4} \right]_{\Omega_p=0}$ . Since the Doppler broadening is much larger than the offset frequency  $\delta$ , it is assumed that  $\chi_{3L}^{(1)}(\omega) \approx \chi_{3L}^{(1)}(\omega + \delta)$ . Also for the weak probe beam, the higher order terms are assumed to be negligible. So the normalized EIT peak height of the strong probe beam can be written as

$$\frac{P_s}{P_w} = 1 + \frac{Im(\chi_{3L}^{(3)})}{Im(\chi_{3L}^{(1)})} \Omega_p^2 + \frac{Im(\chi_{3L}^{(5)})}{Im(\chi_{3L}^{(1)})} \Omega_p^4 + \dots \quad (4.23)$$

We use Eq. (4.23) to match with experimental low probe data. The parameters  $\frac{Im(\chi_{3L}^{(3)})}{Im(\chi_{3L}^{(1)})}$  and  $\frac{Im(\chi_{3L}^{(5)})}{Im(\chi_{3L}^{(1)})}$  will give the estimation of the non-linear susceptibilities.

### 4.5.3 Measurement of nonlinearity

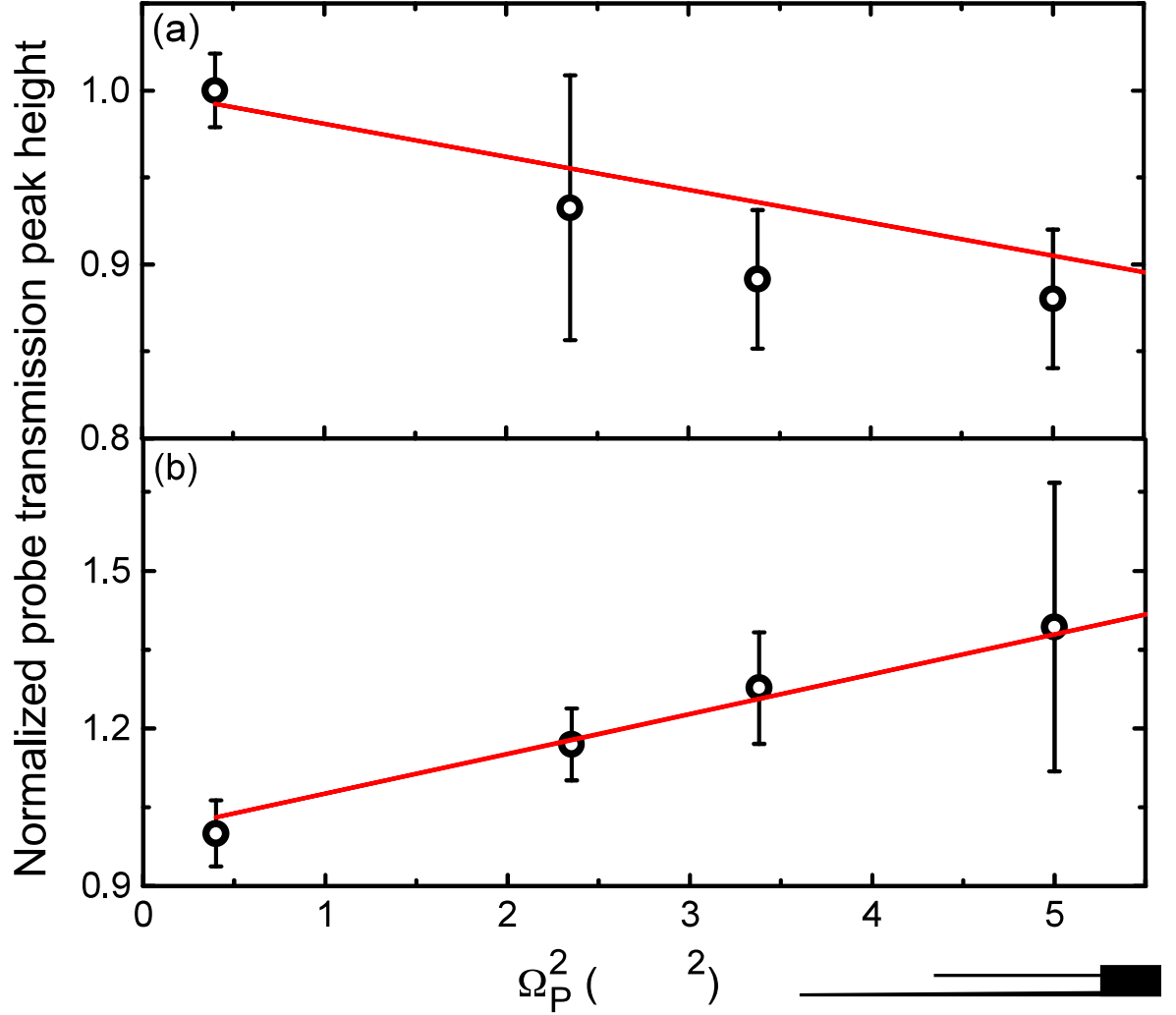


Figure 4.12: Normalized EIT peak height as a function of  $\Omega_p^2$ . The circles are the experimental data with (a)  $\Omega_c = 2.5$  MHz and (b)  $\Omega_c = 0.8$  MHz. The solid lines are the linear fitting with the function  $1 + a\Omega_p^2$  with  $a$  as the fitting parameter.

In principle, the polynomial function (Eq. 4.23) can be used to fit the transmission peak height data, as shown in figure (4.11), to determine the higher order non-linearities. Though the exact solution of the EIT fits the data very well, keeping a few terms in the above polynomial function doesn't fit the data equally well mainly due to large contributions of the higher order terms at higher probe Rabi frequencies. Therefore, we selected the first four data points of figure (4.9) to fit with a function  $1 + a\Omega_p^2$ , where  $a = \frac{\text{Im}(\chi_{3L}^{(3)})}{\text{Im}(\chi_{3L}^{(1)})}$  and gives information about the self phase modulation ( $\chi_{3L}^{(3)}$ ) of the probe light.



Table 4.1: Fitting with  $1 + a\Omega_p^2$

$\Omega_c$ in MHz	$a$ in $\text{MHz}^{-2}$	$\delta a$ in $\text{MHz}^{-2}$
2.5	-0.02	0.004
0.8	0.076	0.006

The fitting parameter and the corresponding error are described in table 4.1 and the theoretical matching of experimental data in the low probe regime is depicted in the fig. (4.12).  $\chi_{3L}^{(3)}$  determined using the above analysis reasonably match with the theoretical calculation. The little discrepancy appears mainly due to the non-zero contribution of higher order terms. A number of data points below 1 MHz may give a better measurement for  $\chi_{3L}^{(3)}$ . Higher order non-linearity cannot be determined accurately as the series diverges very fast by increasing the probe Rabi frequency for this system.

## 4.6 Conclusion and outlook

We have demonstrated a technique based on optical heterodyne. The technique is established for the Rydberg-EIT medium. A suitable model of EIT consisting of two probes and one coupling fields is able to accurately measure the optical non-linearity (self-phase modulation) of a probe beam while propagating through the dispersive medium. The limitation of the technique due to the appearance of a dressed atomic state is discussed. The small signal due to the dressing of atomic state can be avoided by using higher frequency offset which is also prescribed. The technique can also be used to measure the cross phase modulation of the light field propagating through a highly dispersive medium. The technique can be extended to measure the optical nonlinearity of Rydberg EIT in blockade interaction regime in thermal vapor as well as in ultra-cold atoms.

We are interested to investigate Rydberg blockade interaction in the thermal atomic ensemble in EIT regime. In order to observe Rydberg interaction, one has to increase the density of the vapor. The rubidium vapor cell length we have used for the Rydberg-EIT experiment is 5 cm. In the case of EIT, the probe field satisfies single photon resonance. At high vapor density, the probe will be completely absorbed for optical path length of 5 cm. Therefore, sufficient probe light cannot be transmitted through the medium in order to perform the experimental measurement. One of the possible solutions is to use micro vapor cell where the optical path length of the probe field is in micron order. In that case, the absorption of the probe field will

be small enough to perform the experiment. Another way to get the Rydberg excitation is to satisfy two-photon resonance to the Rydberg excited state without satisfying single photon resonance by the probe. In the next chapter, we will use OHDt to detect Rydberg excited atom where the Rydberg excitation will take place via two-photon resonance. The probe field will be stabilized outside the Doppler-broadened spectrum in order to minimize the absorption.

# Bibliography

- [1] I. Friedler, D. Petrosyan, M. Fleischhauer, and G. Kurizki, Phys. Rev. A, **72**, 043803 (2005).
- [2] S. Sevincli, N. Hankel, C. Ates, and T. Pohl, Phys. Rev. Lett., **107**, 153001 (2011).
- [3] A. V. Gorshkov, J. Otterbach, M. Fleischhauer, T. Pohl, and M. D. Lukin, Phys. Rev. Lett., **107**, 133602 (2011).
- [4] J. D. Pritchard, D. Maxwell, A. Gauguier, K. J. Weatherill, M. P. A. Jones, and C. S. Adams, Phys. Rev. Lett., **105**, 193603 (2010).
- [5] V. Parigi, E. Bimbard, J. Stanojevic, A. J. Hilliard, F. Nogrette, R. Tualle-Brouri, A. Ourjoumtsev, and P. Grangier, Phys. Rev. Lett., **109**, 233602 (2012).
- [6] T. Peyronel, O. Firstenberg, Qi-Yu Liang, S. Hofferberth, A. V. Gorshkov, T. Pohl, M. D. Lukin, and V. Vuletić, Nature, **488**, 57 (2012).
- [7] O. Firstenberg, T. Peyronel, Qi-Yu Liang, A. V. Gorshkov, M. D. Lukin, and V. Vuletić, Nature, **502**, 71 (2013).
- [8] S. Baur, D. Tiarks, G. Rempe, and S. Dürr, Phys. Rev. Lett., **112**, 073901 (2014).
- [9] C. Ates, S. Sevincli, and T. Pohl, Phys. Rev. A, **83**, 041802(R) (2011).
- [10] K. J. Weatherill, J. D. Pritchard, R. P. Abel, M. G. Bason, A. K. Mohapatra, and C. S. Adams, J. Phys. B: At. Mol. Opt. Phys., **41**, 201002 (2008).
- [11] A. K. Mohapatra, M. G. Bason, B. Butscher, K. J. Weatherill and C. S. Adams, Nature Phys., **4**, 890 (2008).
- [12] H. Gorniaczyk, C. Tresp, J. Schmidt, H. Fedder, and S. Hofferberth Phys. Rev. Lett., **113**, 053601 (2014).

- [13] M. Khazali, K. Heshami, and C. Simon, *Phys. Rev. A*, **91**, 030301(R) (2015).
- [14] Y.-M. Liu, D. Yan, X.-D. Tian, C.-L. Cui, and J.-H. Wu, *Phys. Rev. A*, **89**, 033839 (2014).
- [15] C. S. Hofmann, G. Günter, H. Schempp, M. Robert-de-Saint-Vincent, M. Gärttner, J. Evers, S. Whitlock, and M. Weidemüller, *Phys. Rev. Lett.*, **110**, 203601 (2013).
- [16] T. Baluktsian, B. Huber, R. Lw, and T. Pfau, *Phys. Rev. Lett.*, **110**, 123001 (2013).
- [17] J. Han, T. Vogt, M. Manjappa, R. Guo, M. Kiffner, and W. Li, *Phys. Rev. A*, **92**, 063824 (2015).
- [18] A. K. Mohapatra, T. R. Jackson, and C. S. Adams, *Phys. Rev. Lett.*, **98**, 113003 (2007).
- [19] H. Schmidt, and A. Imamoglu, *Opt. Lett.*, **21**, 1936 (1996).
- [20] H. Wang, D. Goorskey, and M. Xiao, *Phys. Rev. Lett.*, **87**, 073601 (2001).
- [21] H. Chang, H. Wu, C. Xie, and H. Wang, *Phys. Rev. Lett.*, **93**, 213901 (2004).
- [22] S. Li, X. Yang, X. Cao, C. Zhang, C. Xie, and H. Wang, *Phys. Rev. Lett.*, **101**, 073602 (2008).
- [23] H. Kang, and Y. Zhu, *Phys. Rev. Lett.*, **91**, 093601 (2003).
- [24] H. Lo, P. Su, and Y. Chen, *Phys. Rev. A*, **81**, 053829 (2010).
- [25] W. Chen, K. M. Beck, R. Büker, M. Gullans, M. D. Lukin, H. Tanji-Suzuki, and V. Vuletić, *Science*, **341**, 768 (2013).
- [26] D. Petrosyan, J. Otterbach and M. Fleischhauer, *Phys. Rev. Lett.*, **107**, 213601 (2011).
- [27] J. Sheng, Y. Chao, S. Kumar, H. Fan, J. Sedlacek and J. P. Shaffer, *Phys. Rev. A*, **96**, 033813 (2017).
- [28] M. G. Bason, A. K. Mohapatra, K. J. Weatherill and C. S. Adams, *Phys. Rev. A*, **77**, 032305 (2008).
- [29] L. Ma, D. A. Anderson and G. Raithel, *Phys. Rev. A*, **95**, 061804(R) (2017).
- [30] J. B. Naber, A. Tauschinsky, H. B. van L. van den Heuvell and R. J. C. Spreeuw, *SciPost*, **2**, 015 (2017).

- [31] G. Müller, A. Witch, R. Rinkleff, and K. Danzmann, *Opt. Comm.*, **127**, 37 (1996).
- [32] A. M. Akulshin, A. I. Sidorov, R. J. McLean, and P. Hannaford, *J. Phys. B*, **6**, 491 (2004).
- [33] Y. Han, J. Xiao, Y. Liu, C. Zhang, H. Wang, M. Xiao, and K. Peng, *Phys. Rev. A*, **77**, 023824 (2008).
- [34] A. M. Akulshin, S. Barreiro, and A. Lezama, *Phys. Rev. Lett.*, **83**, 4277 (1999).
- [35] R. W. Boyd, *Nonlinear Optics*, 3rd ed. (Academic, New York, 2008).

# Chapter 5

## Study of two-photon Rydberg excitation using OHDT

The two-photon Rydberg excitation is experimentally studied in cold atoms [1] and also in thermal vapor [2–4]. In EIT medium, two-photon resonant process is also demonstrated to simulate coherent and dissipative quantum many-body system [5]. Using two-photon resonance to the Rydberg state, Rydberg blockade [4, 6–21] and anti-blockade [3] phenomena are studied. The application of the phenomena are to simulate quantum many-body system [21], preparation of entangled state [24] and to study quantum engineering [2, 22, 23, 25–28].

In this chapter, we will describe a process of two-photon Rydberg excitation using OHDT in a doppler broadened atomic medium. The dispersion spectrum of a probe beam due to Rydberg excitation will be measured and explained. We will also discuss the sensitivity of the Rydberg population measurement using OHDT. In this context, a comparative study of OHDT and direct absorption measurement (DAM) will also be discussed.

### 5.1 OHDT to observe two-photon Rydberg excitation

Optical heterodyne detection technique (OHDT) is used to measure dispersion of a probe laser beam while passing through an atomic medium due to two-photon resonance to the Rydberg state. Earlier, Rydberg atoms were detected by opto-galvanic detection using large linear stark effect of Rydberg atoms [33]. After development of micro-channel plate (MCP), it is conventionally used for Rydberg atom detection in cold atomic system [7, 12, 29–32, 34–37]. Though it is not trivial to put electrodes for MCP in thermal atomic vapor experiment, an electrically conducted thermal vapor cell is specially made to detect Rydberg atoms [38]. Channeltron has also used to detect Rydberg excitation [39–41]. All optical techniques are relatively easier to

detect Rydberg excited atoms in thermal vapor experiment. Previously, this kind of technique is used in EIT medium in thermal atomic vapor [?, 42] and also in microcell [43]. The technique is also used to observe cross phase modulation (XPM) of a probe and a control beam in an N system using cold atoms [44–46].

### 5.1.1 Atomic level scheme

An atomic level scheme is depicted in fig. (5.1) for Rydberg excitation via two-photon resonant process using OHDT. Two probe beams at 780 nm wavelength are generated from same laser with frequency offset  $\delta$ . The polarisation of the probes are  $\sigma^+$  and  $\sigma^-$  respectively. The probe laser couples the states  $|g\rangle$  ( $5s_{1/2}$ ) and  $|e\rangle$  ( $5p_{3/2}$ ). A coupling laser of the wavelength 480 nm of  $\sigma^+$  polarisation is introduced to couple  $|e\rangle$  ( $5p_{3/2}$ ) to  $|r\rangle$  ( $ns_{1/2}$ ).

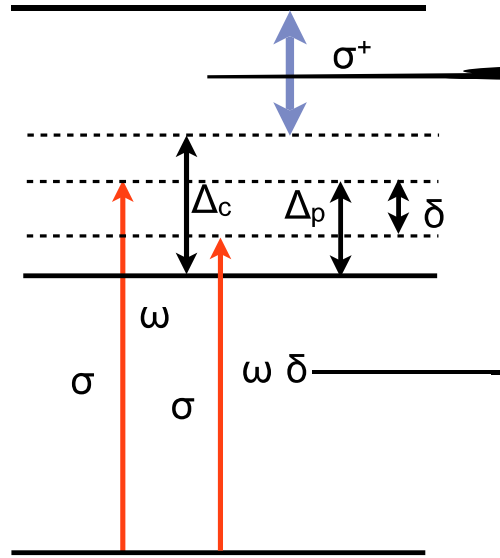


Figure 5.1: Energy level diagram for two-photon transition to the Rydberg state. Two probe beams with  $\sigma^+$  and  $\sigma^-$  polarizations couple the transition  $5s_{1/2}$ ,  $F=3$  ( $|g\rangle$ )  $\rightarrow$   $5p_{3/2}$  ( $|e\rangle$ ) of  $^{85}\text{Rb}$ . The coupling laser with  $\sigma^+$  polarization couples the transition  $5p_{3/2}$  ( $|e\rangle$ )  $\rightarrow$   $ns_{1/2}$  ( $|r\rangle$ ). The probe detuning is  $\Delta_p$  and frequency offset between the probe beams is  $\delta$ .

Since the two-photon process happens from  $5s_{1/2}$  to  $ns_{1/2}$ , only one of the probes will contribute. The net transfer of angular momentum has to be zero in order to satisfy angular momentum conservation for the two-photon process. Therefore, only  $\sigma^-$  probe laser along with  $\sigma^+$  coupling laser couple the two-photon transition to the Rydberg state and  $\sigma^+$  will not participate in two-photon process but serves as a reference beam for OHDT.

### 5.1.2 AOM setup to generate OHDT probes

The heterodyne probe and reference beams are generated from same external cavity diode laser (ECDL) and a frequency offset is introduced by an acousto optic modulator (AOM).

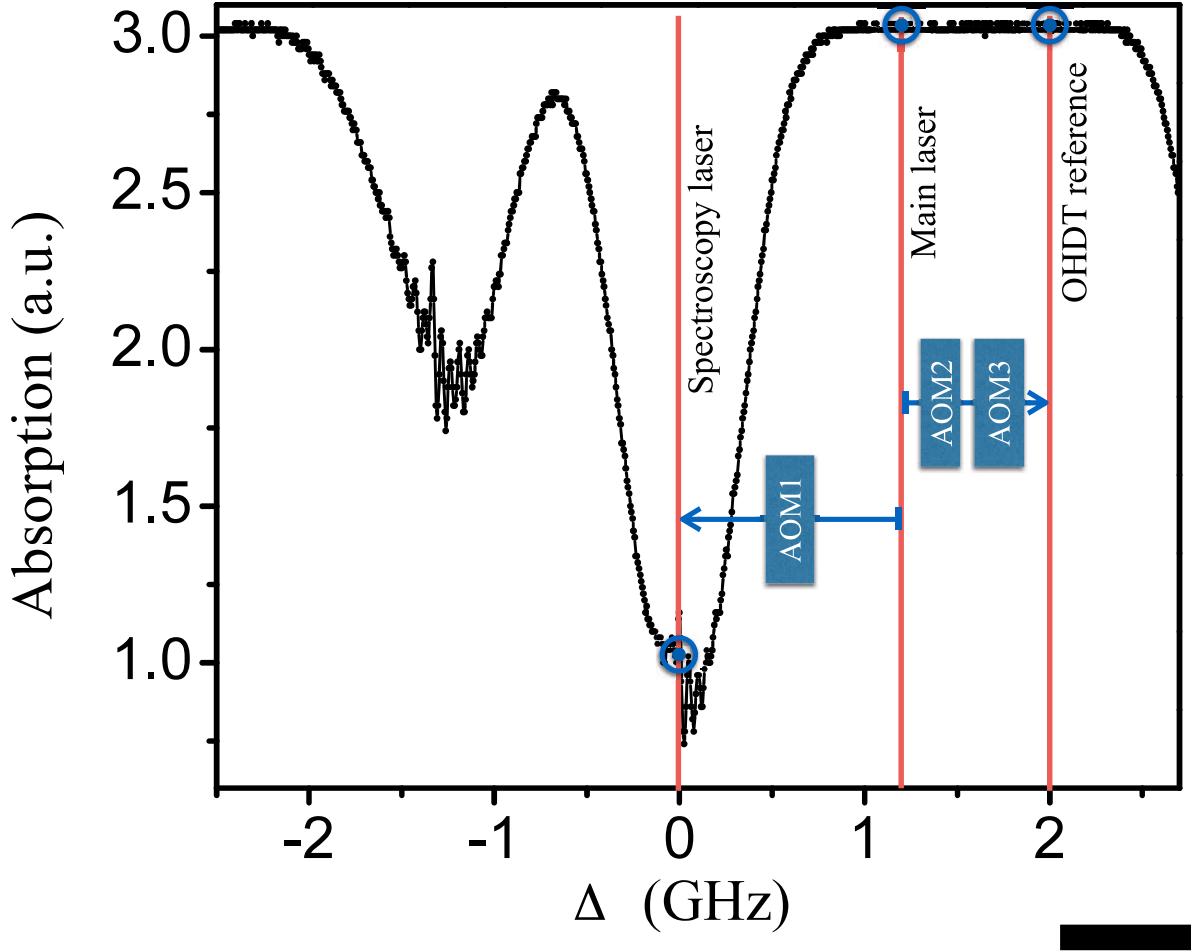


Figure 5.2: Saturation absorption spectroscopic (SAS) lines representing the stabilisation frequencies of the probe and the reference laser. The main laser is used as the probe in heterodyne experiment. The laser for spectroscopy is generated using AOM1 and the heterodyne reference is generated by using AOM2 and AOM3.

The main laser is 1.3 GHz blue shifted from the locking point as shown in fig. (5.2). The frequency shifting is done by using AOM1 (Brimrose: GPF-1500-1000-795) as shown in fig. (5.3). The frequency stabilisation of the laser is done by using saturation absorption spectroscopy (SAS). The main laser is shifted towards blue detuned side by 800 MHz by sequentially using AOM2 and AOM3 (Intraaction: ATM-2001A2) in double pass configuration which is also shown in fig. (5.2). The AOM2 and AOM3 shift the frequency of light by 200 MHz for single pass configuration. Here, AOMs are used in double pass configuration in order



to shift the frequency of light by 400 MHz by each one.

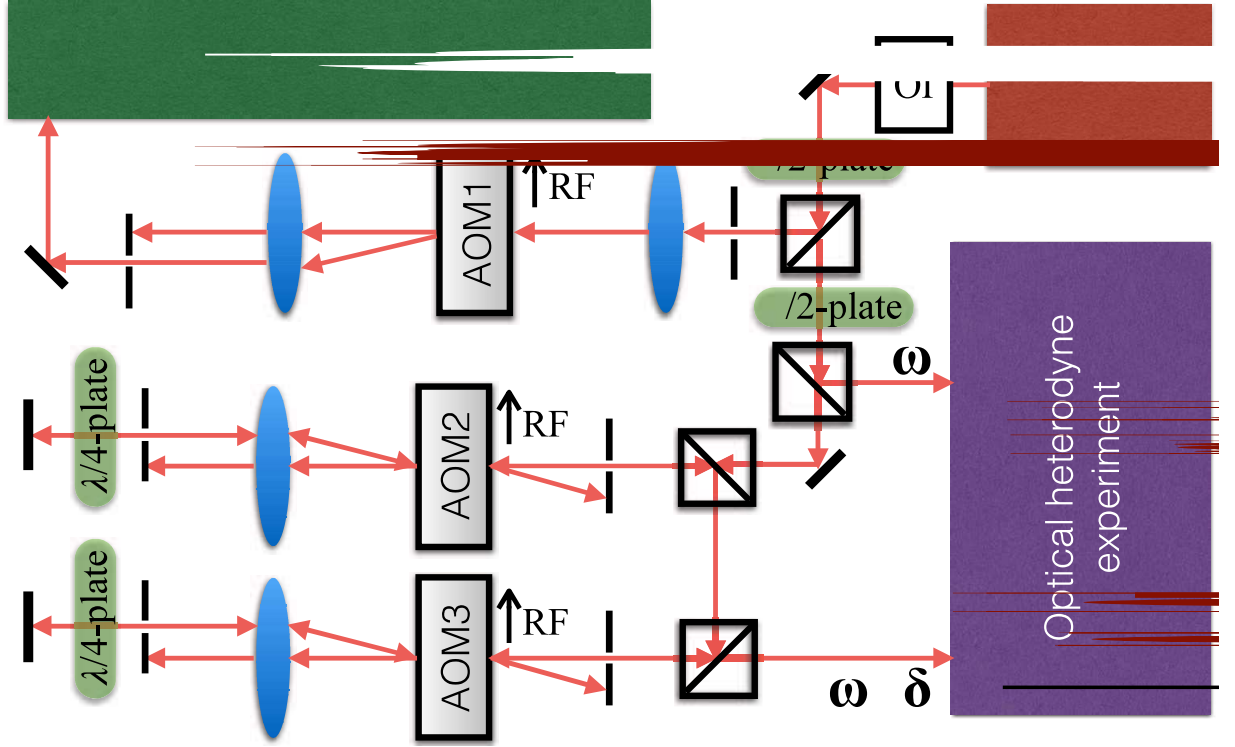


Figure 5.3: AOM setup for the generation of reference and probe beam for OHDT two-photon Rydberg excitation experiment. The spectroscopy laser is generated while main laser passes through single pass AOM1. The OHDT reference is generated while main laser passes through double pass AOM2 and double pass AOM3 setup.

The main beam is used as probe and the 800 MHz shifted light is considered as reference for the OHDT experiment of two-photon resonance to the Rydberg excited state. These two beams are taken to the OHDT experiment.

### 5.1.3 Experimental realisation of two-photon Rydberg excitation

The schematic experimental setup for two-photon Rydberg excitation using OHDT is depicted in fig. (5.4). The probe and reference beams derived from the AOM setup are superposed by a polarising beam splitter (PBS). One part of the superposed beam is detected using a detector (MenloSystems: FPD 310-FV) after passing through the OPS. The interference signal detected by the detector serves as a reference to the OHDT. The other part of the superimposed beam is passed through a  $\frac{\lambda}{4}$ -plate in order to prepare a pair of  $\sigma^+$  and  $\sigma^-$  probe and reference beams. A coupling laser of 480 nm is generated from TA-SHG-Pro and the polarisation is made to be  $\sigma^+$ . Using a dichroic mirror, the coupling beam is overlapped and counter propagated to the

superposed 780 nm lights in a magnetically shielded and temperature controlled rubidium vapor cell. The vapor cell is heated by resistive heater (Thorlab: HT15W) and a sensor (Thorlab: TH10K) is used to measure the temperature of the cell. A PID controller (Thorlab: TC200) is used to stabilise the vapor cell at desired temperature.

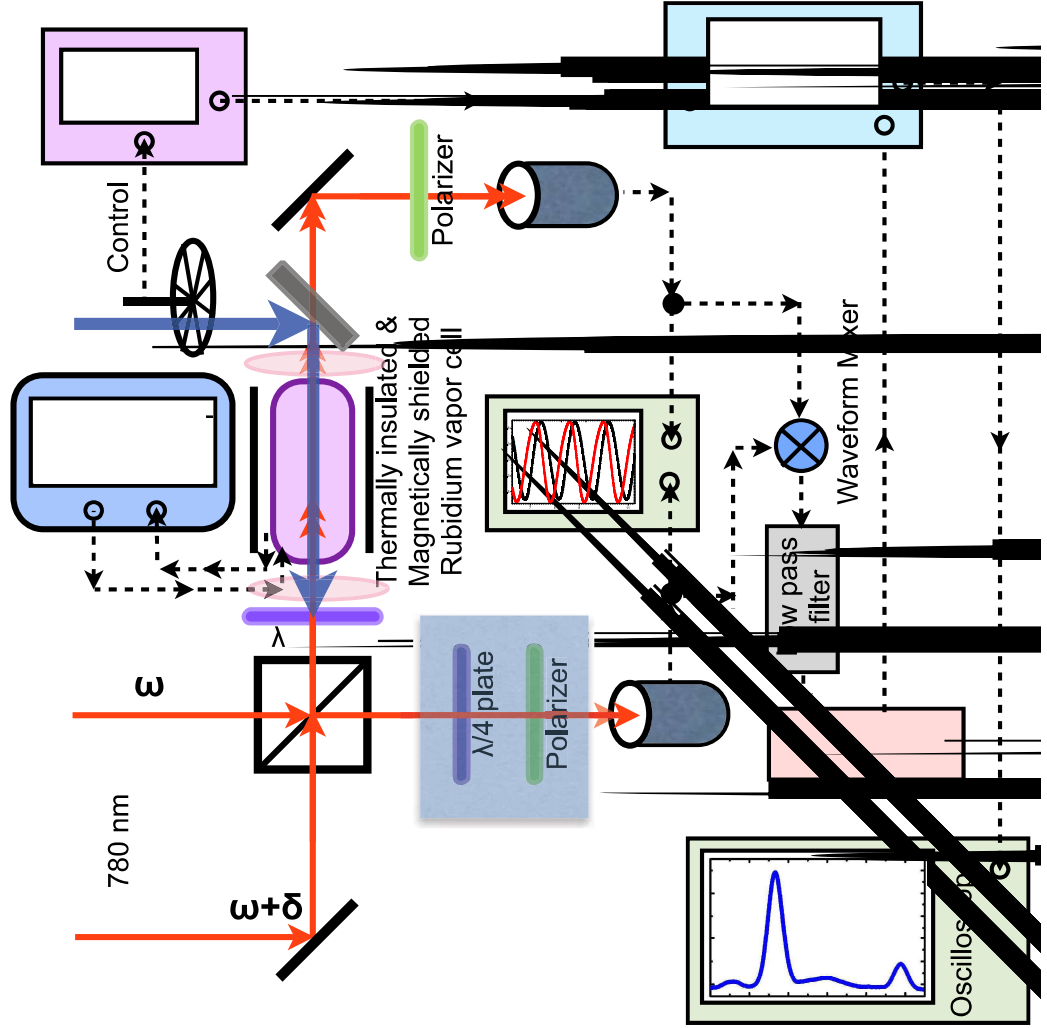


Figure 5.4: Schematic of the experimental set up for two-photon Rydberg excitation using OHDT. The red and blue arrow-lines are 780 nm and 480 nm laser. The dashed lines signify the electrical flow of signal. The density is controlled by using a resistive heater and thermal sensor. They are connected to an external PID temperature controller. The signal to noise ration of the dispersion spectra is very small. In order to improve the signal to noise ration a Lock-in detection is done by using intensity modulation of the blue laser. The intensity modulation is done by using a beam chopper.

After passing through the vapor cell, the superimposed probe and reference beams are transmitted through the dichroic mirror and a polariser is introduced before the detector (MenloSystems: FPD 310-FV) to observe the beat signal. It is to be noted that the probe and reference

beams (780 nm) gets transmitted through the dichroic mirror and the coupling laser of 480 nm gets reflected from the dichroic mirror. The electronic beat signals are monitored by an oscilloscope in order to keep track of their relative phase. The output of the detectors are multiplied by an electronic wave-form mixer (MiniCircuit: ZLW-2H+) and passes through a low pass filter (MiniCircuit: BLP-1.9+) which essentially measures the difference in phase shift between the probe and the reference beam due to the dispersive medium.

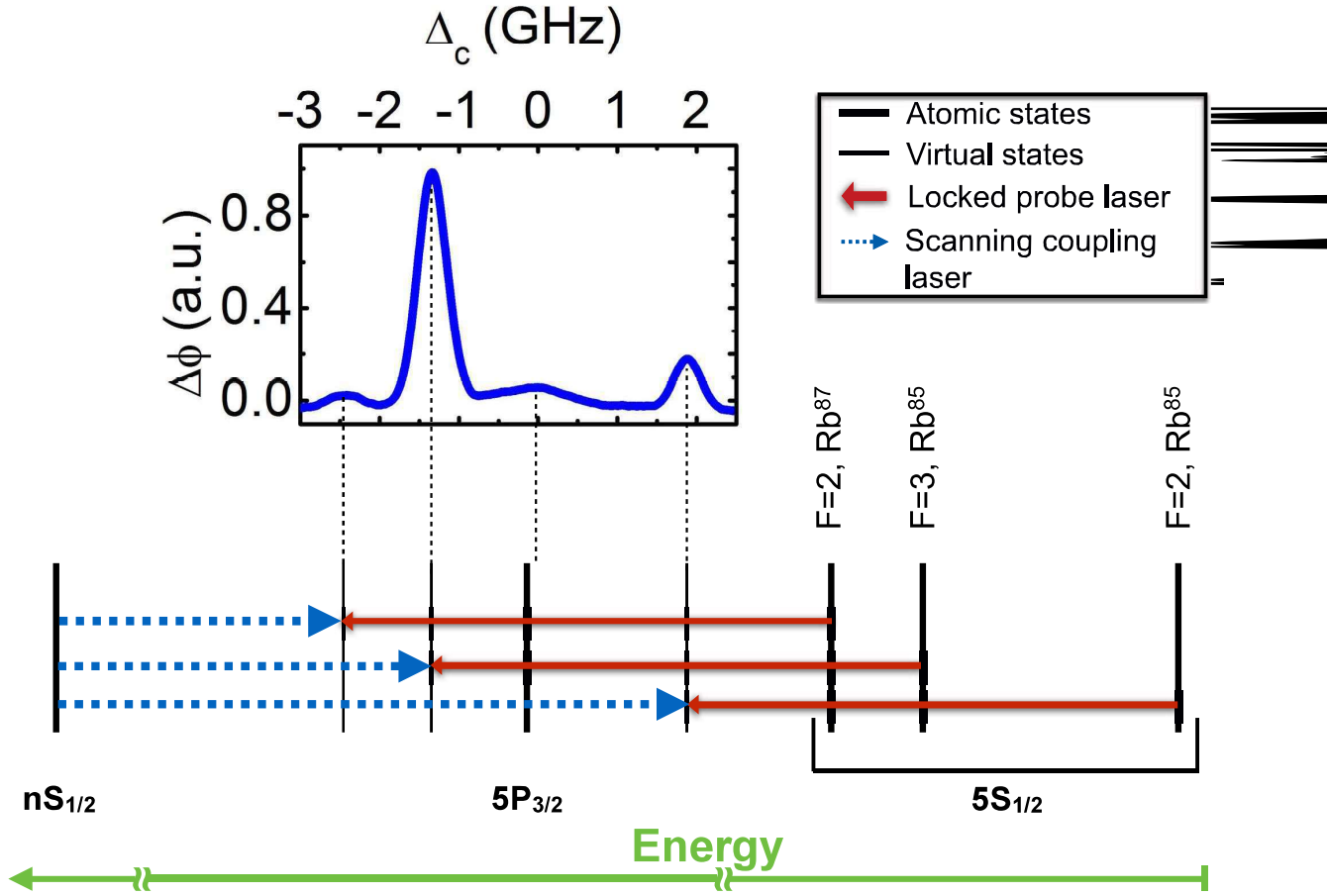


Figure 5.5: Typical dispersion spectrum of a probe beam due to two-photon resonance to the Rydberg state. The spectrum is observed by scanning the coupling over 5 GHz. The induced phase shift in probe is measured due to two-photon coupling to the Rydberg state with principal quantum number  $n = 33$ . The coupling and the probe Rabi frequencies are taken as 24 MHz and 400 MHz respectively. The peaks corresponding to the transitions  $^{85}\text{Rb } 5s_{1/2}(F = 2, 3) \rightarrow 5p_{3/2}$  and  $^{87}\text{Rb } 5s_{1/2}(F = 3) \rightarrow 5p_{3/2}$  are depicted here. The relevant energy levels of rubidium and respective dispersion peaks are depicted.

In order to improve the signal to noise ratio, a mechanical chopper is used to modulate the intensity of the coupling beam at a rate of 6 kHz. A similar electronic signal is generated from the chopper controller which is used as the reference to the lock-in amplifier. The output

of the Lock-in amplifier is monitored using an oscilloscope to measure the phase shift due to two-photon excitation to the Rydberg state. The signal of the wave-form mixer also depends on the amplitude of the beat signals. During the adjustment of the relative phase between two beat signals using OPS, the amplitude may change. In order to compensate the variation, we have used RF-attenuator (MiniCircuti: ZX73-2500-S+) right after each of the detectors (the attenuators are not shown in main setup fig. (5.4)).

The coupling and the probe beams were focused inside the cell using lenses of focal-length 200 mm. The Rayleigh range and minimum beam waist of the coupling laser are given by 12 mm and  $35 \mu\text{m}$  respectively. Also, the Rayleigh range and minimum beam waist of the probe laser are given by 10 mm and  $50 \mu\text{m}$  respectively. The variation of the probe and the coupling Rabi frequencies over the Rayleigh profile can be expressed as,  $\Omega_p(z) = \frac{\Omega_{p0}}{\sqrt{1+(\frac{z}{z_R})^2}}$  and  $\Omega_c(z) = \frac{\Omega_{c0}}{\sqrt{1+(\frac{z}{z_R})^2}}$  respectively. Here,  $\Omega_{p0}$  and  $\Omega_{c0}$  are the peak probe and the peak coupling Rabi frequencies calculated at the center of the Rayleigh profile. The accumulated phase-shift due to the dispersion experienced by the probe laser field is the average effect of the individual Rayleigh profiles of the probe and the coupling Rabi frequencies inside the rubidium vapor cell.

A typical dispersion spectrum is depicted in the fig. (5.5). All the transitions are explained in the figure caption. It is to be noted that the spectral shape of the dispersion looks like absorptive. In order to understand the nature of the dispersion spectrum, a model is developed as follows.

## 5.2 Model for two-photon Rydberg excitation

Let us consider a three-level system with a probe and a coupling laser beam. The Hamiltonian of the system in a suitable rotating frame is given by,  $H = -\frac{\hbar}{2}[(\Omega_p|e\rangle\langle g| + \Omega_c|r\rangle\langle e|) + h.c.] - \hbar[(\Delta_p - k_p v)|e\rangle\langle e| + (\Delta_2 + \Delta k v)|r\rangle\langle r|]$ , where  $\Delta k = k_c - k_p$ . Here the probe and the coupling Rabi frequencies are defined as,  $\Omega_p = \frac{2\mu_{eg}\varepsilon_p}{\hbar}$  and  $\Omega_c = \frac{2\mu_{re}\varepsilon_c}{\hbar}$  respectively.  $\varepsilon_p$  and  $\varepsilon_c$  are the probe and coupling electric field amplitudes respectively. The probe and coupling detunings are given by,  $\Delta_p$  and  $\Delta_c$  respectively. The schematic level diagram is the same as fig. (5.1). The density matrix equation of the system can be given by,  $\dot{\rho} = -\frac{i}{\hbar}[H, \rho] + L_D(\rho)$ . The Lindblad operator and the optical Bloch equations (OBE) for cold atoms in the steady state is given in Sec. 3.2.5. For the thermal atoms, Doppler shifts in the detuning are included as,  $\Delta_p \rightarrow \Delta_p - k_p v$ ,  $\Delta_c \rightarrow \Delta_c + k_c v$  and  $\Delta_2 \rightarrow \Delta_2 + \Delta k v$  in the Eq. (3.17, 3.18, 3.19, 3.20 &

3.21). Here  $v$  is the velocity of the atom interacting with both the laser fields. The steady state OBEs for the thermal atoms are given by,

$$\frac{i}{2}(\Omega_p \rho_{eg} - \Omega_p^* \rho_{ge}) + \Gamma_{eg} \rho_{ee} + \Gamma_{rg} \rho_{rr} = 0 \quad (5.1)$$

$$\frac{i}{2}[\Omega_p(2\rho_{ee} + \rho_{rr}) - \Omega_p - (\Omega_c^* \rho_{gr} + 2(\Delta_p - k_p v) \rho_{ge})] - \frac{\Gamma_{eg}}{2} \rho_{ge} = 0 \quad (5.2)$$

$$\frac{i}{2}[\Omega_p \rho_{er} - \Omega_c \rho_{ge} - 2\delta \rho_{gr}] - \frac{1}{2}(\Gamma_{re} + \Gamma_{rg}) \rho_{gr} = 0 \quad (5.3)$$

$$\frac{i}{2}(\Omega_c^* \rho_{er} - \Omega_c \rho_{re}) - (\Gamma_{re} + \Gamma_{rg}) \rho_{rr} = 0 \quad (5.4)$$

$$\frac{i}{2}[\Omega_p^* \rho_{gr} + \Omega_c(\rho_{rr} - \rho_{ee}) - 2(\Delta_c + k_c v) \rho_{er}] - \frac{1}{2}(\Gamma_{eg} + \Gamma_{re} + \Gamma_{rg}) \rho_{er} = 0 \quad (5.5)$$

The dephasing rate  $\Gamma_{eg}$  is the natural line-width of  $5s_{1/2} \rightarrow 5p_{3/2}$  transition of rubidium which is  $2\pi \times 6$  MHz. The decay rate  $\Gamma_{re}$  is taken to be  $2\pi \times 0.01$  MHz, which is the natural line width of the Rydberg state. The dipole matrix element of the states  $|g\rangle$  and  $|r\rangle$  dephases at the rate  $\frac{\Gamma_{rg}}{2} + \gamma_{rel}$ .  $\Gamma_{rg}$  is due to the transit time decay of atoms and  $\gamma_{rel}$  is the relative laser frequency noise between the probe and the coupling laser. Here, both the decay rates are of the order of  $2\pi \times 500$  kHz. The susceptibility of the probe field is proportional to the density matrix element  $\rho_{eg}$ . The dispersion of the probe field which is proportional to the  $\Re(\rho_{eg})$  can be obtained from Eq. (5.1) and (5.2) as,

$$\begin{aligned} \Re(\rho_{eg}) &= -\frac{\Omega_p}{2(\Delta_p - k_p v)} + \frac{\Omega_p}{2(\Delta_p - k_p v)} \rho_{rr} - \frac{\Omega_c}{2(\Delta_p - k_p v)} \Re(\rho_{rg}) \\ &+ \frac{\Gamma_{eg} \Gamma_{rg}}{2\Omega_p(\Delta_p - k_p v)} \rho_{rr} \end{aligned} \quad (5.6)$$

$$\Im(\rho_{eg}) = \frac{\Gamma_{rg}}{\Omega_p} \rho_{rr} \quad (5.7)$$

The probe laser is 1.3 GHz detuned from intermediate state. Therefore, it will stay unpopulated which allows us to remove the state adiabatically as explained in Sec. 3.2.6 and Sec. 3.2.7. The optical Bloch equation for the effective 2-level system is given by,

$$\dot{\rho}_{gg} = -i(\Omega_{eff} \rho_{gr} - \Omega_{eff}^* \rho_{rg}) + \Gamma_{rg} \rho_{rr} \quad (5.8)$$

$$\dot{\rho}_{rg} = -i(\Delta_{eff} \rho_{rg} + \Omega_{eff}(2\rho_{rr} - 1)) - \frac{\Gamma_{rg}}{2} \rho_{rg} \quad (5.9)$$

Here the effective Rabi frequency and the effective detuning are respectively defined as,  $\Omega_{eff} = \frac{\Omega_p \Omega_c}{[\Delta_p - \Delta_c - (k_p + k_c)v]}$  and  $\Delta_{eff} = 2(\Delta_p + \Delta_c) + 2\Delta k v + \frac{|\Omega_p|^2 - |\Omega_c|^2}{[\Delta_p - \Delta_c - (k_p + k_c)v]}$ . By solving Eq. (5.8) and Eq. (5.9), we get  $\Re(\rho_{rg}) = \frac{2\Delta_{eff}}{\Omega_{eff}} \rho_{rr}$ . The Rydberg population  $\rho_{rr}$  is given by,

$$\rho_{rr} = \frac{\Omega_{eff}}{\Delta_{eff} + 2\Omega_{eff}^2 + \Gamma_{rg}^2} \quad (5.10)$$

Therefore, the  $\rho_{rr}$  and  $\Re(\rho_{rg})$  calculated from effective two-level system can be used to evaluate  $\Re(\rho_{eg})$  and  $\Im(\rho_{eg})$  by using Eq. (5.6) and Eq. (5.7) respectively.

### 5.2.1 Calculation of susceptibility

Let us consider that  $\chi$  is the susceptibility of the probe. The refractive index of the probe can be written as,  $n = 1 + \frac{1}{2}\Re(\chi)$ , by considering  $\chi$  to be small. The susceptibility is related to  $\rho_{eg}$  as,  $\chi = \frac{2n_0|\mu_{eg}|^2}{\epsilon_0\hbar\Omega_p}\rho_{eg}$ . The total susceptibility is expressed as,  $\chi = \chi_{2L} + \chi_{3L}$ . The susceptibility  $\chi_{2L}$  is due to the interaction of the probe laser with the transition  $5s_{1/2} \rightarrow 5p_{3/2}$  in the absence of the coupling laser. In the presence of the coupling laser, the interaction of the probe laser with the transition  $5s_{1/2} \rightarrow ns_{1/2}$  via two-photon process gives the susceptibility  $\chi_{3L}$ .

The first term of Eq. (5.6) is the contribution due to the coupling of the probe with the transition  $|g\rangle(5s_{1/2}) \rightarrow |e\rangle(5p_{3/2})$ . Therefore, we can define as  $\Re(\rho_{eg}^{(2L)}) = -\frac{\Omega_p}{2(\Delta_p - k_p v)}$ . Due to large probe detuning  $\Delta_p - k_p v \gg \Gamma_{eg}, \Gamma_{rg}$  and in the regime,  $\Omega_p \gg \Gamma_{eg}$ , we can neglect the last term of the Eq. (5.6). Then, the Eq. (5.6) takes the form,

$$\Re(\rho_{eg}^{(3L)}) = \frac{1}{2(\Delta_p - k_p v)}[\Omega_p \rho_{rr} - \Omega_c \Re(\rho_{rg})] \quad (5.11)$$

$\Re(\rho_{eg}^{(3L)})$  is the contribution only due to the of the probe participating in two-photon resonance in presence of coupling laser. The Doppler averaged susceptibility of the probe due to two-photon resonance is given by,

$$\chi_{3L} = \frac{2n_0|\mu_{eg}|^2}{\epsilon_0\hbar\Omega_p} \frac{1}{\sqrt{\pi}v_p} \int_{-\infty}^{\infty} \rho_{eg}^{(3L)} e^{-\frac{v^2}{v_p^2}} dv \quad (5.12)$$

Here,  $n_0$  is the density of the vapor and  $\mu_{eg}$  is the dipole coupling strength for the transition  $|g\rangle(5s_{1/2}) \rightarrow |e\rangle(5p_{3/2})$ .

### 5.2.2 Lineshape of dispersion

As we have mentioned earlier, OHDT is only sensitive to the probe dispersion due to the two-photon transition  $5s_{1/2} \rightarrow ns_{1/2}$ . The measure phase shift due to the change in refractive index of the probe due to two-photon process is proportional to  $\Re(\chi_{3L})$ . The comparison between the experimental data and the model is depicted in fig. (5.6). In the experiment, the probe and the coupling laser were focussed inside the atomic medium by using a pair of lenses. Therefore, the probe and the coupling laser has Rayleigh profile inside the medium and hence the Rabi frequencies of the respective lasers follow the same. The peak coupling Rabi frequency is kept

fixed at 24 MHz. The model matches with the profiles for peak probe Rabi frequencies  $\Omega_p = 60$  MHz (fig. (5.6)a) and  $\Omega_p = 400$  MHz (fig. (5.6)b). For fig. (5.6), the density is kept constant at  $2.5 \times 10^{12} \text{ cm}^{-3}$ . The data is taken for the principal quantum number of the Rydberg state  $n = 33$ .

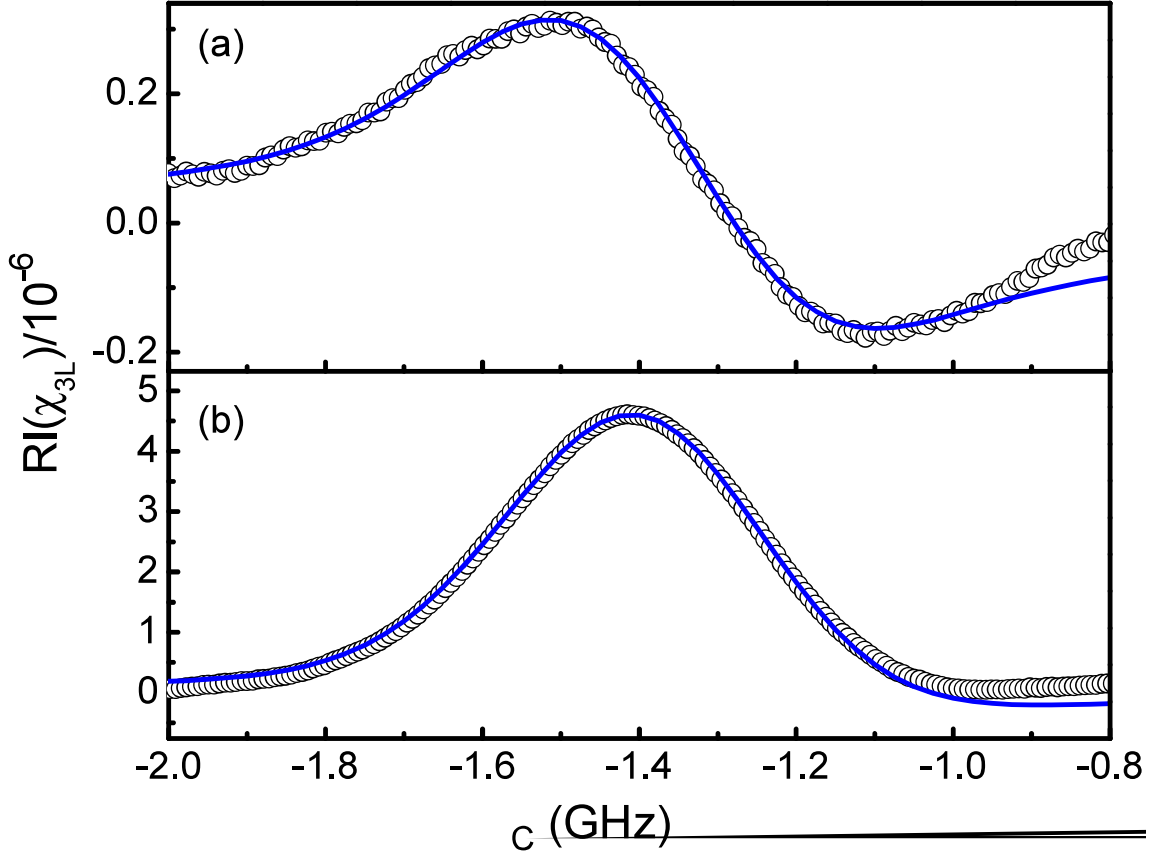


Figure 5.6: (a) Refractive index of the signal probe beam propagating through the medium with coupling scanning over the two-photon resonance. The peak Rabi frequencies of the coupling beam was 24 MHz and of the probe was 60 MHz (a) and 400 MHz (b). The lasers are coupled to the Rydberg state with principal quantum number,  $n = 33$ . Open circles ( $\circ$ ) are the refractive index measured in the experiment, solid circles ( $\bullet$ ) are the calculated refractive index using the exact model of a three-level atom interacting with a probe and a coupling beams. Solid lines are the calculated refractive index using an approximate model by considering the three-level atom as an effective 2-level atom. A multiplication factor accounted for the overall gain in the experimental data was used to compare with theory. The refractive index due to the interaction of the probe with the D2 line ( $\chi_{2L}$ ) is subtracted to show the effect of the two-photon resonance only.

It is observed from the fig. (5.6) that, at the low probe Rabi frequency, the refractive index line-shape looks perfect dispersive whereas, at the higher probe Rabi frequency, the line-shape looks more like absorptive but it is actually a dispersion spectrum. Since the model calculation

matches with the profile in both the regime, hence the above argument is also supported by the model presented. Referring to Eq. 5.12,  $\Re(\rho_{eg})$  contributing to dispersion has a centre  $\rho_{rr}$  and  $\rho_{gr}$ .

In fig. (5.6), it is observed that the dispersion curves deviate from the model at low coupling detuning regime. The reason behind the mismatch is the presence of the dark state near the resonance.

### 5.3 Intensity dependent dispersion

In order to study the intensity dependent dispersion, we kept peak coupling Rabi frequency fixed at  $\Omega_c = 24$  MHz and dispersion peak height is measured by varying the peak probe Rabi frequency up-to 600 MHz. The spectral peak heights are normalised by the spectral height corresponding to the lowest peak probe Rabi frequency of the experiment (100 MHz). The study is done for the densities  $2.5 \times 10^{12} \text{ cm}^{-3}$ ,  $1.25 \times 10^{13} \text{ cm}^{-3}$  and  $3.0 \times 10^{13} \text{ cm}^{-3}$ . The normalised peak height as a function of peak probe Rabi frequency for all the above densities are depicted in fig. (5.7a). The theory generated profile also matches well for each densities.



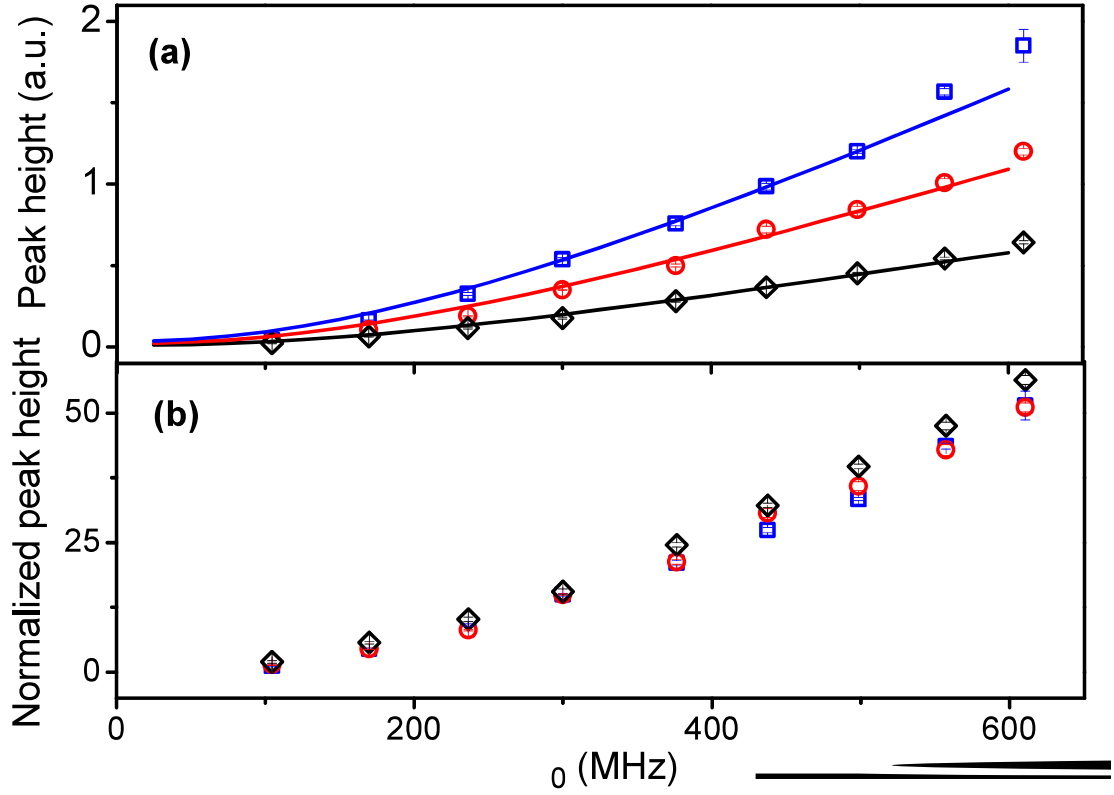


Figure 5.7: (a) Measured dispersion peak height as a function of peak Rabi frequency of probe while coupling to the Rydberg state  $n = 33$  with atomic vapor densities  $2.5 \times 10^{12} \text{ cm}^{-3}$  ( $\diamond$ ),  $1.25 \times 10^{13} \text{ cm}^{-3}$  ( $\circ$ ) and  $3.0 \times 10^{13} \text{ cm}^{-3}$  ( $\square$ ). The peak Rabi frequency of the coupling beam was 13.8 MHz. The solid lines are the fitting using the theoretical model and a multiplication factor is used as the only fitting parameter which can be accounted for the overall gain in the experiment. (b) Dispersion peak height normalized to the peak height of a weak probe beam.

From Eq. (5.12),  $\frac{\Re(\chi_{3L})}{2n_0} = \frac{|\mu_{eg}|^2}{\epsilon_0 \hbar \Omega_p} \frac{1}{\sqrt{\pi} v_p} \int_{-\infty}^{\infty} \Re(\rho_{eg}^{(3L)}) e^{-\frac{v^2}{v_p^2}} dv$ , which is independent of the density  $n_0$ . In the experiment, the dispersion data for each density is normalised by the low probe dispersion of the respective density. Due to the normalisation by low probe dispersion, the density dependence in the dispersion is cancelled as the dispersion linearly varies with density. Therefore, the curves of intensity dependent refractive index for the individual densities should be superposed. As we can see in fig. (5.7b), the experimental data for all densities are superposed with less than 5% error. The observation suggest that the interaction plays a negligible role in this regime of the experiment.

## 5.4 Calibration of phase sensitivity of the electronic waveform mixer

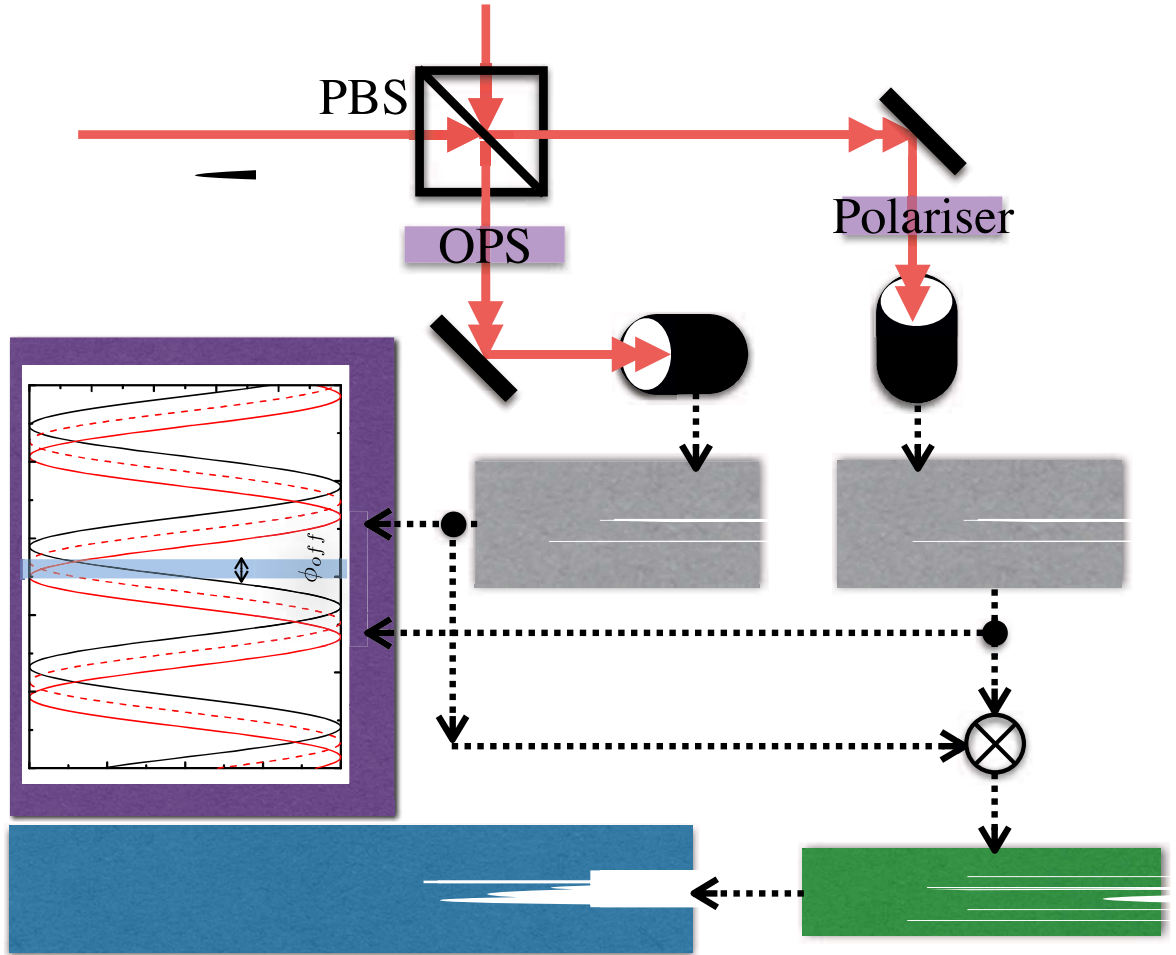


Figure 5.8: Setup for calibration of phase measurement of electronic waveform mixer.

It is required to calibrate the wave-form mixer (MiniCircuit ZLW-2H+) in our experiment to determine the absolute measurement of the nonlinear phase acquired by the probe in the OHDT measurement. In order to do the measurement, we did heterodyne experiment without the atomic medium. The optical and the electronic set up is depicted in the fig. (5.8). Two laser field with frequency offset  $\delta$  superposed on a PBS. One part of superposed beam is passes through the OPS and detected by a FPD and another part of the superposed beam passes through the polariser and is detected by another FPD. The OPS is used to control the relative phase ( $\phi_{off}$ ) between the beat signals detected by the detectors. These two electronic beat signals are monitored by an oscilloscope and the relative phase between the beam is measured from the oscilloscope as shown in fig. (5.8). The electronic beat signals are multiplied by the wave-

form mixer (MiniCircuit ZLW-2H+) and made to pass through a low pass filter (MiniCircuit: BLP-1.9+) which allows only dc signal. The dc signal is monitored by an oscilloscope.

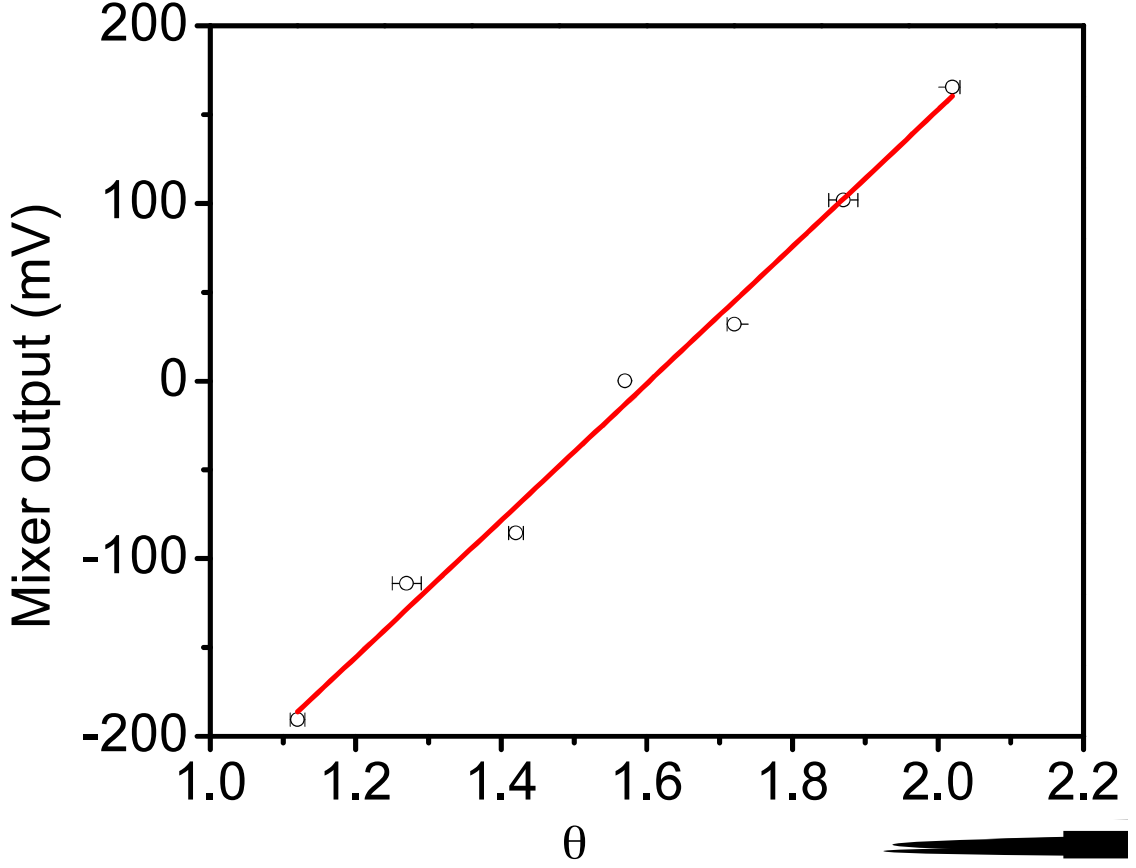


Figure 5.9: Calibration of phase sensitivity of wave-form mixer. The experimental data is linear fitted with the equation  $V = \eta_m \times \theta + V_0$ .

Since the phase sensitivity of the mixer depends on the beat amplitude, both the beat amplitudes are kept constant approximately at 800 mV. The relative phase between the probe and the reference is changed from  $-\frac{\pi}{7}$  radian to  $+\frac{\pi}{7}$  radian with approximately 0.1 radian interval and the dc shift is measured in the oscilloscope. The variation of the phase is done where the phase difference between two beat signals is  $\frac{\pi}{2}$  which is the phase sensitive regime of the experiment.

In order to explain the above statement let us consider the form of the beat signal measured in both the detectors are  $S_1 = A_1 \cos(\omega t)$  and  $S_2 = A_2 \cos(\omega t + \phi_0)$  respectively. After multiplying  $S_1$  and  $S_2$  using an waveform mixer, it passes through a low pass filter to give the signal of the form  $\frac{A_1 A_2}{2} \cos(\phi_0)$ . We know that at  $\phi_0 = \frac{\pi}{2}$ ,  $\cos(\phi_0) = 0$ . In this regime, it becomes most sensitive to phase. That is why the phase sensitivity measurement is done for  $\phi_0 = \frac{\pi}{2}$  with small range of variation from  $-\frac{\pi}{7}$  to  $+\frac{\pi}{7}$ .

During the change of the relative phase between the probe and the reference beam, the beat amplitudes and the relative phase between the beats is changed. The relative phase kept same by adjusting OPS and the amplitudes are kept constant by using the RF-attenuator (MiniCircuit: ZX73-2500-S+) connected at the output of the each detector as shown in fig. (5.8). The calibration curve is shown in fig. (5.9).

The fitting parameters are given by,  $V_0 = -617 \pm 25$  mV and  $\eta_m = 385 \pm 16$  mV/rad. Therefore, the phase sensitivity of the wave-form mixer is found to be 385 mV/rad with beat amplitudes to be 800 mV each. It is to be noted that the mixer sensitivity also includes the gain of the mixer and the low pass filter.

## 5.5 Sensitivity and the precision of the measurement

In OHDT experiment for two-photon Rydberg excitation, the lock-in amplifier is used to improve signal to noise ratio. Therefore, the mixer sensitivity along with the gain of the Lock-in amplifier can be represented by the block diagram as shown in fig. (6.7).

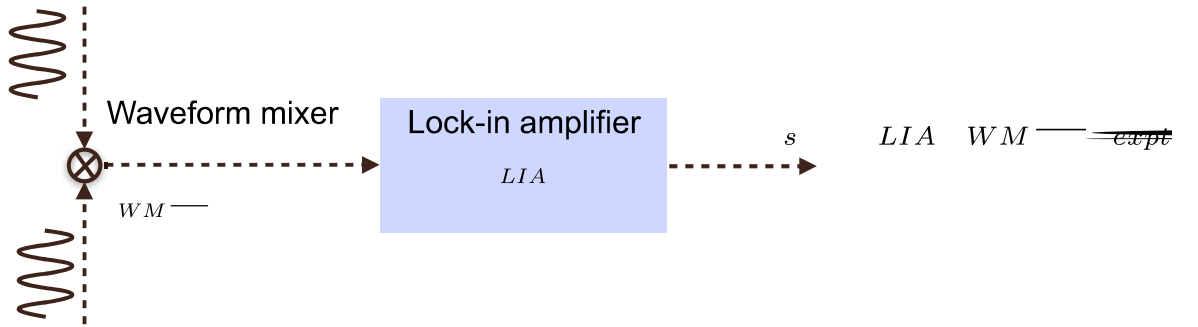


Figure 5.10: Schematic block diagram of electronic operation of beat signals. The objective of the setup to measure the relative phase shift between two incoming electronic beat signals. The incoming beat signals are multiplied by an electronic waveform mixer and the phase-shift information is extracted. Then the signal for the phase shift is amplified using lock-in amplifier.

The mixer sensitivity is found to be  $\eta_m = A_{WM} \frac{d\phi}{dV} = 385$  mV/rad. The lock-in amplifier (Stanford Research Systems: SR830) output voltage can be calculated as,  $V_{o,LIA} = (\frac{V_{in}}{Sensitivity} - offset) \times Expand \times 10$  V, where  $V_{in}$  represents the input voltage to the lock-in amplifier. In the experiment, the lock-in sensitivity is set to 10 mV, the offset is set to 0 V and the expand is set to 1. Therefore,  $V_{o,LIA} = 10^3 \times V_{in} = A_{LIA} V_{in}$ . The lock-in amplifier gain is found to be  $A_{LIA} = 10^3$ . Therefore, the phase shift measured in the experiment can

be represented as,  $\phi_s = \frac{V_o}{\eta_m A_{LIA}}$ , where  $V_o$  is the output dc voltage of the experiment which is measured in the oscilloscope as shown in fig. (5.8). Using this equation, the experimentally measured voltage is converted to phase as shown in fig. (5.11b).

The phase shift ( $\phi_s$ ) due to the two-photon process measured using the heterodyne detection technique is related to the susceptibility  $\Re(\chi_{3L}) = \frac{2\phi_s}{k_p l}$ , where  $l$  length of the rubidium vapor cell. Therefore the phase shift can be calculated from the model using Eq. (5.12) as,

$$\phi_s = \frac{k_p l}{\sqrt{\pi} v_p} \frac{n_0 |\mu_{eg}|^2}{\epsilon_0 \hbar \Omega_p} \int_{-\infty}^{\infty} \Re(\rho_{eg}^{(3L)}) e^{-\frac{v^2}{v_p^2}} dv \quad (5.13)$$

We have measured the phase shift at the peak of the dispersion profile which corresponds to the zero velocity class of atoms. Therefore, the probe and the coupling lasers are resonantly interacting with the zero velocity class of atoms. At the two-photon resonance, the two-photon detuning  $\Delta_{eff}$  will vanish and hence  $\Re(\rho_{rg}) = \frac{2\Delta_{eff}}{\Omega_{eff}} \rho_{rr} = 0$ . Then  $\Re(\rho_{eg}^{(3L)}) = \frac{\Omega_p}{2\Delta_p} \rho_{rr}$  for zero velocity class of atoms. In that case, Eq. (5.13) and (5.12) will respectively have the form,

$$\phi_s = \frac{k_p l}{\sqrt{\pi} v_p} \frac{n_0 |\mu_{eg}|^2}{\epsilon_0 \hbar} \frac{\Omega_{eff}}{2\Delta k \Delta_p} \rho_{rr} \quad (5.14)$$

$$\Re(\chi_{3L}) = \frac{n_0 |\mu_{eg}|^2}{\epsilon_0 \hbar} \frac{\Omega_{eff}}{\sqrt{\pi} v_p \Delta k \Delta_p} \rho_{rr} \quad (5.15)$$

The velocity of the atoms falling within a velocity width  $\frac{\Omega_{eff}}{\Delta k}$  around the zero velocity, will contribute to the two-photon excitation to the Rydberg level. It is to be noted that the phase shift as well as the dispersion of the probe depends on the Rydberg population  $\rho_{rr}$ .

A gaussian fitting is done for the experimental data for phase shift using the formula  $y = y_0 + A e^{-\frac{1}{2} \frac{(x-x_c)^2}{w^2}}$  as shown in fig. (5.11b). The fitting parameters are found to be  $y_0 = 3.5 \pm 0.014 \mu\text{rad}$ ,  $x_c = -1.36 \pm 9.6 \times 10^{-4} \text{ MHz}$ ,  $w = 0.16 \pm 10^{-3} \text{ MHz}$  and  $A = 17 \pm 0.08 \mu\text{rad}$ . The phase shift at the top of the fringe is found to be  $\sim 17 \mu\text{rad}$  and that at the noise level is  $\sim 3 \mu\text{rad}$ . It can be stated that, the minimum phase shift can be measured using this technique is  $3 \mu\text{rad}$  (precision of the phase-shift measurement).

We have seen that the phase shift is proportional to the Rydberg population. The Rydberg population can be evaluated by the Eq. (5.10) where  $\Omega_{eff}^2 \propto P_c$ , the coupling laser power. The formula can be rewritten in terms of coupling laser power  $P_c$  as,  $\phi_s = \frac{P_c^{3/2}}{k_1 + k_2 P_c}$ . The coupling Rabi frequency can be represented as,  $\Omega_c = \sqrt{\frac{P_c}{A_c}}$ , where  $A_c = \pi w_c^2$ , the cross-section of the coupling laser beam. Let us define few quantities  $\beta = \frac{k_p l}{\sqrt{\pi} v_p} \frac{n_0 |\mu_{eg}|^2}{\epsilon_0 \hbar} \frac{1}{2\Delta k \Delta_p}$  and  $\alpha = \frac{\Omega_p}{\sqrt{A_c}(\Delta_p - \Delta_c)}$ .

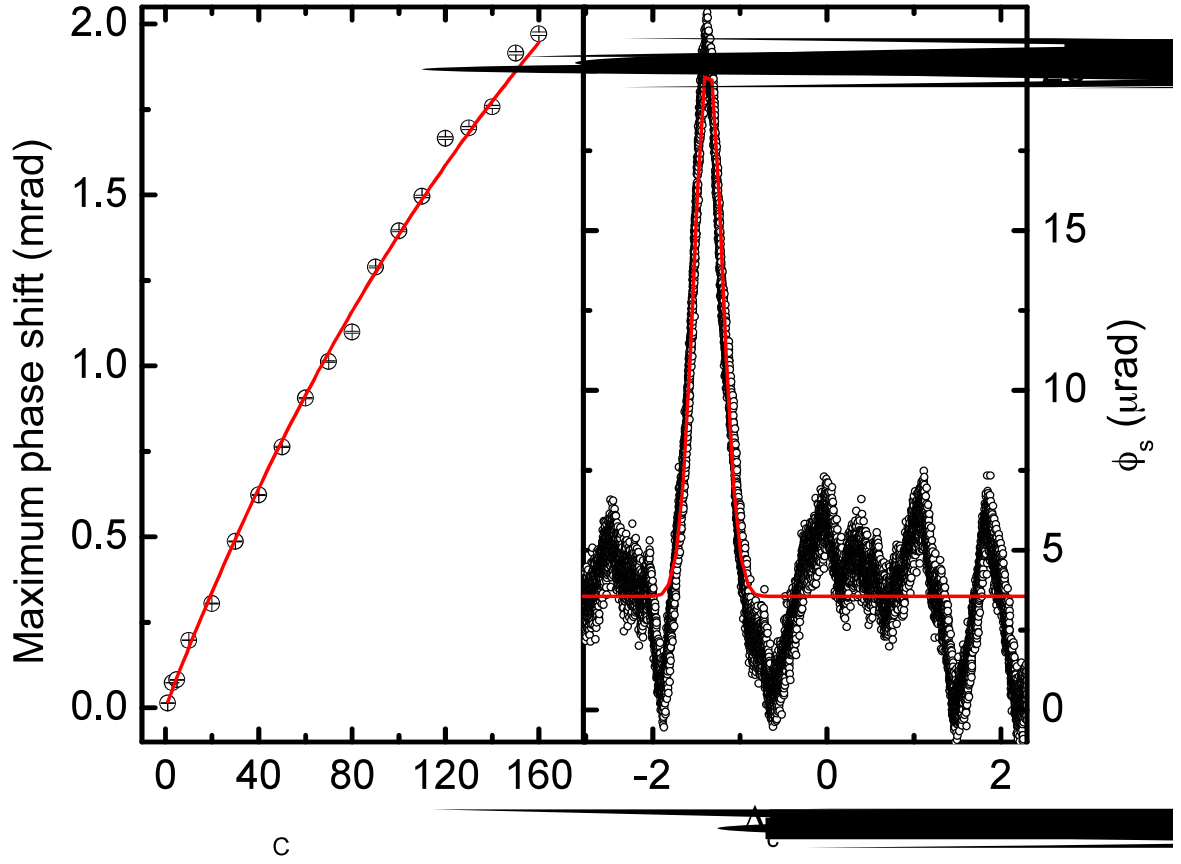


Figure 5.11: Measurement of phase shift of the probe due to two-photon resonance. (a) Using the equation,  $\phi_s = \frac{V_o}{\eta_m A_{LIA}}$ , the phase-shift of the probe at the peak of the dispersion spectrum as a function of the coupling power. Open circles correspond to the measured phase shift using heterodyne detection technique and the solid line is the fitting using the model discussed in the text. (b) Observed dispersion spectrum by scanning the coupling laser over the  $5s_{1/2}(F = 3) \rightarrow ns_{1/2}$  transition of  $^{85}\text{Rb}$  with coupling laser power being 1 mW. The signal is fitted with a gaussian function to determine the phase shift at the peak of the spectrum.

Then, the constant  $k_1$  and  $k_2$  are respectively defined as,  $k_1 = \frac{2\alpha^2}{\beta}$  and  $k_2 = \frac{\Gamma_{rg}^2}{\beta}$ . For vapor cell length  $l = 5$  cm and density  $n_0 = 2.5 \times 10^{12} \text{ cm}^{-3}$ , the parameters are found from the calculation to be  $k_1 \sim 10^{-4}$  and  $k_2 \sim 10^{-2}$ . The fitting of the experimental data in fig. (5.11a) gives  $k_1 = 1.6 \times 10^{-4} \pm 3 \times 10^{-5}$  and  $k_2 = 5.6 \times 10^{-2} \pm 2.6 \times 10^{-3}$ , which matches with the orders of  $k_1$  and  $k_2$  calculated theoretically. This verifies the originality of the measurement.

## 5.6 Precision of the Rydberg population measurement

Using Eq. (5.14), the minimum Rydberg population measured using the setup (corresponding to  $\phi_s = 3 \mu\text{rad}$ ) is  $\rho_{rr} \sim 10^{-7}$ . In contrast with precision of Rydberg population measurement in cold atom system where  $\rho_{rr} \sim 10^{-2}$  [47], OHDT gives better precision.

## 5.7 Comparison between OHDT and direct absorption measurement (DAM)

To compare OHDT with DAM we setup an experiment as depicted in fig. (5.12). A circularly polarised probe beam passes through the atomic medium and transmitted through the dichroic mirror and splitted by a polarising beam splitter (PBS) and detected by two detectors placed at the output ports of the PBS. A coupling beam with opposite circular polarisation with respect to the polarisation of the probe is counter propagated to the probe beam through the atomic medium using the dichroic mirror.

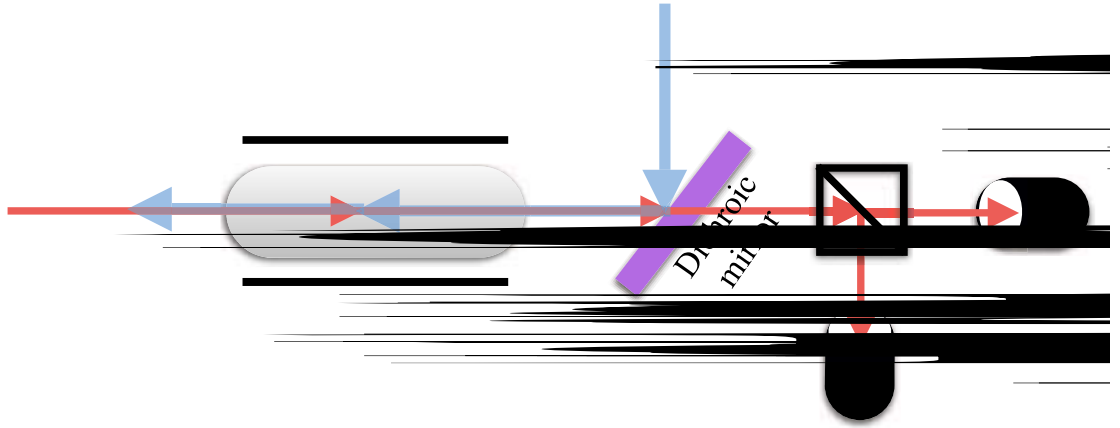


Figure 5.12: Experimental setup for direct absorption measurement (DAM) of probe.

The direct absorption of the probe can be compared with the imaginary part of the susceptibility which is calculated by using Eq. (5.7) as,

$$\Im(\chi_{3L}) = \frac{\Omega_{eff}}{\sqrt{\pi}\Delta k v_p} \frac{n_0 |\mu_{eg}|^2}{\epsilon_0 \hbar} \left( \frac{\Gamma_{rg}}{\Omega_p^2} \right) \rho_{rr} \quad (5.16)$$

is From Eq. (5.16) and Eq. (5.15), the relation between probe absorption and probe dispersion can be derived as,  $\Im(\chi_{3L}) = \frac{2\Gamma_{rg}\Delta_p}{\Omega_p^2} \Re(\chi_{3L})$ . For  $\Gamma_{rg} = 1$  MHz, the probe detuning  $\Delta_p \sim 1$  GHz and the probe Rabi frequency,  $\Omega_p = 250$  MHz the phase shift due to the dispersion ( $k_p l \Re(\chi_{3L})$ ) will be two orders of magnitude larger than the absorption ( $k_p l \Im(\chi_{3L})$ ). For the phase shift  $\phi_s = 17 \mu\text{rad}$ , the absorption is found to be  $\sim 10^{-6}$ . The phase shift at the noise level is  $\phi_s = 3.3 \mu\text{rad}$ . The absorption at the noise level would be  $10^{-7}$ .

A comparison of the direct absorption measurement (DAM) of the probe with OHDT is depicted in the fig. (5.13). A lock-in amplifier was used to get similar signal to noise ratio for

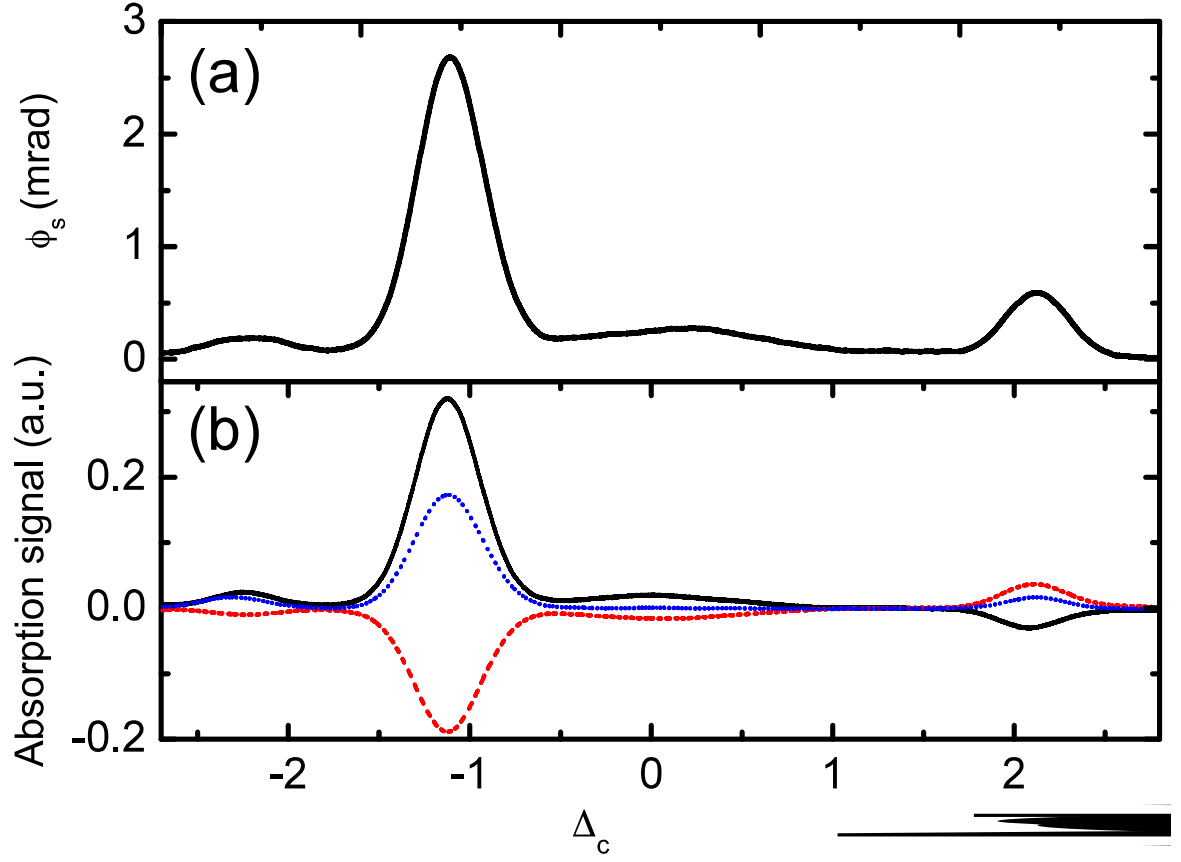


Figure 5.13: Comparison study of DAM and OHDT. (a) The measured phase shift of the probe using heterodyne detection technique. (b) Observed signal from direct probe absorption measurement with coupling being  $\sigma^+$  and probe being  $\sigma^-$ . The solid and the dashed curves correspond to the absorption of linear polarization component in vertical and horizontal directions respectively. The dotted curve corresponds to the total absorption of the probe light.

DAM as OHDT. It is seen from the experiment that DAM is extremely sensitive to the polarisation of the probe light. The absorption of two orthogonal linear polarisation component ( $H$  and  $V$ ) of  $\sigma^-$  probe light are opposite in sign which can be observed in fig. (5.13b). The signs of the absorption signals corresponding to different hyperfine states of the same spectrum are opposite to each other. The total absorption of  $\sigma^-$  polarised light is also shown in the figure. The total absorption of  $H$  and  $V$  polarised light is found to be smaller than that of  $\sigma^-$  light. Therefore there is some polarisation sensitivity issue for DAM which is affecting the measurement process.

The behavior of the absorption spectrum observed from direct probe absorption measurement can only be explained by the small polarisation rotation of the probe field due to the impurity in the circular polarisation of the coupling laser beam. We have seen that for the min-



imum phase shift  $\phi_s \sim 3 \mu\text{rad}$ , the Rydberg population, and the absorption are respectively given by  $10^{-5}$  and  $10^{-7}$ . Such a small absorption can easily be obscured in the polarisation rotation of the probe due to their small polarisation impurity due to non-ideal optical components. Hence, direct probe absorption measurement, in this case, cannot provide a reliable measurement of the Rydberg population for very small absorption. It is to be noted that a small signal is observed at 250 MHz away from the main signal ( $^{85}\text{Rb } F = 3 \rightarrow F'$ ). This is the contribution from the nearby  $^{87}\text{Rb } F = 2 \rightarrow F'$  transition.

In contrast, the signal observed in the heterodyne detection technique as shown in fig. (5.13) is only sensitive to the relative phase between the probe and the reference beams but is insensitive to any small change in their power or polarisation. Hence, the observed dispersion signal giving the information about Rydberg population becomes robust and reliable.

## 5.8 Conclusion

OHDT is an efficient technique to experimentally measure the phase shift due to the dispersion of the probe beam and hence the Rydberg population. The dispersion spectral shape measured in OHDT is explained by the simple non-interacting model presented. Due to less sensitivity of the light polarisation of OHDT, it is expected to give a reliable estimation of the measurable quantities, for example, phase-shift and the Rydberg population. This technique can also be used to detect the Rydberg blockade in cold atoms as well as in thermal atomic vapor. In the next chapter, we will be using OHDT to observe the Rydberg blockade phenomenon.

# Bibliography

- [1] S. A. Saakyan, V. A. Sautenkov, E. V. Vilshanskaya, B. B. Zelener, and B. V. Zelener, *Journal of Phys.: Conference Series*, **653**, 012123 (2015).
- [2] A. K. Mohapatra, T. R. Jackson, and C. S. Adams, *Phys. Rev. Lett.*, **98**, 113003 (2007).
- [3] D. Kara, A. Bhowmick, and A. K. Mohapatra, *Scientific Reports* volume, **8**, 5256 (2018).
- [4] A. Bhowmick, D. Kara, and A. K. Mohapatra *arXiv*: 1802.06599v1 (2018).
- [5] H. Weimer, M. Müller, I. Lesanovsky, P. Zoller, and H. P. Büchler, *Nature Phys.*, **6** 382 (2010).
- [6] D. Tong, S. M. Farooqi, J. Stanojevic, S. Krishnan, Y. P. Zhang, R. Cote, E. E. Eyler, and P. L. Gould, *Phys. Rev. Lett.*, **93**, 063001 (2004).
- [7] T. Cubel Liebisch, A. Reinhard, P. R. Berman, and G. Raithel, *Phys. Rev. Lett.*, **95**, 253002 (2005).
- [8] T. Vogt, M. Viteau, J. Zhao, A. Chotia, D. Comparat, and P. Pillet, *Phys. Rev. Lett.*, **97**, 083003 (2006).
- [9] U. Raitzsch, V. Bendkowsky, R. Heidemann, B. Butscher, R. Löw, and T. Pfau, *Phys. Rev. Lett.*, **100**, 013002 (2008).
- [10] Y. O. Dudin, L. Li, F. Bariani, and A. Kuzmich, *Nature Phys.*, **8**, 790 (2012).
- [11] Y.-Y. Jau, A. M. Hankin, T. Keating, I. H. Deutsch, and G. W. Biedermann, *Nature Phys.*, **12**, 71 (2016).
- [12] K. Singer, M. Reetz-Lamour, T. Amthor, L. G. Marcassa, and M. Weidemüller, *Phys. Rev. Lett.*, **93**, 163001 (2004).

- [13] R. Heidemann, U. Raitzsch, V. Bendkowsky, B. Butscher, R. Löw, Luis Santos, and T. Pfau, Phys. Rev. Lett., **99**, 163601 (2007).
- [14] A. Gaëtan, Y. Miroshnychenko, T. Wilk, A. Chotia, M. Viteau, D. Comparat, P. Pillet, A. Browaeys, and P. Grangier, Nature Physics, **5**, 115 (2009).
- [15] E. Urban, T. A. Johnson, T. Henage, L. Isenhower, D. D. Yavuz, T. G. Walker, and M. Saffman Nature Physics, **5**, 110 (2009).
- [16] P. Schauß, M. Cheneau, M. Endres, T. Fukuhara, S. Hild, A. Omran, T. Pohl, C. Gross, S. Kuhr and I. Bloch, Nature, **491**, 87 (2012).
- [17] J. D. Pritchard, D. Maxwell, A. Gauguier, K. J. Weatherill, M. P. A. Jones, and C. S. Adams, Phys. Rev. Lett., **105**, 193603 (2010).
- [18] T. Peyronel, O. Firstenberg, Qi-Yu Liang, S. Hofferberth, A. V. Gorshkov, T. Pohl, M. D. Lukin, and V. Vuletić, Nature, **488**, 57 (2012).
- [19] O. Firstenberg, T. Peyronel, Qi-Yu Liang, A. V. Gorshkov, M. D. Lukin, and V. Vuletić, Nature, **502**, 71 (2013).
- [20] V. Parigi, E. Bimbard, J. Stanojevic, A. J. Hilliard, F. Nogrette, R. Tualle-Brouri, A. Ourjoumtsev, and P. Grangier, Phys. Rev. Lett., **109**, 233602 (2012).
- [21] T. M. Weber, M. Hönig, T. Niederprüm, T. Manthey, O. Thomas, V. Guarrera, M. Fleischhauer, G. Barontini, and H. Ott, Nature Phys., **11**, 157 (2015).
- [22] A. K. Mohapatra, M. G. Bason, B. Butscher, K. J. Weatherill and C. S. Adams, Nature Phys., **4**, 890 (2008).
- [23] T. Baluktsian, B. Huber, R. Löw, and T. Pfau, Phys. Rev. Lett., **110**, 123001 (2013).
- [24] D. Cano, and J. Fortágh, Phys. Rev. A, **80**, 043413 (2014).
- [25] H. Labubu, S. Ravels, D. Barredo, L. Béguin, F. Nogrette, T. Lahaye, and A. Browaeys, Phys. Rev. A, **90**, 023415 (2014).
- [26] C. Carr, R. Ritter, C. G. Wade, C. S. Adams, and K. J. Weatherill, Phys. Rev. Lett., **111**, 113901 (2013).
- [27] A. K. Kölle, G. Epple, H. Kübler, R. Löw, and T. Pfau, Phys. Rev. A, **85**, 063821 (2012).

- [28] Z. Zhang, H. Zheng, X. Yao, Y. Tian, J. Che, X. Wang, D. Zhu, Y. Zhang, and M. Xiao, *Scientific Reports*, **5**, 10462 (2015).
- [29] M. P. Robinson, B. Laburthe Tolra, Michael W. Noel, T. F. Gallagher, and P. Pillet, *Phys. Rev. Lett.*, **85**, 4466 (2000).
- [30] S. D. Hogan and F. Merkt, *Phys. Rev. Lett.*, **100**, 043001 (2008).
- [31] E. Vliegen, S. D. Hogan, H. Schmutz, and F. Merkt, *Phys. Rev. A*, **76**, 023405 (2007).
- [32] T. Vogt, M. Viteau, A. Chotia, J. Zhao, D. Comparat, and P. Pillet, *Phys. Rev. Lett.*, **99**, 073002 (2007).
- [33] D. K. Doughty, and J. E. Lawler, *Appl. Phys. Lett.*, **45**, 611 (1984).
- [34] M. Brune, S. Haroche, V. Lefevre, J. M. Raimond, and N. Zagury, *Phys. Rev. Lett.*, **65**, 976 (1990).
- [35] K. R. Overstreet, A. Schwettmann, J. Tallant, and J. P. Shaffer, *Phys. Rev. A*, **76**, 011403(R) (2007).
- [36] A. Schwarzkopf, D. A. Anderson, N. Thaicharoen, and G. Raithel, *Phys. Rev. A*, **88**, 061406(R) (2013).
- [37] J. D. Carter, O. Cherry, and J. D. D. Martin, *Phys. Rev. A*, **86**, 053401 (2012).
- [38] D. Barredo, H. Kübler, R. Daschner, R. Löw and T. Pfau, *Phys. Rev. Lett.*, **110**, 123002 (2013).
- [39] I. I. Ryabtsev, D. B. Tretyakov, I. I. Beterov, and V. M. Entin, *Phys. Rev. A*, **76**, 012722 (2007).
- [40] M. Viteau, M. G. Bason, J. Radogostowicz, N. Malossi, D. Ciampini, O. Morsch, and E. Arimondo, *Phys. Rev. Lett.*, **107**, 060402 (2011).
- [41] R. Faoro, C. Simonelli, M. Archimi, G. Masella, M. M. Valado, E. Arimondo, R. Man-  
nella, D. Ciampini, and O. Morsch, *Phys. Rev. A*, **93**, 030701(R) (2016).
- [42] A. M. Akulshin, A. I. Sidorov, R. J. McLean, and P. Hannaford, *J. Phys. B*, **6**, 491 (2004).
- [43] H. Kübler, J. P. Shaffer, T. Baluktsian, R. Löw, and T. Pfau, *Nature Phot.*, **4**, 112 (2010).

- [44] H. Kang, and Y. Zhu, Phys. Rev. Lett., **91**, 093601 (2003).
- [45] H. Lo, P. Su, and Y. Chen, Phys. Rev. A, **81**, 053829 (2010).
- [46] Y. Han, J. Xiao, Y. Liu, C. Zhang, H. Wang, M. Xiao, and K. Peng, Phys. Rev. A, **77**, 023824 (2008).
- [47] F. Karlewski, M. Mack, J. Grimm, N. Sádor and J. Fortágh, Phys. Rev. A, **91**, 043422 (2015).

## Chapter 6

# Study of Rydberg blockade in thermal vapor

Strong Rydberg-Rydberg interaction induced cooperative atom-light interaction opens up wide range of applications in quantum simulation of many-body system [1–10], realisation of single photon source [11, 12], enhanced Kerr nonlinearity for single photons [13–16] and Kerr nonlinearity for classical light [17]. It also provides scope to do quantum information processing using photons [2, 18, 19]. In a dense ensemble of atoms, a coherently driven Rydberg excitation by a laser, leads to Rydberg blockade phenomenon which is extensively studied in cold atoms [20–28], Bose-Einstein condensation (BEC) [29–33] and BEC in optical lattice [34]. The presence of the Rydberg blockade interaction in an ensemble of atoms, the system forms a many-body entangled state [35, 36] which is useful for the emerging study of interest for quantum computation with Rydberg atoms [2, 19, 20, 37–42]. Contextually, the optically driven Rydberg blockade interaction and Rydberg anti-blockade interactions are studied in dissipative system [43]. In presence of dissipation, the Rydberg blockade induced many-body effect is studied theoretically [44–46]. Another theoretical study recently reported that the presence of dissipation leads a pure quantum system involving Rydberg blockade interaction to a classical system [47]. An experimental study of dissipative Rydberg interaction in cold atoms is also been reported [48].

Recent developments in thermal atom experiments of Rydberg excitation generates huge technological interests due to less complexity in comparison with the cold atomic system. An experiment with thermal atoms of Rydberg excitation in mean field regime shows a non-equilibrium phase transition [49–52]. Coherent Rabi oscillation driven by van der Waals interaction in thermal vapor in presence of dephasing is observed [53]. The strongly correlated

growth of the Rydberg aggregates due to interaction is also observed [54]. Here, the atomic ensemble is considered to be frozen and driven by a pulsed laser field. A partial suppression of Rydberg excitation is observed in an atomic beam [55] where multi-atom coherence is absent.

In this chapter, we will discuss the observation of the Rydberg blockade using OHDT. A simplified classical model explains the existence of the Rydberg blockade in the thermal atomic ensemble. But, the model is not good enough to precisely evaluate fundamental quantities, for example, the interaction strength and the blockade radius. This leads us to the construction of a quantum many-body model of the Rydberg blockade based on superatom. We will also discuss the many-body model which will be used to analyze the experimental data. The analysis confirms the existence of van der Waals blockade in the thermal vapor. A verification of the fundamental scaling of van der Waals interaction strength ( $C_6$ ) with the principal quantum number will also be mentioned.

## 6.1 Initial experiment to realise Rydberg blockade

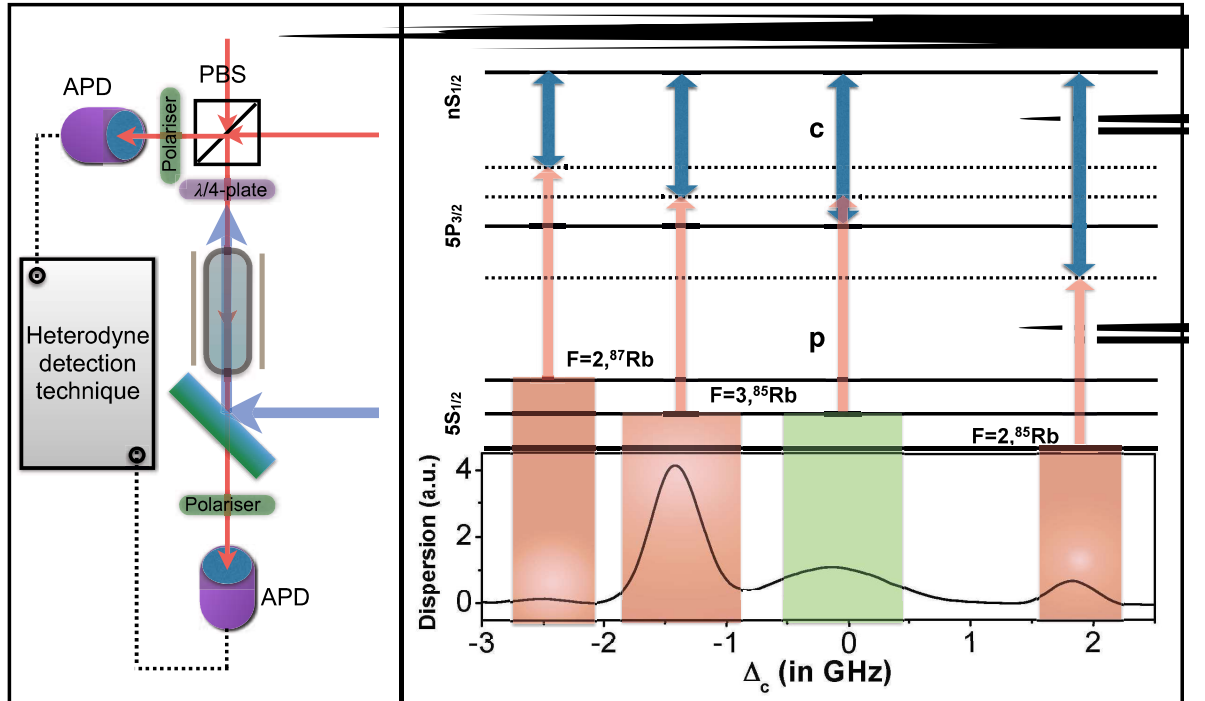


Figure 6.1: A simplified schematic of the experimental setup (a). The atomic-level diagram to explain the observed dispersion signal (b). The resonance peaks corresponding to the two-photon resonances of  $^{85}\text{Rb}$  and  $^{87}\text{Rb}$  are depicted.

The detailed experimental setup to study Rydberg blockade interaction in thermal atomic vapor is depicted in fig. (5.4). A simplified version of the experimental setup is given in fig. (6.1.a). The coupling laser frequency is scanned to observe the dispersion signal of a probe beam due to two-photon Rydberg excitation while the probe beam is passing through the thermal atomic ensemble as shown in fig. (6.1.b). The dispersion signal corresponding to the transition  $5s_{1/2}(F = 3) \rightarrow 5p_{3/2} \rightarrow ns_{1/2}$  of  $^{85}\text{Rb}$  (the orange shaded area) is used for the analysis of the Rydberg blockade using the classical model. The signal is observed for the Rydberg excited state corresponding to the principal quantum number  $n = 60$  and the density of the vapor is  $3 \times 10^{13} \text{ c.c.}^{-1}$ .

The asymmetry of the main signal appears due to strong Rydberg blockade action at the red detuned side of the two photon resonance. Here dispersion of the probe is strongly suppressed due to the Rydberg blockade. At the other side of the two photo resonance the Rydberg blockade interaction is negligible. The asymmetric nature of the dispersion signal is the signature of strong Rydberg blockade interaction which is shown in fig. (6.1). The dispersion at the peak of the spectrum (for the orange shaded transition  $5s_{1/2}(F = 3) \rightarrow 5p_{3/2} \rightarrow ns_{1/2}$  of  $^{85}\text{Rb}$  in fig. (6.1)) is taken to study intensity dependent dispersion as shown in fig. (6.2) using the classical model.

### 6.1.1 Classical model of Rydberg blockade

Let us consider the number of atoms per blockade sphere to be  $N_b$ , which can be evaluated for the given density of the atomic vapor and the given blockade radius. The probability of simultaneous multiple excitations of  $n$  atoms out of  $N_b$  atoms to the Rydberg state is given by the probability distribution as  $P_n = {}^{N_b}C_n \rho_{rr}^n (1 - \rho_{rr})^{(N_b-n)}$ , where the Rydberg population  $\rho_{rr}$  is the solution of OBE of 3-level system with a probe and a coupling laser discussed in Sec. 3.2.5. For the events of simultaneous multiple Rydberg excitations, only one Rydberg excitation is taken into account to evaluate the effective Rydberg population  $\rho_{rr}^{(b)}$ , which can be calculated as,  $\rho_{rr}^{(b)} = (P_0 + \sum_{n=1}^{N_b} \frac{P_n}{n}) \rho_{rr}$ . Then the dispersion of the probe is determined by replacing  $\rho_{rr}^{(b)}$  in equation 5.15. The theoretical curves generated using the model is shown in figure (6.2). If we consider the blockade radius to be  $2.2 \mu\text{m}$  then it fits well with the experimental data.

In strong probe regime,  $\Re(\rho_{ge}) = \frac{\Omega_p}{2\Delta_p} \rho_{rr}$ , the suppression in dispersion peak height hap-



pens due to the suppression of Rydberg population, which is the signature of the Rydberg blockade interaction. The ions inside the cell have negligible effect which was confirmed by analysing Rydberg EIT for principal quantum number  $n = 60$ .

### 6.1.2 Intensity dependent dispersion

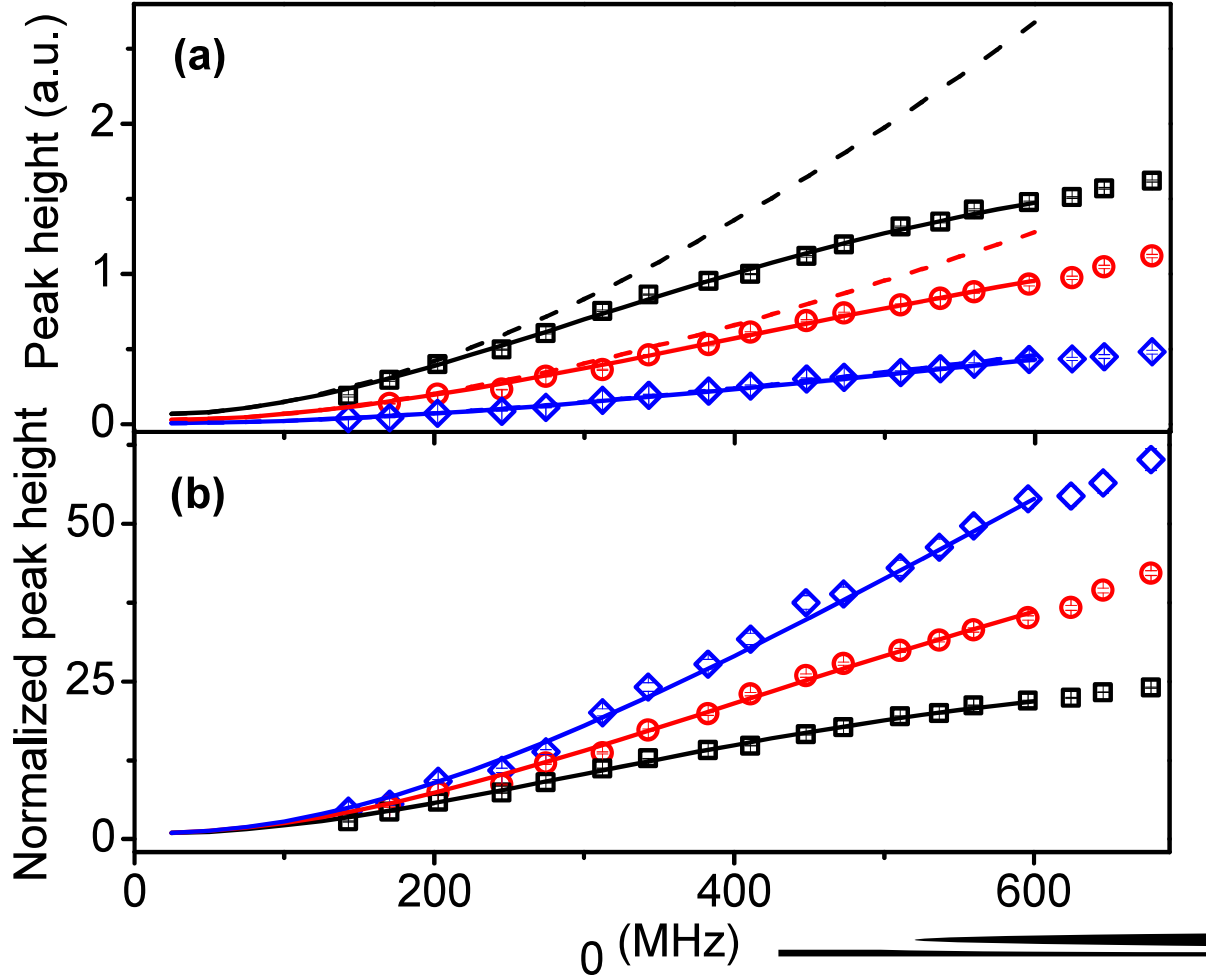


Figure 6.2: (a) Measured dispersion peak height as a function of peak probe Rabi frequency of probe beam coupling to the Rydberg state  $n = 60$  with atomic vapor densities  $2.5 \times 10^{12} \text{ cm}^{-3}$  ( $\diamond$ ),  $1.25 \times 10^{13} \text{ cm}^{-3}$  ( $\circ$ ) and  $3.0 \times 10^{13} \text{ cm}^{-3}$  ( $\square$ ). The peak Rabi frequency of coupling beam was 8.5 MHz. The solid lines are the fitting using theoretical model including interaction induced dephasing and Rydberg blockade. A multiplication factor and blockade radius are used as the fitting parameters. The dotted lines are generated from the model with interaction induced dephasing and without blockade. (b) Dispersion peak height normalized to the peak height of a weak probe beam.

For the analysis of the intensity dependent dispersion, the peak of the dispersion corresponding to the transition  $5s_{1/2}(F = 3) \rightarrow 5p_{3/2} \rightarrow ns_{1/2}$  of  $^{85}\text{Rb}$  (as depicted in fig. (6.1)) is recorded for different probe Rabi frequencies by keeping both the beat signals of heterodyne detection experiment same. In this way the gain of the experiment will same for all the intensity dependent dispersion data. In fig. (6.2a), the dashed curves are generated from the calculation of population dependent dephasing by taking  $\Gamma_{rr} = 500$  MHz (black curve) and 1 GHz (red curve). It is observed that the dispersion peak height is reduced for higher  $\Gamma_{rr}$  but the functional form is monotonically increasing with probe Rabi frequency and doesn't display any feature of saturation. Hence the population dependent dephasing cannot explain the experimentally observed dispersion saturation, whereas the classical blockade model matches well with the experimentally measured dispersion peak height data.

Fig. (6.2b) is the normalized dispersion peak height for different density which shows the nonlinear dependence on density. This phenomenon also perfectly matches with the classical model of the Rydberg blockade.

### 6.1.3 Population dependent dephasing

In order to exclude the possibility of the suppression in the dispersion peak as an artefact of the interaction induced dephasing, we introduced a Rydberg population dependent dephasing of the dipole matrix element  $\rho_{rg}$  similar to the model discussed in reference [53]. Rydberg population ( $\rho_{rr}$ ) decays at the rate  $\Gamma_{rg}$  and  $\rho_{rg}$  decays at a rate  $\frac{\Gamma_{rg}}{2} + \gamma_{rel} + \rho_{rr}\Gamma_{rr}$ . Here,  $\gamma_{rel}$  is the relative laser frequency noise between probe and coupling laser and  $\rho_{rr}\Gamma_{rr}$  is the population dependent dephasing. In the presence of the population dependent dephasing, the steady state OBE of effective 2-level system will be modified as,

$$-i(\Omega_{eff}\rho_{gr} - \Omega_{eff}^*\rho_{rg}) + \Gamma_{rg}\rho_{rr} = 0 \quad (6.1)$$

$$-i[\Delta_{eff}\rho_{rg} + \Omega_{eff}(2\rho_{rr} - 1)] - (\frac{\Gamma_{rg}}{2} + \gamma_{rel} + \Gamma_{rr}\rho_{rr}) = 0 \quad (6.2)$$

The dephasing  $\Gamma_{rg} + 2\gamma_{rel}$  is taken as 1 MHz in this model. Above two equations gives a cubic equation for Rydberg population which is given by,

$$A\rho_{rr}^3 + B\rho_{rr}^2 + C\rho_{rr} + D = 0 \quad (6.3)$$

The coefficients of the Eq. (6.3) are given by,  $A = 4\Gamma_{rr}^2\Gamma_{rg}$ ,  $B = 4\Gamma_{rg}^2\Gamma_{rr} + 16\Omega_{eff}^2\Gamma_{rr}$ ,  $C = 8\Delta_{eff}^2\Gamma_{rg} + \Gamma_{rg}^3 + 8\Omega_{eff}^2(\Gamma_{rg} - \Gamma_{rr})$  and  $D = -4\Omega_{eff}^2\Gamma_{rg}$ . Looking at the coefficients of

the cubic equation, one can deduce that out of the 3 solutions of  $\rho_{rr}$ , one is positive real and the other two solutions are either negative real or complex conjugate to each other. The positive solution of  $\rho_{rr}$  is determined by solving the cubic equation numerically and is replaced to determine  $\rho_{rg}$ . Replacing both of these terms in the Eq. (5.15), the dispersion of the probe beam is determined. The dispersion peak height is calculated using this model is shown in figure (6.2a).

In conclusion, the Rydberg blockade is demonstrated in thermal vapor and the blockade radius is measured to be  $2.2 \mu\text{m}$ . The van der Waals coefficient ( $C_6$ ) for the Rydberg state  $n = 60$  is  $140 \text{ GHz}/\mu\text{m}^6$  [17]. The typical width of the two-photon resonance is about  $500 \text{ MHz}$  which can be determined from the figure (5.6). Hence, the Rydberg blockade radius for this system should be approximately  $2.5 \mu\text{m}$  which differ from our experimental result by less than 15%. The analysis using the model explains that the suppression happens due to the presence of Rydberg blockade interaction. It is to be noted that we have introduced blockade classically and a full quantum mechanical model may give a better estimate for the blockade radius and the van der Waals interaction strength. We have observed that Rydberg population on the blue-detuned side of the two-photon excitation spectrum to the Rydberg state is enhanced whereas the red-detuned side is suppressed. Such an asymmetry observed in the spectrum cannot be explained by the above classical model. So the underlying physics for the whole spectrum could be more complicated than the above-mentioned model.

## 6.2 Superatom model of Rydberg blockade

In two-photon resonance signal in fig. (6.1), a small peak is observed at  $\Delta_c = 0 \text{ GHz}$  (the green shaded region) which is explained using a process called Rydberg anti-blockade or interaction facilitated excitation (IFE) [56]. For repulsive van der Waals interaction, it appears at the blue-detuned side of the two-photon resonance signal as shown in fig. (6.3). The Rydberg anti-blockade interaction enhances the Rydberg population as explained in Sec. (2.3.4) which results an asymmetric two-photon resonance signal. In the gray region of fig. (6.3), both the interactions namely the Rydberg anti-blockade and the Rydberg blockade are present in the system which would be difficult to model. The red detuned side of the two-photon resonance signal (the red shaded region of fig. (6.3)) is strongly dominated by Rydberg blockade interaction. In this region, the Rydberg anti-blockade has negligible effect. Hence, the red-detuned side of the two-photon resonance signal is the good region to perform the experiment in order to demonstrate Rydberg blockade.

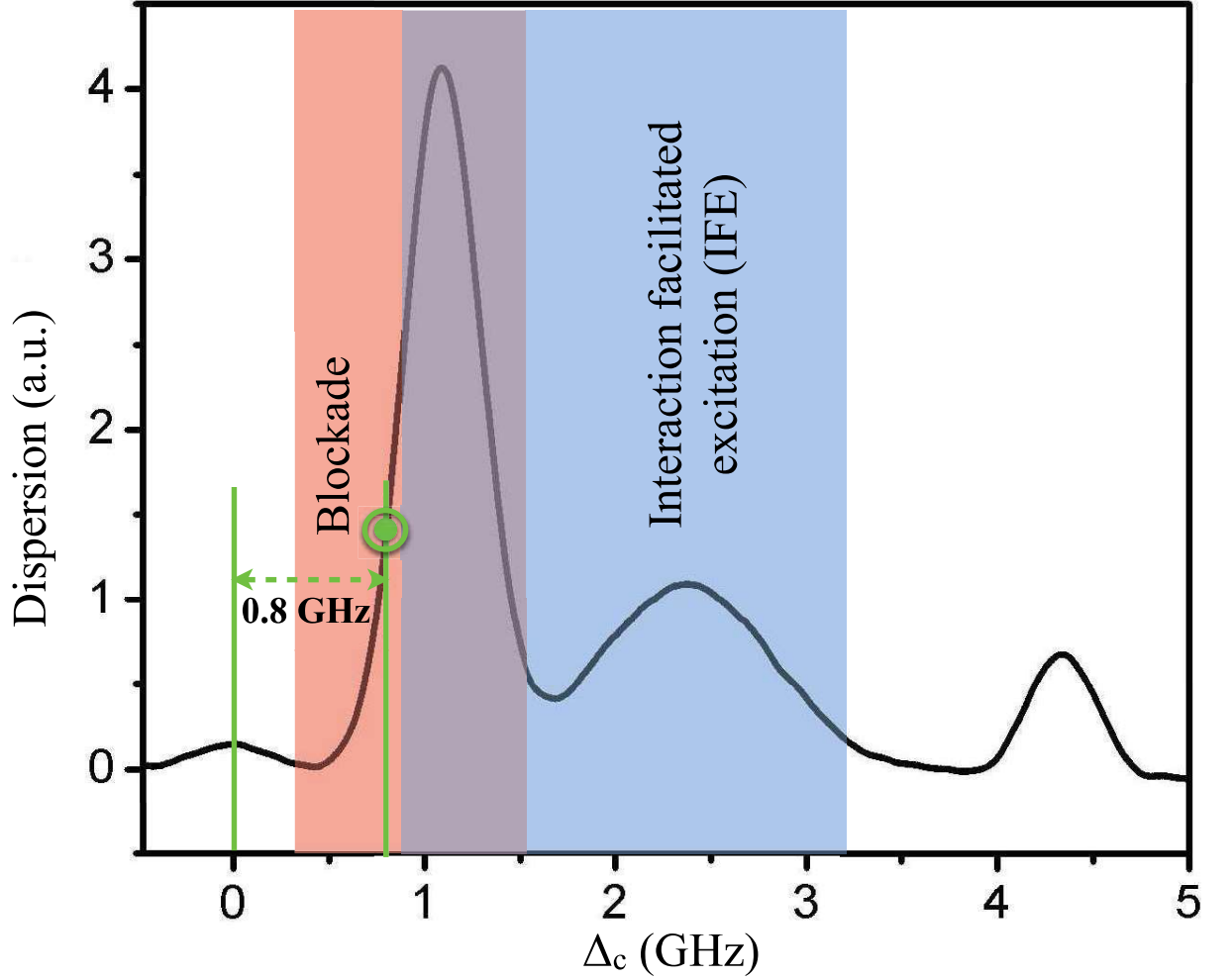


Figure 6.3: Rydberg anti-blockade interaction dominates in the blue shaded region and contributes negligibly in the orange shaded region. Both Rydberg blockade and anti-blockade interactions have significant contribution in the grey shaded region of the spectrum. The Rydberg blockade interaction dominates in the orange shaded region and contributes less in the blue shaded region.

In the presence of blockade and anti-blockade interaction, density dependent spectral shift for the peak corresponding to the  $5s_{1/2}(F=3) \rightarrow ns_{1/2}$  of  $^{85}\text{Rb}$  transition cannot be ruled out. The Rydberg excitation laser frequency is far detuned for the transition  $5s_{1/2}(F=2) \rightarrow ns_{1/2}$  of  $^{87}\text{Rb}$ . The density of  $^{87}\text{Rb}$  is also three times smaller than the density of  $^{85}\text{Rb}$ . Hence, the interactions can safely be neglected for the  $5s_{1/2}(F=2) \rightarrow ns_{1/2}$  of  $^{87}\text{Rb}$  transition which is used as a reference point in the experiment. Dispersion is measured at a point 0.8 GHz blue detuned to the reference point which is 400 MHz red detuned to the two-photon resonant peak of interest. The density dependent phase-shift of the probe is experimentally measured for

different quantum number states of Rydberg excitation ( $n = 35, 40, 45, 50$  &  $53$ , where  $n$  is principal quantum number of the Rydberg excited state) at the same point which is depicted in fig. (6.4).

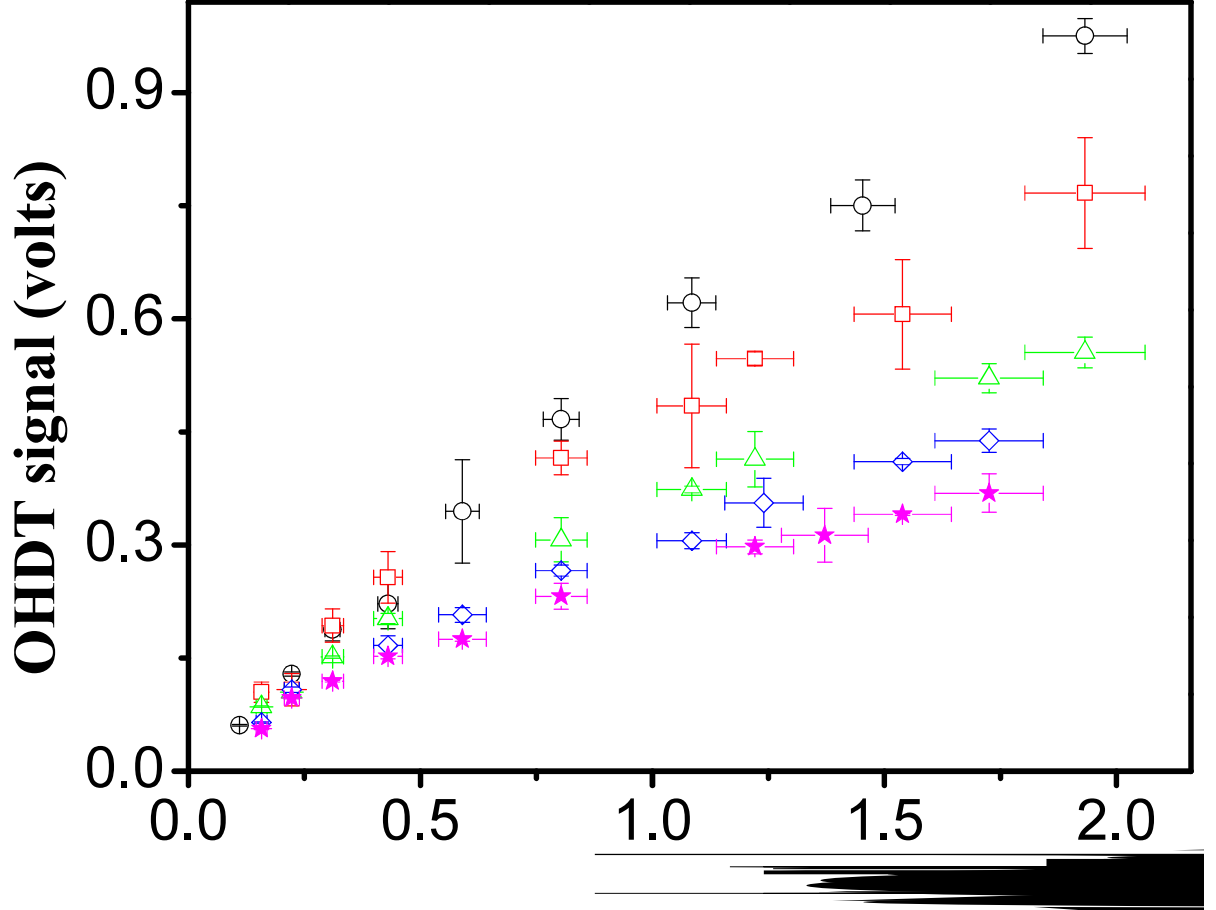


Figure 6.4: Experimental data of density dependent phase-shift. Measurement of nonlinear dispersion in the experiment due to the two-photon transition to the Rydberg states with principal quantum numbers  $n = 35$  ( $\circ$ ),  $n = 40$  ( $\square$ ),  $n = 45$  ( $\triangle$ ),  $n = 50$  ( $\diamond$ ) and  $n = 53$  ( $\bullet$ ).

As principal quantum number increases, the blockade radius increases. For a particular density of atoms, the number of atoms in the blockade sphere  $N_b$  increases for higher principal quantum number states. In the blockade sphere only one atom out of  $N_b$  is excited. Since the phase-shift due to the dispersion of the probe is proportional to the Rydberg population, suppression in the phase acquired by the probe is observed in the experiment.

There is a possibility of spontaneous ion formation due to collision of the Rydberg atoms with the background gas. The interaction due to spontaneously generated ions will introduce

the interaction potential as  $\frac{C_4}{r^4}$  [57]. Since  $C_4$  depends on the polarizability of the Rydberg state, it scales as  $n^{*7}$ . The ionic interaction is attractive for the  $ns_{1/2}$  states of rubidium and hence the shift in the Rydberg energy level would be expected towards the red-detuned side of the spectrum. The dephasing due to the ions would broaden the spectrum. If the ion would be present in our system, then the associated dephasing and shifting of the spectrum will enhance the Rydberg population in red-detuned side whereas it would be suppressed in the blue-detuned side of the spectrum. In the experiment, we observe exactly the opposite and hence we safely rule out the presence of the ion in the system. The ionization cross-section of the Rydberg atoms due to collision with the background gas depends on Rydberg density which is found to be two orders of magnitude smaller than the Rydberg density where the effect of the ions are observed in the Rydberg-EIT system in thermal vapor as reported in the reference [57]. The observation of suppression in Rydberg population in the red detuned side of the spectrum clearly suggest the Rydberg blockade due to the repulsive van der Waals interactions of  $s$ -orbital states.

In order to explain the density-dependent phase shift of a probe as observed in fig. (6.4), we constructed a quantum many-body model based on superatom formation due to the Rydberg blockade interaction. It is observed that in the thermal ensemble of atoms a certain velocity class of atoms within a velocity width  $\frac{\Omega_{eff}}{\Delta_{eff}}$  which resonantly interacting with the probe and the coupling laser, contribute to the Rydberg blockade process. Using this observation, the superatom model of Rydberg blockade is constructed.

### 6.2.1 Many-body superatom equation (MSE) of Rydberg blockade

Let us consider  $N$  identical atoms interacting via Rydberg interaction. The many-body Hamiltonian of the system can be written as,

$$\mathbb{H} = \sum_{i=1}^N \mathbf{I}^{i-1} \otimes H^{(i)} \otimes \mathbf{I}^{N-i} + \sum_{i<j}^N V_{ij} |r\rangle_i \langle r|_j \langle r|_i \langle r|_j \quad (6.4)$$

where  $H^{(i)}$  is the Hamiltonian of the  $i$ th atom which is given by,

$$H^{(i)} = -\frac{\hbar}{2} \begin{pmatrix} 0 & \Omega_{eff} \\ \Omega_{eff}^* & \Delta_{eff} \end{pmatrix}.$$

$\mathbf{I}$  represents a rank 2 identity matrix [17] and  $V_{ij}$  represents the strength of the van der Waals interaction between atom  $i$  and atom  $j$  which is given by  $V = \frac{C_6}{R_{ij}^6}$  where  $R_{ij}$  is the distance between the atom  $i$  and atom  $j$ . The master equation of the system can be written as,

$$\dot{\rho} = -\frac{i}{\hbar} [\mathbb{H}, \rho] + \mathbb{L}_D \quad (6.5)$$

Here,  $\rho$  represents total density matrix of  $N$ -atom system. The decays and decoherences of the system can be incorporated in the Lindblad operator given by

$$\begin{aligned}\mathbb{L}_D = & \mathbb{L}_{D1} \otimes \rho^{(2)} \otimes \cdots \otimes \rho^{(N)} + \rho^{(1)} \otimes \mathbb{L}_{D2} \otimes \cdots \otimes \rho^{(N)} \\ & + \cdots + \rho^{(1)} \otimes \rho^{(2)} \otimes \cdots \otimes \mathbb{L}_{DN}\end{aligned}\quad (6.6)$$

Here,  $\mathbb{L}_{Di}$  and  $\rho^{(i)}$  represent the lindblad operator and the density matrix of  $i$ th atom respectively [58]. The schematic level diagram for  $N$ -interacting Rydberg atoms is depicted in fig. (6.5).

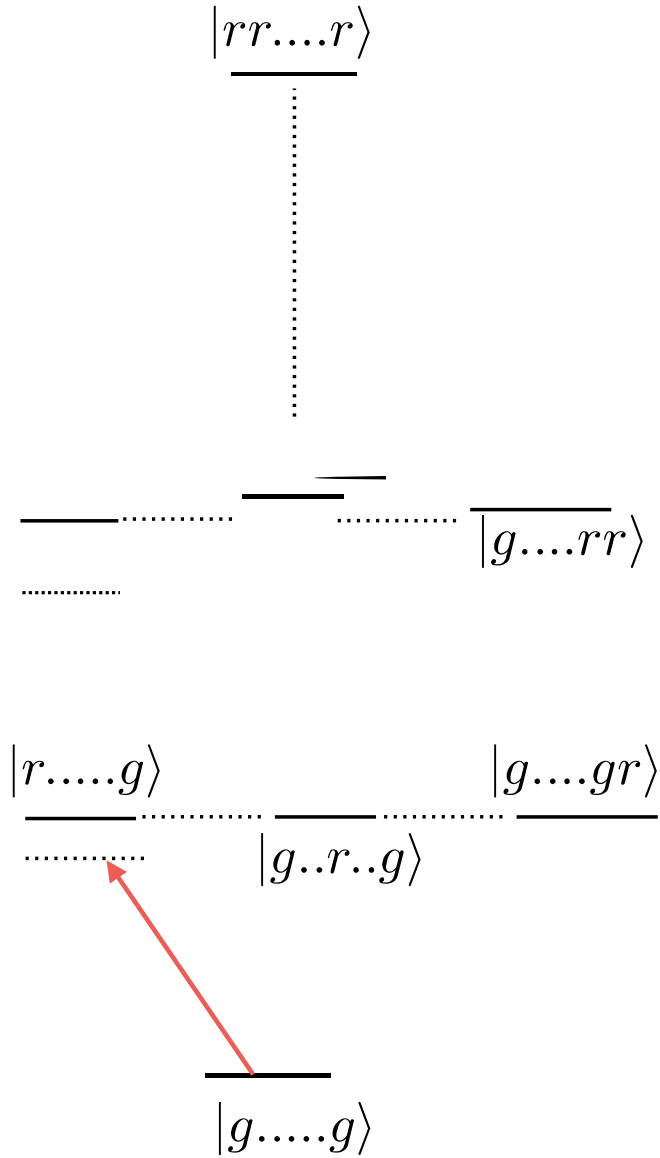


Figure 6.5: Schematic energy level diagram of  $N$ -interacting atoms.

The dephasing processes accounted by  $\mathbb{L}_D$  are the population dephasing  $\Gamma_{rg}$ . The transit time decay of atoms through the laser beam is  $\frac{\Gamma_{rg}}{2}$ . The relative laser frequency noise between probe and the coupling laser is symbolised as  $\gamma_{rel}$  which is typically taken as  $\sim 300$  kHz. The superatom dephasing  $\Gamma_s$  is introduced in the dipole matrix elements of single excited states.

### 6.2.2 Dephasing method

The transit of the atom through the beam is given by,  $\Gamma_{rg} = \frac{v_p}{2w}$ . The most probable velocity for the experiment in room temperature is of the order of  $250 \text{ ms}^{-1}$  and the beam waist is  $\sim 75 \mu\text{m}$ . Then the transit of the atom through the beam is  $\Gamma_{rg} \sim 1.5 \text{ MHz}$ . The population decay is negligible with respect to dephasing due to atom transit through the beam.

### 6.2.3 Superatom dephasing

Superatom dephasing ( $\Gamma_s$ ) is the combination of the transit time dephasing due to transverse velocity of atoms ( $\Gamma_{vt}(r_b)$ ) and the dephasing due to the difference in longitudinal velocity ( $\Gamma_{diff}$ ) as  $\Gamma_s = \Gamma_{vt}(r_b) + \Gamma_{diff}$ .

#### Transit time dephasing due to transverse velocity of atoms, $\Gamma_{vt}(r_b)$

The transit time decay through the Rydberg blockade due to the transverse velocity of atoms is given by  $\Gamma_{vt}(r_b) = \frac{\langle v_t \rangle}{2r_b}$ , where  $r_b$  is the blockade radius. For the principal quantum number of Rydberg excited state  $n = 53$  the Rydberg blockade radius  $r_b$  is  $\sim 5 \mu\text{m}$ . Then for typical most probable velocity  $v_p = 250 \text{ ms}^{-1}$ , the dephasing rate due to the transit through blockade is  $\approx 20 \text{ MHz}$ . For smallest blockade radius the transit through blockade is  $80 \text{ MHz}$ . When the effective Rabi frequency is smaller than the dephasing rate then the transit rate through the blockade does not change much. In order to model the experimental data, we took the dephasing through blockade  $\sim 50 \text{ MHz}$ .



### Dephasing due to the difference in longitudinal velocity of the atoms, $\Gamma_{diff}$

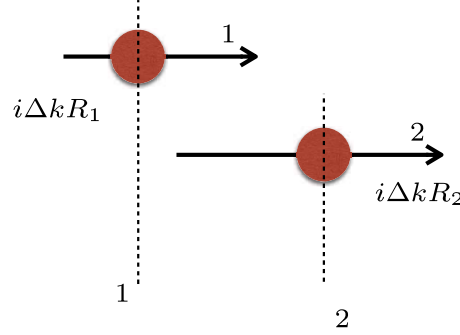


Figure 6.6: The phase difference due to atoms in different longitudinal velocity.

The atoms with different longitudinal velocity falling within the velocity width  $\frac{\Omega_{eff}}{\Delta k}$  will contribute to the blockade process. They are also different in position which are symbolised as  $R_1$  and  $R_2$  corresponding to the velocities  $v_1$  and  $v_2$  respectively as depicted in fig. (6.6). The phase acquired by the atoms are  $\Delta k R_1$  and  $\Delta k R_2$  for the velocities  $v_1$  and  $v_2$  respectively.

The phase difference can be calculated as,  $\Delta\phi = \Delta k \Delta R$ . The dephasing rate,  $\lim_{\Delta t \rightarrow 0} \frac{\Delta\phi}{\Delta t} = \frac{d\phi}{dt} = \Delta k \lim_{\Delta t \rightarrow 0} \frac{\Delta R}{\Delta t} = \Delta k \Delta v$ . The difference in the velocities can be approximated as,  $\Delta v = \frac{\Omega_{eff}}{\Delta k}$ . Therefore the dephasing rate  $\Gamma_{diff} = \frac{d\phi}{dt} = \Delta k \frac{\Omega_{eff}}{\Delta k} = \Omega_{eff}$ .

### Optical Bloch equation for $N$ -interacting Rydberg atoms

The optical Bloch equation (OBE) for 2, 3 and 4-interacting Rydberg atoms are calculated. Using method of mathematical induction, the OBE for  $N$ -interacting atoms are derived. The detail of the calculation can be found in [59, 60]. The many-body superatom equation (MSE) of Rydberg blockade for  $N$ -interacting Rydberg atoms can be derived from steady state master equation as,

$$\begin{aligned} &\Omega_{eff}[1 - \{(N+1) + (N-1)\frac{\Gamma_{rg}}{\Gamma_d}\}\rho_{22} + (N-1)\rho_{14}] + 2\Delta_{eff}\rho_{12} \\ &+ 2i(N-1)\Gamma_{rg}\rho_{24} - i(\Gamma_{rg} + 2\gamma_{rel})\rho_{12} = 0 \end{aligned} \quad (6.7)$$

$$2\Omega_{eff}\rho_{12} - 2\Omega_{eff}(N-3)\rho_{24} + 2[(N-1)\Delta_{eff} + 2V - i(\Gamma_{rg} + 2\gamma_{rel})]\rho_{14} = 0 \quad (6.8)$$

$$\Omega_{eff}\Im(\rho_{12}) + \Gamma_{rg}\rho_{22} = 0 \quad (6.9)$$

$$\Omega_{eff}(1 + \frac{\Gamma_{rg}}{\Gamma_d})\rho_{22} - \Omega_{eff}\rho_{14} + 2(\Delta_{eff} + 2V)\rho_{24} - i(3\Gamma_{rg} + 2\gamma_{rel})\rho_{24} = 0 \quad (6.10)$$

Here,  $\Gamma_d = \Gamma_{rg} + 2\gamma_{rel} + \Gamma_s$ . These four equations can be solved to find the Rydberg population and hence the dispersion of the probe field.

### 6.3 Analysis of density dependent phase-shift measurement using MSE

The nonlinear phase shift of probe propagating through the medium with density  $n_0$  and path length  $l$  can be written as,

$$V_s = G\phi_s \quad (6.11)$$

The  $\Re(\chi_{3L})$  can be expressed as,

$$\Re(\chi_{3L}) = n_0 \int_{-\infty}^{\infty} \xi(v) f(v) \rho_{rr} dv \quad (6.12)$$

where  $\rho_{rr}$  is the Rydberg population and  $f(v) = \frac{1}{\sqrt{\pi}v_p} e^{-v^2/v_p^2}$ , with  $v_p$  being the most probable velocity of the atoms. The vapor density was determined from the temperature of the vapor and the respective errors were determined from the uncertainties in the measurement of the temperature. In the regime,  $\Omega_p \gg \Omega_c$  as used in the experiment,  $\xi(v) \approx \frac{\mu_{eg}^2 k_p l}{2\epsilon_0 \hbar (\Delta_p - k_p v)}$  with  $k_p$  being the probe wave vector. The fitting function depends on the overall gain ( $G$ ) of the experiment and the blockade radius ( $r_b$ ). All the experimental parameters are kept constant during the study of density dependent phase-shift for different principal quantum number states of Rydberg excitation. The coupling Rabi frequency scales with principal quantum number of the Rydberg state as,  $n^{3/2}$ . For the study of density dependent phase-shift in the different quantum number states the coupling power are adjusted in order to keep same coupling Rabi frequency for all the data. The probe Rabi frequency was kept same for all the data. Since the Rydberg population does not change appreciably in the non-interacting regime, the argument of the integration is a constant which will help to find gain of the experiment. In the measurement of density dependent phase-shift, the gain parameter can be evaluated in non-interacting regime as follows.

#### 6.3.1 Gain of the OHDT experiment

The phase-shift experienced by the probe due to the dispersion is given by  $\phi_s = \frac{k_p l}{2} \Re(\chi_{3L})$ . Therefore the phase-shift can be evaluated as,

$$\phi_s = \frac{k_p l}{2} n_0 \int_{-\infty}^{\infty} \xi(v) f(v) \rho_{rr} dv \quad (6.13)$$

Comparing Eq. (6.11) and (6.13), we get,

$$V_s = Gn_0 \left[ \frac{k_p l}{2} \int_{-\infty}^{\infty} \xi(v) f(v) \rho_{rr} dv \right] \quad (6.14)$$

In Eq. (6.14), the term inside the third bracket does not depend on density in non-interacting regime. Therefore the slope of the density dependent OHDT signal due to the dispersion gives the value of gain.

A Monte Carlo simulation is done to evaluate the mean and standard deviation of gain from the experimental data. The mean and the standard deviation of the density, as well as the phase shift corresponding to the individual data point, are known. We have generated the normal distribution of the density and the phase shift for individual experimental data points by taking respective errors as full-width half maxima (FWHM) of the distribution which peaked at the respective mean experimental values. There are two normal distributions for each experimental data point with respect to the error in density and the error in phase shift measurement. We have sampled 1000 points from the density and the phase shift distributions for each of the experimental data. The  $\chi^2$ -fitting (Appendix C) using the formula Eq. (6.14) is done to fit all the individual density-dependent phase shift profiles to find the statics of the gain parameter. This process gives a distribution of gain as shown in fig. (6.7a). The distribution with a Gaussian function is fitted which is given by,  $P(G) = P_0 + \frac{A}{\delta G \sqrt{\frac{\pi}{2}}} e^{-2(\frac{G - \langle G \rangle}{\delta G})^2}$ . The fitting parameters are given in the Table. (6.1).

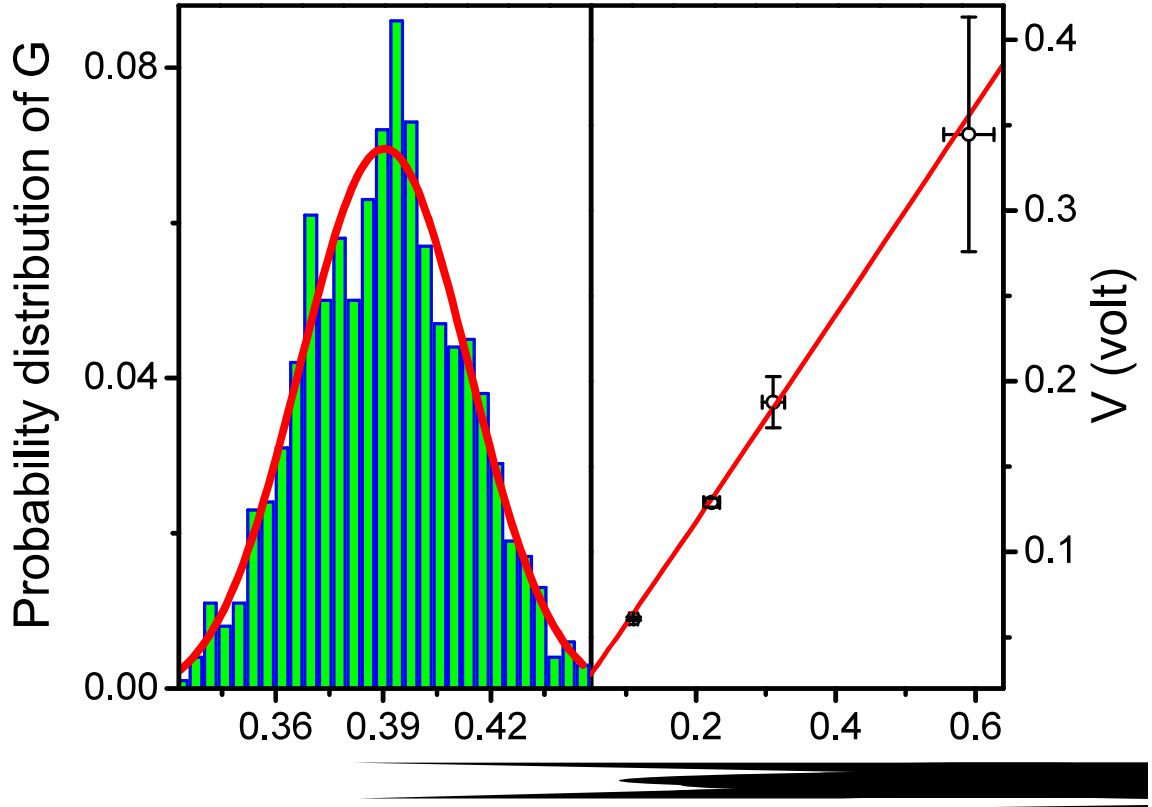


Figure 6.7: Evaluation of overall gain of the experiment. (a) The probability distribution of gain generated by fitting 1000 sample of possible curves generated due to 1000 times repeated measurement in the non-interacting regime (for  $n = 35$  in low-density regime). The distribution is fitted by a Gaussian curve from which mean ( $\langle G \rangle$ ) and standard deviation  $\delta G$  is evaluated. (b) Fitting of the experimental data for  $n = 35$  at the low-density regime. The fitted line is generated by using the average gain  $\langle G \rangle$ .

Table 6.1: Gaussian fitting of the gain distribution.

Fitting parameter	Fitted value
$P_0$	$-0.0014 \pm 0.0004$
$\langle G \rangle$	$0.39 \pm 9 \times 10^{-4}$
$\delta G$	$0.047 \pm 0.0004$
$A$	$0.004 \pm 5 \times 10^{-4}$
$FWHM$	0.055
$Height$	0.07

There the gain is found to be  $\langle G \rangle = (0.39 \pm 0.047)$  V/mrad. The goodness of the gain fitting is depicted in fig. (6.8). The number of experimental data points  $dof = n_d - n_{para} = 4$  for

the gain fitting and the number of parameter  $n_{para} = 1$ . Then, the degrees of freedom  $dof = 3$  (Appendix C). From the distribution depicted in the fig. (6.8), the most of  $\chi^2/dof$  is less than 0.2 and the total distribution situated  $\chi^2/dof < 1$  which signifies that the fitting for gain is good (Appendix C).

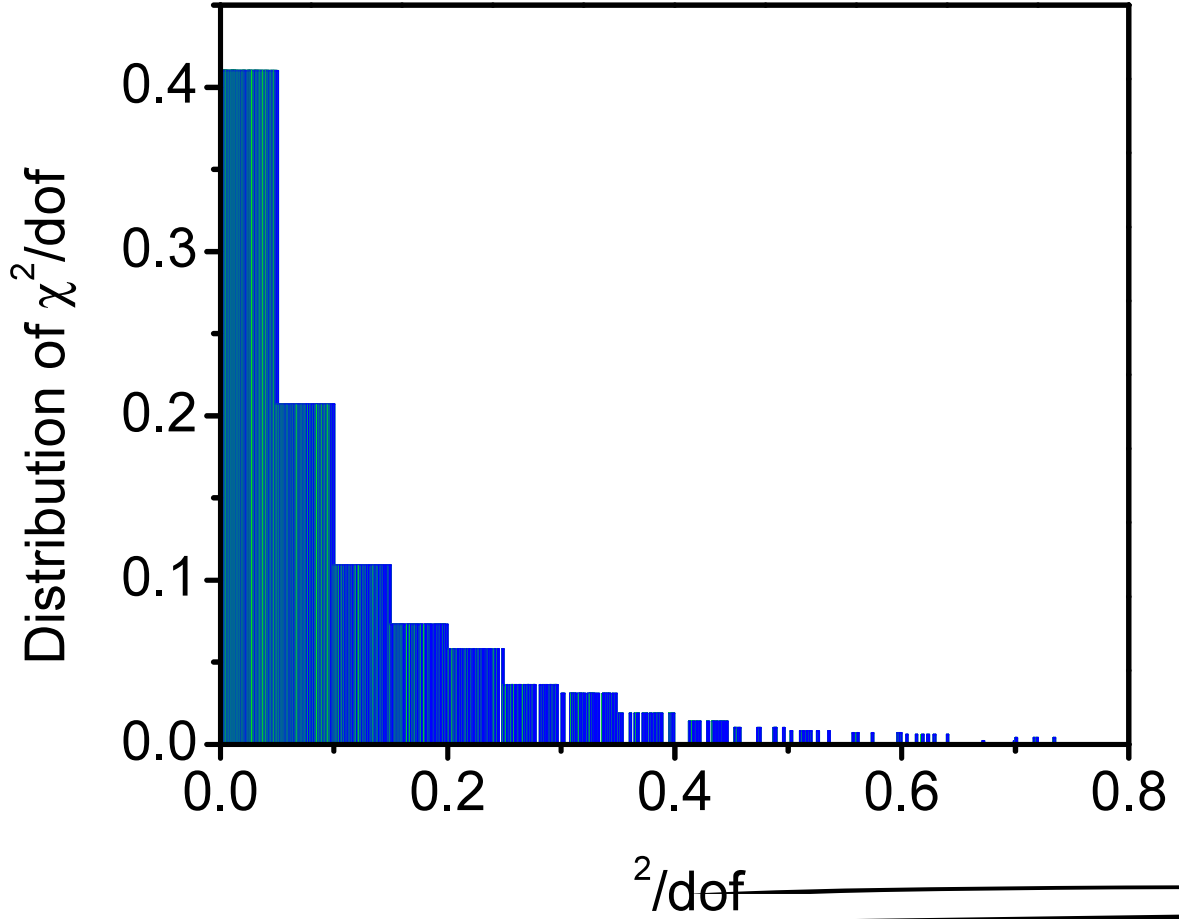


Figure 6.8: Goodness of the gain fitting.

### 6.3.2 Density dependent phase shift and the evaluation of Rydberg blockade radius $r_b(n)$

In an ensemble of atoms, in presence of the Rydberg excitation field, only one Rydberg excitation is allowed inside the blockade volume. This single excitation suppresses the other atoms from getting excited inside the blockade volume. Even though the other atoms inside the blockade volume are not excited, they contribute to the susceptibility collectively. All the

atoms inside the blockade volume participating in cooperative blockade process collectively are called as a single superatom. The average number of atoms inside the blockade sphere can be found as  $\bar{N}_b = n_0 V_b$ , where  $n_0$  is the density of the atomic vapor and  $V_b$  is the blockade volume. The number of atoms present in each blockade sphere follows the Poisson distribution which is characterized by  $\bar{N}_b$ . The distribution can be written as,  $P(\bar{N}_b, N_b) = \frac{\bar{N}_b^{N_b} e^{-\bar{N}_b}}{N_b!}$ . Then the total susceptibility of the probe can be represented as

$$\chi = \sum_{N_b=1}^{\infty} P(\bar{N}_b, N_b) \chi_{sup}(N_b) \quad (6.15)$$

Here  $\chi_{sup}(N_b)$  is the susceptibility experienced by the probe due to a superatom containing  $N_b$  number of atoms inside the blockade sphere. The  $\chi_{sup}(N_b)$  is calculated by using MSE.

As we have seen from Eq. (6.15), the number of atoms present in each superatom follows the Poisson distribution. Therefore, the  $\rho_{avg}$  can also be calculated as

$$\rho_{avg} = \sum_{N=1}^{\infty} P(\bar{N}_b, N) \rho_{rr}(N) \quad (6.16)$$

Where  $P(\bar{N}_b, N)$  is a Poisson distribution function. It is observed that due to the wave-vector mismatch, all the atoms present in the blockade sphere cannot contribute to the Rydberg blockade process. The atoms within the velocity range from  $\tilde{v} - \frac{\Omega_{eff}}{2\Delta k}$  to  $\tilde{v} + \frac{\Omega_{eff}}{2\Delta k}$  contribute to the Rydberg blockade process, where  $\tilde{v}$  is velocity of atoms which resonantly interact with the probe and the coupling laser.  $\tilde{v}$  can be found from the equation  $\Delta_{eff}(\tilde{v}) = 0$ , which gives,  $\tilde{v} = \frac{1}{\Delta k} [\Delta_p + \Delta_c + \frac{\Omega_p^2 - \Omega_c^2}{4(\Delta_p - \Delta_c)}]$ . The number of atoms per blockade can be calculated as,  $N_b = \frac{4\pi}{3} r_b^3 n_0 f(\tilde{v}) \left( \frac{\Omega_{eff}}{\Delta k} \right)$ . The fitting function for the density dependent phase-shift is given by,

$$V_s = G n_0 \int_{-\infty}^{\infty} \xi(v) f(v) \rho_{avg} dv \quad (6.17)$$

For the fitting, we need to construct the Gradient vector and Hessian matrix as discussed in Appendix C. Here,  $r_b^3$  is a fitting parameter. Therefore, it is required to find a differentiation of the fitting equation with respect to  $r_b^3$ . The average number of atoms  $\bar{N}_b$  contributing to the Rydberg blockade process strongly depend on  $r_b^3$ . The transit time decay due to transverse velocity of atoms  $\Gamma_{vt}$  is a function of Rydberg blockade radius  $r_b$ . Hence, the Rydberg population  $\rho_{rr}$  also depends on  $r_b$  but it is a slowly varying function of  $r_b$  and hence the  $r_b$  dependance of  $\rho_{rr}$  can be neglected [67]. Then, the differentiation of  $\rho_{avg}$  with respect to  $r_b^3$  is given by,

$$\frac{\partial}{\partial r_b^3} [\rho_{avg}] = \frac{4\pi}{3} n_0 f(\tilde{v}) \frac{\Omega_{eff}}{\Delta k} \sum_{N=1}^{\infty} \left( \frac{N}{\bar{N}_b} - 1 \right) P(\bar{N}_b, N) \rho_{rr}(N) \quad (6.18)$$

Eq. (6.18) is used to construct the Hessian matrix for  $\chi^2$ -fitting of the experimental data.

The Rydberg population  $\rho_{rr}(N)$  of Eq. (6.16) & (6.18) is calculated by using MSE. The decay rates are taken to be  $\Gamma_{rg} = 1.5$  MHz,  $\gamma_{rel} = 300$  kHz,  $\Gamma_{diff} = 1$  MHz and  $\Gamma_{vt}(r_b) = \frac{v_t}{2r_b}$ . Since  $r_b$  is in  $\mu\text{m}$   $\Gamma_{vt}(r_b)$  is in MHz. We took  $\Gamma_{vt}(r_b) = 50$  MHz.

A similar Monte Carlo approach and  $\chi^2$ -fitting is done for density dependent phase shift data as we discussed for the fitting process to find the gain. For particular principal quantum number, we simulate repetitive measurement of density dependent phase shift. Then, sampled gain from a normal distribution with FWHM  $\delta G = 0.047$  V/mrad and peaked at  $\langle G \rangle = 0.39$  V/mrad in order to do  $\chi^2$  fitting for 1000 dispersion dependent phase shift profiles to find the statistics of the parameter  $r_b^3$ . We repeat the process for all the principal quantum number states ( $n = 35, 40, 45, 50$  &  $53$ ). For each quantum number state,  $\langle r_b^3 \rangle$  and  $\delta r_b^3$  determined from the fitting are shown in Table (6.2). By taking the  $\langle r_b^3 \rangle$ , the fitted curves and the experimental data for all the principal quantum number states are shown in fig. (6.9).

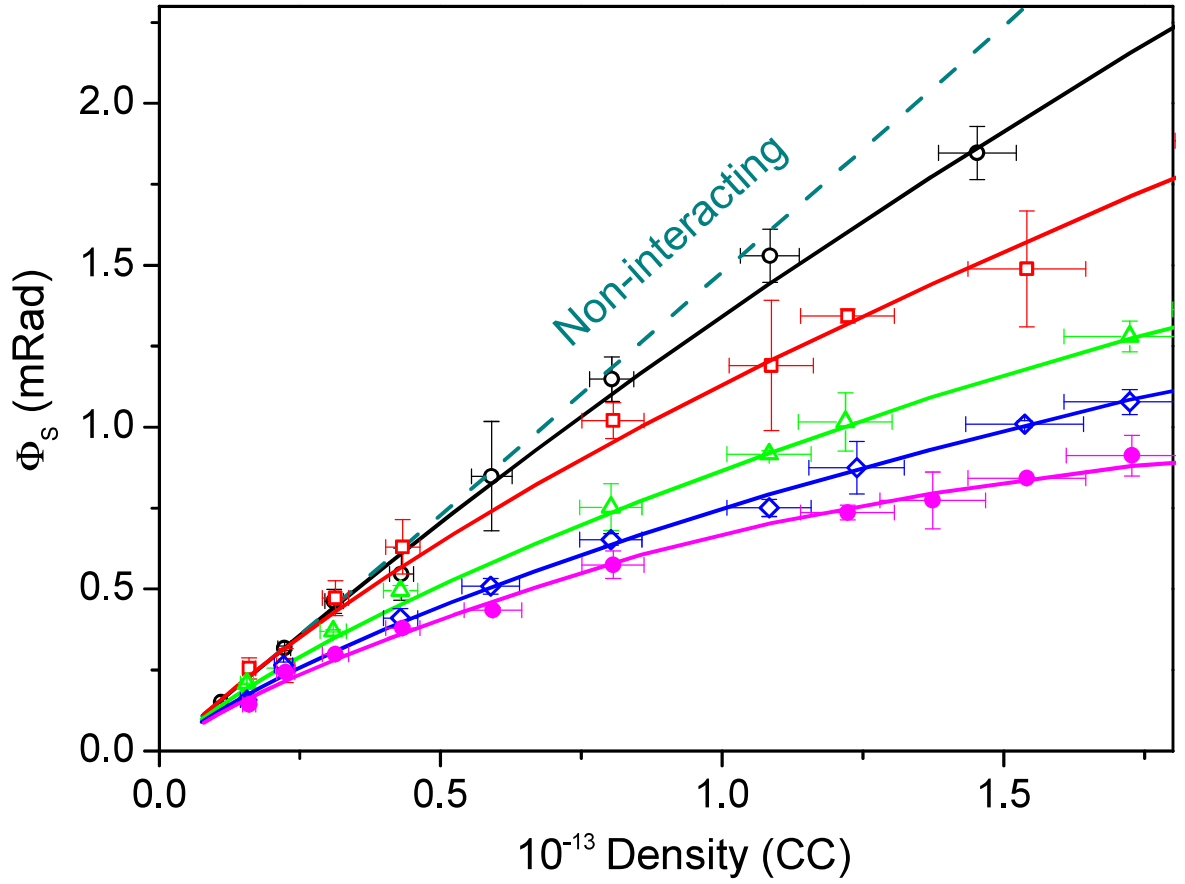


Figure 6.9: Non-linear absolute phase shift of the probe measured in the experiment due to the two-photon transition to the Rydberg states with principal quantum numbers  $n = 35$  ( $\circ$ ),  $n = 40$  ( $\square$ ),  $n = 45$  ( $\triangle$ ),  $n = 50$  ( $\diamond$ ) and  $n = 53$  ( $\bullet$ ). The solid lines are the  $\chi^2$ -fitted curves using the model described in the text. The dotted line is the expected signal for the non-interacting atomic ensemble.

The goodness of the  $\chi^2$  fitting is depicted in the fig. (6.10). The degrees of freedom for the data corresponding to  $n = 35, 40, 45$  and  $50$  is 8 since the number of data point is 9 and the number of parameter to be fitted is 1. For  $n = 53$  the number of experimental data points are 10. Therefore the degrees of freedom is 9.



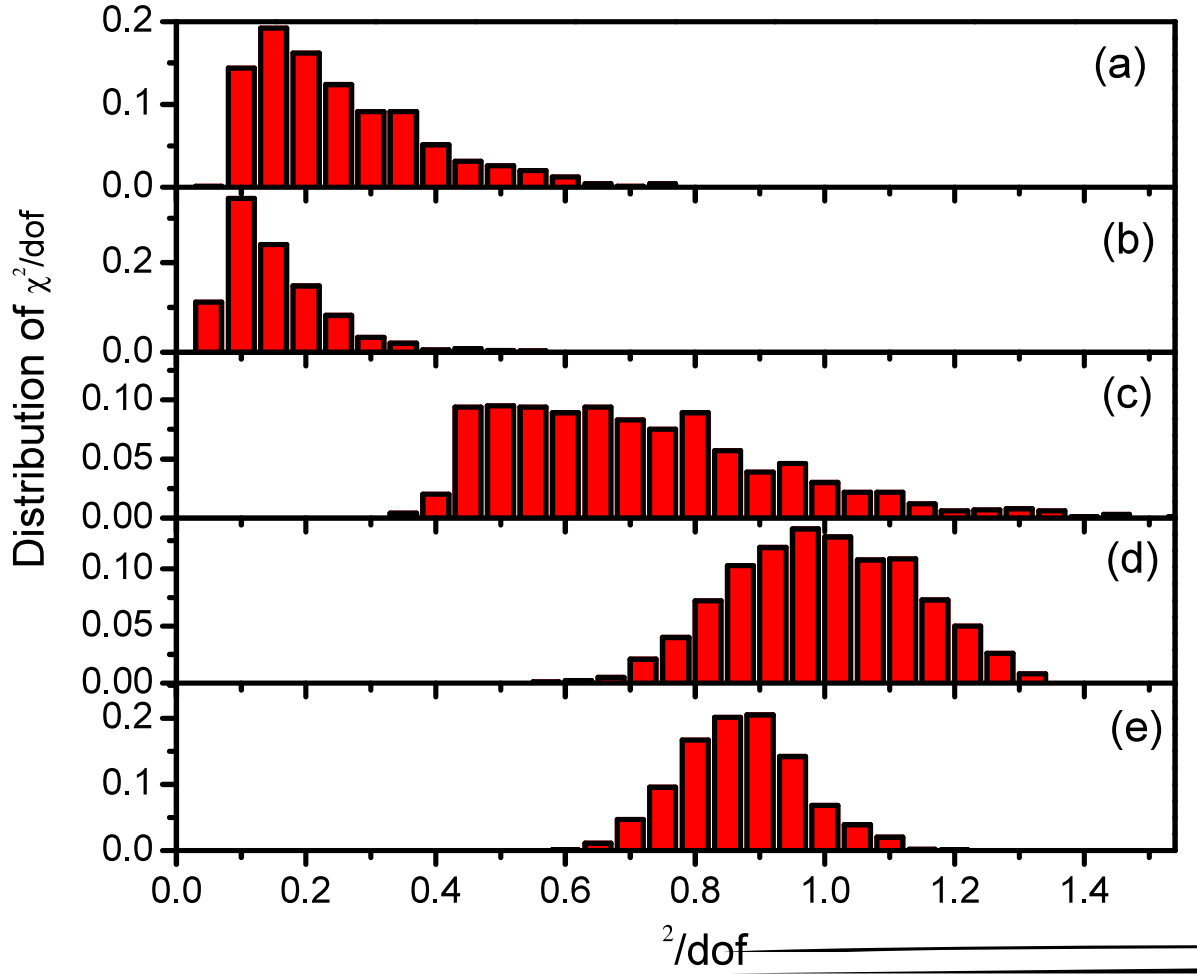


Figure 6.10: Goodness of the density dependent phase shift fitting. (a)  $n = 35$ , (b)  $n = 40$ , (c)  $n = 45$ , (d)  $n = 50$  and (e)  $n = 53$ .

It is to be noted that the distribution of  $\chi^2/dof$  for all principal quantum numbers are below 2 which is good. From the fitting the principal quantum number dependent statistics of  $r_b^3$  is given in the Table. (6.2).

Table 6.2: Blockade radius from the statistical analysis of density dependent phase shift data

$n$	$r_b^3$	$\delta r_b^3$ (Error in $r_b^3$ )
35	28.4	3.0
40	62	6.2
45	130.7	13.6
50	230	24
53	315	36

### 6.3.3 $r_b^3$ scaling with respect to the principal quantum number $n^*$

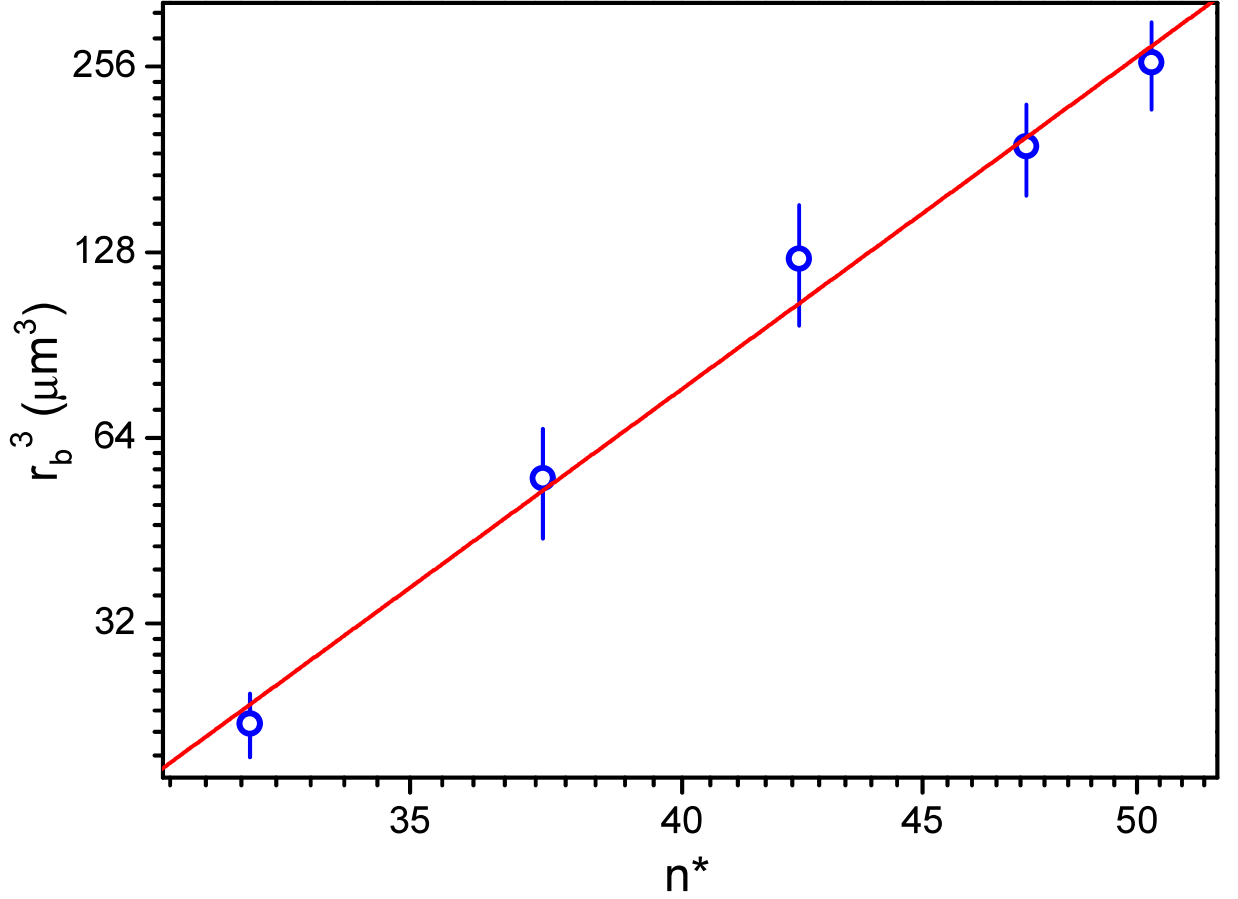


Figure 6.11:  $r_b^3$  as a function of  $n^*$ . The solid line is the fitting to find,  $r_b^3 = (1.5 \pm 0.6) \times 10^{-7} \times n^{*5.47 \pm 0.3} \mu\text{m}^3$ .

The reduced principal quantum number is defined as  $n^* = n - \delta_0$  with  $\delta_0$  being the quantum defect [58,61–66]. For our calculation, the quantum defect is taken as  $\delta_0 = 2.641$ . We have also done Monte Carlo simulation and  $\chi^2$  fitting of principal quantum number dependent  $r_b^3$ . The data points are plotted in the fig. (6.11) which are directly taken from the Table (6.2). Gaussian distributions are generated by taking respective  $\delta r_b^3(n^*)$  as FWHM and centred at  $r_b^3(n^*)$ . We sampled 10000 data points for each of the  $r_b^3$  and simulated repetitive experiment measurement. Therefore, 10000 principal quantum number dependent  $r_b^3$  profiles are generated for the same experimental situation and  $\chi^2$ -fitting is done in log scale with the equation,  $\log r_b^3 = a \log n^* + b$ . The fitted line is depicted in fig. (6.11). The statistical distribution of the fitted parameters give  $a = 5.47 \pm 0.3$  and  $b = -15.6 \pm 1.12$ .

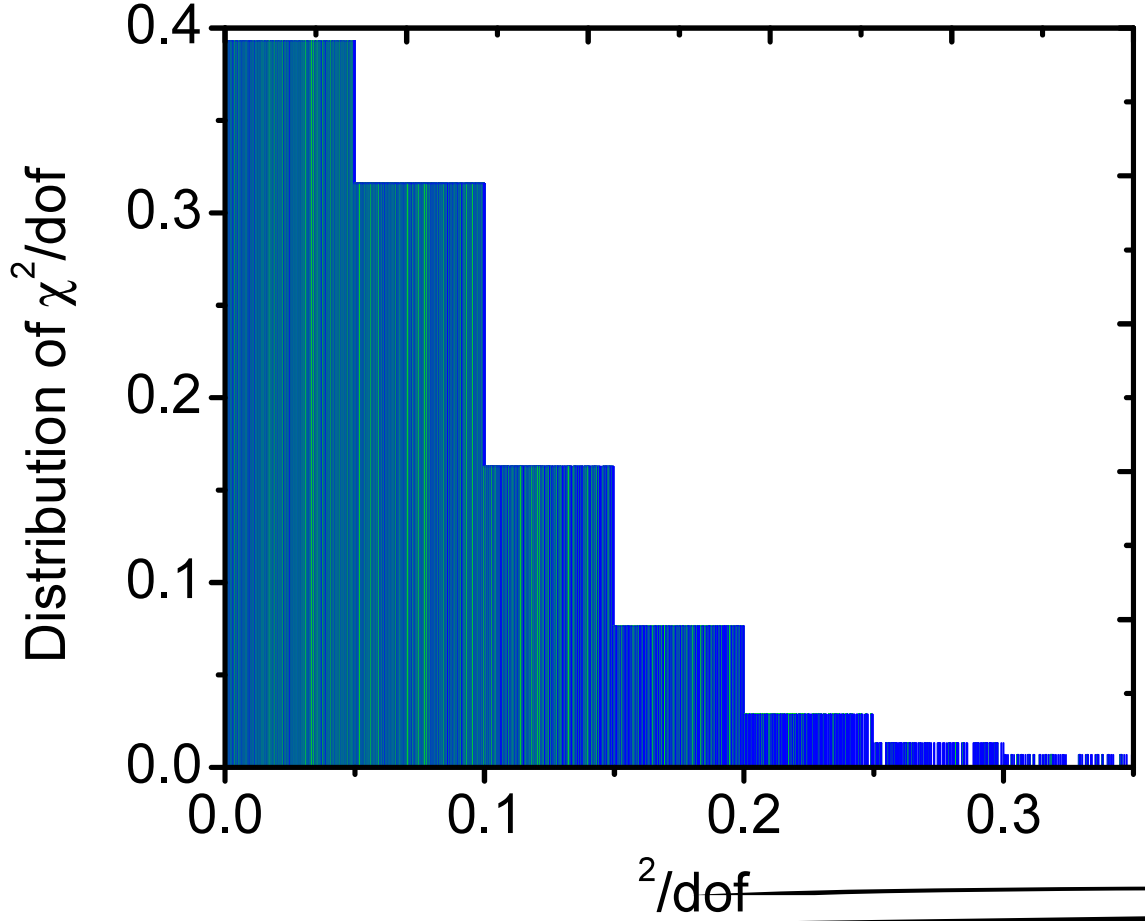


Figure 6.12: Goodness of the principal quantum number dependent  $r_b^3$  fitting.

The scaling law of  $r_b^3$  with principal quantum number is found to be  $r_b^3 = (1.5 \pm 0.6) \times 10^{-7} \times n^{5.47 \pm 0.3} \mu\text{m}^3$ . The van der Waals interaction strength is given by,  $C_6 = \hbar\Omega_{eff}r_b^6$  and hence  $C_6 \sim n^{11}$  with below 6% error. This gives the direct evidence of superatom formation due to Rydberg blockade interaction in the thermal vapor. The goodness of the principal quantum number dependent  $r_b^3$  fitting is depicted in fig. (6.12). It is to be noted from the distribution that the  $\chi^2/dof$  is less than 1 for all the fitting. Therefore the quality of the fitting is very good.

## 6.4 Conclusion and application

The experiment and the analysis with MSE confirm that the multi-atom coherence due to the formation of the superatom is possible in the thermal atomic vapor. The verification of the

van der Waals interaction scaling law,  $C_6 \sim n^{*11}$  confirms the existence of van der Waals type Rydberg blockade in the thermal vapor. This is the first ever evidence of multi-atom coherence due to the Rydberg blockade interaction in thermal atomic vapor using continuous wave. The observation opens up a provision to do quantum engineering and Rydberg quantum optics using thermal atomic vapor. Using micron size vapor cell and focussing the laser beam tightly to the order of blockade radius, one can perform the experiment with a single blockade sphere.

It also claims the strong nonlinearity due to the multi-atom coherence at the single photon level. In order to observe the single photon non-linearity it is necessary to satisfy the condition  $\Omega_{eff} \geq \Gamma_d$ , where  $\Omega_{eff} = \sqrt{N_b}\Omega$  and  $\Gamma_d$  is the total dephasing of the system which is typically of the order of 3 MHz. The two-photon Rabi frequency  $\Omega$  is inversely proportional to the minimum beam waist of the laser beam. For single photon power 0.25 pW [13], the two-photon Rabi frequency is given by  $\Omega = 3$  MHz for minimum beam waist of 100  $\mu\text{m}$ . Then, the superatom Rabi frequency is given by  $\Omega_{eff} = \sqrt{N_b}\Omega = 6.15$  MHz  $> \Gamma_d$  for the vapor density of  $10^{15}$  c.c $^{-1}$ . Therefore the single photon nonlinearity due to multi-atom can be observed. Therefore the thermal vapor system is a good candidate to do Rydberg quantum optics which is advantageous for technological advancement towards quantum engineering.

# Bibliography

- [1] H. Weimer, M. Müller, I. Leshanovsky, P. Zoller, and H. P. Büchler, *Nature Phys.* **6** 382 (2010).
- [2] M. Saffman, T. G. Walker, and K. Mølmer, *Rev. Mod. Phys.* **82**, 2313 (2010).
- [3] P. Schauß, M. Cheneau, M. Endres, T. Fukuhara, S. Hild, A. Omran, T. Pohl, C. Gross, S. Kuhr and I. Bloch, *Nature* **491**, 87 (2012).
- [4] X. L. Zhang, A. T. Gill, L. Isenhower, T. G. Walker, and M. Saffman, *Phys. Rev. A* **85**, 042310 (2012).
- [5] A. Dauphin, M. Müller, and M. A. Martin-Delgado, *Phys. Rev. A* **86**, 053618 (2012).
- [6] H. Labubu, S. Ravels, D. Barredo, L. Béguin, F. Nogrette, T. Lahaye, and A. Browaeys, *Phys. Rev. A* **90**, 023415 (2014).
- [7] D. W. Schönleber, A. Eisfeld, M. Genkin, S. Whitlock, and S. Wüster, *Phys. Rev. Lett.* **114**, 123005 (2015).
- [8] H. Labuhn, D. Barredo, S. Ravets, S. de Lèsèleuc, T. Macri, T. Lahaye, and A. Browaeys, *Nature* **534**, 667 (2016).
- [9] H. Bernien, S. Schwartz, A. Keesling, H. Levine, A. Omran, H. Pichler, S. Choi, A. S. Zibrov, M. Endres, M. Greiner, V. Vuletić and M. D. Lukin, *Nature* **551**, 579 (2017).
- [10] S. de Lèsèleuc, S. Weber, V. Lienhard, D. Barredo, H. P. Büchler, T. Lahaye, and A. Browaeys, *Phys. Rev. Lett.* **120**, 113602 (2018).
- [11] M. Saffman, and T. G. Walker, *Phys. Rev. A* **66**, 065403 (2002).
- [12] Y. O. Dudin, and A. Kuzmich, *Science* **336**, 887 (2012).

- [13] T. Peyronel, O. Firstenberg, Qi-Yu Liang, S. Hofferberth, A. V. Gorshkov, T. Pohl, M. D. Lukin, and V. Vuletić, *Nature* **488**, 57 (2012).
- [14] D. E. Chang, V. Vuletić, and M. D. Lukin, *Nature Photonics* **8**, 685 (2014).
- [15] H. Busche, P. Huillery, S. W. Ball, T. Ilieva, M. P. A. Jones, and C. S. Adams *et al.*, *Nature Physics* **13**, 655 (2017).
- [16] O. Firstenberg, T. Peyronel, Qi-Yu Liang, A. V. Gorshkov, M. D. Lukin, and V. Vuletić, *Nature* **502**, 71 (2013).
- [17] J. D. Pritchard, D. Maxwell, A. Gauguier, K. J. Weatherill, M. P. A. Jones, and C. S. Adams, *Phys. Rev. Lett.* **105**, 193603 (2010).
- [18] D. Jaksch, J. I. Cirac, P. Zoller, S. L. Rolston, R. Côté, and M. D. Lukin, *Phys. Rev. Lett.* **85**, 2208 (2000).
- [19] M. D. Lukin, M. Fleischhauer, R. Cote, L. M. Duan, D. Jaksch, J. I. Cirac, and P. Zoller, *Phys. Rev. Lett.* **87**, 037901 (2001).
- [20] D. Tong, S. M. Farooqi, J. Stanojevic, S. Krishnan, Y. P. Zhang, R. Cote, E. E. Eyler, and P. L. Gould, *Phys. Rev. Lett.* **93**, 063001 (2004).
- [21] K. Singer, M. Reetz-Lamour, T. Amthor, L. G. Marcassa, and M. Weidemüller, *Phys. Rev. Lett.* **93**, 163001 (2004).
- [22] R. Heidemann, U. Raitzsch, V. Bendkowsky, B. Butscher, R. Löw, Luis Santos, and T. Pfau, *Phys. Rev. Lett.* **99**, 163601 (2007).
- [23] U. Raitzsch, V. Bendkowsky, R. Heidemann, B. Butscher, R. Löw, and T. Pfau, *Phys. Rev. Lett.* **100**, 013002 (2008).
- [24] E. Urban, T. A. Johnson, T. Henage, L. Isenhower, D. D. Yavuz, T. G. Walker, and M. Saffman *Nature Physics* **5**, 110 (2009).
- [25] A. Gaëtan, Y. Miroshnychenko, T. Wilk, A. Chotia, M. Viteau, D. Comparat, P. Pillet, A. Browaeys, and P. Grangier, *Nature Physics* **5**, 115 (2009).
- [26] T. Pohl, E. Demler, and M. D. Lukin, *Phys. Rev. Lett.* **104**, 043002 (2010).

- [27] T. Cubel Liebisch, A. Reinhard, P. R. Berman, and G. Raithel, Phys. Rev. Lett. **95**, 253002 (2005).
- [28] T. Vogt, M. Viteau, J. Zhao, A. Chotia, D. Comparat, and P. Pillet, Phys. Rev. Lett. **97**, 083003 (2006).
- [29] N. Malossi, M. M. Valado, E. Arimondo, O. Morsch, and D. Ciampini, J. of Phys.: Conference Series **594**, 012041 (2015).
- [30] R. Heidemann, U. Raitzsch, V. Bendkowsky, B. Butscher, R. Löw, and T. Pfau, Phys. Rev. Lett. **100**, 033601 (2008).
- [31] J. Wang, M. Gacesa, and R. Côté, Phys. Rev. Lett. **114**, 243003 (2015).
- [32] T. Karpiuk, M. Brewczyk, K. Rzażewski, A. Gaj, J. B. Balewski, A. T. Krupp, M. Schlagmüller, R. Löw, S. Hofferberth, and T. Pfau, N. J. Phys. **17**, 053046 (2015).
- [33] N. Henkel, R. Nath, and T. Pohl, Phys. Rev. Lett. **104**, 195302 (2010).
- [34] M. Viteau, M. G. Bason, J. Radogostowicz, N. Malossi, D. Ciampini, O. Morsch, and E. Arimondo, Phys. Rev. Lett. **107**, 060402 (2011).
- [35] Y. O. Dudin, L. Li, F. Bariani, and A. Kuzmich, Nature Physics **8**, 790 (2012).
- [36] T. M. Weber, M. Hning, T. Niederprüm, T. Manthey, O. Thomas, V. Guarrera, M. Fleischhauer, G. Barontini, and H. Ott, Nature Physics **11**, 157 (2015).
- [37] T. Keating, K. Goyal, Y.-Y. Jau, G. W. Biedermann, A. J. Landahl, and I. H. Deutsch Phys. Rev. A **87**, 052314 (2013).
- [38] M. Saffman, J. Phys. B: At. Mol. Opt. Phys. **49**, 202001 (2016).
- [39] P. Z. Zhao, X.-D. Cui, G. F. Xu, Erik Sjöqvist, and D. M. Tong, Phys. Rev. A **96**, 052316 (2017).
- [40] T. Wilk, A. Gaëtan, C. Evellin, J. Wolters, Y. Miroshnychenko, P. Grangier, and A. Browaeys, Phys. Rev. Lett. **104**, 010502 (2010).
- [41] L. Isenhower, E. Urban, X. L. Zhang, A. T. Gill, T. Henage, T. A. Johnson,\* T. G. Walker, and M. Saffman, Phys. Rev. Lett. **104**, 010503 (2010).

- [42] I. Friedler, D. Petrosyan, M. Fleischhauer, and G. Kurizki, *Phys. Rev. A* **72**, 043803 (2005).
- [43] J. T. Young, T. Boulier, E. Magnan, E. A. Goldschmidt, R. M. Wilson, S. L. Rolston, J. V. Porto, and A. V. Gorshkov, *Phys. Rev. A* **97**, 023424 (2018).
- [44] A. W. Glaetzle, R. Nath, B. Zhao, G. Pupillo, and P. Zoller, *Phys. Rev. A* **86**, 043403 (2012).
- [45] D. Petrosyan, M. Höning, and M. Fleischhauer, *Phys. Rev. A* **87**, 053414 (2013).
- [46] D. W. Schönleber, M. Gärttner, and J. Evers, *Phys. Rev. A* **89**, 033421 (2014).
- [47] E. Levi, R. Gutiérrez, and I. Lesanovsky, *J. Phys. B: At. Mol. Opt. Phys.* **49**, 184003 (2016).
- [48] N. Malossi, M. M. Valado, S. Scotto, P. Huillery, P. Pillet, D. Ciampini, E. Arimondo, and O. Morsch, *Phys. Rev. Lett.* **113**, 023006 (2014).
- [49] C. Carr, R. Ritter, C. G. Wade, C. S. Adams, and K. J. Weatherill, *Phys. Rev. Lett.* **111**, 113901 (2013).
- [50] N. Šibalić, C. G. Wade, C. S. Adams, K. J. Weatherill, and T. Pohl, *Phys. Rev. A* **94**, 011401(R) (2016).
- [51] F. Letscher, O. Thomas, T. Niederprüm, M. Fleischhauer, and H. Ott, *Phys. Rev. X* **7**, 021020 (2017).
- [52] N. R. de Melo, C. G. Wade, N. Šibalić, J. M. Kondo, C. S. Adams, and K. J. Weatherill, *Phys. Rev. A* **93**, 063863 (2016).
- [53] T. Baluktsian, B. Huber, R. Löw, and T. Pfau, *Phys. Rev. Lett.* **110**, 123001 (2013).
- [54] A. Urvoy, F. Ripka, I. Lesanovsky, D. Booth, J. P. Shaffer, T. Pfau, and R. Löw, *Phys. Rev. Lett.* **114**, 203002 (2015).
- [55] S. Yoshida, J. Burgdörfer, X. Zhang, and F. B. Dunning, *Phys. Rev. A* **95**, 042705 (2017).
- [56] D. Kara, A. Bhowmick, and A. K. Mohapatra, *Scientific Reports* volume **8**, 5256 (2018).
- [57] D. Weller, A. Urvoy, A. Rico, R. Löw, and H. Kübler, *Phys. Rev. A* **94**, 063820 (2016).



- [58] J. D. Pritchard. Cooperative Optical Non-linearity in a blockaded Rydberg Ensemble, a Ph.D. thesis. Durham University (2011).
- [59] A. Bhowmick, D. Kara, and A. K. Mohapatra arXiv: 1802.06599v1 (2018).
- [60] The detailed calculation for 2, 3, 4 and  $N$ -interacting is done by Dushmanta Kara.
- [61] C. E. Burkhardt and J. J. Leventhal. Topics in atomic physics. Springer Science+Business Media, Inc., 233 Spring Street, New York, NY 10013, USA (2006).
- [62] G. W. F. Drake, and R. A. Swainson, Phys. Rev. A **44**, 5448 (1991).
- [63] B. Sanguinetti, H. O. Majeed, M. L. Jones, and B. T. H. Varcoe, J. Phys. B: At. Mol. Opt. Phys. **42**, 165004 (2009).
- [64] V. A. Sautenkov, S. A. Saakyan, E. V. Vilshanskaya, D. A. Murashkin, B. B. Zelener, and B. V. Zelener, Laser Phys. **26**, 115701 (2016).
- [65] V. A. Kosteleck and M. M. Nieto, Physical Review A **32**, 3243 (1985).
- [66] M. Mack, F. Karlewski, H. Hattermann, S. Höckh, F. Jessen, D. Cano, and J. Fortágh, Phys. Rev. A **83**, 052515 (2011).
- [67] D. Kara *et. al* "Study of multi-atom dephasing in Rydberg blockade" (under preparation).

# Chapter 7

## Experiment towards Ultra-cold atoms

In atomic physics, the objects of our study are atoms. At room temperature, the atom flies at the speed of the jet airplane. Historically, the atomic physicists studied atoms which have the speed of a jet airplane. It would always be better to have an ensemble of atoms which are very slow or at rest, so that one can perform precision measurement on atoms [1–7]. The first motivation to have cold atoms is to build atomic clocks [8–12]. Nowadays the atom clocks are used to maintain time and frequency standard. Contextually, the cold atoms are also used to study Rydberg blockade [13–24]. In thermal atoms, the line-width of a transition is dominated by the Doppler effect due to the atomic motion, which follows the Maxwell Boltzmann velocity distribution corresponding to the temperature of the ensemble. Cooling of atoms near the Doppler limit  $\sim 100 \mu\text{K}$  helps to get rid of Doppler broadening. In the experiment with thermal atoms (chapter 6), the dephasing of the system is mostly dominated by superatom dephasing and relative laser frequency noise between the probe and the coupling laser. The relative laser frequency noise can be reduced by locking the lasers in EIT transition line. The superatom dephasing consists of the dipole dephasing due to the transverse velocity of the atoms relative to the laser propagation and the dipole dephasing due to the difference in velocity of the constituent atoms. In the frozen ensemble of atoms, both the dephasing will be neglected. As a result the multi-atom coherence will be dominated by superatom Rabi frequency only [17, 30–33].

On further cooling by the evaporative cooling process, Bose-Einstein condensation (BEC) can be reached. The typical size of the cold atom is few mm whereas the typical size of BEC is few  $\mu\text{m}$ . Therefore, for the Rydberg excitation to a large quantum number state (e.g.  $n = 70$ ), the Rydberg blockade radius will be larger than the size of the BEC. In this case, the total BEC collectively participates in the cooperative Rydberg excitation in a single Rydberg blockade [25, 26]. It is also observed for BEC loaded in the optical lattice [27]. Since the number

density of the BEC is very high ( $\sim 10^{12} \text{ c.c.}^{-1}$ ), a very strong Rydberg blockade interaction can be probed. A study of Rydberg excited electron coupled with BEC is also performed [28, 29].

The objective of laser cooling and trapping of atoms is not only to increase the spatial density of atoms but also the phase-space density of atoms. Cooling the atomic sample in momentum space helps to reduce the micro-motion of atoms inside the spatial trap. It reduces the decay of the excited state of the atom due to collision or transit-time phenomena which leads to narrow line-width of the atomic transition. There is a significant application of narrow atomic transition in the field of precision spectroscopy.

## 7.1 Design of cold-atom setup

In order to prepare the cold atoms in lab, it is required to have a vacuum chamber which can sustain ultrahigh vacuum and a magneto optical setup to trap atoms inside the vacuum chamber. In this section, we will discuss the optical and mechanical designs for cold atom setup. The objective of having cold atoms is to study Rydberg blockade induced many-body effect and Rydberg quantum optics.

## 7.2 Optical setup

A strategic frequency setup is shown in fig. (7.1). Here, we need to have a saturation absorption spectroscopy to stabilise the laser frequency on a cross-over transition line (as we have discussed in Sec. 3.3 and 3.4) as shown in the fig. (7.1). AOM1 is used to generate the frequency of light where the laser has to be stabilised. AOM2 is used to generate MOT beams. In order to generate spin polarise beam, we have used AOM3. Using AOM4 and AOM5 experimental probe lights are generated. AOM6 is required to generate the light to be used in Rydberg-EIT locking in order to reduce relative frequency noise between probe and coupling laser, which will be used in the heterodyne detection experiment. The optical setup for cold atom and Rydberg experiment is depicted in fig. (7.2). The laser light is generated from an ECDL and passes through the optical isolator (OI) to prevent any optical feedback from any other optical component used in the experiment. The saturation absorption spectroscopy (SAS) is done in order to stabilise the laser in a particular rubidium spectral line. The optical setup for SAS is depicted in the sector A in fig. (7.2). In the sector B of fig. (7.2), the laser beams for optical trap is generated by using AOM2. A repump laser prepared by using a different ECDL,

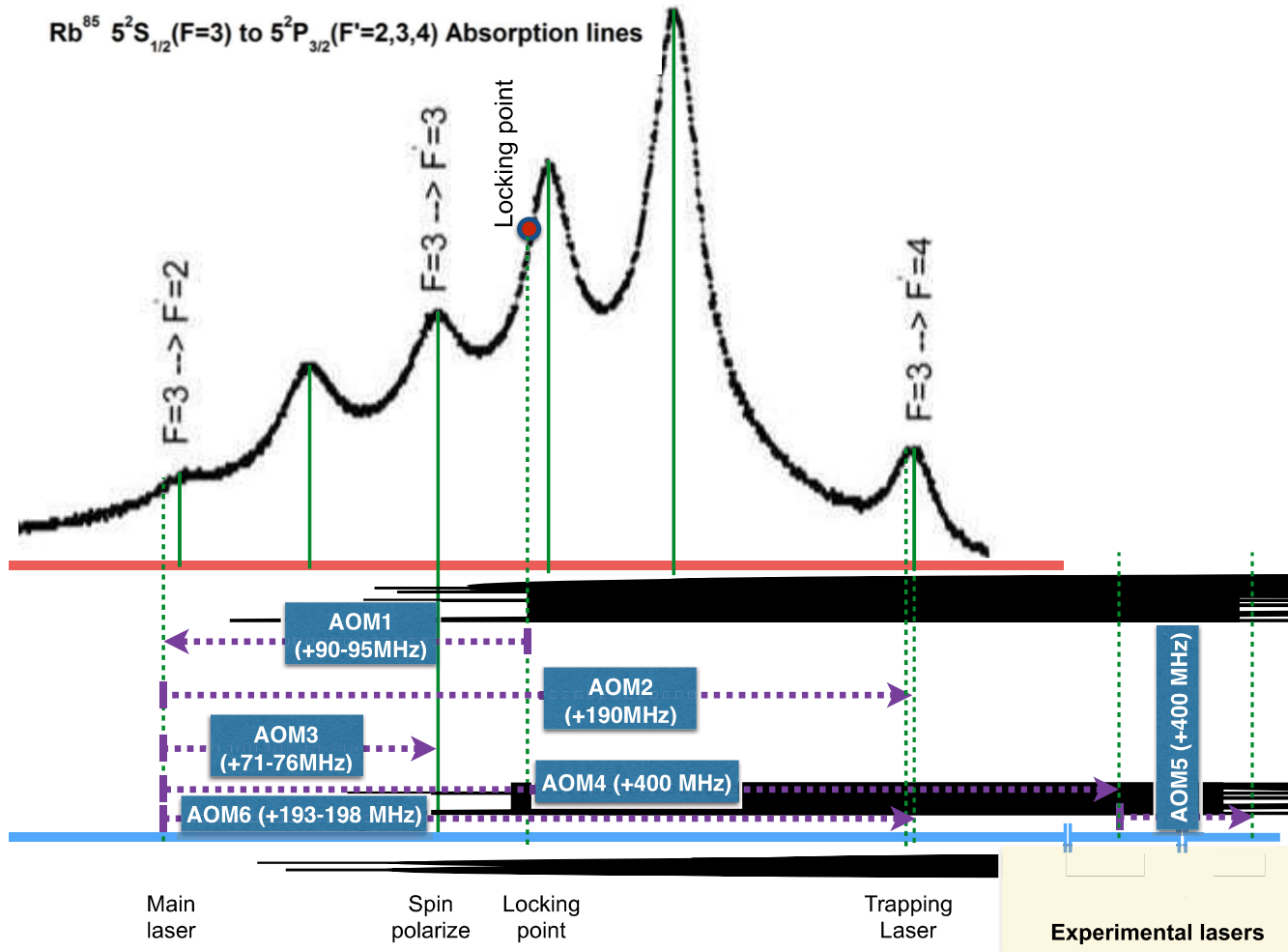


Figure 7.1: Frequencies of light required to trap atoms and generation of probe lights for experiment.

is taken to the setup using a fiber. The repump laser is mixed with the MOT beam by using a PBS and they are splitted into 3 equal powers and coupled with three different fibers. These lights will be used for optical trap as well molasses cooling. Sector C of fig. (7.2) is designed to prepare spin polarise light by using AOM3. The probes for optical heterodyne detection technique are generated in sector D of fig. (7.2). The AOM4 shifts the frequency of the main laser in such a way that the generated laser will be typically 180 MHz blue detuned from the atomic transition  $5S_{1/2}(F=3) \rightarrow 5P_{3/2}(F'=4)$  in order to get rid of absorption of probe. Another probe is generated by taking the output of the AOM4 and made to double pass through AOM5 so that they have the frequency offset around 400 MHz, which is much greater than the expected linewidth of the two photon resonance signal in cold atom system.

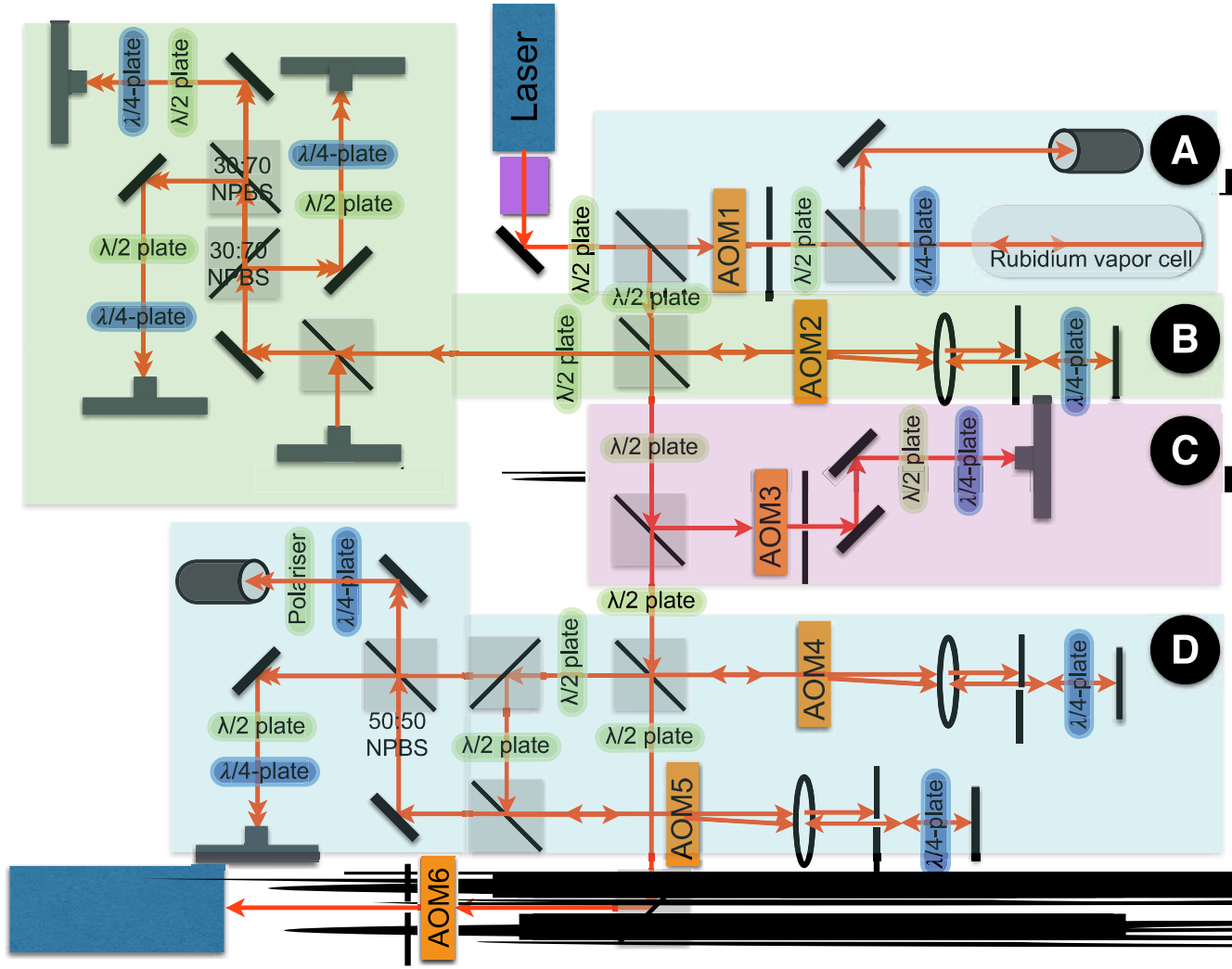


Figure 7.2: Optical setup to trap atoms and to perform experiment. Note that the beam splitter which are not marked are PBS.

### 7.2.1 Generation and stabilisation of repump laser

As we have mentioned in the Sec. ?? that, due to the quadruple decay the population cannot go to initial state. Therefore, the atoms cannot contribute to the trapping process and may go outside the trap. In order to avoid the loss, a repump laser is required. An ECDL operating at the 780 nm is used to derive a laser beam which passes through an optical isolator. Then, a saturation absorption spectroscopy (SAS) is done as shown in fig. (7.3). The optical signal for SAS is detected by a FPD (Appendix.A). The electronic signal from FPD is taken to Digilock-110 which is connected to SC-110. The frequency of the laser is scanned by SC-110. The laser frequency is locked by Digilock-110 as we described in Sec. 3.4. Here, one part of the laser

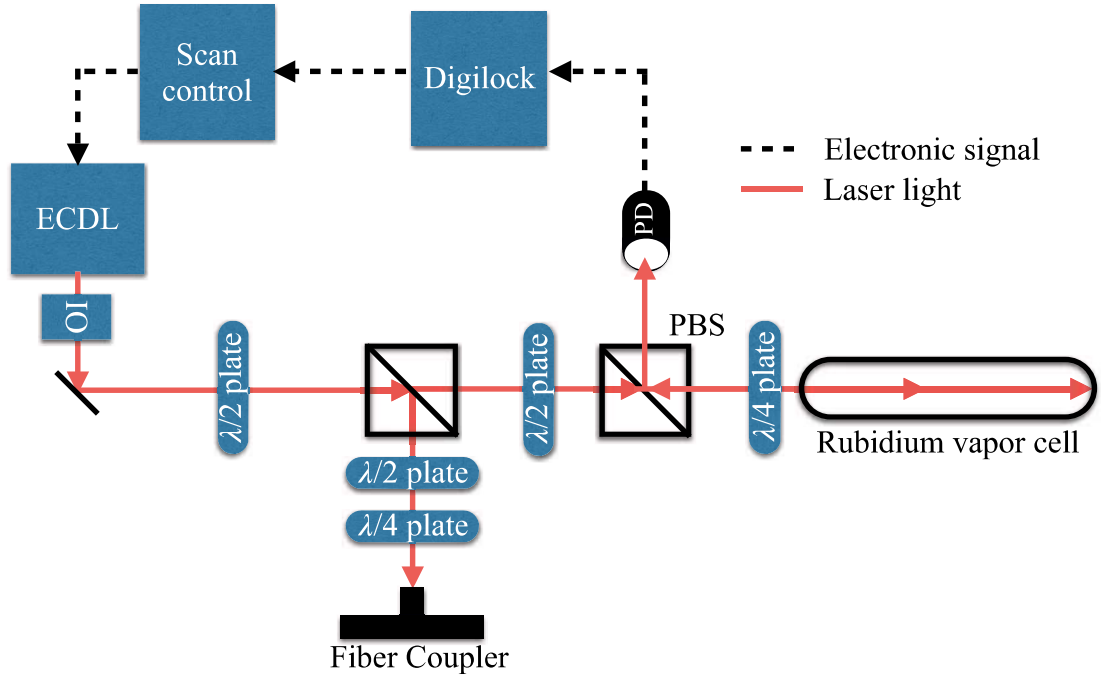


Figure 7.3: Generation and stabilisation of repump laser.

beam is used to lock the laser and another part is coupled to a fiber. The other part of the fiber is depicted in sector B of fig. (7.2), where repump gets mixed with trapping laser.

### 7.2.2 Stabilisation of TA-SHG-Pro

The coupling laser for optical heterodyne detection technique has to be derived from Toptica TA-SHG-Pro. In order to minimise the relative laser frequency noise between probe and the coupling laser, the coupling laser has to be locked in Rydberg-EIT signal. Then, the phase of the probe and the coupling laser will be correlated and hence the relative laser noise reduces. TA-SHG-Pro has a master laser operating at 960 nm, which passes through two tapered amplifier (TA) to trigger the second harmonic generation (SHG) process by a non-linear crystal placed inside the cavity as shown in fig. (7.4). The master laser is scanned by an external scan control module SC-110. The output of the SHG-cavity has wavelength of 480 nm. The output of the blue laser is splitted into two part. One part is used in OHDT experiment for Rydberg excitation and rest of it is used to make Rydberg-EIT. Since experimental probe is blue detuned, the coupling laser has to be red detuned. In order to make the blue laser resonant for the transition  $5P_{3/2} \rightarrow nS_{1/2}$ , an AOM setup is required to shift the frequency of the blue laser. A double pass AOM alignment is depicted in fig. (7.4). The frequency shift of the blue laser is such

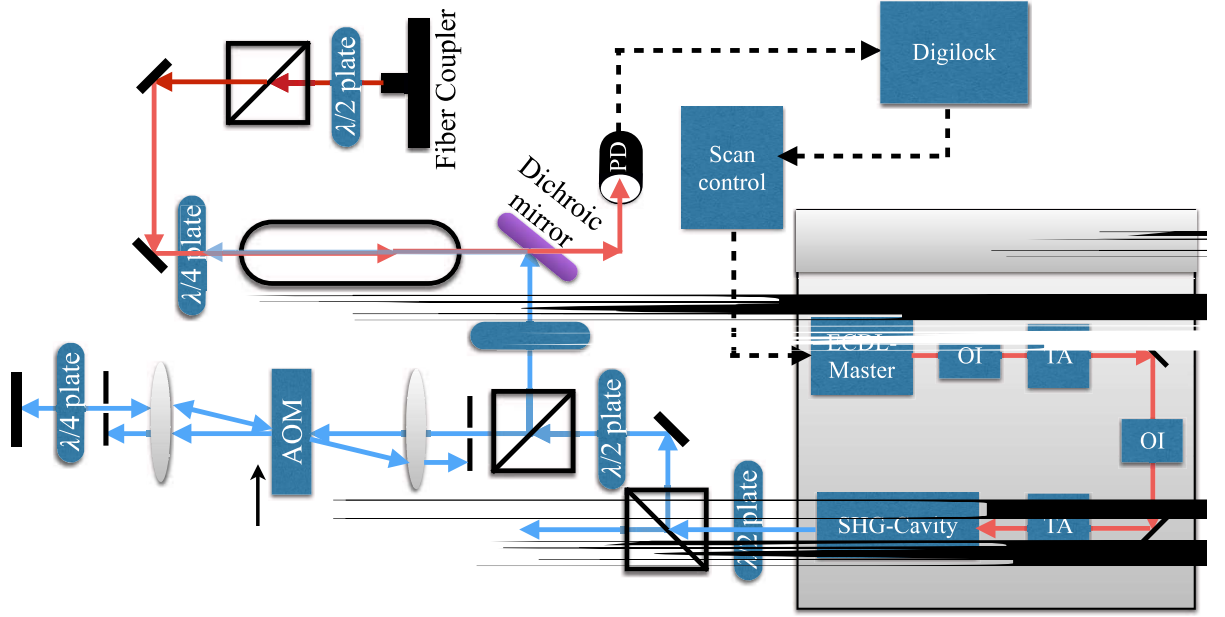


Figure 7.4: Setup for stabilisation of blue laser on Rydberg-EIT signal. The blue arrows signify the laser light of wavelength 480 nm. The red arrows coming out from a fiber coupler has the wavelength of 780 nm. The red arrows inside the TA-SHG-Pro has the wavelength 960 nm. The dashed line directs the flow of the electronic signal.

that together with 780 nm laser it will satisfy Rydberg-EIT condition. A dichroic mirror is placed to counter propagate the blue laser to the 780 nm laser inside the medium. The optical EIT signal is detected by a FPD (Appendix. A). The electronic signal of the FPD is taken to Digilock-110 to lock the master laser in EIT-transition line. The similar mechanism has to be used as described in Sec. 3.4.

### 7.3 Vacuum setup

In order to prepare cold atom, we have designed a vacuum chamber which can sustain ultra high vacuum. The mechanical design of the chamber is done such that the trapping optical field and the lasers involved in OHDT can easily enter into the chamber and exit from the chamber. The schematic diagram of cold Rydberg experiment is given in fig(7.5). The objective of getting ultra-high vacuum is to reduce the scattering of rubidium atom from the natural gas elements. Natural gas contains 78.084% of  $N_2$  and 20.946% of  $O_2$ . Rest of the contents are  $H_2$ ,  $He$ ,  $N_2O$ ,  $NO_2$ ,  $CO_2$ ,  $CH_4$  etc. There are few inert gas, for example  $Ar$ ,  $Ne$ ,  $Kr$ ,  $Xe$  etc. The cold rubidium atom can collide with all these room temperature atoms and molecules and can acquire kinetic energy. With sufficiently higher kinetic energy, the atoms can easily fly out of

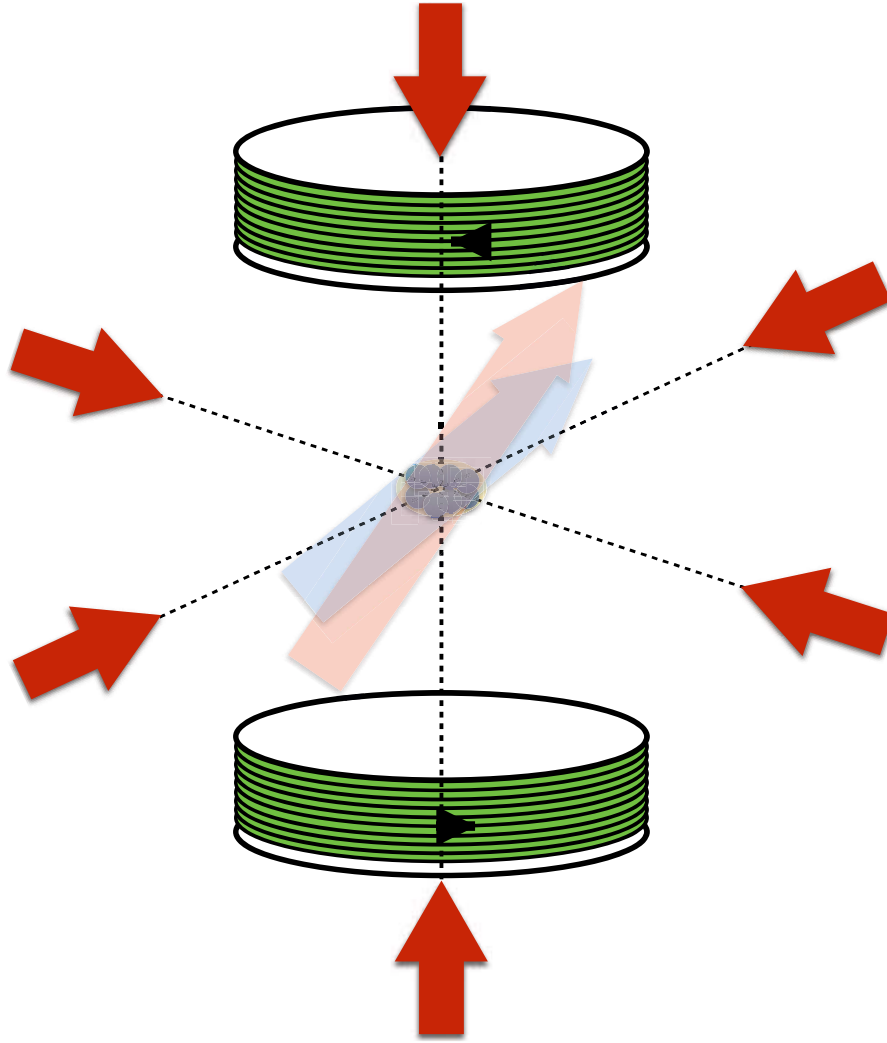


Figure 7.5: Realisation of experiment on Rydberg excited cold atoms. The red lasers are the MOT lasers. The blue and the orange lasers together satisfy the two photon resonance to the Rydberg excited state.

the trap. Hence the trapping will be inefficient. Our goal is to reach the vacuum of the order  $10^{-11}$  mbar, where the density of natural gas is expected to be almost absent and hence, increase the stability of cold atom.

### 7.3.1 Design of vacuum chamber and flange multiplexer

The spherical octagonal vacuum chamber has eight DN40CF flange in each arm of the octagon and two DN100CF flange is placed as shown in fig. (7.6.a). The width of the chamber is 2.78 inch. Since we need two experimental probe and one coupling beam to enter the chamber in order to do Rydberg experiment, we have designed a flange multiplexer. The flange multiplexer



contains a one DN63CF flange perpendicular to its base and four units of DN40CF which has  $15^\circ$  inclination with the DN63CF-tube and the base of the multiplexer is DN100CF as depicted in fig. (7.6.b). The flange multiplexer is designed in such a way that the anti-Helmholtz coil can be held in its rim. The vacuum chamber along with flange multiplexer is shown in the fig. (7.6.c). A commercial flange multiplexer is connected to the right end of the vacuum chamber.

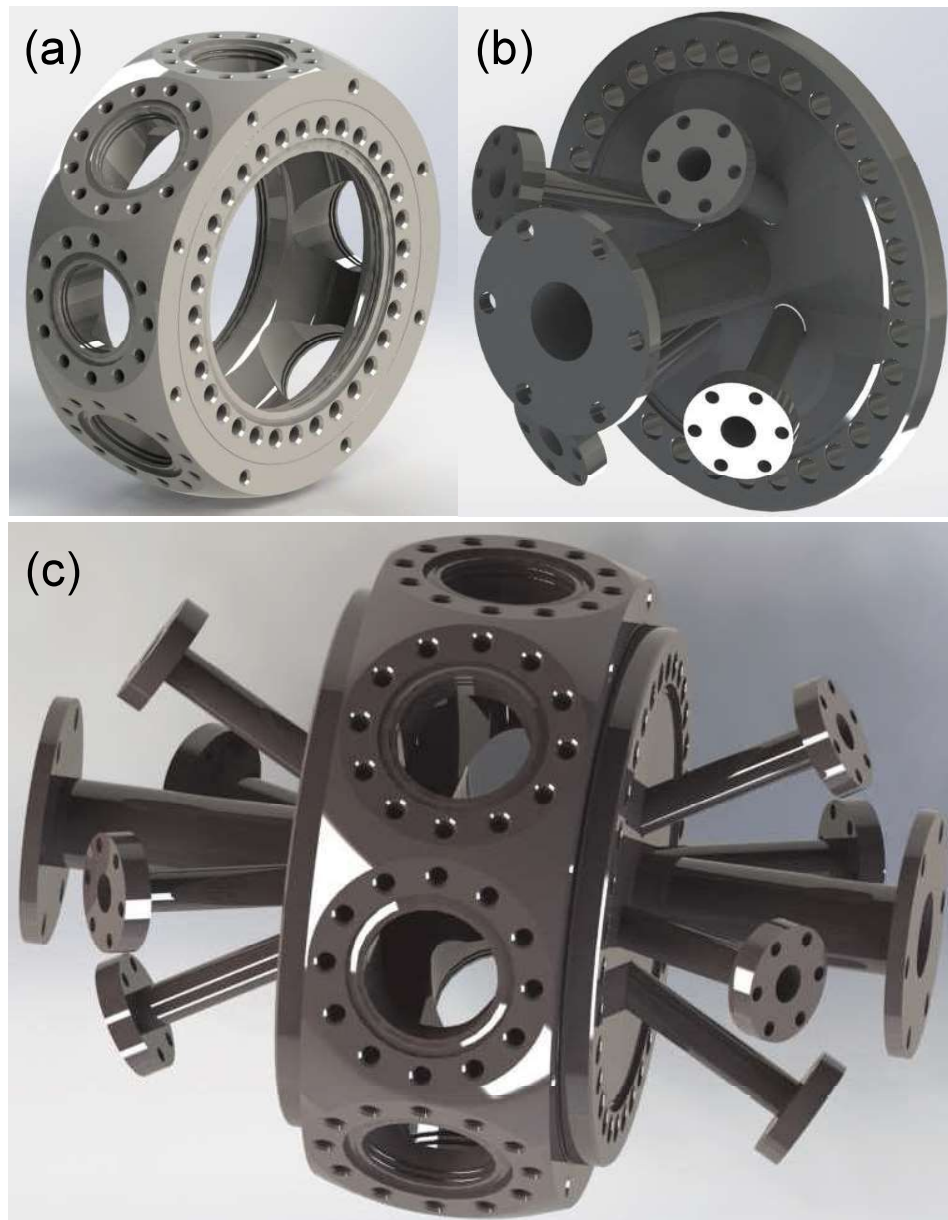


Figure 7.6: (a) Spherical octagonal chamber. (b) Flange multiplexer. (c) Flange multiplexer connected with main chamber.

### 7.3.2 Integrated mechanical design for vacuum setup

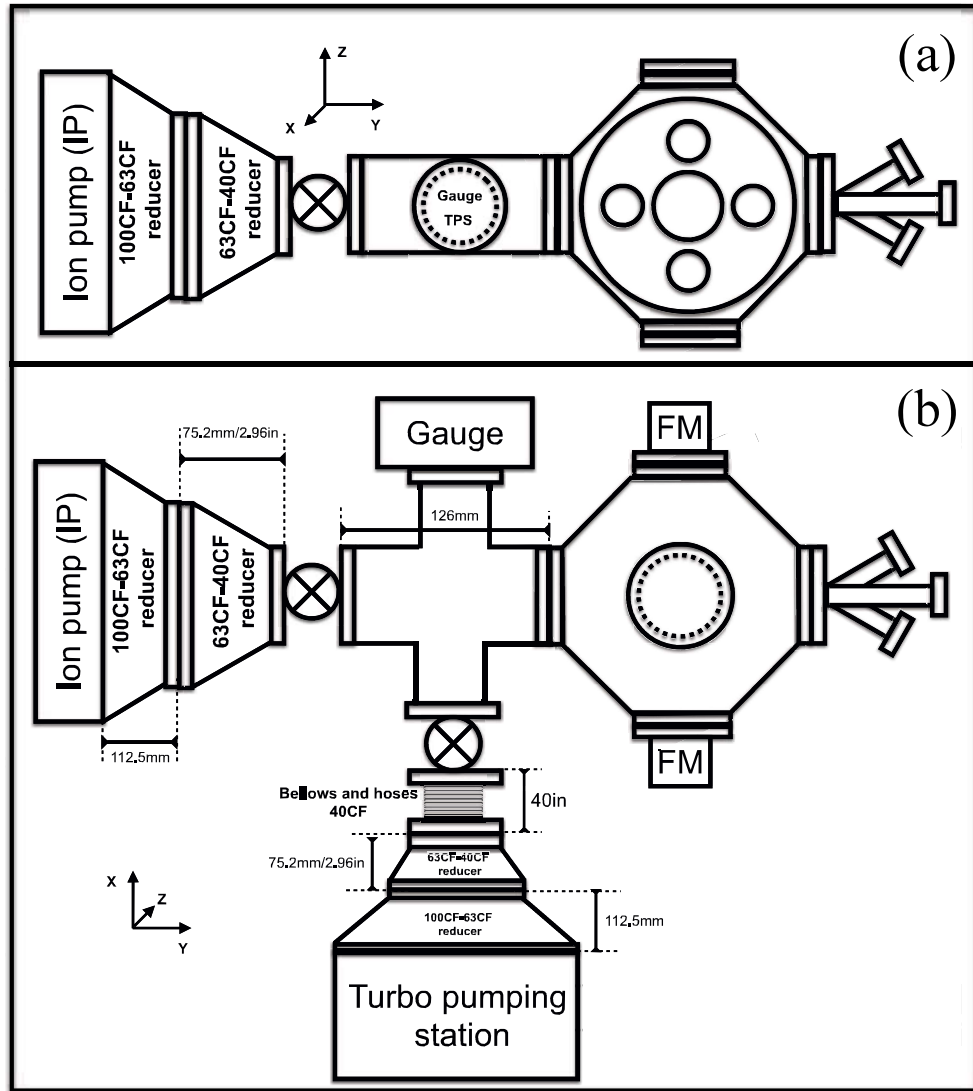


Figure 7.7: Pump and gauge assembly with vacuum chamber.

In order to have ultra high vacuum inside the chamber a turbo pumping station and an ion pump are required. Turbo pumping station (TPS) creates vacuum upto  $10^{-7}$  Torr from atmospheric pressure. A pressure gauge is connected with the pumping station in order to monitor the pressure inside the assembly. The turbo pumping station with DN100CF inlet flange is connected to a flexible bellow of DN40CF via a series of DN100CF to DN63CF reducer and DN63CF to DN40CF reducer. The bellow is connected to a DN40CF four-way-cross via a gate-valve. This four-way-cross is connected to one of the DN40CF flange of the vacuum chamber. After reaching the pressure of  $10^{-7}$  Torr by TPS, it has to be switched off and

the gate valve has to be closed. An ion pump (with DN100CF inlet flange) brings the pressure to  $10^{-11}$  Torr which is connected to the four-way-cross via a series of DN100CF to DN63CF reducer and DN63CF to DN40CF reducer. A gate valve is placed between the reducer and the four-way-cross. An ultra high vacuum gage is connected to the left over port of the four-way-cross in order to monitor vacuum inside the assembly. Note that, the UHV-gauge has to be switched on when the pressure of the assembly reaches to  $10^{-7}$  Torr. The integrated vacuum is depicted in two different views in fig. (7.7.a) and fig. (7.7.b) respectively.

### 7.3.3 Opto-Mechanical cage system design

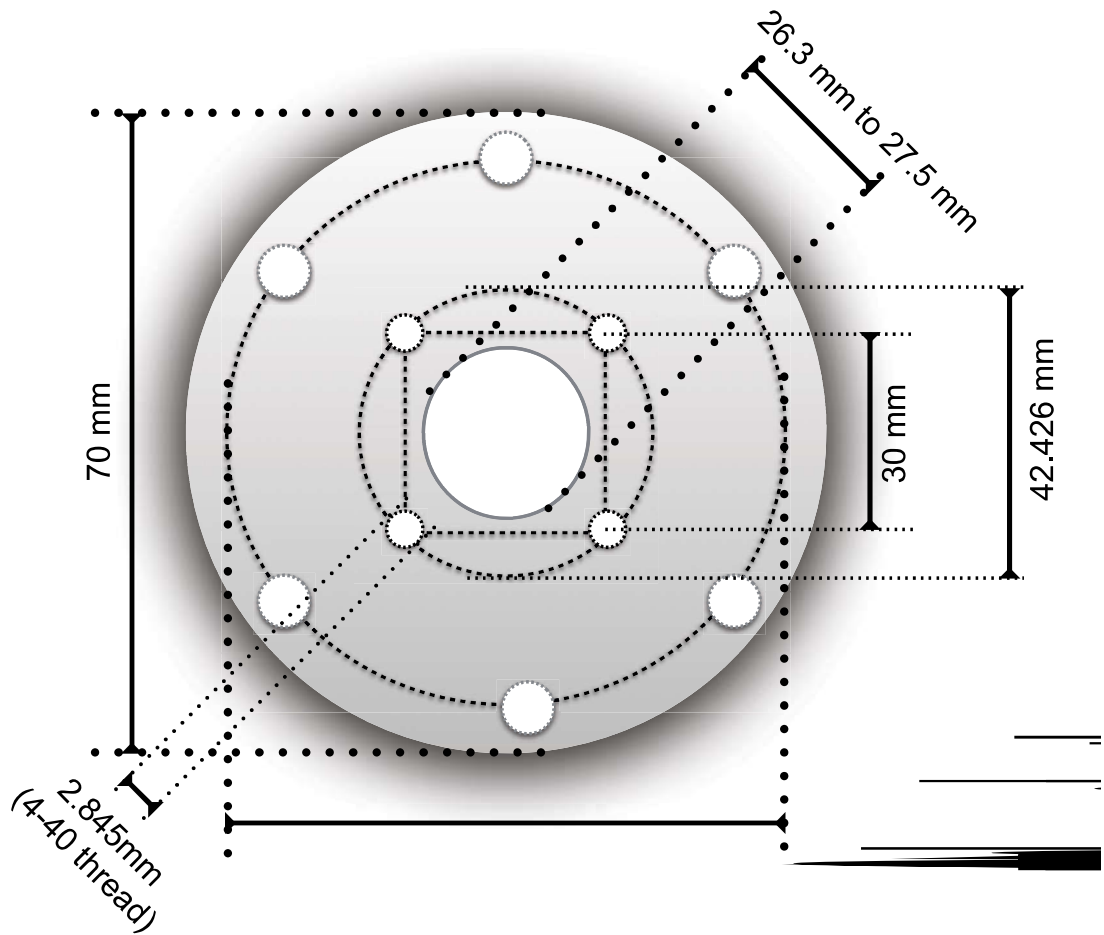


Figure 7.8: Design of cage adapter.

An opto-mechanical cage system is required to mount and align the MOT beam in vacuum chamber. The cage system has to be mounted on a cage adapter and the cage adapter should be connected to the DN40CF view port of the vacuum chamber. The design of cage adapter

is depicted in fig. (7.8). The optical cage assembly is connected to the cage adapter. There

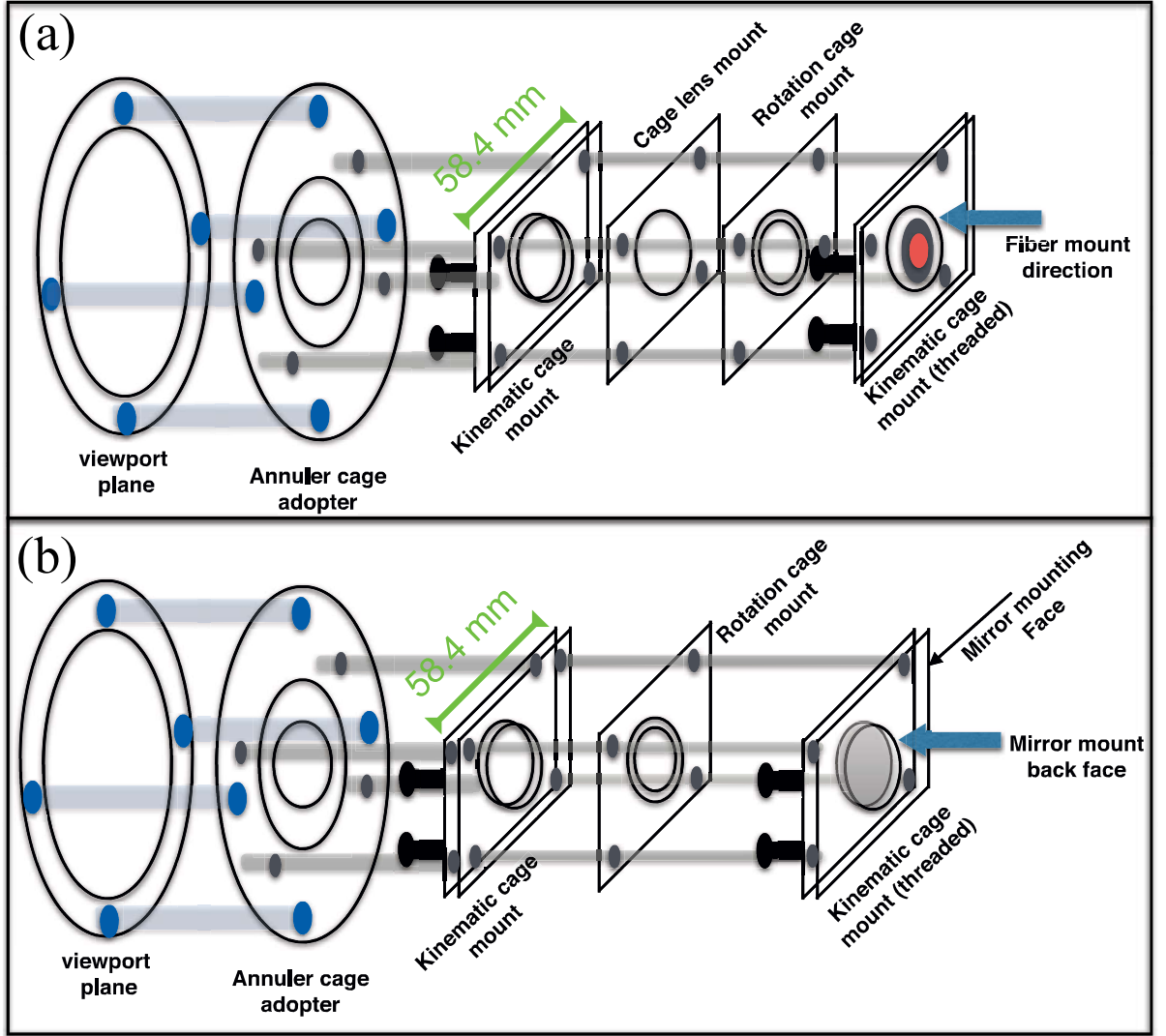


Figure 7.9: Opto-mechanical cage assembly. (a) Assembly for input MOT beam to the chamber. (b) Assembly for retro-reflected MOT beam.

are two assembly setups that are depicted in fig. (7.9.a & b). fig. (7.9.a) is the design for input MOT beam. The MOT beams are prepared and taken from the optical setup described in fig. (7.2) using a fiber. The other end of the fiber is connected to the kinematic cage mount (threaded) by a terminated fiber mount. Since, the fiber mount does not have any collimator, the laser starts diverging as soon as it comes out of the fiber. A lens with a cage lens mount is also placed such a way that the laser light at the output of the lens will have the diameter of 1 cm. A cage rotation mount with a  $\frac{\lambda}{4}$ -plate is inserted in order to make perfect circularly polarised light for MOT. All these mounts are connected with one face of a kinematic mount by

4 cage rods. The other side of the kinematic mount is connected to the cage adapter by using another set of 4 cage rods. The kinematic mount is used to align whole cage assembly with respect to the viewport. The kinematic fiber mount aligns the laser with respect to the cage assembly. fig. (7.9.a) is a similar design without the lens where a mirror with kinematic cage mirror mount replaces the fiber mount. The assembly is designed to retro reflect the trapping beam to the chamber. A  $\frac{\lambda}{4}$ -plate is placed in such a way that the polarisation of the incident circularly polarised light can be flipped.

# Bibliography

- [1] J. Ye, S. Blatt, M. M. Boyd, S.M. Foreman, E. R. Hudson, T. Ido, B. Lev, A. D. Ludlow, B. C. Sawyer, B. Stuhl and T. Zelevinsky, AIP Conference Proceedings, **869**, 80 (2006).
- [2] J. Wang, L. Zhou, R.-b. Li, M. Liu, and M.-s. Zhan, Front. Phys. China, **4(2)**, 179 (2009).
- [3] F. Sorrentino, M. de Angelis, A. Bertoldi, L. Cacciapuoti, A. Giorgini, M. Prevedelli, G. Rosi, G. M. Tino, JEOS:RP, **4**, 090250 (2009).
- [4] S.-Y. Lan, P.-C. Kuan, B. Estey, P. Haslinger, and H. Müller, Phys. Rev. Lett., **108**, 090402 (2012).
- [5] G. Rosi, F. Sorrentino, L. Cacciapuoti, M. Prevedelli, and G. M. Tino, Nature, **510**, 518 (2014).
- [6] S. Hamzeloui, N. Arias, V. Abediyeh, D. Martínez, M. Gutiérrez, E. Uruñuela, E. del Rio, E. Cerda-Méndez, E. Gomez and V. M. Valenzuela, Journal of Physics: Conference Series, **698**, 012011 (2016).
- [7] Z. Xibo, and Y. Jun, National Science Review, **3(2)**, 189 (2016).
- [8] A. Bauch, Meas. Sci. Technol., **14**, 1159 (2003).
- [9] G. K. Campbell, and W. D. Phillips, Phil. Trans. R. Soc. A, **369**, 4078 (2011).
- [10] D. Calonico EPJ Web of Conferences, **58**, 03002 (2013).
- [11] T.L. Nicholson, S. L. Campbell, R. B. Hutson, G. E. Marti, B. J. Bloom, R. L. McNally, W. Zhang, M. D. Barrett, M. S. Safronova, G. F. Strouse, W. L. Tew, and J. Ye, Nature Com., **6**, 6896 (2015).
- [12] I. Dutta, D. Savoie, B. Fang, B. Venon, C. L. Garrido Alzar, R. Geiger, and A. Landragin, Phys. Rev. Lett., **116**, 183003 (2016).

- [13] D. Tong, S. M. Farooqi, J. Stanojevic, S. Krishnan, Y. P. Zhang, R. Cote, E. E. Eyler, and P. L. Gould, Phys. Rev. Lett., **93**, 063001 (2004).
- [14] K. Singer, M. Reetz-Lamour, T. Amthor, L. G. Marcassa, and M. Weidemüller, Phys. Rev. Lett., **93**, 163001 (2004).
- [15] T. Cubel Liebisch, A. Reinhard, P. R. Berman, and G. Raithel, Phys. Rev. Lett., **95**, 253002 (2005).
- [16] T. Vogt, M. Viteau, J. Zhao, A. Chotia, D. Comparat, and P. Pillet, Phys. Rev. Lett., **97**, 083003 (2006).
- [17] R. Heidemann, U. Raitzsch, V. Bendkowsky, B. Butscher, R. Löw, Luis Santos, and T. Pfau, Phys. Rev. Lett., **99**, 163601 (2007).
- [18] U. Raitzsch, V. Bendkowsky, R. Heidemann, B. Butscher, R. Löw, and T. Pfau, Phys. Rev. Lett., **100**, 013002 (2008).
- [19] E. Urban, T. A. Johnson, T. Henage, L. Isenhower, D. D. Yavuz, T. G. Walker, and M. Saffman Nature Physics, **5**, 110 (2009).
- [20] A. Gaëtan, Y. Miroshnychenko, T. Wilk, A. Chotia, M. Viteau, D. Comparat, P. Pillet, A. Browaeys, and P. Grangier, Nature Physics, **5**, 115 (2009).
- [21] V. Parigi, E. Bimbard, J. Stanojevic, A. J. Hilliard, F. Nogrette, R. Tualle-Brouri, A. Ourjoumtsev, and P. Grangier, Phys. Rev. Lett., **109**, 233602 (2012).
- [22] A. Schwarzkopf, R. E. Sapiro, and G. Raithel, Phys. Rev. Lett., **107**, 103001 (2011).
- [23] G. Günter, M. Robert-de-Saint-Vincent, H. Schempp, C. S. Hofmann, S. Whitlock, and M. Weidemüller, Phys. Rev. Lett., **108**, 013002 (2012).
- [24] M. Viteau, P. Huillery, M. G. Bason, N. Malossi, D. Ciampini, O. Morsch, E. Arimondo, D. Comparat, and P. Pillet, Phys. Rev. Lett., **109**, 053002 (2012).
- [25] N. Malossi, M. M. Valado, E. Arimondo, O. Morsch, and D. Ciampini, J. of Phys.: Conference Series **594**, 012041 (2015).
- [26] R. Heidemann, U. Raitzsch, V. Bendkowsky, B. Butscher, R. Löw, and T. Pfau, Phys. Rev. Lett., **100**, 033601 (2008).

- [27] M. Viteau, M. G. Bason, J. Radogostowicz, N. Malossi, D. Ciampini, O. Morsch, and E. Arimondo, *Phys. Rev. Lett.*, **107**, 060402 (2011).
- [28] J. Wang, M. Gacesa, and R. Côté, *Phys. Rev. Lett.*, **114**, 243003 (2015).
- [29] T. Karpiuk, M. Brewczyk, K. Rzażewski, A. Gaj, J. B. Balewski, A. T. Krupp, M. Schlagmüller, R. Löw, S. Hofferberth, and T. Pfau, *N. J. Phys.*, **17**, 053046 (2015).
- [30] Y. O. Dudin, and A. Kuzmich, *Science*, **336**, 887 (2012).
- [31] H. Weimer, M. Müller, I. Lesanovsky, P. Zoller, and H. P. Büchler, *Nature Phys.*, **6** 382 (2010).
- [32] T. M. Weber, M. Hning, T. Niederprüm, T. Manthey, O. Thomas, V. Guarrera, M. Fleischhauer, G. Barontini, and H. Ott, *Nature Physics*, **11**, 157 (2015).
- [33] C. Tresp. Rydberg polaritons and Rydberg superatoms-novel tools for quantum nonlinear optics, a Ph.D. thesis, Stuttgart university (2017).
- [34] H. J. Metcalf and P. van der Straten, *Laser cooling and trapping*. Springer Science+Business Media, Inc., 175 Fifth Avenue, New York, NY 10010, USA (1999).
- [35] S. Chu, L. Hollberg, J. E. Bjorkholm, A. Cable, and A. Ashkin, *Phys. Rev. Lett.*, **55**, 48 (1985).
- [36] P. D. Lett, R. N. Watts, C. I. Westbrook, W. Phillips, P. L. Gould, and H. Metcalf, *Phys. Rev. Lett.*, **61**, 169 (1988).
- [37] C. Salomon, J. Dalibard, W. Phillips, A. Clairon, and S. Guellati, *Europhys. Lett.*, **12**, 683 (1990).
- [38] E. Raab, L., M. Prentiss, A. Cable, S. Chu, and D. E. Pritchard, *Phys. Rev. Lett.*, **59**, 2631 (1987).
- [39] C.J. Foot. *Atomic Physics*. Oxford University Press. ISBN 978-0-19-850696-6 (2005).
- [40] C. Monroe, W. Swann, H. Robinson, and C. Wieman *Phys. Rev. Lett.*, **65**, 1571 (1990).



# Chapter 8

## Summary and future plan

The existence of the Rydberg blockade in thermal atomic vapor is found while driving the atomic ensemble by the continuous optical field. An optical heterodyne detection technique (OHDT) is developed to investigate the Rydberg blockade experimentally. The OHDT is established in the Rydberg electromagnetically induced transparency (EIT) medium. The measurement of absorption and dispersion of a probe beam while passing through the atomic medium is demonstrated using this technique. A model of EIT involving two probe lasers and a coupling laser is presented to explain the experimental observations. The nonlinear susceptibility of the probe beam is estimated from the experiment. To study the Rydberg interaction, it is required to perform the experiment in the high-density regime of the atomic vapor. But the absorption of the probe beam is higher in the higher density of vapor because it satisfies the single photon resonance condition while studying the Rydberg EIT. In order to study strong Rydberg interaction in the high density of atomic vapor, the probe laser is stabilized far detuned from single photon resonance but together with coupling laser, it satisfies two-photon resonance condition to the Rydberg excited state. The probe laser is stabilized outside the Doppler-broadened hyperfine transition of  $^{85}\text{Rb}$  so that the experiment can be carried out with minimal probe absorption.

The dispersion spectrum of the probe beam observed in this experiment looks like an absorptive signal. The dispersion fringe shape is explained by using a non-interacting model involving a three-level system with a probe and a coupling laser. It is found that the fringe shape is dispersive for the low probe Rabi frequency and it becomes absorptive for higher probe Rabi frequency. This observation is supported by the model presented.

The precision of OHDT for the measurement of the Rydberg population and the phase-shift due to dispersion is studied. It is found out that the minimum Rydberg population measured

using the technique is  $10^{-7}$  and the minimum phase-shift due to the dispersion is  $3 \mu\text{radians}$ . A comparison study of OHDT with direct absorption measurement (DAM) of the probe is also studied. Since OHDT does not get affected by small polarisation rotation due to the imperfection of the optical component used in the experiment, the sensitivity of OHDT to measure phase shift and the Rydberg population is much reliable than that of DAM.

The technique is extended to study the Rydberg blockade in the thermal atomic vapor. A model based on classical counting confirms the existence of the Rydberg blockade phenomenon. A many-body model based on superatom formation due to the Rydberg blockade interaction is also presented. A suppression of density-dependent phase-shift due to dispersion is observed in the experiment for strong Rydberg-Rydberg interaction regime. The many-body model presented agrees well with the observation. A fundamental scaling law of van der Waals interaction strength ( $C_6$ ) with the principal quantum number of the Rydberg excited state is verified by the analysis of the experimental data using the many-body model. This confirms that van der Waals type Rydberg blockade exists in the thermal atomic vapor. The formation of superatom in thermal atomic ensemble justifies the first ever evidence of multi-atom coherence in thermal vapor while driven by a continuous laser field. This opens up the provision to do Rydberg quantum optics using thermal atomic ensemble such as the design of coherent single photon source.

A cold atom setup is designed in order to carry out the study of Rydberg blockade with the frozen atomic ensemble. The OHDT experiment for the Rydberg blockade can also be done using the cold atom system. Using the technique, the dispersion spectrum of a probe interacting with cold atoms can be studied. It is observed that the transition from non-interacting to Rydberg blockade is a second order phase transition [1, 2]. The Rydberg blockade provides ordering in the system as shown in fig. (8.1). The cold-atom system is required to study the phase transition phenomenon more precisely. The anti-blockade interaction can also be studied here. We have seen that by changing two-photon detuning from red-detuning to blue-detuning the interaction can be changed from Rydberg blockade to Rydberg anti-blockade. Therefore a phase diagram can be constructed in terms of two-photon Rabi frequency, two-photon detuning and the density of vapor.

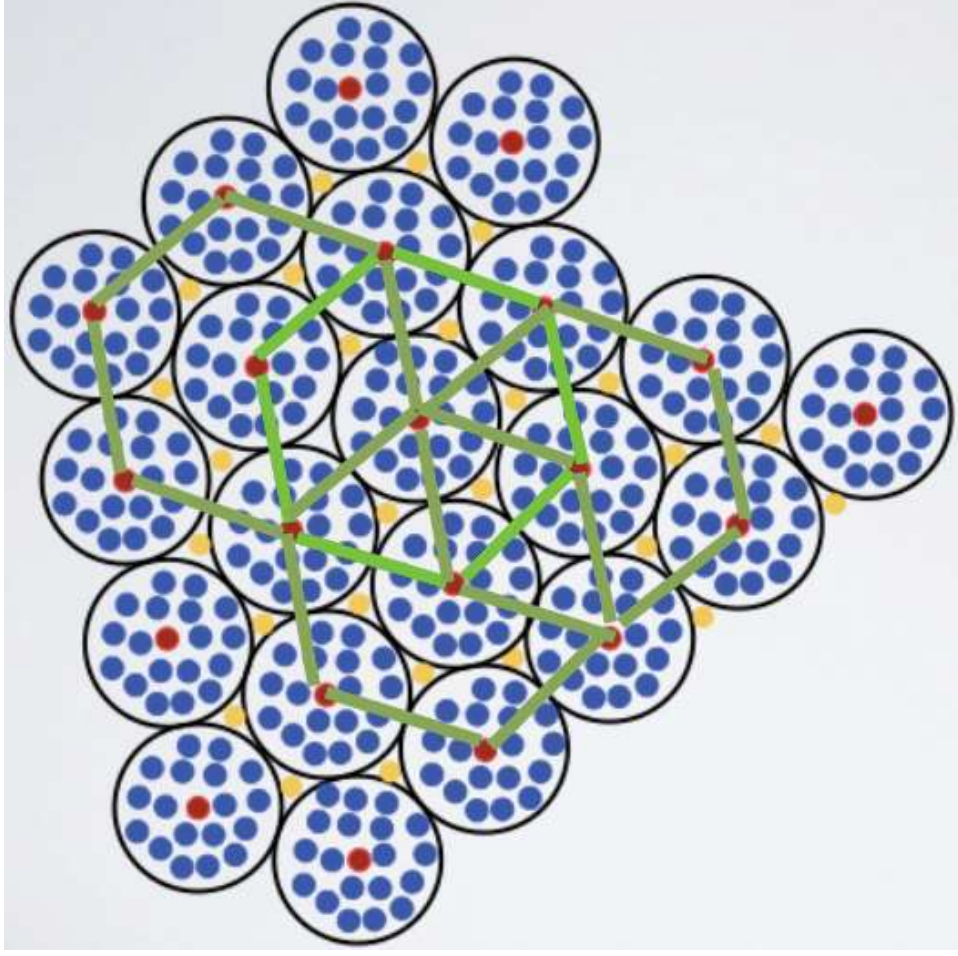


Figure 8.1: Ordered phase created by the Rydberg blockade interaction. The superatoms are arranged such a way that they can form an ordered structure. In order to picturesque the order, the imaginary green lines are used.

As we have mentioned that the Rydberg-EIT experiment cannot be extended to perform experiments in high densities in order to study Rydberg blockade interaction. The issue is the large probe absorption due to larger optical path length inside the rubidium vapor cell. One of the prescription to get rid of this problem is to reduce the optical path length to the order of  $\mu\text{m}$  range [3] as shown in fig. (8.2). The accumulated phase shift due to the Rydberg blockade interaction can be measured fig. (8.2a). On further reduction of the optical path length to few  $\mu\text{m}$ , as shown in fig. (8.2b) which allows performing the experiment with single blockade sphere.

Due to the Rydberg blockade action, the Rabi frequency is modified as  $\sqrt{N_b}\Omega_{eff}$  where  $N_b$  is the number atoms inside the blockade sphere. In our experiment, a very small fraction of

velocity class of atoms contribute to the blockade sphere due to wave-vector mismatch ( $\Delta k$ ) between the probe and the coupling laser in the two-photon resonance process. Using multiple photon cascaded process the wave-vector mismatch can be reduced. The all the velocity class will contribute to the blockade process. In this way, the Rabi frequency can be increased two order of magnitudes more than our current experiment which is expected to be useful for Rydberg nonlinear quantum optics at single photon level.

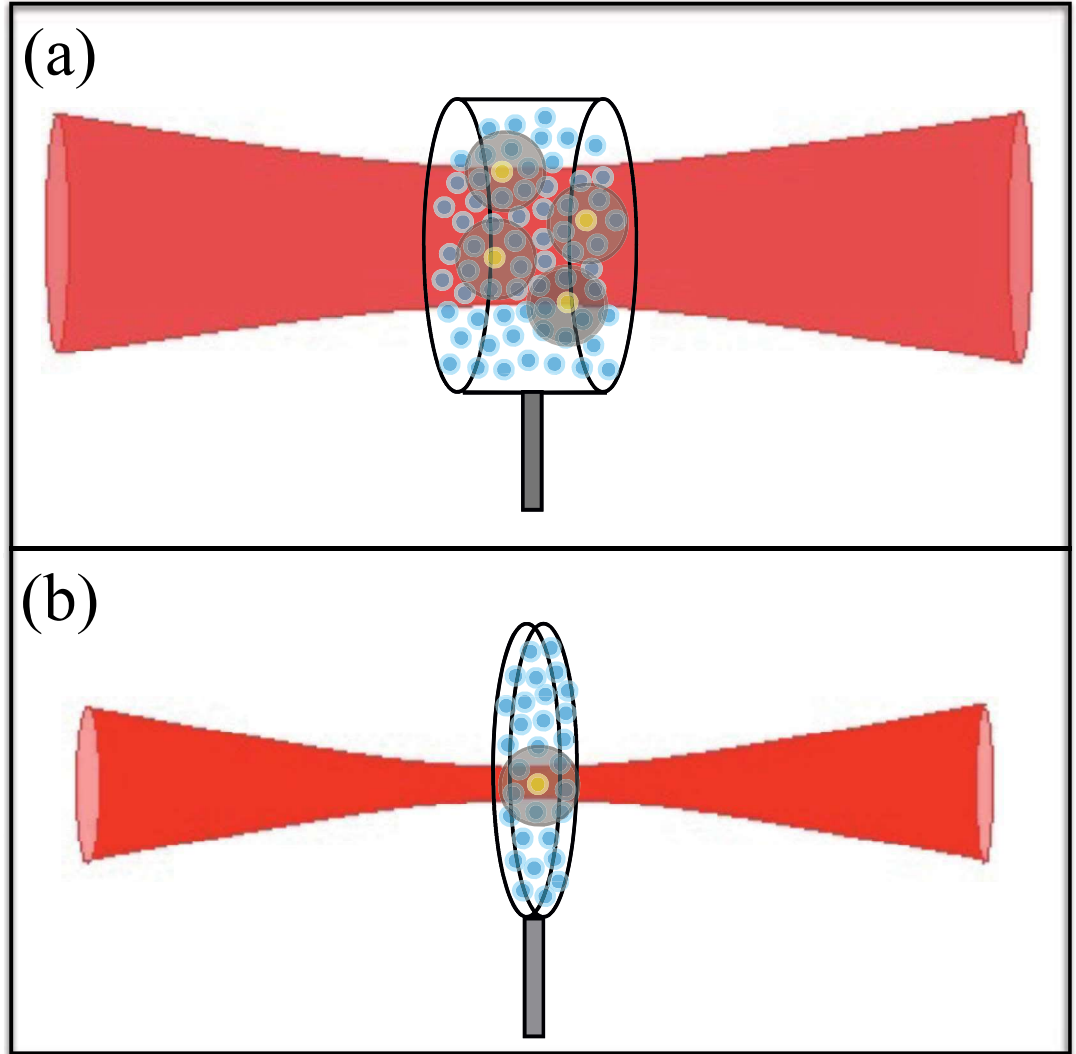


Figure 8.2: Rydberg-EIT in the thin atomic vapor cell. (a) Thin vapor cell with optical path length  $\sim 100 \mu\text{m}$ . This kind of vapor cell provides us to work with few Rydberg blockade sphere. (b) Thin vapor cell with optical path length  $\sim 10 \mu\text{m}$ . The typical Rydberg blockade radius for Rydberg excitation to the state having principal quantum number,  $n = 100$  is  $10 \mu\text{m}$ . Therefore this kind of setup gives us the provision to do experiment with single blockade sphere.

The postulate of Kramers Kronig relation for linear optics does not hold true for the system. The modification of the causal function due to cooperative Rydberg interaction is another fundamentally interesting problem to solve.

# Bibliography

- [1] H. Weimer, R. Löw, T. Pfau, and H. P. Büchler, Phys. Rev. Lett., **101**, 250601 (2008).
- [2] J. Honer, Hendrik Weimer, T. Pfau, and H. P. Büchler, Phys. Rev. Lett., **105**, 160404 (2010).
- [3] H. Kübler, J. P. Shaffer, T. Baluktian, R. Löw, and T. Pfau, Nature Phot., **4**, 112 (2010).

## Appendix A

### Design of a fast photo-detector

Fast photo-detectors (FPD) are frequently used in optics experiment. In our experiment we have used FPD for monitoring the atomic spectroscopy signal and also stabilising laser frequency on spectroscopic signal. A circuit design of a FPD has been presented in fig .(A.1) using a pair of photodiodes (S1223-01, Hamamatsu).

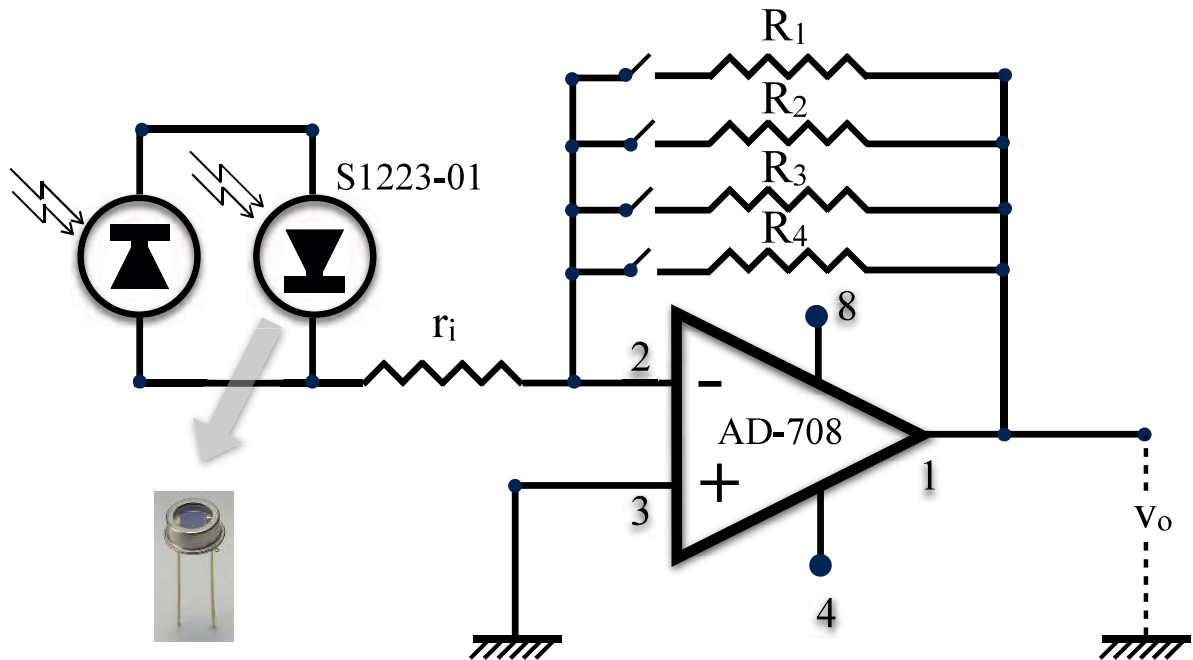


Figure A.1: Electronic design of fast photodetector circuit.

The photodiodes are connected to the main circuit in opposite orientation to each other. The reason behind the setup is to have the provision to do differential optical detection of two optical fields. The photodiode signals are taken to a OP-AMP inverting amplifier. An AD-708 chip has been used for OP-AMP. Pin 8 and 4 are used for bias which are given by  $+v_{cc}$  and  $-v_{cc}$

respectively. Here  $v_{cc,max} = 22$  V. If  $v_{pd}$  is the net photodiode signal, then the output amplifier signal is given by,  $v_0 = -\frac{R_f}{r_i}v_{pd}$  where  $r_i$  is the net input resistance and the bridge resistance  $R_f$  can be any one of  $R_1$ ,  $R_2$ ,  $R_3$  and  $R_4$ . The gain of the amplifier,  $A_v = -\frac{R_f}{r_i}$  can varied by choosing different bridge resistances. In our detector, we have used 10 k $\Omega$ , 100 k $\Omega$ , 1 M $\Omega$  and 10 M $\Omega$ .



## Appendix B

### Electronic design of AOM driver

In optics experiment, AOMs are used for frequency shifting, frequency modulation of laser light and controlling the laser intensities. It is made of single birefringent crystal. In order to drive the crystal an external radio frequency (RF) source is required. The RF driver is commercially available and also can be home made.

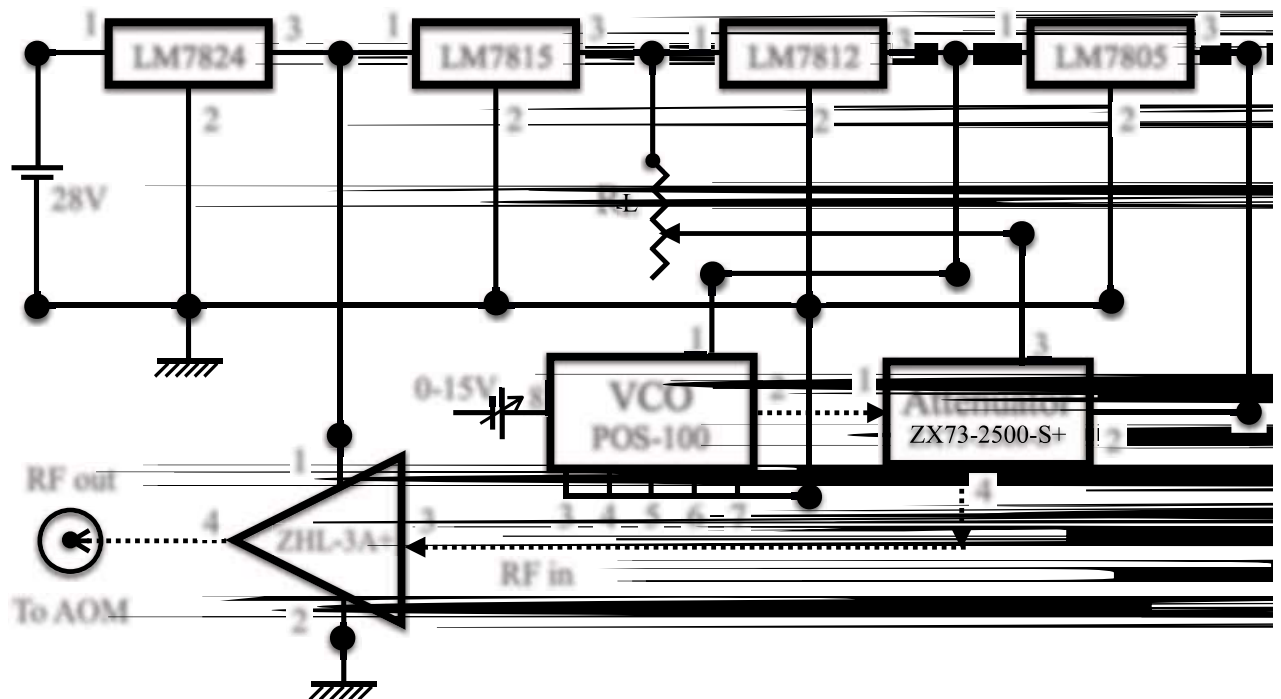


Figure B.1: Electronic design of an AOM driver.

The AOM RF driver is made of voltage controlled oscillator (VCO) (POS-100, Mini circuit), an RF attenuator (ZX73-2500-S+, Mini circuit) and an amplifier (ZHL-3A+, Mini circuit). When 12 V bias is on at the pin 1 of VCO, the variation of input control dc voltage at pin 8

from 1 to 15 V is able to vary the RF output frequency from 44 to 104 MHz. The output RF signal appears at the pin 2 of VCO. A low noise dc voltage source has been used to derive input control voltage for the VCO in our experiment. An RF voltage variable attenuator has been used at the output of the VCO in order to control the output power of VCO. Pin 2 has been used to bias the attenuator. A control dc voltage of 0-15 V has been applied to pin 3 in order to control the RF attenuation from 4 to 40 dB. An RF amplifier has been used to amplify the output voltage to optimally drive AOM crystal. The voltage regulators LM7824, LM7815, LM7812 and LM7805 has been used to generate bias and control voltages for VCO, attenuator and amplifier.

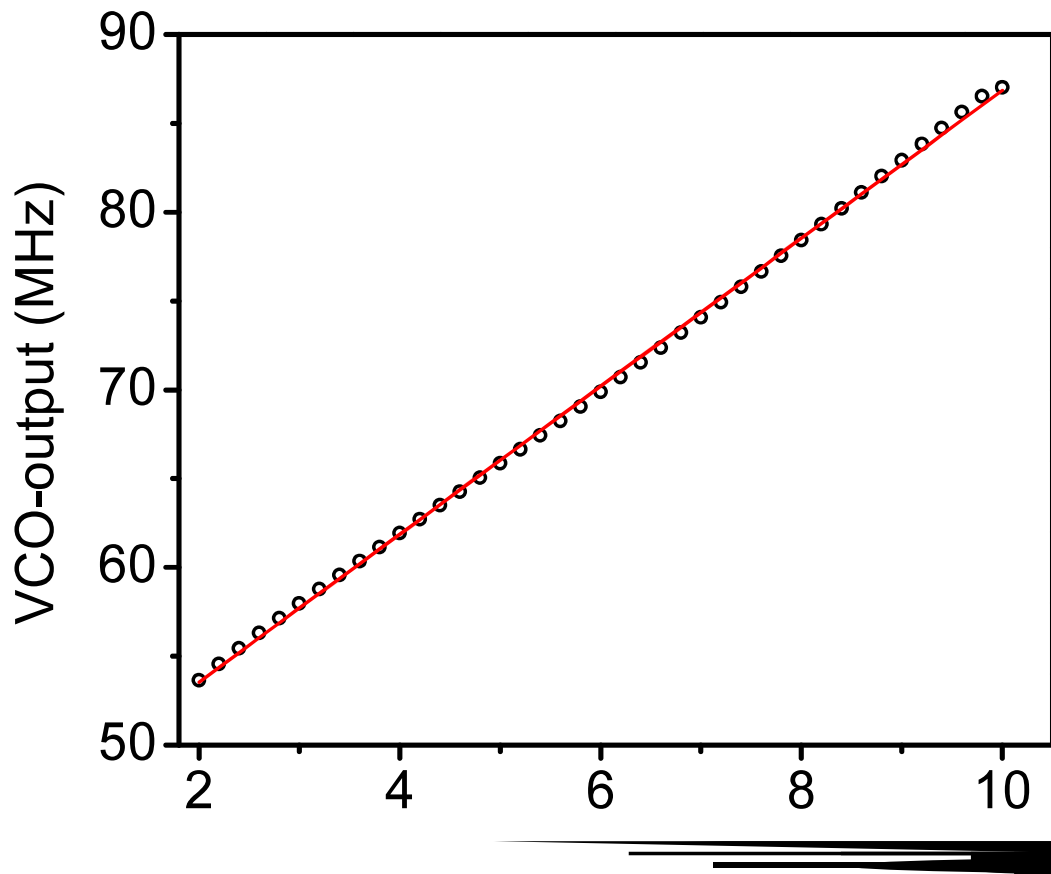


Figure B.2: VCO characteristic curve.

The VCO characteristic curve is depicted in fig. (B.2). Therefore any desired frequency shift of the light can be introduced by a particular dc control voltage obtained from the characteristic curve.

# Appendix C

## Fitting of a function numerically and goodness of fitting

In this appendices we will describe how to fit a data set using a function. In this context, we explain the methodology of nonlinear  $\chi^2$  fitting and weighted  $\chi^2$  fitting. We will also discuss a way to test the goodness of fitting.

### C.1 $\chi^2$ -fitting

Let us consider a function  $F(\mathbf{a}, x)$  where  $x$  is the variable of the function and  $\mathbf{a} = (a_1, a_2, \dots)$ , represents the parameter space of the function  $F$ . Consider a data set with  $n$  data point which can be represented as  $f_1, f_2, \dots, f_n$ . Then the  $\chi^2$  defiation can be represented as,

$$\chi^2(\mathbf{a}) = \sum_{i=1}^n \frac{1}{\sigma_i^2} (f_i - F(\mathbf{a}, x_i))^2 \quad (\text{C.1})$$

For an arbitrary parameter space, the  $\chi^2$  is represented geometrically in the fig. (C.1). The sum over all the area of the squares in the figure gives the  $\chi^2$  value. The objective is to find out a parameter space where the total area will minimise and hence the  $\chi^2$ . The curve for optimised set of parameters  $\mathbf{a}$  for which the  $\chi^2$  is minimised, depicted by a dashed curve in fig. (C.1).

One of the efficient way of optimising parameter space by constructing the gradient vector and the Hessian matrix for differential parameter space and solve it iteratively [1]. The gradient vector and the Hessian matrix of the function is given by,

$$\frac{\partial \chi^2}{\partial a_j} = 2 \sum_{i=1}^n \frac{1}{\sigma_i^2} (F(\mathbf{a}, x_i) - f_i) \frac{\partial F}{\partial a_j} \quad (\text{C.2})$$

$$\frac{\partial^2 \chi^2}{\partial a_j \partial a_k} = 2 \sum_{i=1}^n \frac{1}{\sigma_i^2} \frac{\partial F}{\partial a_j} \frac{\partial F}{\partial a_k} + 2 \sum_{i=1}^n \frac{1}{\sigma_i^2} (F(\mathbf{a}, x_i) - f_i) \frac{\partial^2 F}{\partial a_j \partial a_k} \quad (\text{C.3})$$

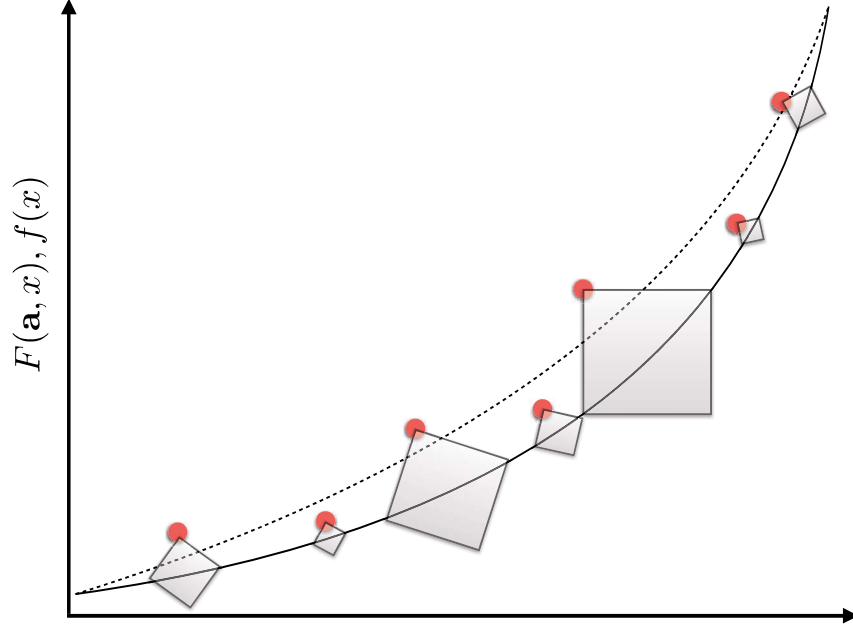


Figure C.1: A representation of  $\chi^2$  difference of a set of data points from a function with an arbitrary parameter space (depicted as a solid line). The dashed line represents the same function with optimised parameter space which gives minimum  $\chi^2$  value.

In the Hessian matrix (Eq. (C.3)), the second term contains  $r_i = \frac{1}{\sigma_i^2}(F(\mathbf{a}, x_i) - f_i)$  which is small near the optimum parameter space. Hence, it is customary to neglect this term. The advantage of neglecting this term is to calculate the Hessian matrix without calculating the second derivative of the function  $F(\mathbf{a}, x)$ .

The Jacobian matrix of the residual is defined as  $J_{ij} = \frac{\partial r_j}{\partial a_i}$ . Then we can rewrite the gradient vector and the Hessian matrix as,  $g(\mathbf{a}) = 2\mathbf{J}\mathbf{r}$  and  $G(\mathbf{a}) = 2\mathbf{J}\mathbf{J}^T$  respectively. We can directly use the Newton's method which gives the iteration  $J^{(k)}J^{(k)T}\delta\mathbf{a} = -J^{(k)}\mathbf{r}^{(k)}$  which has to be solved for  $\delta\mathbf{a}$  followed by the equation  $\mathbf{a}^{(k+1)} = \mathbf{a}^{(k)} + \delta\mathbf{a}$ . Here the Jacobian  $J^{(k)}$  has to be evaluated at  $\mathbf{a} = \mathbf{a}^{(k)}$ . The equations which has to be solved in each iteration are the algebraic equations. The set of algebraic equations can be solved by singular value decomposition (SVD) [1].

## C.2 Goodness of the fitting

The goodness of the fitting is characterised by the quantity  $\chi^2/dof$ .  $dof$  is the degrees of freedom which is defined by  $dof = N_{data} - N_{parameter}$ . Here  $N_{data}$  is the number of data point

present in the data set and  $N_{parameter}$  is the number of parameter (dimension of the parameter space) has to be fitted in the fitting process. There exist a thumb rule for the goodness of  $\chi^2$ -fitting. For  $\chi^2/dof \leq 1$ , it is the best fitting for  $\chi^2$ . If  $1 < \chi^2/dof \leq 2$ , the fitting is acceptable. If  $\chi^2/dof > 2$ , the fitting cannot be acceptable or it is a bad fitting.

# Bibliography

- [1] H. M. Antia (2002), "Numerical methods for scientists and engineers", Hindustan Book Agency (India), P 19 Green Park Extension, New Delhi 110016, India.

# Optical nonlinearity of Rydberg electromagnetically induced transparency in thermal vapor using the optical-heterodyne-detection technique

Arup Bhowmick,<sup>\*</sup> Sushree S. Sahoo, and Ashok K. Mohapatra<sup>†</sup>

*School of Physical Sciences, National Institute of Science Education and Research, Bhubaneswar 752050, India*

(Received 27 June 2016; published 22 August 2016)

We discuss the optical-heterodyne-detection technique to study the absorption and dispersion of a probe beam propagating through a medium with a narrow resonance. The technique has been demonstrated for Rydberg electromagnetically induced transparency in rubidium thermal vapor and the optical nonlinearity of a probe beam with variable intensity has been studied. A quantitative comparison of the experimental result with a suitable theoretical model is presented. The limitations and the working regime of the technique are discussed.

DOI: [10.1103/PhysRevA.94.023839](https://doi.org/10.1103/PhysRevA.94.023839)

## I. INTRODUCTION

Self-phase modulation (SPM) and cross-phase modulation (XPM) are at the heart of strong photon-photon interactions inside a medium which plays an important role in building quantum gates [1,2], quantum entanglement [3], and non-demolition measurement [4] of single photons. Strong XPM of photons based on electromagnetically induced transparency (EIT) has been theoretically proposed [5] and demonstrated in thermal vapors [6–8] as well as in cold atoms [9–11]. Enhanced SPM of photons mediated by Rydberg blockade interaction in atomic vapor has been proposed [12–14]. Rydberg blockade induced photon-photon interaction has been experimentally demonstrated for weak classical light [15,16] and single photons in cold atoms [17,18].

EIT based XPM has been measured using various interferometric techniques [6–10]. Optical heterodyne is one of such techniques which has been extensively used for the measurement of absorption and dispersion of coherent two-photon transition in an atomic ensemble [19], Zeeman coherence induced anomalous dispersion [20], and enhanced Kerr nonlinearity in two-level atoms [21]. The technique has also been used to measure the XPM of a probe and a control beam in an  $N$  system using cold atoms [9,10,22]. The basic principle of the technique is based on using two probe beams propagating through the dispersive medium with a frequency offset larger than the resonance linewidth. Both the beams cannot be on resonance while scanning their frequencies and hence they undergo different phase shifts. This differential phase shift appears in their beat signal which can be measured by comparing with the phase of a reference beat signal of the same two beams and gives information about the dispersion. If the probe beams are sufficiently weak, then the measured optical nonlinearity using this technique can be compared with the standard models involving a single probe beam. However, if the intensity of one of the probe beams is increased, then the strong probe beam dresses the atoms interacting with the weak probe beam which leads to the erroneous measurement of the nonlinearity. If both the probe beams are strong then the issue is even more serious.

In this paper, we have demonstrated this technique to measure the SPM of a probe beam propagating through a Rydberg EIT medium in rubidium thermal vapor. We show that the observed probe transmission and dispersion cannot be explained with the standard EIT theory for the probe beam with large intensity. We present a model of EIT consisting of a strong-coupling beam and two probe beams with a frequency offset to explain the experimental data. The paper is organized as follows. In the next section, we discuss the theoretical model. The experimental method of heterodyne-detection technique is presented in Sec. III followed by the measurement of optical nonlinearity in Sec. IV.

## II. THEORETICAL MODEL

In order to explain the transmission and dispersion of a probe beam propagating through a Rydberg EIT medium, we consider a model of a three-level atomic system interacting with two probe laser fields and a coupling laser field in ladder configuration as shown in Fig. 1(a). The coupling laser field with frequency  $\omega_c$  counterpropagates the copropagating probe beams with frequencies  $\omega_p$  and  $\omega_p + \delta$  through the vapor cell. The probe field with frequency  $\omega_p + \delta$  is considered as a weak field. In a suitable rotating frame and with rotating wave approximation (RWA), the total Hamiltonian of the system can be written as

$$\mathbf{H} = \frac{\hbar}{2} \begin{pmatrix} 0 & \Omega_{p1}^* + \Omega_{p2}^* e^{i\delta t} & 0 \\ \Omega_{p1} + \Omega_{p2} e^{-i\delta t} & 2(\Delta_p - k_p v) & \Omega_c^* \\ 0 & \Omega_c & 2(\Delta_2 - \Delta k v) \end{pmatrix},$$

where  $\Omega_{p1}$ ,  $\Omega_{p2}$ , and  $\Omega_c$  are the Rabi frequencies of the strong probe, weak probe, and the coupling beams, respectively.  $k_c$  and  $k_p$  are the wave vectors of the coupling and probe lasers with  $\Delta k = k_p - k_c$ . The two-photon detuning is given by  $\Delta_2 = \Delta_p + \Delta_c$ .  $v$  is the velocity of the atoms in the vapor. The density matrix equation is given by  $\dot{\rho} = \frac{-i}{\hbar} [H, \rho] + \mathcal{L}_D(\rho)$ .  $\mathcal{L}_D(\rho)$  is the Lindblad operator which takes care of the decoherences in the system. The population decay rate of the channels  $|r\rangle \rightarrow |e\rangle$  is denoted by  $\Gamma_{re}$  and  $|e\rangle \rightarrow |g\rangle$  is denoted by  $\Gamma_{eg}$ . Due to the finite transit time of the thermal atoms through the cross section of the beams, we include the population decay rate of the Rydberg state to the ground state as  $\Gamma_{rg}$ . In our model, the decay time scales used are  $\Gamma_{re} = 10$  kHz,  $\Gamma_{eg} = 6$  MHz, and  $\Gamma_{rg} = 200$  kHz.

<sup>\*</sup>arup.b@niser.ac.in

<sup>†</sup>a.mohapatra@niser.ac.in

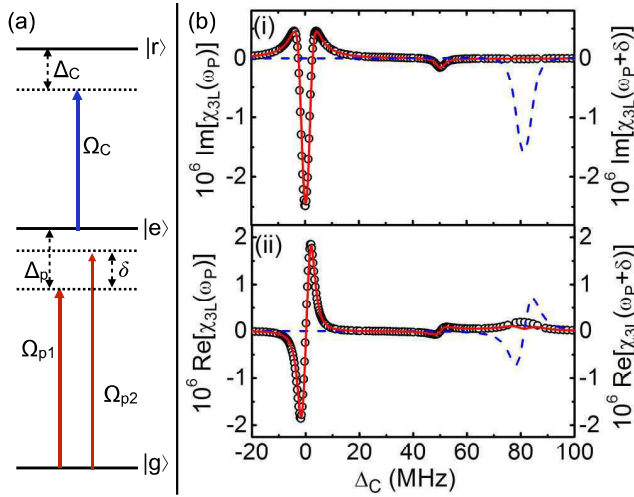


FIG. 1. (a) Energy-level diagram of EIT in ladder configuration. Two probe fields couple the transition  $|g\rangle \rightarrow |e\rangle$ . The coupling laser couples the transition  $|e\rangle \rightarrow |r\rangle$ . The probe (coupling) detuning is  $\Delta_p$  ( $\Delta_c$ ) and the frequency offset between the probe beams is  $\delta$ . (b) Imaginary (i) and real (ii) part of  $\chi_{3L}(\omega_p)$  and  $\chi_{3L}(\omega_p + \delta)$  as a function of coupling laser detuning. The parameters used in the model are  $\Delta_p = -50$  MHz,  $\delta = 50$  MHz,  $\Omega_{p1} = 5$  MHz,  $\Omega_{p2} = 0.5$  MHz,  $\Omega_c = 2.5$  MHz,  $k_c = \frac{1}{480}$  nm $^{-1}$ , and  $k_p = \frac{1}{780}$  nm $^{-1}$ . Doppler averaging was done using temperature of the vapor to be  $T = 300$  K. The blue dotted and red solid lines are susceptibilities of the strong and the weak probe beam, respectively. The open circles show the susceptibility of the weak probe beam calculated using the approximation discussed in the text.

The steady-state density matrix equations are solved perturbatively. A similar approach is used to calculate the

four-wave mixing in two-level atoms as discussed in [24]. The density matrix of the system can be expanded as  $\rho = \rho^{(0)} + \rho^{(1)}e^{-i\delta t} + \rho^{(-1)}e^{i\delta t}$  and substituted in the density matrix equations. Equating the coefficients of  $e^{-i\delta t}$  with  $\delta = 0$  gives the zeroth-order equations:

$$\frac{\Omega_{p1}}{2} \rho_{eg}^{(0)} - \frac{\Omega_{p1}^*}{2} \rho_{ge}^{(0)} - i\Gamma_{eg}\rho_{ee}^{(0)} - i\Gamma_{rg}\rho_{rr}^{(0)} = 0, \quad (1)$$

$$\frac{\Omega_c^*}{2} \rho_{er}^{(0)} - \frac{\Omega_c}{2} \rho_{re}^{(0)} + i\Gamma_2 \rho_{rr}^{(0)} = 0, \quad (2)$$

$$\left(\Delta_p - k_p v - i\frac{\Gamma_{eg}}{2}\right) \rho_{ge}^{(0)} - \frac{\Omega_{p1}}{2} (2\rho_{ee}^{(0)} \rho_{rr}^{(0)} - 1) + \frac{\Omega_c^*}{2} \rho_{gr}^{(0)} = 0, \quad (3)$$

$$\left(\Delta_2 - \Delta_k v - i\frac{\Gamma_2}{2}\right) \rho_{gr}^{(0)} - \frac{\Omega_{p1}}{2} \rho_{er}^{(0)} + \frac{\Omega_c}{2} \rho_{ge}^{(0)} = 0, \quad (4)$$

$$\left(\Delta_c + k_c v - i\frac{\Gamma_3}{2}\right) \rho_{er}^{(0)} - \frac{\Omega_c}{2} (\rho_{rr}^{(0)} + \rho_{ee}^{(0)}) + \frac{\Omega_{p1}^*}{2} \rho_{gr}^{(0)} = 0, \quad (5)$$

where  $\Gamma_2 = \Gamma_{re} + \Gamma_{rg}$  and  $\Gamma_3 = \Gamma_{eg} + \Gamma_{re} + \Gamma_{rg}$ . The zeroth-order equations are the same as the equations of EIT for the probe beam with Rabi frequency  $\Omega_{p1}$  and can be solved exactly. Equating the coefficients of  $e^{-i\delta t}$  gives the first-order equations which can be solved if the second-order terms are neglected. Hence, the model is valid if one of the probe beams is weak. The first-order equations in the steady state are given by

$$\left(\Delta_p + \delta - k_p v + i\frac{\Gamma_{eg}}{2}\right) \rho_{eg}^{(1)} + \frac{\Omega_c}{2} \rho_{rg}^{(1)} - \frac{\Omega_{p1}}{2} (2\rho_{ee}^{(1)} + \rho_{rr}^{(1)}) - \frac{\Omega_{p2}}{2} (2\rho_{ee}^{(0)} + \rho_{rr}^{(0)} - 1) = 0, \quad (6)$$

$$\left(\Delta_2 + \delta - \Delta_k v + i\frac{\Gamma_2}{2}\right) \rho_{rg}^{(1)} + \frac{\Omega_c}{2} \rho_{eg}^{(1)} - \frac{\Omega_{p1}}{2} \rho_{re}^{(1)} - \frac{\Omega_{p2}}{2} \rho_{re}^{(0)} = 0, \quad (7)$$

$$\left(\Delta_c + \delta + k_c v + i\frac{\Gamma_3}{2}\right) \rho_{re}^{(1)} - \frac{\Omega_{p1}}{2} \rho_{rg}^{(1)} - \frac{\Omega_c}{2} (\rho_{rr}^{(1)} - \rho_{ee}^{(1)}) = 0, \quad (8)$$

$$\left(\Delta_p - \delta - k_p v - i\frac{\Gamma_{eg}}{2}\right) \rho_{ge}^{(1)} + \frac{\Omega_c}{2} \rho_{gr}^{(1)} - \frac{\Omega_{p1}}{2} (2\rho_{ee}^{(1)} + \rho_{rr}^{(1)}) = 0, \quad (9)$$

$$\left(\Delta_2 - \delta - \Delta_k v - i\frac{\Gamma_2}{2}\right) \rho_{gr}^{(1)} + \frac{\Omega_c}{2} \rho_{ge}^{(1)} - \frac{\Omega_{p1}}{2} \rho_{er}^{(1)} = 0, \quad (10)$$

$$\left(\Delta_c - \delta + k_c v - i\frac{\Gamma_3}{2}\right) \rho_{er}^{(1)} + \frac{\Omega_c}{2} (\rho_{ee}^{(1)} - \rho_{rr}^{(1)}) - \frac{\Omega_{p2}}{2} \rho_{gr}^{(0)} - \frac{\Omega_{p1}}{2} \rho_{gr}^{(1)} = 0, \quad (11)$$

$$\frac{\Omega_c}{2} (\rho_{re}^{(1)} - \rho_{er}^{(1)}) - \delta \rho_{rr}^{(1)} - i\Gamma_2 \rho_{rr}^{(1)} = 0, \quad (12)$$

$$\frac{\Omega_{p1}}{2} (\rho_{eg}^{(1)} - \rho_{ge}^{(1)}) + \frac{\Omega_c}{2} (\rho_{er}^{(1)} - \rho_{re}^{(1)}) + \frac{\Omega_{p2}}{2} \rho_{ge}^{(0)} - \delta \rho_{ee}^{(1)} - i\Gamma_{eg} \rho_{ee}^{(1)} + i\Gamma_{re} \rho_{rr}^{(1)} = 0. \quad (13)$$

Using the fact that  $\rho_{ij}^* = \rho_{ji}$ , it can be shown that  $\rho_{ij}^{(0)*} = \rho_{ji}^{(0)}$  and  $\rho_{ij}^{(1)*} = \rho_{ji}^{(-1)}$ . Assuming that the system is closed and using  $\rho_{gg} + \rho_{ee} + \rho_{rr} = 1$ , we get eight independent first-order equations.



Zeroth-order equations are solved numerically in steady state for the zeroth-order matrix elements  $\rho_{i,j}^{(0)} \forall i, j$  and are substituted in the first-order equations. The first-order equations are then solved numerically in steady state to determine  $\rho_{eg}^{(1)}$ . The susceptibility of the strong probe averaged over the thermal motion of the atoms can be calculated as  $\chi(\omega_p) = \frac{2N|\mu_{eg}|^2}{\epsilon_0 \hbar \Omega_{p1}} \frac{1}{\sqrt{2\pi} v_p} \int_{-\infty}^{\infty} \rho_{eg}^{(0)} e^{-v^2/2v_p^2} dv$  where  $v_p$  is the most probable speed of the atoms,  $N$  is the density, and  $\mu_{eg}$  is the dipole moment of the transition  $|g\rangle \rightarrow |e\rangle$ . Similarly, the susceptibility of the weak probe can be determined using  $\chi(\omega_p + \delta) = \frac{2N|\mu_{eg}|^2}{\epsilon_0 \hbar \Omega_{p2}} \frac{1}{\sqrt{2\pi} v_p} \int_{-\infty}^{\infty} \rho_{eg}^{(1)} e^{-v^2/2v_p^2} dv$ . Heterodyne-detection technique is sensitive only to the two-photon transition and hence the susceptibility of the probe in the absence of the coupling beam cannot be detected. To compare with the experiment, we define the susceptibility only due to two-photon transition as  $\chi_{3L}(\omega_p) = \chi(\omega_p) - \chi_{2L}(\omega_p)$  and  $\chi_{3L}(\omega_p + \delta) = \chi(\omega_p + \delta) - \chi_{2L}(\omega_p + \delta)$ , where  $\chi_{2L}$  is the susceptibility of the probes in the absence of the coupling beam.  $\chi_{3L}$  calculated from the model is depicted in Fig. 1(b). As shown in the figure, two EIT peaks associated with both the probe beams are observed. However, the frequency difference between the EIT peaks does not match with the offset frequency, but is scaled as  $\frac{k_c}{k_p} \delta$ . The scaling can easily be understood by investigating the EIT equations. The EIT resonance peak for the strong probe is observed if  $\Delta_2 - \Delta k v = 0$  and  $\Delta_p - k_p v = 0$ . So EIT resonance of the strong probe appears at  $\Delta_c = -\frac{k_c}{k_p} \Delta_p$ . Similarly, the EIT peak for the weak probe is observed if  $\Delta_2 + \delta - \Delta k v = 0$  and  $\Delta_p + \delta - k_p v = 0$ . Hence, the EIT peak of the weak probe appears at  $\Delta_{c1} = -\frac{k_c}{k_p} (\Delta_p + \delta)$ . So the spectral difference between the EIT peaks ( $\Delta_{c1} - \Delta_c$ ) is found to be  $\frac{k_c}{k_p} \delta$ . As a similar effect of wave-vector mismatch, spectral difference of Rydberg EIT peaks associated with the hyperfine transition in rubidium thermal vapor is scaled by  $(1 - \frac{k_p}{k_c})$  and has been reported in [23].

As shown in Fig. 1(b), an unexpected small peak is observed for the weak probe susceptibility when the coupling laser is detuned by 50 MHz from the weak probe EIT peak. In order to get an insight of the origin of this peak, we use the following approximations to simplify the first-order equations. Since the probe beam is weak, it cannot raise the population in the excited states. Hence,  $\rho_{ee}^{(1)} \approx \rho_{rr}^{(1)} \approx 0$ . Using this approximation, the first-order equations are reduced to

$$\left( \Delta_p + \delta - k_p v + i \frac{\Gamma_{eg}}{2} \right) \rho_{eg}^{(1)} + \frac{\Omega_c}{2} \rho_{rg}^{(1)} + \frac{\Omega_{p2}}{2} (2\rho_{ee}^{(0)} + \rho_{rr}^{(0)} - 1) = 0, \quad (14)$$

$$\left( \Delta_2 + \delta - \Delta k v + i \frac{\Gamma_2}{2} \right) \rho_{rg}^{(1)} + \frac{\Omega_c}{2} \rho_{eg}^{(1)} - \frac{\Omega_{p1}}{2} \rho_{re}^{(1)} - \frac{\Omega_{p2}}{2} \rho_{re}^{(0)} = 0, \quad (15)$$

$$\left( \Delta_c + \delta + k_c v + i \frac{\Gamma_3}{2} \right) \rho_{re}^{(1)} - \frac{\Omega_{p1}}{2} \rho_{rg}^{(1)} = 0. \quad (16)$$

In the absence of the strong probe beam,  $\Omega_{p1} = 0$  and all the zeroth-order matrix elements are equal to zero and Eq. (16) leads to  $\rho_{re}^{(1)} = 0$ . Under this condition, it can be shown that Eqs. (14) and (15) exactly give the EIT equations in the weak probe limit. In the presence of the strong probe beam with frequency offset  $\delta = 50$  MHz, the extra zeroth-order terms in the equations lead to the appearance of the small peak. To understand it further, let the weak probe interact with the zero velocity class of atoms. So, the main EIT peak of the weak probe appears at  $\Delta_c = 0$ . The presence of the strong probe dresses the same zero velocity class of atoms which are excited to the  $|r\rangle$  state via two-photon resonance for  $\Delta_c = 50$  MHz. Hence,  $\rho_{rr}^{(0)}$  in Eqs. (14) and (15) are nonzero for the zero velocity class of atoms which interact with the weak probe beam and contribute to  $\chi_{3L}(\omega_p + \delta)$ . Since the strong probe beam resonantly interacts with a different velocity class of atoms, the two-photon resonance for that velocity class is shifted due to wave-vector mismatch and the corresponding EIT peak appears at 81.25 MHz. To show that the above approximation is valid, we calculated  $\chi_{3L}(\omega_p + \delta)$  using Eqs. (14) and (15) which is shown in Fig. 1(b) and the approximation holds very well.

Due to the wave-vector mismatch in this case, the small peak is resolved from the EIT peak of the strong probe and a standard model for EIT with a single probe field and a coupling field can be used to compare with the experimental data. If the wave vectors are the same, e.g., in the case of  $\Lambda$  EIT in alkali atoms, the small peak cannot be resolved from the EIT peak of the strong probe and hence the model with two probes fields and a coupling field presented here should be used to compare with the experiment. Alternatively, the small peak can be reduced by changing the offset frequency. Using our model, the transmission peak height of the small peak is studied as a function of the offset frequency which is shown in Fig. 2. It shows that the small peak height reduces significantly for higher offset frequency.

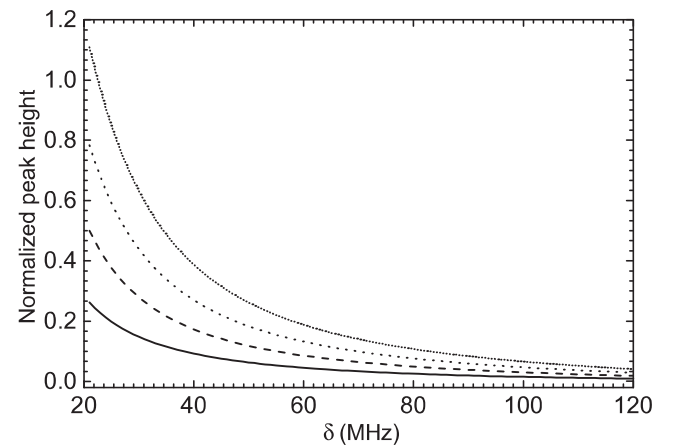


FIG. 2. Variation of the EIT transmission peak height due to dressed atoms as a function of beat frequency. The curves are generated using the model for the coupling Rabi frequency 2.5 MHz and for probe Rabi frequencies 4 MHz (solid line), 6 MHz (dashed line), 8 MHz (big dotted line), and 10 MHz (small dotted line).

### III. EXPERIMENTAL METHOD

The schematic of the experimental setup is shown in Fig. 3. An external cavity diode laser operating at 780 nm is used to derive two probe beams. A frequency offset of 50 MHz was introduced between the probe beams by using acousto-optic modulators. Both the beams were superimposed using a polarizing cube beam splitter (PBS). The interference beats of the probes were detected using two fast photodetectors by introducing polarizers at both the output ports of the PBS. The probe beams coming out of one of the output ports of the PBS propagate through a magnetically shielded rubidium vapor cell with an optical path length of 5 cm. The coupling beam was derived from a frequency doubled diode laser operating at 478–482 nm and it counterpropagates the probe beams through the vapor cell. The beat detected at the other output port of the PBS was used as reference. Since the frequency offset between the probe beams is larger than the Rydberg EIT resonance in thermal vapor [23], they undergo different phase shift and absorption while scanning the coupling laser through the EIT resonance. This differential phase shift of the probe beams will change the phase of the signal beat which can be measured by comparing it with the phase of the reference beat. Since the beat signals are the outputs of the same interferometer, the noise due to vibration or acoustic disturbances is strongly suppressed.

The light intensity falling at the signal detector is

$$I_s \propto |E_1|^2 e^{-k \text{Im}[\chi(\omega)]} + |E_2|^2 e^{-k \text{Im}[\chi(\omega+\delta)]} + 2|E_1||E_2| e^{-\frac{k}{2} \text{Im}[\chi(\omega)+\chi(\omega+\delta)]} \cos(\delta t + \phi_s + \phi_{\text{off}}),$$

where  $E_1$  and  $E_2$  are the electric-field amplitudes of the strong and weak probes, respectively,  $\phi_s = \frac{kL}{2} \text{Re}[\chi_{3L}(\omega) - \chi_{3L}(\omega + \delta)]$ , and  $\phi_{\text{off}}$  is the phase difference of the probe beams in the absence of the coupling field which remains constant if the probe frequencies are kept constant during the

experiment. Using a high pass filter, the beat signal detected by the signal detector has the form

$$D_s = A_s e^{-\frac{kL}{2} \text{Im}[\chi_{3L}(\omega)+\chi_{3L}(\omega+\delta)]} \cos(\delta t + \phi_s + \phi_{\text{off}}),$$

where  $A_s \propto 2|E_1||E_2|$ . Similarly, the beat signal at the reference detector has the form  $D_r = A_r \cos(\delta t + \phi_r)$ , where  $A_r$  and  $\phi_r$  are the amplitude and phase of the beat signal of the reference detector.  $\phi_r$  can be controlled using an external phase shifter. These two beat signals are multiplied by an electronic waveform mixer and are passed through a low pass filter. The output of the low pass filter gives a dc signal of the form

$$S_L = 2A_r A_s e^{-\frac{kL}{2} \text{Im}[\chi_{3L}(\omega)+\chi_{3L}(\omega+\delta)]} \cos(\phi_s + \phi_0),$$

where  $\phi_0 = \phi_r + \phi_{\text{off}}$ . Assuming  $\phi_s$  to be small and setting  $\phi_0 = 0$ , the signal becomes sensitive to the amplitudes of the probe beams and hence gives the information about the transmission of the probe beams through the medium. After subtracting the offset (in the absence of the coupling laser) from the signal,

$$S_L \approx 2A_s A_r [e^{-\frac{kL}{2} \text{Im}[\chi_{3L}(\omega)+\chi_{3L}(\omega+\delta)]} - 1]. \quad (17)$$

If  $\phi_0$  is set to  $\frac{\pi}{2}$ , then  $S_L$  becomes strongly sensitive to  $\phi_s$  and hence the refractive index of the probe beams due to Rydberg EIT can be measured. In this case,

$$S_L \approx 2A_s A_r e^{-\frac{kL}{2} \text{Im}[\chi_{3L}(\omega)+\chi_{3L}(\omega+\delta)]} \phi_s. \quad (18)$$

It is worthwhile to mention that the observed dispersive signal depends linearly on  $\phi_s$  and hence is proportional to  $\{\text{Re}[\chi_{3L}(\omega)] - \text{Re}[\chi_{3L}(\omega + \delta)]\}$ .

To work in the phase as well as amplitude sensitive regimes,  $\phi_0$  can be controlled by varying the phase of the reference beat signal using an electronic phase shifter. However, in our experiment, the phase is controlled optically and we call it an optical phase shifter (OPS). To realize the OPS, one  $\frac{\lambda}{4}$  plate is introduced before the polarizer at the output of the PBS. The probe beam transmitted (reflected) by the PBS after passing through the  $\frac{\lambda}{4}$  plate becomes  $\sigma^+$  ( $\sigma^-$ ) and can be expressed as  $\sigma^\pm = \frac{1}{\sqrt{2}}(|H\rangle + e^{\pm i\frac{\pi}{2}}|V\rangle)$ . If the polarizer after the  $\frac{\lambda}{4}$  plate selects the  $|H\rangle$ -polarized component, then the phase difference between both the probe beams falling on the detector is zero. Now, if the angle of the polarizer axis is rotated by  $90^\circ$ , then  $|V\rangle$  is selected and the phase difference between the beams becomes  $\pi$ . Hence, by rotating the polarizer axis, the phase of the reference beat signal can be varied between zero and  $\pi$  without compromising the amplitude.

The typical transmission and dispersion signals of the probes propagating through the Rydberg EIT medium are shown in Fig. 4. The probe laser frequency was stabilized on the atomic transition ( $5S_{1/2}$ ,  $F=2 \rightarrow 5P_{3/2}$ ) of  $^{87}\text{Rb}$  and the coupling laser frequency was scanned through the Rydberg EIT resonance. The frequency offset between the probe beams is 50 MHz, which is much greater than the EIT resonance width (about 3 MHz in thermal vapor [23]). Hence, two distinct EIT transmission peaks are observed as shown in Fig. 4(a) when the phase difference between the beat signals was set to zero. When the phase difference was set to  $\pi/2$ , two respective dispersion signals were observed as shown in Fig. 4(c). Due to the wave-vector mismatch between the probe

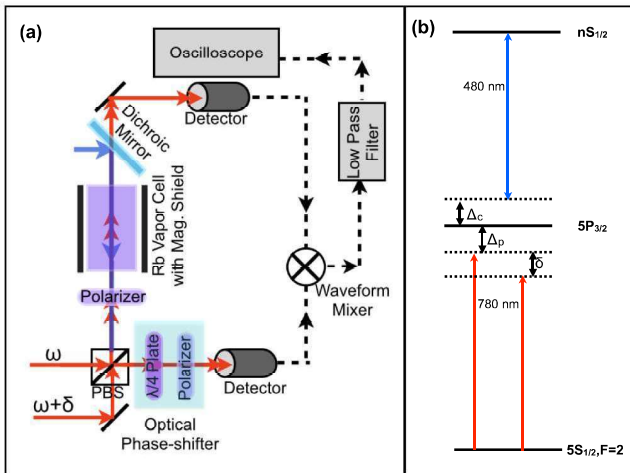


FIG. 3. (a) Schematic of the experimental setup for heterodyne detection technique to measure the transmission and dispersion of the Rydberg EIT medium. (b) Energy-level diagram for Rydberg EIT in  $^{87}\text{Rb}$ . Two probe beams couple the transition  $5S_{1/2}$ ,  $F=2 \rightarrow 5P_{3/2}$ . The coupling laser couples the transition  $5P_{3/2} \rightarrow nS_{1/2}$ . The coupling detuning is  $\Delta_c$ , probe detuning is  $\Delta_p$ , and frequency offset between the probe beams is  $\delta$ .

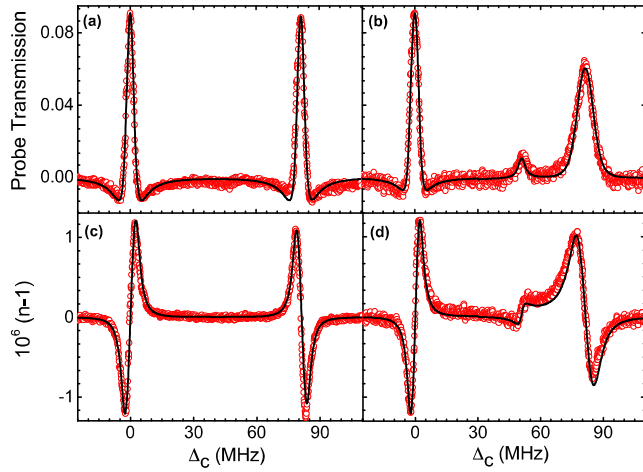


FIG. 4. Absolute transmission and dispersion of the probe beams propagating through the Rydberg EIT medium after subtracting the offset due to their interaction with the  $5S_{1/2}$ ,  $F = 2 \rightarrow 5P_{3/2}$  transition in the absence of the coupling beam. EIT (a) transmission and (c) dispersion signals of both the probes with Rabi frequency 600 kHz each. EIT (b) transmission and (d) dispersion signals of both the probes with Rabi frequencies, 600 kHz and 6.5 MHz, respectively. The coupling Rabi frequency was 2.5 MHz in all the cases. The red open circles are experimental data points and the black solid lines are the curves generated by the model. The absolute transmission and dispersion were determined from the theoretical calculation for the given experimental parameters.

and the coupling beams, the frequency difference between the transmission or dispersion peaks respective to both the probe beams is scaled by  $\frac{k_c}{k_p}$  as discussed in Sec. II. We observe the frequency difference between these peaks to be 81.25 MHz, which is consistent with the above scaling. With the increased Rabi frequency of the strong probe, the small peak at the beat frequency appears as discussed in Sec. II and shown in Figs. 4(b) and 4(d). The  $1/e^2$  radius of the probe (coupling) is measured to be 0.7 mm (1.2 mm). The power of the weak probe used in the experiment was  $0.125 \mu\text{W}$ . The strong probe power was varied in the range of 0.125 to  $15 \mu\text{W}$ . Probe Rabi frequency is estimated as  $\Omega_p = \Gamma_{eg} \sqrt{\frac{I}{2I_{\text{sat}}}}$ . For  $^{87}\text{Rb}$ , the saturation power is  $I_{\text{sat}} = 1.64 \text{ mW/cm}^2$ , and lifetime of the  $5P_{3/2}$  state is  $\Gamma_{eg} = 6 \text{ MHz}$ . The coupling Rabi frequency is determined by fitting the EIT transmission peak for a weak probe beam.

#### IV. MEASUREMENT OF OPTICAL NONLINEARITY

In order to study the optical nonlinearity, the weak probe Rabi frequency was set to 600 kHz and the strong probe Rabi frequency is varied from 600 kHz to 6.5 MHz. The EIT peak height of the weak probe is used as reference to normalize the EIT peak height of the strong probe beam. The beat frequency is chosen sufficiently large such that the peak due to the dressed atoms is well resolved from the main EIT peak of the strong probe beam. The normalized transmission peak height of the probe beam as a function of its Rabi frequency is shown in Fig. 5. The curves generated using the above model fit well

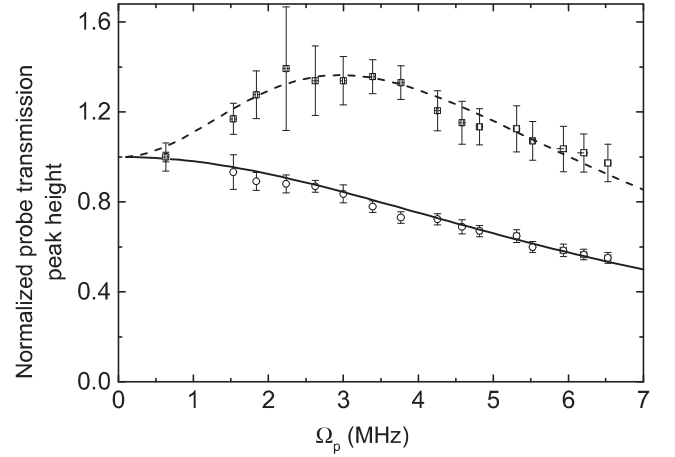


FIG. 5. Normalized EIT transmission peak height as a function of probe Rabi frequency by keeping coupling Rabi frequency fixed at 2.5 MHz ( $\circ$ ) and 800 kHz ( $\square$ ). The solid and dashed lines are the curves generated using the model for the same experimental parameters.

with the experimental data as shown in Fig. 5. In this particular case, since the main EIT peak is well resolved from the peak due to the dressed atom, the standard EIT model using a single probe beam also fits well with the peak height data and shows very little deviation from our model.

To determine the contributions of the higher-order susceptibilities to the EIT peak, we do the following analysis.

The EIT peak height of the weak probe is given by

$$P_w = S_L(\Delta_c = 0) = 2A_s A_r \left[ e^{-\frac{k_L}{2} \text{Im}[\chi_{3L}(\omega + \delta)]} - 1 \right].$$

Similarly the EIT peak height of the strong probe beam is given by

$$P_s = S_L\left(\Delta_c = \frac{k_c}{k_p} \delta\right) = 2A_s A_r \left[ e^{-\frac{k_L}{2} \text{Im}[\chi_{3L}(\omega)]} - 1 \right].$$

Assuming that  $\chi_{3L}(\omega)$  and  $\chi_{3L}(\omega + \delta)$  are small, the ratio is  $\frac{P_s}{P_w} \approx \frac{\text{Im}[\chi_{3L}(\omega)]}{\text{Im}[\chi_{3L}(\omega + \delta)]}$ .

The Taylor expansion of the susceptibility is given by

$$\chi_{3L} = [\chi_{3L}]_{\Omega_p=0} + \frac{1}{2!} \left[ \frac{\partial^2 \chi_{3L}}{\partial \Omega_p^2} \right]_{\Omega_p=0} \Omega_p^2 + \frac{1}{4!} \left[ \frac{\partial^4 \chi_{3L}}{\partial \Omega_p^4} \right]_{\Omega_p=0} \Omega_p^4 + \dots$$

Since  $\chi_{3L}$  is an even function of  $\Omega_p$ , all the odd-order terms in the expansion are zero.  $\chi_{3L}$  can be expressed as

$$\begin{aligned} \chi_{3L} &= \chi_{3L}^{(1)} + \chi_{3L}^{(3)} E_p^2 + \chi_{3L}^{(5)} E_p^4 + \dots \\ &= \chi_{3L}^{(1)} + \chi_{3L}^{(3)} \left[ \frac{\hbar}{2\mu} \right]^2 \Omega_p^2 + \chi_{3L}^{(5)} \left[ \frac{\hbar}{2\mu} \right]^4 \Omega_p^4 + \dots \end{aligned}$$

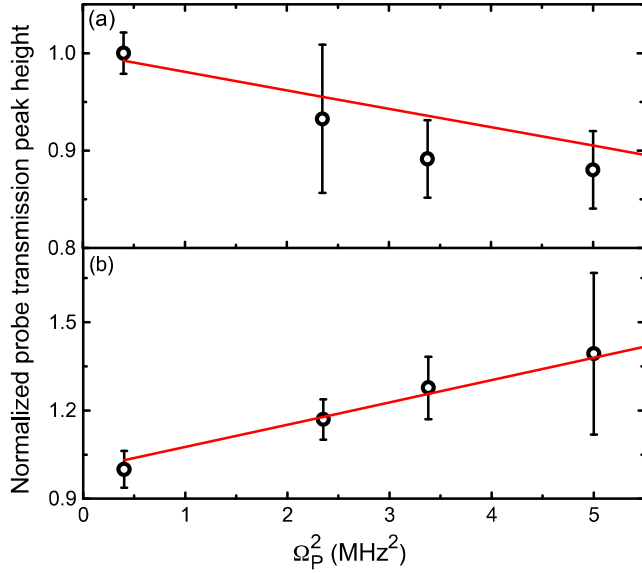


FIG. 6. Normalized EIT peak height as a function of  $\Omega_p^2$ . The circles are the experimental data with (a)  $\Omega_c = 2.5$  MHz and (b)  $\Omega_c = 0.8$  MHz. The solid lines are the linear fitting with the function  $1 + a\Omega_p^2$  with  $a$  as the fitting parameter.

where  $E_p$  is the probe electric field. Comparing both the equations, we get  $\chi_{3L}^{(1)} = \chi_{3L}(\Omega_p = 0)$ ,  $\chi_{3L}^{(3)} = \frac{1}{2!} \left[ \frac{2\mu}{\hbar} \right]^2 \left[ \frac{\partial^2 \chi_{3L}}{\partial \Omega_p^2} \right]_{\Omega_p=0}$ ,  $\chi_{3L}^{(5)} = \frac{1}{4!} \left[ \frac{2\mu}{\hbar} \right]^4 \left[ \frac{\partial^4 \chi_{3L}}{\partial \Omega_p^4} \right]_{\Omega_p=0}$ . Since the Doppler broadening is much larger than the offset frequency  $\delta$ , it is assumed that  $\chi_{3L}^{(1)}(\omega) \approx \chi_{3L}^{(1)}(\omega + \delta)$ . Also for the weak probe beam, the higher-order terms are assumed to be negligible. So the normalized EIT peak height of the strong probe beam can be written as

$$\frac{P_s}{P_w} = 1 + \frac{\text{Im}(\chi_{3L}^{(3)})}{\text{Im}(\chi_{3L}^{(1)})} \Omega_p^2 + \frac{\text{Im}(\chi_{3L}^{(5)})}{\text{Im}(\chi_{3L}^{(1)})} \Omega_p^4 + \dots$$

In principle, the above polynomial function can be used to fit the transmission peak height data as shown in Fig. 5 to determine the higher-order nonlinearities. Though the exact solution of the EIT fits the data very well, keeping a few terms

in the above polynomial function does not fit the data equally well mainly due to large contributions of the higher-order terms at higher probe Rabi frequencies. Therefore, we selected the first four data points of Fig. 5 to fit with a function  $1 + a\Omega_p^2$  where  $a = \frac{\text{Im}(\chi_{3L}^{(3)})}{\text{Im}(\chi_{3L}^{(1)})}$  and gives information about the self-phase modulation ( $\chi_{3L}^{(3)}$ ) of the probe light. From the fitting as depicted in Fig. 6, we find the value of “ $a$ ” to be  $-0.02 \pm 0.004$  and  $0.076 \pm 0.006 \text{ MHz}^{-2}$  with coupling Rabi frequencies 2.5 and 0.8 MHz, respectively. To compare with the theory,  $\chi_{3L}^{(3)} = \frac{1}{2!} \left[ \frac{2\mu}{\hbar} \right]^2 \left[ \frac{\partial^2 \chi_{3L}}{\partial \Omega_p^2} \right]_{\Omega_p=0}$  was calculated using the same experimental parameters and the value of “ $a$ ” was found to be  $-0.014$  and  $0.064 \text{ MHz}^{-2}$  with coupling Rabi frequencies equal to 2.5 and 0.8 MHz, respectively.  $\chi_{3L}^{(3)}$  determined using the above analysis reasonably match with the theoretical calculation. The discrepancy is mainly due to the nonzero contribution of higher-order terms. A larger number of data points below 1 MHz may give a better measurement for  $\chi_{3L}^{(3)}$ . Higher-order nonlinearity cannot be determined accurately as the series diverges very fast by increasing the probe Rabi frequency for this system.

## V. CONCLUSION

We have demonstrated a technique based on optical heterodyne and presented a suitable model to measure the optical nonlinearity (self-phase modulation) of a probe beam propagating through a dispersive medium accurately. The technique can also be used to measure the cross-phase modulation of the light field propagating through a highly dispersive medium. Recently, the technique has been used to demonstrate the blockade in two-photon excitations to the Rydberg state in thermal vapor [25]. We would like to extend this technique to measure the optical nonlinearity of Rydberg EIT in the blockade interaction regime in thermal vapor as well as in ultracold atoms.

## ACKNOWLEDGMENTS

We acknowledge Dushmanta Kara for assisting in performing the experiment. This experiment was financially supported by the Department of Atomic Energy, Government of India.

- [1] G. J. Milburn, *Phys. Rev. Lett.* **62**, 2124 (1989).
- [2] I. L. Chuang and Y. Yamamoto, *Phys. Rev. A* **52**, 3489 (1995).
- [3] M. D. Lukin and A. Imamoglu, *Phys. Rev. Lett.* **84**, 1419 (2000).
- [4] N. Imoto, H. A. Haus, and Y. Yamamoto, *Phys. Rev. A* **32**, 2287 (1985).
- [5] H. Schmidt and A. Imamoglu, *Opt. Lett.* **21**, 1936 (1996).
- [6] H. Wang, D. Goorskey, and M. Xiao, *Phys. Rev. Lett.* **87**, 073601 (2001).
- [7] H. Chang, H. Wu, C. Xie, and H. Wang, *Phys. Rev. Lett.* **93**, 213901 (2004).
- [8] S. Li, X. Yang, X. Cao, C. Zhang, C. Xie, and H. Wang, *Phys. Rev. Lett.* **101**, 073602 (2008).
- [9] H. Kang and Y. Zhu, *Phys. Rev. Lett.* **91**, 093601 (2003).
- [10] H. Y. Lo, P. C. Su, and Y. F. Chen, *Phys. Rev. A* **81**, 053829 (2010).
- [11] W. Chen, K. M. Beck, R. Büker, M. Gullans, M. D. Lukin, H. Tanji-Suzuki, and V. Vuletić, *Science* **341**, 768 (2013).
- [12] I. Friedler, D. Petrosyan, M. Fleischhauer, and G. Kurizki, *Phys. Rev. A* **72**, 043803 (2005).
- [13] S. Sevincli, N. Henkel, C. Ates, and T. Pohl, *Phys. Rev. Lett.* **107**, 153001 (2011).
- [14] A. V. Gorshkov, J. Otterbach, M. Fleischhauer, T. Pohl, and M. D. Lukin, *Phys. Rev. Lett.* **107**, 133602 (2011).
- [15] J. D. Pritchard, D. Maxwell, A. Gauguier, K. J. Weatherill, M. P. A. Jones, and C. S. Adams, *Phys. Rev. Lett.* **105**, 193603 (2010).
- [16] V. Parigi, E. Bimbard, J. Stanojevic, A. J. Hilliard, F. Nogrette, R. Tualle-Broui, A. Ourjoumtsev, and P. Grangier, *Phys. Rev. Lett.* **109**, 233602 (2012).

- [17] T. Peyronel, O. Firstenberg, Qi-Yu Liang, S. Hofferberth, A. V. Gorshkov, T. Pohl, M. D. Lukin, and V. Vuletić, *Nature (London)* **488**, 57 (2012).
- [18] O. Firstenberg, T. Peyronel, Qi-Yu Liang, A. V. Gorshkov, M. D. Lukin, and V. Vuletić, *Nature (London)* **502**, 71 (2013).
- [19] G. Müller, A. Witch, R. Rinkleff, and K. Danzmann, *Opt. Commun.* **127**, 37 (1996).
- [20] A. M. Akulshin, S. Barreiro, and A. Lezama, *Phys. Rev. Lett.* **83**, 4277 (1999).
- [21] A. M. Akulshin, A. I. Sidorov, R. J. McLean, and P. Hannaford, *J. Opt. B: Quantum Semiclass. Opt.* **6**, 491 (2004).
- [22] Y. Han, J. Xiao, Y. Liu, C. Zhang, H. Wang, M. Xiao, and K. Peng, *Phys. Rev. A* **77**, 023824 (2008).
- [23] A. K. Mohapatra, T. R. Jackson, and C. S. Adams, *Phys. Rev. Lett.* **98**, 113003 (2007).
- [24] R. W. Boyd, *Nonlinear Optics*, 3rd ed. (Academic, New York, 2008).
- [25] A. Bhowmick, D. Kara, and A. K. Mohapatra, *arXiv:1605.06603v1* (2016).